BULGARIAN CHEMICAL COMMUNICATIONS

Editorial

On the occasion of the 50th volume of our journal
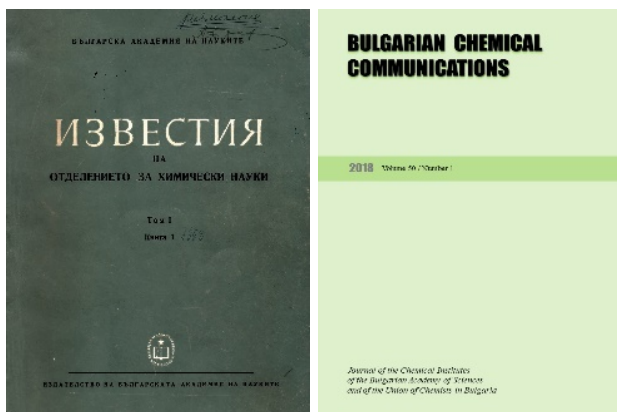
It was in 1968, when our journal has been founded. Its first name was "Communications of the Department of Chemistry" at the Bulgarian Academy of Sciences. The editorial board has included Bulgarian scientists only, but all of them with significant contributions to chemistry in the world science as a whole. There were the prominent names of D. Ivanov and B. Kurtev in organic chemistry, R. Kaischev and S. Hristov in physical chemistry, G. Bliznakov in inorganic chemistry and catalysis, D. Elenkov in chemical engineering, N. Yordanov and A. Trifonov in analytical chemistry, D. Shopov in organic catalysis, I. Panayotov in polymer science, etc. There were no foreign members of the editorial board, which was understandable for that period of time, but the names of the Bulgarian scholars in the list were good pledge for the journal quality. There were four regular issues annually for each volume.

This journal was a continuation of five separate journals on different areas of chemistry appearing in different periods from 1951 to 1967, but with modest success due to the potentials of the three existing chemical institutes in that period of time. The integration of the efforts of the Bulgarian scientists in chemistry had positive impact on the journal quality and encouraged the efforts of other Bulgarian scientists to publish their results in it. The Bulgarian Academy of Sciences was able to support financially the publication activity of its institutes. Since that time the journal is one of the Bulgarian academic issues included in the international exchange of periodicals due to its broad profile.

Until 1989 the journal was written in Bulgarian mainly with sporadic articles in other languages (Russian, English, German and French) which did not contribute to its international authority and acquaintance. After that (in 1992) it was decided to edit the journal in English only, with abstracts in Bulgarian at the end of each paper. The formal name was changed to Bulgarian Chemical Communications with translation into Bulgarian. There was an international editorial board composed in this period of time. Since 1992 the editorial board decided to publish issues dedicated to anniversaries of famous scholars in chemistry or comprising the contributions to different scientific events.

The new political and economic conditions, as well as the freedom of choice of the Bulgarian scholars to publish their scientific results abroad wherever they wanted led to a certain loss of interest to our journal. It was a hard period of time, when for the editors was difficult to find funds for the publishing process, as well as to convince the chemists in Bulgaria and abroad to publish their results in our journal. It was a critical period for the existence of the journal at all. The support of the National Scientific Fund and of some other foundations was very important for the journal survival and its further development and progress.

There was an impact-factor assigned to the journal by Thomson-Reuters in 2010. This fact had a crucial importance for the journal authority and the interest to it. Since that time the progress is enormous: there are more than 20 papers in each regular issue. Many special issues dedicated to anniversaries or conference proceedings are published. Now the contributors to the journal are from more than 25 countries throughout the globe. There were thirteen such special issues for the year 2017 and twelve more are planned for 2018! After the hard times in the 1990s the future of BCC seems brighter and more successful.

Here is suitable to mention the contribution of all members of the editorial board as well as the efforts and expertise of the journal scientific secretaries, i.e. Prof. A. Trifonov, Assoc. Prof. G. Kadinov, Assoc. Prof. Ch. Bonev, Prof. D. Yankov and Prof. E. Ivanova. Let us hope that BCC will progress in future strengthening its international authority and significance.

Prof. Venko Beschkov
Editor-in-Chief

Kinetic and equilibrium modeling of the removal of Cr (VI) ions by chemically treated *Zea mays* (Corn) cob from aqueous solutions

A. R. Abbas[1]*, Misbah[1,2], M. Riaz[1]*, M. A. Hanif [2], M. Suleman[3], Y. Gull[4]

[1]Department of Chemistry, University of Sargodha, Women Campus Faisalabad, Pakistan
[2]Department of Chemistry, University of Agriculture, Faisalabad-38040, Pakistan
[3]Department of Chemistry, Women University of Azad Jammu & Kashmir, Bagh, Pakistan
[4]Department of Chemistry, University of Sargodha, Sub-Campus Bhakkar, Bhakkar 30000, Pakistan

In the present study, biosorption of Cr (VI) from aqueous solutions was conducted using chemically treated *Zea mays* (corn) cob. The effect of various parameters like biosorbent size and dose, pH, contact time and initial metal concentration necessary for establishment of equilibrium biosorption of Cr (VI) ion using chemically treated *Zea mays* (corn) cob was studied. Biosorbent was treated with different chemicals such as NaOH, acetone and HCl for surface modification. The biosorbent dose providing maximum percentage removal (23.7 %) was 0.3 g, while with 0.5 g maximum metal uptake (14.2 mg/g) was observed. The *Zea mays* (corn) cob biosorbent shows maximum adsorption capacity for different pretreated and untreated samples. For estimation of the removal of metal, Cr (VI) concentration was analysed before and after the biosorption process by atomic absorption spectrophotometry (AAS). SEM and EDX analysis provided information on the biosorption of Cr (VI) on the biosorbent surface. The data obtained were analyzed using Langmuir isotherm and Freundlich isotherm models, pseudo first- and pseudo second-order kinetic models. From the result it followed that Langmuir isotherm and pseudo second-order kinetic model best fitted the experimental data having higher R^2 value. Finally, the results were analyzed statistically.

Keywords: Biosorption, Cr (VI), corn cob, Langmuir isotherm, Freundlich isotherm

INTRODUCTION

The world is facing a major environmental problem of water pollution with heavy metals. For the control of environmental pollution from industrial waste water, the removal of toxic heavy metals is essential. Heavy metals such as Cr, Cu, Cd, Zn, etc., are released by many industries in wastewater. Human beings are suffering from heavy metals which cause many diseases such as brain damage. Their removal from waste water is necessary as they cannot be easily degraded. Various physical and chemical methods are available to remove toxic metals present in industrial wastewater. However, they are energy consuming and expensive. Low-cost treatment systems suitable for our environment are needed. Assessing the hazard of chemical contaminants in water, one of the pathways is the uptake of pollutants from water by plants [1].

Biosorption process has major advantages; the use of low-cost biosorbent materials is helpful in minimizing the concentrations of heavy metals. [2]. Research on biosorption indicated that the metallic species are deposited through different sorption processes on solid biosorbents, and these sorption processes are complex phenomena such as chelation, complexation, ion exchange, etc. Toxic metal ions removal from polluted water by biosorbents is of importance because the latter have a high area-to-volume ratio and provide a large contact area for metal binding [3]. The *Zea mays* (corn) cob was used as a biosorbent, due to its abundance and cost effectiveness. Its availability in most developing countries makes it a strong candidate for biosorption. Corn cob was considered to be a waste material and was used as a biosorbent for pollutants removal from aqueous solutions [4]. However, corn cob would be practical, economical and useful as a metal biosorbent by direct utilization [5].

As per earlier reports *Zea mays* (corn) cob contains protein, lignin, hemicelluloses and cellulose groups. They contain carboxyl and hydroxyl groups present on cell surface of *Zea mays* (corn) cob biosorbent and are specified for metal binding, differing in affinity due to their negative charge which binds with the positive charge of the metal [6].

Cr (VI) is a toxic metal ion which is being extensively used in processing and manufacturing plants and it is present in high concentrations in the industrial wastewater of metal finishing plants, electroplating, petroleum refineries, textiles, welding, varnishes, dyes, pulp manufacture facilities and chemical industries. Chromium metal is toxic to humans and is generated by textile industry tanning and electroplating [7]. The conventional processes generally used for the

* To whom all correspondence should be sent.
E-mail: amtur_rehman@yahoo.com and riaz_453@yahoo.com

removal of chromium include precipitation as Cr $(OH)_2$, membrane filtration, reverse osmosis, ion exchange and adsorption on activated carbon. These treatments are not completely effective and are very expensive [8,9]. The main aim and objective of this study was the removal of Cr (VI) from aqueous solution and the characterization of the *Zea mays* (corn) cob.

EXPERIMENTAL

Sample preparation

Zea mays (corn) cob biosorbent used in this work was collected from local areas of Okara Pakistan. The cobs were washed comprehensively with tap and distilled water to make the surface clean from dust. After this the whole biosorbent was sun-dried and ground for further application. The ground biosorbent was sieved using various mesh size sieves (0.50, 1.00, 1.40, 1.70 mm) for optimization of the particle size in order to achieve maximum removal of metal ions by the biosorbent. Finally, the biosorbent was obtained in the form of powder.

Preparation of chromium stock solution

Potassium dichromate ($K_2Cr_2O_7$) was used for preparing the chromium stock solution. For obtaining 1000 ppm Cr (VI) stock solution, potassium dichromate $K_2Cr_2O_7$ (2.835 g) was dissolved in distilled water in a 1.0 L volumetric flask. Analytical grade reagents were used for stock solution preparation.

Chemical treatments

The biosorbent was treated with chemicals: 0.1M NaOH, acetone and HCl, for surface modification. After treatment with chemicals the biosorbent was used for further experiments [10].

Batch mode adsorption studies

The effects of various parameters: biosorbent size and dose, initial metal concentration, pH, and kinetics were studied. For biosorption studies all experiments were conducted in batch mode. Biosorbent was not chemically treated for optimization of biosorbent size and dose. The effects of other parameters like initial metal concentration, pH, and kinetics on the biosorption of metal ions using chemically treated *Zea mays* (corn) cob biosorbent were investigated.

In order to achieve maximum removal of metal ions, optimization of the biosorbent particle size (0.5, 1.00, 1.40, 1.70 mm) and dose of biosorbent (0.05, 0.10, 0.15, 0.20, 0.25, 0.30, 0.35 g) was performed. For optimization of pH, the values were adjusted to 1.0, 2.0, 0, 3.0, 4.0, 5.0 and 7.0. The pH experiments were conducted by using a buffer solution of 0.1 M HCl & NaOH [11]. Initial metal concentrations in the range of 25, 50, 100, 200, 400, 600, 800, 1000 ppm were used [12]. The contact time was varied in the range of 15, 30, 60, 120, 180, 240 min and 24 h. The quantitative uptake of metal ions showed the potential of the biosorbent for removal of heavy metals. Biosorbent samples were dipped in a 100 ppm stock solution separately for 24 h with stirring at 200 rpm. Solutions were filtered with Whatman filter paper (0.011mm) and after 10-fold dilution the filtrate was analyzed for the metal ions by AAS.

Removal efficiency of metal ion

The chromium removal percentage (R %) was determined by using the equation:

Removal efficiency (R %) = $(C_i-C_e)/C_i \times 100$ (1)

where C_e and C_i are equilibrium and initial concentration of Cr (VI) metal (ppm).

Adsorption capacity of metal ion

By using equation (1) the metal ion uptake was calculated. This equation is as follows:

$$q = V (C_i-C_e)/m \times 1000 \qquad (2)$$

where q is metal uptake or adsorption capacity of metal ion (mg/g), V is the sample volume (mL), m is the dose or mass of dry biosorbent (g), C_i, C_e are initial and equilibrium metal concentrations (ppm).

Atomic absorption spectrophotometric (AAS) analysis

Atomic absorption spectrophotometry (AAS) was used for determination of metal ion concentration.

Scanning electron microscopy (SEM) analysis

By scanning electron microscopy images of *Zea mays* (corn) cob biosorbent were recorded by using electron through electron gun. Scanning electron microscopy was also used to analyze the complex surface morphology of the biosorbent. SEM provides high resolution and magnification of field [13].

Energy dispersive X-ray (EDX) analysis

Energy dispersive X-ray (EDX) analysis is an advanced technique used for elemental and chemical characterization of the biosorbent. The energy-dispersive X-ray spectrometer measured X-rays energy emitted from a biosorbent sample in the

form of graph peaks and measured the biosorbent elemental composition [14].

RESULTS AND DISCUSSION

Effect of biosorbent size

The metal uptake (mg/g) against size (mm) of *Zea mays* (corn) cob biosorbent is shown in Fig. 1. Different biosorbent sizes (0.50-1.70 mm) were used in the experiment. The maximum uptake of Cr (VI) was observed at 0.5 mm. It was evident that by decreasing size down to 0.5 mm biosorption increased due to increased surface area and number of active sites [15]. The increase in size from 1.0 to 1.70 mm resulted in reduction of biosorbent active sites and adsorption capacity of metal uptake decreased [16,17].

Effect of biosorbent dose

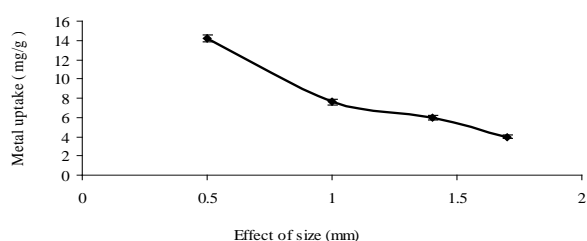Biosorbent dose had a very important effect on the removal of Cr (VI) in the batch mode adsorption studies. Adsorption experiments were carried out by varying biosorbent dose (0.05-0.35 g/100 ml). The Cr (VI) removal from *Zea mays* (corn) cob as a function of biosorbent dose is presented in Fig. 2. The optimum dose and mesh size of the *Zea mays* (corn) cob biosorbent for Cr (VI) removal were 0.3 g and 0.50 mm, respectively. From the results it followed that, by increasing biosorbent dose from 0.05 to 0.30 g the Cr (VI) percentage removal increased due to complexation of Cr (VI) ions with the biosorbent. More binding sites became available and increased the rate of percentage removal of the metal ion. However, with 0.35 g biosorbent dose slow increase in removal and slow attainment of equilibrium between biosorbent and adsorbate was noted [18]. With further increase in dose after 0.30 g, the removal of metal decreased due to the interference by the dense outer layer of cells or screening effect of the biosorbent [19].
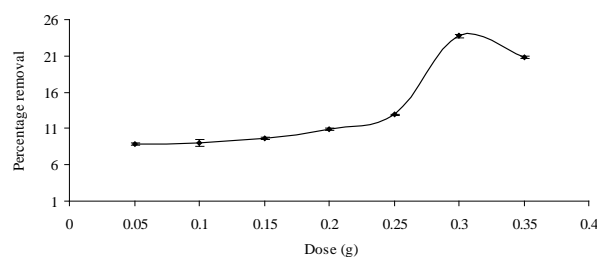

Fig. 1. Effect of size on Cr (VI) biosorption by *Zea mays* (corn) cob biosorbent

Fig. 2. Effect of dose on Cr (VI) biosorption by *Zea mays* (corn) cob biosorbent

Effect of biosorbent pH

The effect of biosorbent pH on Cr (VI) adsorption by *Zea mays* (corn) cob was studied at different pH values from 1.0 to 7.0 (Fig. 3). Cr (VI) adsorption capacity increased by increasing pH from 1.0 to 2.0, then it decreased from pH 3.0 to 7.0. Cr (VI) adsorption capacity was maximum at pH 2. At pH 1 the adsorption capacity of the metal ion was lower as compared to pH 2 due to the acidic nature of chromium solution, because more protonation caused less adsorption. The effect of pH can be interpreted on the basis of the chromium specification and Cr (VI) adsorption by the biosorbent. At lower pH, the solution of chromium ions contains a smaller number of hydrogen chromate ions and a larger number of dichromate $(Cr_2O_7^{2-})$ ions. According to the overall equilibrium, the dichromate $(Cr_2O_7^{2-})$ ions were shifted by equilibrium in the range of pH 3 to 7. Furthermore, the biosorbent surface at pH 2 may be positively charged. At pH 2, $HCrO_4^-$ ion from chromium solution binds to the acidic functional groups on the biosorbent surface through electrostatic attraction and adsorption of Cr (VI)

onto biosorbent. On further pH from 3.0 to 7.0, biosorption decreased because carboxylate groups exist in alkali conditions in deprotonated form and surface charge on the biosorbent became negative. As per earlier reports on other biosorbent same trend was observed [20,21].
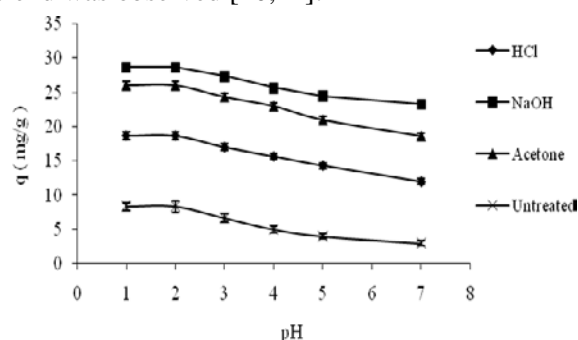

Fig. 3. pH effect on Cr (VI) by *Zea mays* (corn) cob biosorbent

Effect of chemical treatment

The chemical treatments of *Zea mays* (corn) cob may reduce or enhance the adsorption capacity of the biosorbent. It may change the biosorbent surface either by exposure of greater metal binding sites and masking or removing the functional

9

groups in the biosorbent. All three chemically treated and untreated samples exhibited different biosorption capabilities in the following order: NaOH > acetone > HCl > untreated sample. Maximum increase in Cr (VI) biosorption was shown by NaOH treated *Zea mays* (corn) cob biosorbent as shown in Fig. 4. Treatment with NaOH of biosorbent lignocellulose materials caused a decrease in polymerization degree, crystallinity, leading, swelling and increase in internal surface area, separation or disruption of biosorbent structural linkages between carbohydrates and lignin [22]. Treatment of the biosorbent with acetone caused a slight increase in the Cr (VI) adsorption capacity of *Zea mays* (corn) cob biosorbent. Treatment with acetone removed the lipid and protein fractions from the biosorbent surface. Hence, this treatment improved the adsorption capacity and exposure of more metal binding sites of biosorbent [23]. HCl was used to treat the lignocellulose materials of the biosorbent. After HCl treatment, binding of H^+ ions to the biosorbent caused a lower adsorption of Cr (VI). This result indicated that HCl may covalently bind to the biosorbent adsorbing surface and destroy the H^+ ions of their adsorbing groups. Thus, biosorbent electronegativity may change due to H^+ ions of HCl resulting in a decrease in adsorption capacity of the biosorbent [24].
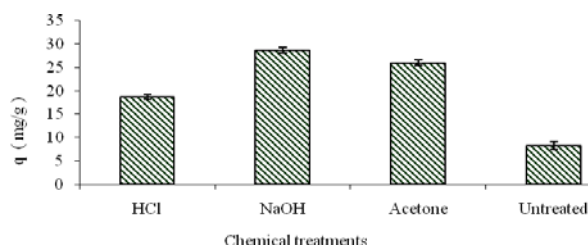

Fig. 4. Effect of treatment of *Zea mays* (corn) cob biosorbent

Effect of biosorbent initial metal concentration

By increasing initial metal ion concentration from 25 to 800 ppm the adsorption capacity/metal uptake of the biosorbent increased. Saturation of the biosorbent at 800 to 1000 ppm was done by further increase in initial metal ion concentration. Different metal ion concentrations from 25-1000 ppm were used as shown in Fig. 5. Initial metal concentration from 25 to 200 ppm showed greater

adsorption as compared to 200-800 ppm. Concentration ranges from 25 to 200 ppm, increased the metal uptake by NaOH treated sample (5.33 to 38.75 mg/g), acetone treated sample (4.33 to 33.33 mg/g), HCl treated sample (3.67 to 30.33 mg/g) and untreated sample (3.00 to 25.00 mg/g) and minor increase in adsorption was observed from 200 to 800 ppm while concentration ranges from 800 to 1000 ppm seem to be saturated. Adsorption capacity of the metal ion increased at higher concentrations because, through intraparticle diffusion the metal diffused to the biosorbent surface. However, the metal occupies the biosorbent adsorption sites more rapidly at low concentrations [25].
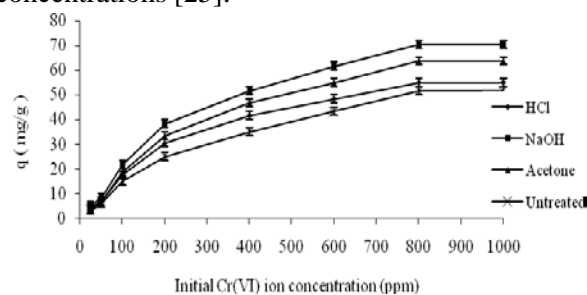

Fig. 5. Effect of initial Cr (VI) concentrations by *Zea mays* (corn) cob biosorbent

Isotherms for biosorption of chromium

The Freundlich and Langmuir isotherm adsorption models were applied to the equilibrium data of *Zea mays* (corn) cob biosorption of Cr (VI) [26].

Langmuir isotherm for biosorption of chromium

The Langmuir isotherm equation for biosorption of Cr (VI) was chosen for the estimation on the biosorbent surface of complete mono layer coverage and maximum adsorption capacity of metal ion on the biosorbent surface as shown in Fig. 6. The Langmuir related parameters are shown in Table 1. Equilibrium data were used to correlate the data with the help of Langmuir equation by using the equation [27]:

$$C_e/q_e = 1/q_{max} K_L + (1/q_{max}) C_e \qquad (3)$$

where K_L is Langmuir isotherm constant (ppm), C_e is equilibrium adsorption of metal concentration (ppm),

Table 1. Langmuir and Freundlich isotherms for Cr (VI) biosorption on *Zea mays* (corn) cob biosorbent

Treatment of biosorbent	Experimental	Langmuir isotherm constants			Freundlich isotherm constants			
	q_{max} (mg/g)	X_m (mg/g)	K_L (L/mg)	R^2	q_e (mg/g)	K_F (mg/g)	1/n	R^2
Untreated	63.66	79.36	0.0022	0.9049	4124.4	2.2977	0.7337	0.9672
HCl	55.00	68.96	0.0050	0.9763	2445.1	1.0480	0.6424	0.9085
Acetone	51.66	82.64	0.0050	0.9606	2379.8	1.1102	0.6393	0.9012
NaOH	70.33	79.36	0.0071	0.9833	1411.6	1.8902	0.5771	0.9091

$q_{max.}$ is maximum biosorbent monolayer adsorption capacity (mg/g).

The graph, (C_e/q_e) vs. C_e was drawn. By applying Langmuir equation, intercept K_L and slope $(1/q_{max})$ were calculated. The Langmuir isotherm model as compared to Freundlich isotherm model fitted better to the experimental data as shown from the value of its constants. R^2 and q_{max} values of each pretreated or untreated sample were found: NaOH (0.9809, 70.33 mg/g), acetone (0.9595, 51.66 mg/g), HCl (0.9738, 55.00 mg/g) and untreated sample (0.9678, 63.66 mg/g).
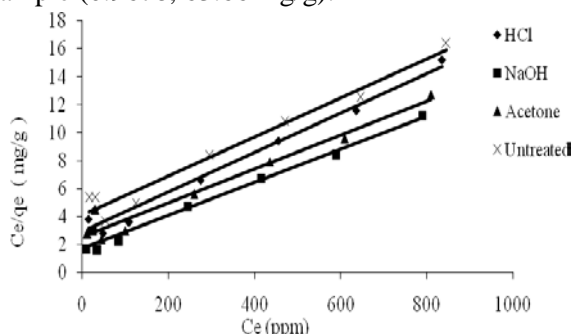

Fig. 6. Langmuir isotherm for Cr (VI) biosorption by *Zea mays* (corn) cob biosorbent

Freundlich isotherm for biosorption of chromium

At a given temperature it presents the equilibrium relationship between the concentrations of metal in the adsorbent and in the fluid phase. Freundlich isotherm can be applied in case of intermediate and low concentration ranges or it can be presented as isotherm equation of empirical adsorption [28]:

$$\ln q_e = \ln K_f + n \ln C_e \qquad (4)$$

where n and K_f are the Freundlich constants, C_e is concentration of metal at equilibrium (ppm), q_e is adsorption capacity of biosorbent at equilibrium (mg/g). The Freundlich isotherm graph, log q_e *vs.* log C_e is presented in Fig. 7.
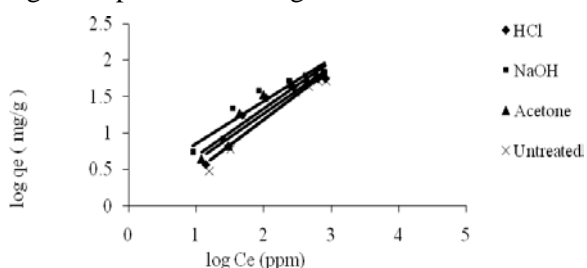

Fig. 7. Freundlich isotherm for Cr (VI) biosorption by *Zea mays* (corn) cob biosorbent

Separation factor (R_L)

In a batch adsorption process, the separation factor can be used to calculate unfavorable or favorable adsorption system. The graph of initial metal concentration vs. separation factor (R_L) of adsorption of Cr (VI) on *Zea mays* (corn) cob is presented in Fig. 8. R_L values between 1 and 0 show the favorable isotherm. From the Langmuir isotherm based equation R_L was calculated [29]:

$$R_L = 1/ (1 + K_L C_i) \qquad (5)$$

where C_i is initial Cr (VI) concentration (ppm), K_L is Langmuir constant, R_L parameter presents the shape of the isotherm and nature of the sorption process: $R_L = 1$ = linear isotherm, $R_L > 1$ = unfavorable isotherm, $R_L = 0$ = irreversible isotherm, $0 < R_L < 1$ = favorable isotherm.
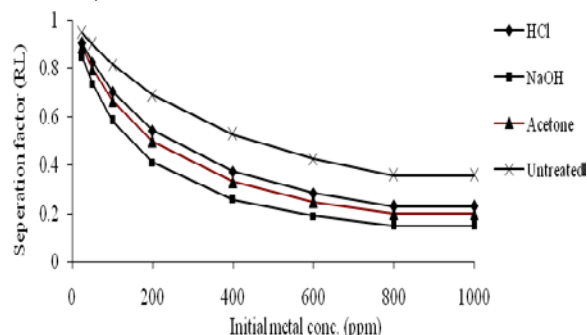

Fig. 8. Separation factor against initial metal concentration for biosorption of Cr (VI) by *Zea mays* (Corn) cob biosorbent

Surface coverage (θ)

By using Langmuir type equation the part of biosorbent surface covered by Cr (VI) was studied (Eq. (6) and Fig. 9).

$$\theta = K_L C_i (1-\theta) \qquad (6)$$

Where C_i is initial Cr (VI) concentration (ppm), K_L is Langmuir adsorption coefficient. The surface coverage increased and the surface was almost completely covered with monolayer by increase in initial Cr (VI) concentration from 25 to 800 ppm. The rate of adsorption became independent if Cr (VI) concentration was higher than 800 ppm. This is because at higher levels of concentration of Cr (VI) the surface coverage decreased extensively [30].
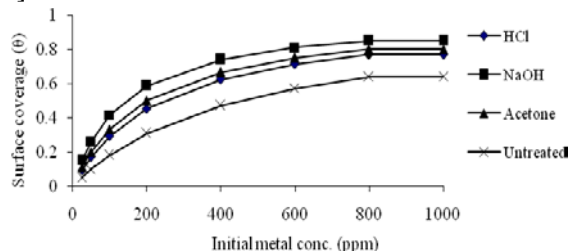

Fig. 9. Surface coverage (θ) *vs.* initial Cr (VI) concentration (ppm) for *Zea mays* (corn) cob biosorbent

Effect of kinetics

The kinetics of Cr (VI) adsorption is shown in Fig. 10. After the first 15 min the adsorption capacity of Cr (VI) was found to be fast and indicating an equilibration point after 180 min. Cr (VI) adsorption capacity was found to increase slowly until saturation level was attained. Most favorable time observed was 180 min at which metal adsorption capacity was 82.9 (0.30 g, 0.50 mm) for *Zea mays* (corn) cob biosorbent. The adsorption process of Cr (VI) took place in two stages. The first stage was more rapid than the second stage, because in the first 120 min 70% adsorption was completed. In the second stage 30% progressive adsorption was observed. The rapid initial biosorption may be attributed to accumulation of metal on biosorbent surface and the large surface area of the biosorbent. In the second stage a slower occupation of biosorbent sites was noted. The reason for the slower process after the saturated level is that initially deposited metal ions enter to the inside through intra-particle dispersion of the biosorbent. Other similar studies are in accordance with these observations [31]. In case of *Zea mays* (corn) cob the contact time increased with the increase in Cr (VI) adsorption capacity of biosorbent. Fast adsorption occurred from 15 to 120 min, accelerated biosorption was observed later on, because of the availability of vacant surface sites in a large number of initially biosorbent for adsorption and after some time due to repulsive forces the remaining vacant surface sites may be exhausted between the bulk and solid phase of molecules of biosorbent [32].

Adsorption kinetic studies

The adsorption kinetic studies of *Zea mays* (corn) cob biosorbent describe the rate of Cr (VI) ion uptake which controls the equilibrium time. These adsorption kinetic models integrated first- and second-order equations.
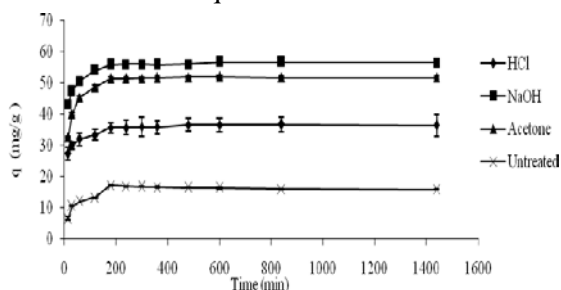

Fig. 10. Effect of kinetics on Cr (VI) biosorption by *Zea mays* (corn) cob biosorbent

Pseudo first-order model

The pseudo first-order rate equation is described as:

$$\log (q_e - q_t) = \log (q_e) - (k_1/2.303)t \tag{7}$$

where q_e is Cr (VI) metal ion concentration adsorbed by the biosorbent mass at equilibrium (mg/g), q_t is Cr adsorbed by the biosorbent measured in (mg/g), k_1 is rate constant (min^{-1}) [33]. A graph plot of time *vs.* log (q_e-q_t) presents a straight line of intercept of log (qe).and slope (k_1/2.303) as shown in Fig. 11.
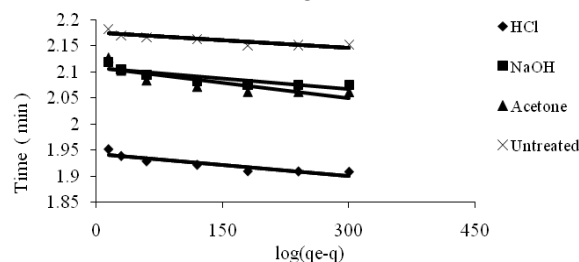

Fig. 11. Kinetic modeling of the biosorption of Cr (VI) by *Zea mays* (corn) cob pseudo first-order model
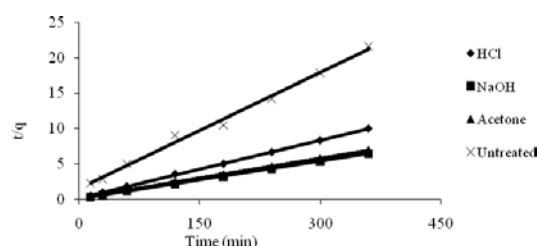

Fig. 12. Kinetic modeling by Cr (VI) *Zea mays* (corn) cob pseudo second order model.

Pseudo second-order model

Adsorption data of this model are given by an equation:

$$t/q_t = 1/K_2(q_e)^2 + (1/q_e)t \tag{8}$$

where q_t and q_e are the adsorption capacities at time t and at equilibrium, K_2 is the equilibrium rate constant (g/mg min). The graph of time *vs.* t/q has a slope (1/qe) and intercept of $1/k_2 (q_e)^2$ as shown in Fig. 12. From the result it is obtained that R^2 and q_e values of each treated or untreated sample (see Table 2) are: NaOH (0.9999, 56.81 mg/g), acetone (0.9999, 53.19 mg/g), HCl (0.9997, 36.63 mg/g) and untreated sample (0.9938, 18.24 mg/g). Hence, pseudo second-order is the most favorable isotherm for *Zea mays* (corn) cob biosorbent [34].

Scanning electron microscopy

The scanning electron micrographs of *Zea mays* (corn) cob biosorbent before and after Cr (VI) adsorption are shown in Figs. 13 and 14 respectively.

Table 2. Pseudo first- and pseudo second-order kinetic models for Cr (VI) biosorition on *Zea mays* (corn) cob biosorbent

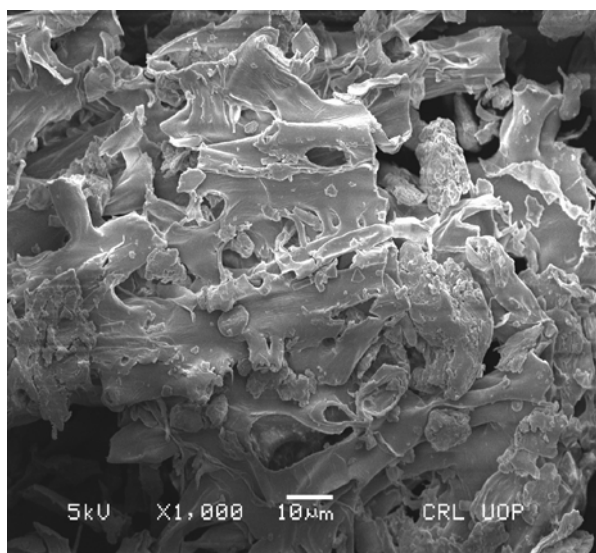| Treatment of biosorbent	Experimental	Pseudo first-order constants			Pseudo second-order constants		
	q_{max}(mg/g)	qe(mg/g)	k_1(min^{-1})	R^2	qe(mg/g)	k_2(g/mg min)	R^2
Untreated	15.933	149.86	2.30×10^{-4}	0.8005	18.24	2.06×10^{-3}	0.9938
HCl	36.466667	87.72	2.30×10^{-4}	0.8234	36.63	3.78×10^{-3}	0.9997
Acetone	51.733	128.43	4.60×10^{-4}	0.7199	53.19	1.95×10^{-2}	0.9999
NaOH	15.933	128.43	2.30×10^{-4}	0.7623	56.81	3.13×10^{-3}	0.9999

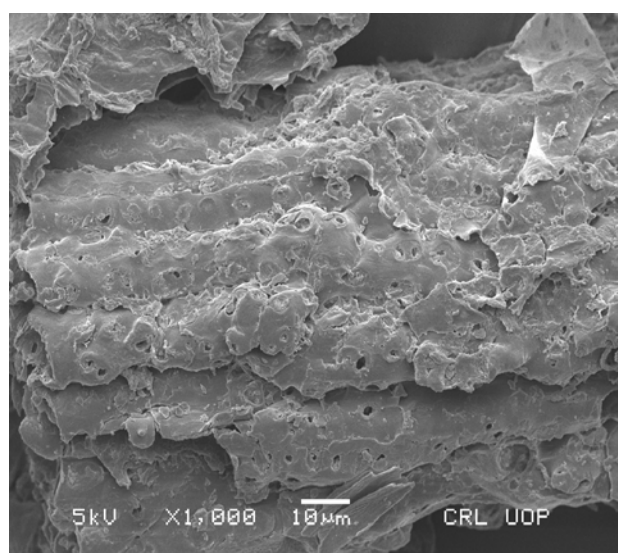**Fig. 13.** SEM image of *Zea mays* (corn) cob biosorbent before Cr (VI) adsorption

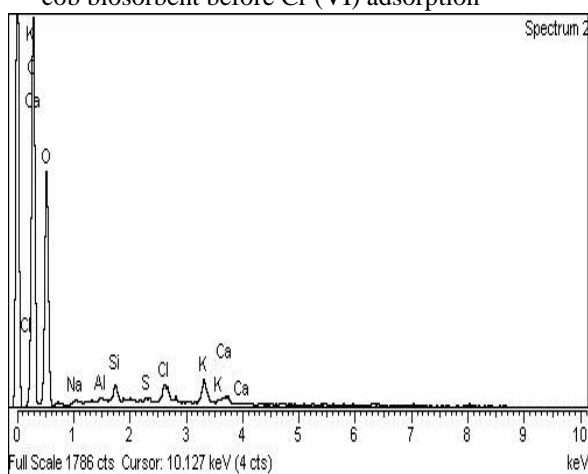**Fig.14.** SEM image of *Zea mays* (corn) cob biosorbent after Cr (VI) adsorption

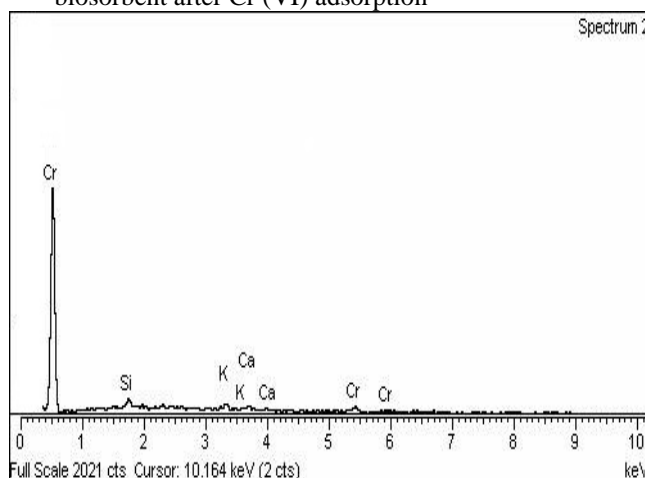**Fig. 15.** EDX spectra of *Zea mays* (corn) cob before Cr (VI) adsorption

Fig. 16. EDX spectra of *Zea mays* (corn) cob after Cr (VI) adsorption

The surface morphology of different parts of both biosorbent materials would facilitate the adsorption of metal ions and the surface was found to be porous and irregular. The SEM micrographs of the biosorbent showed that pores with different shapes and different sizes existed on the external surface of *Zea mays* (corn) cob. The SEM micrograph of *Zea mays* (corn) cob before Cr (VI) adsorption showed larger surface area, pore space, pore volume and number of pores available (Fig. 13) while after Cr (VI) adsorption there was reduction of surface area, pore space and number of

pores available (Fig. 14) due to binding of positive sites of Cr (VI) with negative sites of biosorbent. Hence, metal adsorption was found to be maximum [12].

Energy dispersive X-ray analysis

The energy dispersive X-ray (EDX) spectra of *Zea mays* (corn) cob biosorbent before and after Cr (VI) adsorption are shown in Figs. 15 and 16, respectively. The EDX peaks for Cr (VI) were observed and this technique was used qualitatively. The EDX spectra show absence of Cr (VI) peak

before biosorption and appearance of Cr (VI) adsorption peak after biosorption. Appearance of Cr (VI) peaks means that the biosorbent adsorbed the Cr (VI) metal ion because biosorbent surface has active groups such as oxygen, carbon and nitrogen groups which bind the metal ion [35].

CONCLUSIONS

The present work shows that the dried biosorbent of *Zea mays* (corn) cob has ability to remove heavy metals like Cr (VI) from aqueous solutions. In batch mode adsorption studies different parameters were optimized, like biosorbent size and dose, initial metal concentration, pH, and contact time.

Effect of biosorbent size and dose: Effect of biosorbent size and dose was optimized without pretreatment of biosorbent with chemicals. Optimum size was found to be 0.5 mm. Higher adsorption was observed for biosorbents chemically pretreated with sodium hydroxide, acetone and hydrochloric acid. Biosorbent treated with chemicals showed adsorption capacity in the following order: NaOH > acetone > HCl > untreated sample. The optimum biosorbent dose was 0.3 g, and the optimum size was 0.5 mm.

Effect of pH, initial concentration and contact time: The *Zea mays* (corn) cob biosorbent showed maximum adsorption capacity for different pretreated (NaOH, acetone, HCl) and untreated samples. The effect of pH, initial metal concentration and contact time for treated and untreated samples was studied and maximum adsorption was observed at pH 2, 800 ppm and 180 min, respectively.

Kinetic isotherm model and surface characterization: Kinetic isotherm models such as pseudo second-order and Langmuir isotherm adsorption model were also studied for removal of Cr (VI). Biosorbent samples were analyzed before and after biosorption by SEM for surface morphology of biosorbent and EDX. The presence of metal ion peak confirmed that the biosorbent adsorbs Cr (VI) metal ions. It can be concluded from the present study that chemically treated *Zea mays* (corn) cob powder could be employed as an eco-friendly and cost-effective biosorbent for removal of heavy metal from aqueous solution.

REFERENCES

1. S. Yapoga, Y. B. Ossey, V. Kouame, *Int. J. Conserv. Sci.* **4**, 81 (2013).
2. . F. Ekmekyapar, A. Aslan, Y. K. Bayhan, A. Cakici, *J. Hazard. Mater.* **137**, 293 (2006).
3. S. Pandiyan, D. Mahendradas, *Eur. J. Sci. Res* **52**, 345 (2011).
4. W. Tsai, C. Chang, S. Wang, C. Chang, S. Chien, H. Sun, *Res. Coserv. Rec.* **32**, 43 (2001).
5. J.-L. Lin, H. M. Keener, R. H. Essenhigh, *Combust. Flame* **100**, 271 (1995).
6. B. Barl, C. G. Biliaderis, E. D. Murray, A. W. Macgregor, *J. Sci. Food Agri.* **56**, 195 (1991).
7. M. Saifuddin, P. Kumaran, *Electron. J. Biotechnol.* **8**, 43 (2005).
8. G. Rojas, J. Silva, J. A. Flores, A. Rodriguez, M. Ly, H. Maldonado, *Sep. Purif. Technol.* **44**, 31 (2005).
9. Y. Sag, Y. Aktay, *Process Biochem.* **36**, 157 (2000).
10. R. De Carvalho, K. H. Chong, B. Volesky, *Biotechnol. Prog.* **11**, 39 (1995).
11. G. M. Matei, J. K. Kiptoo, N. K. Oyaro, A. O. Onditi, *Facta Univ. Phys. Chem. Technol.* **12**, 1 (2014).
12. D. Krishna, R. P. Sree, *Int. J. Appl. Sci. Eng.* **11**, 171 (2013).
13. S. Renganathan, J. Kalpana, M. Dharmendira Kumar, M. Velan, *CLEAN–Soil, Air, Water* **37**, 901 (2009).
14. J. Goldstein, D. E. Newbury, P. Echlin, D. C. Joy, A. D. Romig Jr, C. E. Lyman, C. Fiori, E. Lifshin, Scanning electron microscopy and X-ray microanalysis: a text for biologists, materials scientists, and geologists, 2nd Edition ed. Springer Science & Business Media, New York, 2012.
15. G. Agarwal, H. K. Bhuptawat, S. Chaudhari, *Bioresour. Technol.* **97**, 949 (2006).
16. V. K. Gupta, I. Ali, *J. Colloid Interface Sci.* **271**, 321 (2004).
17. V. Sarin, K. K. Pant, *Bioresour. Technol.* **97**, 15 (2006).
18. M. Rao, A. Parvate, A. Bhole, *Indian J. Environ. Prot.* **22**, 17 (2002).
19. N. R. Bishnoi, A. Pant, P. Garima, *J. Sci. Ind. Res.* **63**, 813 (2004).
20. D. Park, Y.-S. Yun, J. M. Park, *Chemosphere* **60**, 1356 (2005).
21. A. J. Priya, S. R. Gajulapalli, K. Abburi, V. M. Boddu, *Bioremediat. J.* **12**, 145 (2008).
22. Y. Sun, J. Cheng, *Bioresour. Technol.* **83**, 1 (2002).
23. R. Ashkenazy, L. Gottlieb, S. Yannai, *Biotechnol. Bioeng.* 55, 1 (1997).
24. F. Bux, H. Kasan, *Water S. A.* **20**, 73 (1994).
25. S. Bai, T. E. Abraham, *Bioresour. Technol.* **79**, 73 (2001).
26. U. Freundlich, *Z. Phys. Chem* **57**, 387 (1906).
27. M. A. Hussain, A. Salleh, P. Milow, *Am. J. Biochem. Biotechnol.* **5**, 75 (2009).
28. M. Temkin, V. Pyzhev, *Acta Physio. Chim.* **12**, 217 (1940).
29. M. A. Hanif, R. Nadeem, H. N. Bhatti, N. R. Ahmad, T. M. Ansari, *J. Hazard. Mater.* **139**, 345 (2007).
30. M. Riaz, R. Nadeem, M. A. Hanif, T. M. Ansari, *J. Hazard. Mater.* **161**, 88 (2009).

31. M. R. Sangi, A. Shahmoradi, J. Zolgharnein, G. H. Azimi, M. Ghorbandoost, *J. Hazard. Mater.* **155**, 513 (2008).

32. S. Qaiser, A. R. Saleemi, M. Umar, *J. Hazard. Mater.* **166**, 998 (2009).

33. G. Donmez, Z. Aksu, *Process Biochem.* **38**, 751 (2002).

34. Y. Sag, Y. Aktay, *Biochem. Eng. J.* **12**, 143 (2002).

35. M. Figueira, B. Volesky, H. Mathieu, *Environ. Sci. Technol.* **33**, 1840 (1999).

КИНЕТИЧНО И РАВНОВЕСНО МОДЕЛИРАНЕ НА СОРБЦИЯТА НА CR (VI) ВЪРХУ ХИМИЧНО МОДИФИЦИРАНИ КОЧАНИ ОТ ЦАРЕВИЦА (*ZEA MAYS*) ВЪВ ВОДЕН РАЗТВОР

А. Р. Абас[1]*, Мисбах[1,2], М. Риаз[1]*, А. Ханиф[1], М. Сулеман[3], И. Гул[4]

[1]*Департамент по химия, Университет на Саргода, Женски кампус, Файзалабад, Пакистан*

[2] *Департамент по химия, Селскостопански университет, Файзалабад 38040, Пакистан*

[3]*Департамент по химия, Женски университет на Азад Джаму и Кашмир, Баг, Пакистан*

[4] *Департамент по химия, Университет на Саргода, кампус Бхакар, Бхакар 30000, Пакистан*

(Резюме)

В настоящата статия е изследвана биосорбцията на Cr (VI) върху химично обработени кочани от царевица (*Zea mays*). Изследвано е влиянието на различни параметри като размер на частиците и количество на биосорбента, pH, време за контакт и първоначална концентрация на металния йон върху достигането на сорбционно равновесие. Биосорбентът е обработен предварително с различни реагенти като NaOH, ацетон и HCl за модифициране на повърхността му. Количеството биосорбент, осигуряващо максимално извличане (23.7 %) е 0.3 g, докато с 0.5 g извличането е 14.2 mg/g. За оценка на степента на сорбция, концентрацията на Cr (VI) е определяна преди и след биосорбцията чрез AAS анализ. Чрез SEM и EDX анализ е получена информация за биосорбцията на Cr (VI) върху повърхността на сорбента. Получените данни са анализирани с помощта на изотермите на Langmuir и Freundlich и с кинетични модели от псевдопърви и псевдовтори порядък. От резултатите следва, че изотермата на Langmuir и кинетичният модел от псевдовтори порядък съответстват най-добре на експерименталните данни (най-високи стойности на R^2). Резултатите са обработени статистически.

Preparation of carbon paste electrode containing polyaniline-activated carbon composite for amperometric detection of phenol

H. Arslan[1]*, D. Şenarslan[2], B.S. Çevrimli[3], H. Zengin[4], D. Uzun[1], F. Arslan[1]

[1]**Department of Chemistry, Faculty of Sciences, Gazi University, 06500, Ankara, Turkey*
[2]*Department of Chemistry, Institute of Sciences, Gazi University, Ankara, Turkey*
[3]*Department of Chemical Technology, Ataturk Vocational College, University of Gazi, 06500 Ankara, Turkey*
[4]*Department of Chemistry, Faculty of Arts and Sciences, Gaziantep University, Gaziantep, Turkey*

In this study, a novel carbon paste electrode was prepared using the salt form of polyaniline (pani)-activated carbon composite sensitive to phenol. Polyphenol oxidase enzyme was immobilized to the modified carbon paste electrode by cross-linking with glutaraldehyde. The amperometric determination is based on the electrochemical reduction of o-quinone generated in the enzymatic reaction of phenol at -0.15 V *vs.* Ag/AgCl. The effects of pH and temperature were investigated and optimum values were found to be 8.0 and 45 °C, respectively. The linear working range of the electrode was 1.0×10^{-6} - 5.0×10^{-5} M, R^2 =0.9819. The storage stability and operation stability of the enzyme electrode were also studied.

Keywords: Phenol, polyphenol oxidase, biosensor, polyaniline (pani), polyaniline activated carbon composite, carbon paste

INTRODUCTION

Carbon paste electrodes are widely used in electroanalysis owing to their low background current, wide potential window, chemical inertness, simple and fast preparation from inexpensive materials. Carbon paste electrodes (CPE) can also be easily modified with electrocatalysts or enzymes by means of simply mixing the modifier into the carbon paste matrix. In addition, the carbon paste electrode offers a renewable electrode surface [1].

A large variety of phenolic compounds exists. Some of them may have harmful effects for the health [2]. Their accurate determination is of great importance due to their toxicity and persistency in the environment, and the detrimental effect of phenols on human health requires a strict directive for the identification and quantification of such compounds [3-5].

For phenolic compounds determinations, polyphenol oxidase (also known as tyrosinase, EC 1.14.18.1), which is a copper containing enzyme, is used [6]. This enzyme catalyses phenol oxidation and *o*-quinone is the product of the enzymatic reaction. This is accomplished in two reaction steps. In the first step, tyrosinase oxidizes phenol into the corresponding catechol. In the second step, the catechol is oxidized into *o*-quinone. Amperometric reduction of the generated o-quinone is then used as the quantification method [7, 8].

A variety of methods for the immobilization of tyrosinase with an electrochemical transducer have been reported such as cross-linking on the surface of electrodes [9-11], incorporation within a carbon paste matrix [12, 13], entrapment in polymer films [6, 14, 15].

In this study, a novel carbon paste electrode using the salt form of polyaniline (pani)- activated carbon composite sensitive to phenol, was prepared. Polyphenol oxidase enzyme was immobilized on the carbon paste electrode containing polyaniline-activated carbon by cross-linking with glutaraldehyde. The optimum working conditions of the modified carbon paste (MCPE) with respect to the substrate concentration, the pH and temperature were investigated. The storage stability and operation stability of the biosensor were investigated.

Materials and methods

Apparatus: The electrochemical studies were carried out using a CHI 660B electrochemical workstation with a three-electrode cell. The working electrode was a carbon paste (diameter of 1.0 cm, length of 5 mm) Teflon electrode. The auxiliary and reference electrodes were Pt wire and Ag/AgCl electrode (3 M KCl), respectively. The pH values of the buffer solutions were measured with an Orion Model 5 Star pH/ion meter. Temperature control was achieved with a Grant W14 thermostat.

Chemicals: Polyphenol oxidase (EC 1.14.18.1, with an activity of 10 unit/mL) and phenol were purchased from Sigma. Graphite powder and nujol were supplied by Merck and Sigma, respectively. All other chemicals were obtained from Sigma. All

---

* To whom all correspondence should be sent.
E-mail: halit@gazi.edu.tr; dr.halitarslan@gmail.com

solutions were prepared using double distilled water.

Preparation of modified carbon paste electrode (MCPE)

The carbon paste was prepared with 2 mg polyaniline-activated carbon composite by thoroughly mixing 100 µL of nujol with 0.15 g of graphite powder in a mortar [16]. Polyaniline-activated carbon composite was synthesized according to Zengin and Kalaycı [17]. For the preparation of the carbon paste electrode a glass tube (diameter of 1.0 cm, length of 0.5 cm) was filled with the paste. Height of the paste in the tube was 0.5 cm. The electrode surface was smoothed on a paper to produce a reproducible working surface. Electric contacts were made by platinum wire. 75 µL of polyphenol oxidase enzyme (10 unit/mL), 1 mg of bovine serum albumin, 50 µL of 0.1M phosphate buffer of pH 8.0 and 30 µL of 2.5% glutaraldehyde were dropped upon the carbon paste electrode containing polyaniline - activated carbon composite. The electrode was dried at room temperature and washed with buffer solution (0.1 M phosphate buffer, pH 8.0,) several times in order to remove the non-immobilized excess enzyme and glutaraldehyde. The electrode was kept in a refrigerator at 4° C in phosphate buffer when it was not in use.

Electrochemical measurements

The quantification of phenol was achieved *via* electrochemical detection of the enzymatically released *o*-quinone. The modified carbon paste electrode (MCPE) was immersed into the phosphate buffer (0.1 M) of pH 8.0. The solution contained 0.1 M sodium perchlorate as supporting electrolyte. The electrode was brought to equilibrium by keeping at -0.15 V (*vs*. Ag/AgCl electrode (3 M KCl)). Steady current (i_a) was recorded. Phenol solution was added to the cell and the system was stirred. The currents (i_b) obtained at -0.15 V were recorded. The current values ($\Delta i = i_b - i_a$) were plotted against the phenol concentrations.

RESULTS AND DISCUSSION

In this study, we reported a new amperometric biosensor for the determination of phenol. Polyphenol oxidase (tyrosinase) enzyme was immobilized onto a carbon paste electrode containing polyaniline-activated carbon by cross-linking with glutaraldehyde. The amperometric determination is based on the electrochemical reduction of o-quinone generated in the enzymatic reaction of phenol at -0.15 V *vs*. Ag/AgCl. Reaction scheme 1 shows the phenol determination.

According to this scheme, a biochemical reaction occurs between phenol in solution and tyrosinase enzyme which are immobilized onto the carbon paste electrode containing polyaniline-activated carbon. Firstly, phenol is oxidized to catechol. Then, the catechol is oxidized into *o*-quinone. By taking the electron, oxygen is reduced to H_2O. Phenol determination was made by measuring the reduction current to *o*-quinone on the electrode surface.

The parameters affecting the performance of the biosensor and the optimum working conditions were investigated.
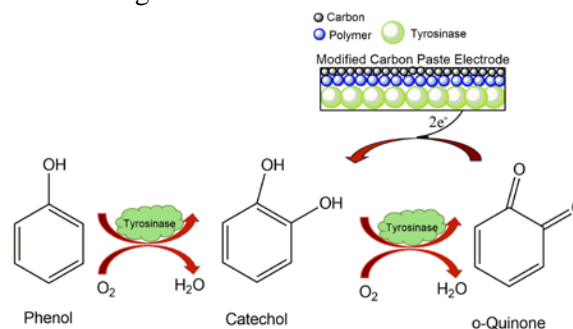
Scheme 1. Reaction scheme of phenol determination

Working potential

After preparing the modified carbon paste electrode (MCPE), the electrochemical reduction of o-quinone generated in the enzymatic reaction of phenol was carried out at different potentials (-0.07, -0.11, -0.15, -0.19 V) (Fig. 1). In all cases, as shown in Figure 1, the highest current differences and correlation coefficient were obtained at -0.15 V. Therefore, -0.15 V was used as working potential in the following studies.
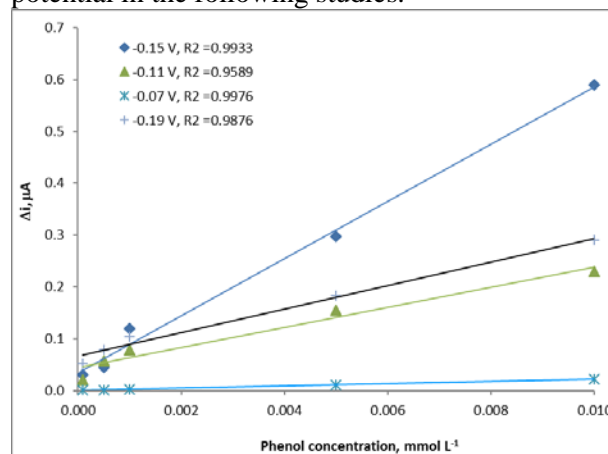

Fig. 1. The effect of potential on the response of the modified carbon paste electrode to *o* quinone (at 25 °C, 0.1 M pH =8.0 phosphate buffer, -0.15 V operating potential).

Determination of optimum pH

Since enzyme activity is dependent on the ionization state of the amino acids in the active site,

pH plays an important role in maintaining the proper conformation of an enzyme. The effect of pH on the response to phenol of MCPE was determined in 0.1 M phosphate buffer, in the pH range 6.0-10.0. The measurements were performed at a constant phenol concentration of 1.0×10^{-5} M. Figure 2 shows that the maximum response was obtained at pH 8.0. For MCPE, pH values different from 8.0 were employed in the literature (pH 7.5; 6.5) [14, 18]. In another study by Arslan *et al.* the optimum pH was found to be 8.0 [15].
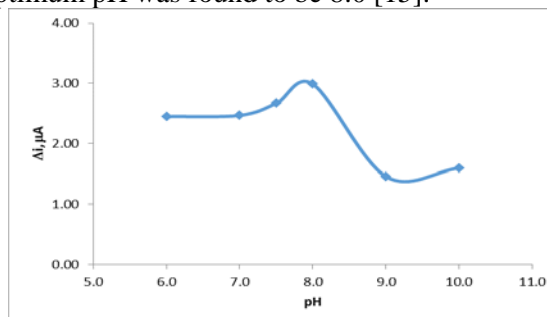

Fig. 2. Effect of pH on the response of MCPE (at 25 °C, 1.0×10^{-5} M phenol, -0.15 V operating potential).

Determination of optimum temperature

Enzymes are known to be sensitive to changes in temperature. The relationship between reaction rate of an enzyme and temperature is exponential. The temperature influence on the response of phenol MCPE was tested between 20ºC and 60ºC at pH 8.0 using constant phenol concentration of 1.0×10^{-5} M. As seen from the Figure 3, the current difference increases with temperature up to 45ºC and decreases afterwards. The highest electrode response was obtained at 45ºC. For MCPE, temperature values different from 45ºC were employed in literature (30, 40, 21 ºC) [9, 15, 18]. The study was carried out at 25ºC due to the difficulties involved in working at 45 °C.
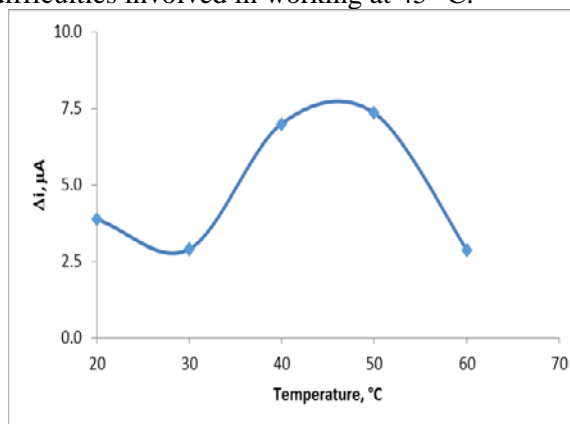

Fig. 3. The effect of temperature on the response of MCPE (at pH 8.0, 1.0×10^{-5} M phenol at -0.15 V operating potential).

Effect of substrate concentration on response of MCPE and calibration curve

The effect of substrate concentration on the reaction rate, catalyzed by immobilized PPO, was studied using varying concentrations (1.0×10^{-6} – 1.0×10^{-3} M) of phenol (Figure 4). The linear working range of the electrode was 1.0×10^{-6} - 5.0×10^{-5} M, $R^2 = 0.9819$ (Figure 5).

It is seen that the linearity of graphs is highly satisfactory and they could be used for the quantitative determination of phenol. The detection limit of the biosensor was 5.0×10^{-7} M and the response time of the biosensor was 200 s.

Kinetic parameters $I_{max(app)}$ and $K_{m(app)}$ for the enzyme biosensor were calculated as 3.47 µA, 0.69 mM respectively. Km values for immobilized polyphenol oxidase presented in the literature are 100, 0.67 mM [14, 19]. This was attributed to the fact that the polymer used and the type of immobilization were different.
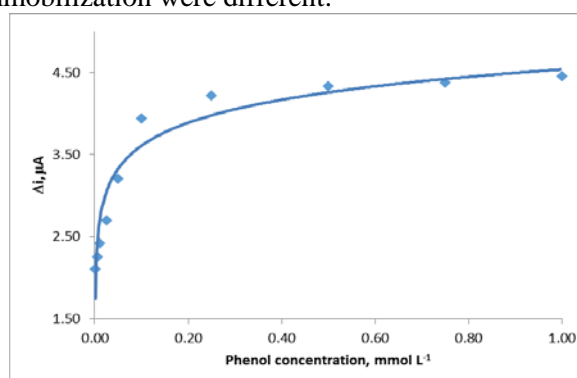
Fig. 4. The effect of phenol concentration upon the amperometric response of MCPE (in pH 8.0 phosphate buffer and at a -0.15 V operating potential, 25 °C).
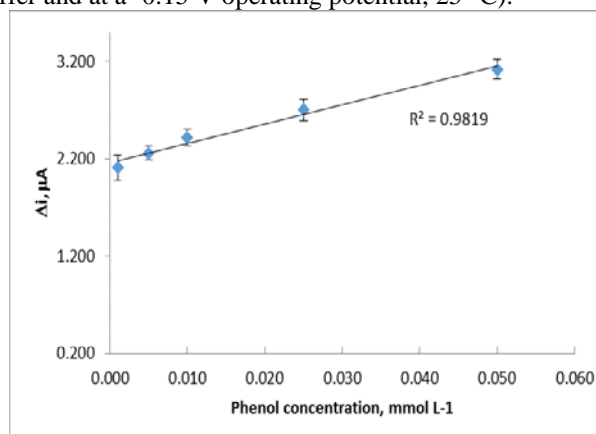

Fig. 5. The calibration curve of the MCPE (in pH 8.0 phosphate buffer and at a -0.15 V operating potential, 25 °C)

The operational stability of the MCPE

The operational stability of MCPE was studied by performing the activity assay (under optimum conditions) 15 times in the same day (Figure 6).

The relative standard deviation obtained after 15 measurements at a constant phenol concentration of 1.0×10^{-5} M was found to be 2.75%.

Storage stability of MCPE

The activity assay was applied within 35 days to determine the storage stability of the immobilized enzyme. As shown in Figure 7, during the 35 days, the response of MCPE decreased. An activity loss of 53 % was observed on the 35th day.
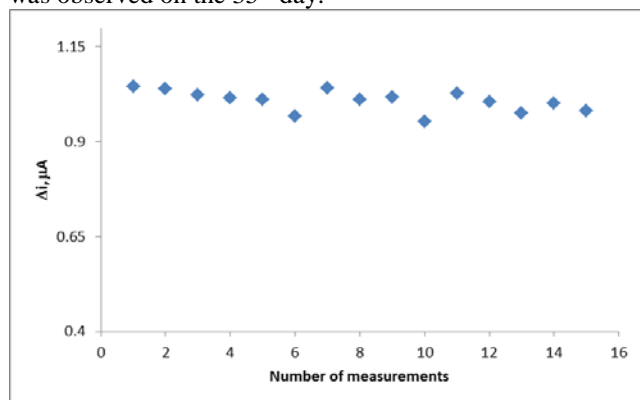

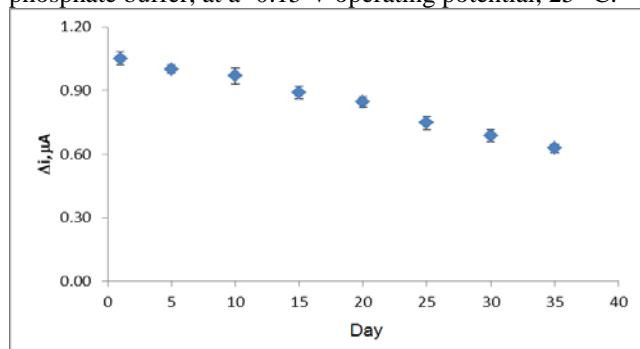**Fig. 6.** Operational stability of MCPE in pH 8.0 phosphate buffer, at a -0.15 V operating potential, 25 °C.

Fig. 7. Storage stability of MCPE (in pH 8.0 phosphate buffer, at -0.15 V operating potential, 25 °C and 1.0×10^{-5} M phenol concentration).

Interference effects

Several cations found in wastewater, such as Cd^{2+}, Pb^{2+}, Sn^{2+}, As^{3+}, As^{5+}, Cr^{3+}, Cr^{6+}, Sb^{3+}, Mn^{2+}, Co^{2+}, Cu^{2+}, Ni^{2+}, were studied for any interfering effect on the analysis of phenol. 1.0×10^{-2} M - 1.0×10^{-5} M concentrations of cations were added. It was observed that Cd^{2+}, Pb^{2+}, Sn^{2+}, As^{3+}, As^{5+}, Cr^{3+}, Cr^{5+}, Sb^{3+}, Mn^{2+}, Co^{2+}, and Ni^{2+} had no interfering effects on the analysis of phenol. However, interfering effect of copper (1.0×10^{-2} - 1.0×10^{-5} M) on the analysis of phenol was observed.

CONCLUSION

In this study, polyphenol oxidase was successfully immobilized on a polyaniline (pani)-activated carbon composite. The experimental results showed clearly that the biosensor exhibited good performance in the determination of phenol. It was found that operational stability and long-term storage stability of the phenol biosensor were good.

Phenol biosensor prepared in this study is useable in a wide concentration range 1.0×10^{-6} - 5.0×10^{-5} M ($R^2 = 0.9819$). It has a very low detection limit (5.0×10^{-7} M) and an acceptable response time for a biosensor (200 s). It gives perfect reproducible results (the relative standard deviation is 2.75 % after 15 measurements). Also it has good storage stability (gives 47 % of the initial amperometric response at the end of the 35th day). The $K_{m(app)}$ and $I_{max(app)}$ values of polyphenol oxidase enzyme immobilized in polyaniline (pani)- activated carbon composite are 0.69 mM and 3.47 µA, respectively. MCPE proposed in this study is easy to prepare and highly cost-effective.

***Declaration of interest**: The authors report no conflicts of interest. The authors alone are responsible for the content and writing of the paper.*

REFERENCES

1. F. Arduini, F.Di. Giorgio, A. Amine, F. Cataldo, D. Moscone, G. Palleschi, *Anal. Lett.,* **43**, 1688 (2010).
2. B. Wang, S. J. Dong, *J. Electroanal. Chem.* **487**, 45 (2000).
3. J. P. Hervás Pérez, E. Sánchez-Paniagua López, M.López-Cabarcos, B. López-Ruiz, *Biosens. Bioelectron.*, **22**, 429 (2006).
4. K. R. Rogers, J. Y. Becker, J. Wang, F. Lu, *Field Anal. Chem. Technol.,* **3**, 161 (1999).
5. S. E. Stanca, I. C. Popescu, L. Oniciu, *Talanta*, **61**, 501 (2003).
6. S. Tembe, S. Inamdar, S. Haram, M. Karve, S. F. D. Souza, *J. Biotechnol.*, **128**, 80 (2007).
7. A. Gutés, F. Céspedes, S. Alegret, M. del Valle, *Biosens. Bioelectron.,* **20**, 1668 (2005).
8. Y. Wang, Y. Hasebe, *Anal. Bioanal. Chem.*, **399**, 1151 (2010).
9. S.E. Stanca, I. C. Popescu, *Bioelectrochem.*, **64**, 47 (2004).
10. V. Carralero Sanz, M. Luz Mena, A. González-Cortés, P. Yáñez-Sedeño, J. M. Pingarrón, *Anal. Chim. Acta*, **528**,1 (2005).
11. P. Wang, M. Liu, J. Kan, *Sens. Actuators B: Chem.*, **140(2)**, 577 (2009).
12. M. C. Rodriguez, G. A. Rivas, *Anal. Chim. Acta*, **459**, 43 (2002).
13. P. Mailleya, E. A Cummings, S. Mailley, S. Cosnier, B. R. Eggins, E. McAdams,. *Bioelectrochem.*, **63**, 291 (2004).
14. S. Kıralp, L. Toppare, Y. Yagcı, *Int. J. Biol. Macromolec.,* **33(1-3)**, 37 (2003).
15. H. Arslan, F. Arslan, *Artif. Cell Blood Sub.*, **39**, 341 (2011).
16. Ö. Çolak, H. Arslan, H. Zengin, G. Zengin, *Int. J. Electrochem. Sci.*, **7,** 6988 (2012).

17. H. Zengin, G. Kalaycı, *Mater. Chem. Phys.*, **120**, 46 (2010).
18. H. Xue, Z. Shen, *Talanta*, **57**, 289 (2002).
19. M. L. Pedano, G. A. Rivas, *Talanta*, **53**, 489 (2000).

ПРИГОТВЯНЕ НА ВЪГЛЕРОДЕН ПАСТООБРАЗЕН ЕЛЕКТРОД, СЪДЪРЖАЩ ПОЛИАНИЛИН-АКТИВИРАН ВЪГЛЕРОДЕН КОМПОЗИТ ЗА АМПЕРОМЕТРИЧНО ОПРЕДЕЛЯНЕ НА ФЕНОЛ

Х. Арслан[1]*, Д. Шенарслан[1], Б.С. Чевримли[2], Х. Зенгин[3], Д. Узун[1], Ф. Арслан[1]

[1] *Департамент по химия, Научен факултет, Гази университет, 06500, Анкара, Турция*

[2] *Департамент по химична технология, Професионален колеж Ататюрк, Гази университет, 06500, Анкара, Турция*

[4] *Департамент по химия, Факултет по наука и изкуства, Газиантеп университет, Газиантеп, Турция*

(Резюме)

Приготвен е нов въглероден пастообразен електрод с използване на полианилинов активиран въглероден композит, чувствителен към фенол. Полифенол оксидазен ензим е имобилизиран към модифициран въглероден пастообразен електрод чрез омрежване с глутаралдехид. Амперометричното определяне се основава на електрохимичната редукция на *о*-хинон, генериран от ензимната реакция на фенол при -0.15 V спрямо Ag/AgCl. Изследвано е влиянието на pH и температурата, като оптималните стойности са съответно 8.0 и 45 °C. Линейният работен интервал на електрода е 1.0×10^{-6} - 5.0×10^{-5} M, $R^2 = 0.9819$. Изследвани са стабилността при съхранение и работната стабилност.

Employing reverse osmosis for the removal of *ortho*-toluidine from wastewater

Aref Shokri

Young Researchers and Elite Club, Arak Branch, Islamic Azad University, Arak, Iran

Ortho-Toluidine (OT) is a dangerous and persistent organic pollutant in the industrial wastewater and needs treatment before disposal. In this project, the performance of reverse osmosis membrane system (RO 90) for the removal of OT from aqueous solutions is investigated. The influence of different operational variables such as pressure, concentration, pH and the volumetric flow rate of feed was considered in the removal performance of the OT. The influence of feed flow rate on the rejection percentage and the permeate flux was not the same. The results showed that at the optimum conditions obtained for rejection, (feed concentration at 80 mg/l, the pressure of feed at $50 \times 10^5 N/m^2$, pH at 7, and feed flow rate at $8 \times 10^{-5} m^3/s$), the rejection percentage and the permeate flux were 97.8%, and $38.5 \times 10^4 \ m^3/m^2.s$, respectively.

Keywords: rejection percentage; ortho-toluidine; reverse osmosis; permeate flux; industrial wastewater.

INTRODUCTION

Ortho-Toluidine (OT) is an aromatic amine employed as an intermediate in the dyeing and petrochemical industries with numerous uses in rubber handling, chemical production, pesticides, pharmaceuticals, etc. [1]. *O-Toluidine* can also be absorbed in living organisms and convert to a number of compounds which are active endotoxins. According to its many environmental concerns and opposing effects on human health, it has received growing attention in recent decades [2].

Membrane technologies are valuable approaches for wastewater treatment because of the many benefits such as low power consumption, high quality of water and low area requisite [3]. The reverse osmosis (RO) is one of membrane technologies that can remove organic pollutants [4]. RO processes can significantly decrease the volume of waste streams and the pollutants are concentrated into a small volume compared to the total waste size. Both organic and inorganic contaminants can be removed instantaneously by RO membrane processes. Additional gains of RO process are: energy saving, simple design and easy work, in comparison with customary processes. But fouling, scaling, and concentration polarization can decrease the efficiency of the RO process [5, 6]. The RO system cannot degrade toxic pollutants, but it can transfer the pollutants from one phase to another and this subject is one of the main limitations of RO techniques. In the separation and reuse of pollutants it can be considered as a useful method for wastewater treatment.

Several processes have been used to remove OT from wastewater, including Fenton [7] and photo Fenton [8] processes, catalytic ozonation [9], electrochemical [10], UV/H$_2$O$_2$ [11] and other AOPs [12]. In this paper the removal of OT from aqueous solution by reverse osmosis using a RO90 polyamide membrane, and the effect of different experimental conditions such as pressure, volumetric flow rate, pH and concentration of feed was studied.
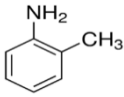
EXPERIMENTAL

Materials. O-Toluidine (99.5%) was of reagent grade, obtained from Merck. The features of *o*-toluidine are shown in Table 1. The pK$_a$ is the acid dissociation constant at which the organic molecule loses a hydrogen atom and becomes negatively charged; log K$_{ow}$ displays the hydrophobicity of the organic molecule. A thin film composite polymeric membrane (RO 90) produced by Alfa Laval (Manufacturer Dow chemical) was employed. Other analytical grade reagents used in this work were sodium hydroxide and sulfuric acid, supplied from Merck. Distilled water was used throughout.

Experimental setup. The schematic of the experimental setup is presented in Fig. 1. The feed tank was a 2 L glass vessel. The set up was equipped with an RO membrane, diaphragm pump (HEADON model HF-8367) with maximum flow rate of $10^{-4} m^3/s$, membrane module, pressure gauge, and a diaphragm valve. The maximum pressure of the membrane was 55 × 10^5 N/m^2. The regulation of the feed flow rate was performed by a flow meter combined with needle valve on the feed stream. A second globe valve was used for pressure tuning. A pressure gauge was installed for monitoring the inlet feed pressure.

---

*) To whom all correspondence should be sent:
E-mail: aref.shokri3@gmail.com

Table1. Some physico-chemical properties of *o*-toluidine.

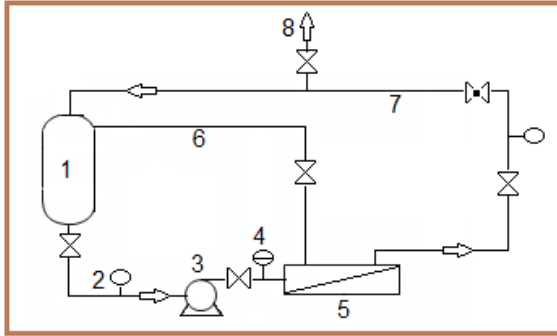| Molecular formula	Structural formula	Molecular weight (g/mol)	Water solubility (g/L) (25°C)	Log $K_{o/w}$	pK$_a$	Density at 20/4 °C (water = 1)
C_7H_9N	NH$_2$ CH$_3$	107.15	15	1.32	4.44	1.004

Fig. 1. The schematic diagram of the RO setup; (1) Feed tank, (2) Instrumentation device, (3) Diaphragm pump, (4) Pressure indicator, (5) Membrane module, (6) Reject line, (7) Permeate line, (8) Sampling valve.

Procedure. A stock solution was prepared by dissolving the required amount of OT in distilled water. The solubility of OT in water in alkaline medium is more than under acidic and neutral conditions. Concentrations of 40, 80, 120 and 160 mg/l of OT were prepared by diluting the stock solution for exploring the effect of feed concentration. For considering the effect of pH, different pH at 5, 7, 9 and 11 were adjusted by adding sodium hydroxide and sulfuric acid. The effect of feed flow rate at 2, 4, 6, and 8 × $10^{-5} m^3/s$ and the influence of feed pressure at 20 to 50 kPa was investigated. All experiments were performed at 25°C. The feed solution was pumped into the membrane module with the chosen pressure and flow rate. The rejected and permeated streams were spilled back to the feed reservoir. Samples from permeate and rejected lines were withdrawn until finding the steady state condition. The steady state condition was achieved after 70 min of recirculation. The rejection of Solute was estimated as:

$$R = \left(1 - \frac{C_p}{C_f}\right) \times 100 \qquad (1)$$

Where C_F and C_P are the feed and permeate concentration, respectively [13]. The permeate flux (J_p) can be defined as the volume flowing *via* the membrane per unit area and time (m³/m²s). In this

study, the feed solution was diluted and the velocity of the feed was high, therefore the concentration polarization and fouling were insignificant and minor deviations from ideal mass transfer were observed. As it can be seen from the following equation, the solvent flow (J_w) depends on the hydraulic pressure used across the membrane (ΔP), minus the difference in the osmotic pressures of the solutions on the permeate and feed side of the membrane ($\Delta\pi$):

$$J_w = A_w(\Delta P - \Delta\pi) \qquad (2)$$

Where A_w is the water permeability constant, which can be influenced by the properties of the membrane and $\Delta\pi$ signifies the osmotic pressure difference across the active layer of the membrane [14]. The solute flux (J_s) depends on the differences in solute concentration across the membrane:

$$J_s = B_s (C_s - C_p) \qquad (3)$$

B_s is the solute permeability constant, which depends on the solute composition and the membrane structure, with the following value:

$$B_s = \frac{K_s D_s}{l} \qquad (4)$$

Where K_s is the solute distribution coefficient, D_s is the solute diffusion coefficient, and l is the membrane width. The permeate concentration can be introduced as $C_p = J_s/J_w$ [15].

The OT concentrations in feed and permeate solutions were determined by spectrophotometry at 281 nm, using a UV–Vis spectrophotometer (Agilent, 5453, U.S.A.).

RESULTS AND DISCUSSION

Effect of feed pressure. The effect of feed pressure on OT rejection and permeation at pH 7, feed concentration of 40 mg/l and volumetric flow rate of $2 \times 10^{-5} m^3/s$ in the range of 20–50 kPa was tested and showed in Figs. 2 A and B. As can be seen, the rejection of OT increased from 73.2 to 80% with the increase in pressure from 20 to 50 kPa. Based on the Spiegler–Kedem–Katchalsky

model, the driving force for solvent and solute transport is pressure and concentration, respectively. In addition, the solute flux is less pressure-dependent than water flux [14]. Therefore, the water flux (J_w) is enhanced directly with pressure and the solute flux is due to the concentration difference and water flux. Concentration polarization increases the osmotic pressure [16], but in this project, it was not considerable because of high feed velocity. The increase in rejection with practical pressure is expected from equation 2, where ΔP is the only variable, supposing that the constants A_w and B_s are not relying on pressure. Higher fluxes derived from higher trans-membrane pressures result in lower permeate concentrations, which leads to higher rejections. Similar results were achieved by other researchers for the removal of organic pollutants by nano filtration and reverse osmosis membranes [17].

The effect of pressure on the permeate flux is presented in Fig. 2B. The permeate flux was increased from 33.5 to $39.0 \times 10^4 \ m^3/m^2.s$ with an increase in operating pressure from 20 to 50 kPa. Based on Eqs. 2 and 3, J_w was increased with operating pressure, but J_s is not influenced and is only determined by the concentration difference across the membrane. So, an increase in permeation rate is only owing to the enhancement in water flux.
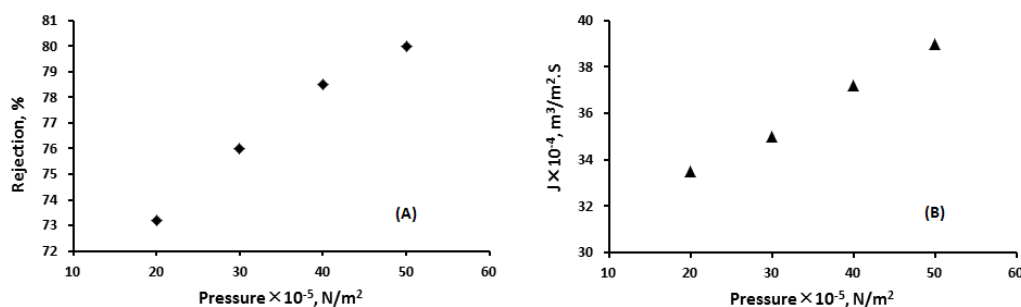

Fig.2. Effect of feed pressure on rejection percentages (A) and permeate flux (B); (feed concentration 40 mg/l, pH 7, and feed flow rate at $2 \times 10^{-5} m^3/s$).

Effect of feed concentration. The effect of initial feed concentration on rejection and permeate flux of the OT is shown in Figs. 3 A and B. The osmotic pressure was increased with increase in feed concentration and according to Eq. (2) the water flux was reduced. By rising in the feed concentration, the accumulation of OT and concentration polarization are increased, therefore the rejection of the OT was decreased. The results showed that at 80 and 40 mg/l, maximum and minimum rejections of the OT were observed at 89.2 and 80%, respectively. At low concentration (40 mg/l), the osmotic pressure difference was low, so based on Eq. (2), water flux was considerable and the concentration of OT on the membrane surface was low, so the flux of OT was low. But at a concentration of 40 mg/l, the water flux is so high that can transport the dissolved OT in the membrane surface to the permeate side. When feed concentration increases, the slight variation in the rejection was occurred as it has been described by other researchers with other organic compounds [18].

As it can be observed, there were no noteworthy variations in permeate flux with increases in feed concentration, which can be clarified by the sum of two contrary effects: the reduction in the water flux as a consequence of the increase in $\Delta\Pi$ and the enhancement in solute flux according to the increase in feed concentration.

Effect of feed pH. As it can be seen from Figs. 4 A and B, the effect of feed pH on rejection and permeation flux was investigated in the range of 5–11. The maximum rejection was obtained at pH 7 and the minimum rejection at pH 10. In alkaline solutions, ionization of the polyamide membrane occurred and the membrane surface was negatively charged because of the free carboxylic acid groups in the structure [19]. Rejection changes with pH are seemingly related to the existence of ionizable groups in the membrane structure and to the net charge of the OT molecule as a result of its dissociation equilibrium [20]. The pKa of OT is 4.44 and thus, at pH values higher than 4.44, the toluidinium amount will decrease because of the formation of neutral toluidine.
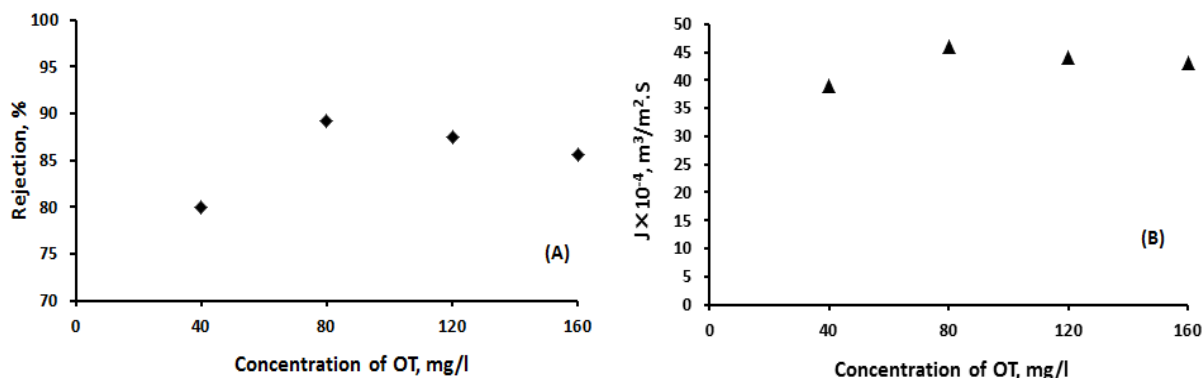
Fig.3. Influence of feed concentration in rejection percentages (A) and permeate flux (B); (feed pressure $50 \times 10^5 N/m^2$, pH 7, and feed flow rate at $2 \times 10^{-5} m^3/s$).

The increase in rejection between pH 5 and 7 can originate from the retention of the remaining toluidinium cations by the negative carboxylate groups in the membrane. At pH values higher than 7, rejection decreases because the amounts of toluidinium cations considerably decrease and neutral OT is not taken in by the negative charge of the membrane. Similar results, that pK_a value had a very significant role in the rejection of 4NP, were obtained by Ozaki and Li [21].

The pH has a strong effect on the permeation behavior of polyamide membranes owing to the superficial charge of the membrane and the net charge of the organic pollutant. Minimum permeate flux is obtained at pH of 5.

At pH 5, both membrane surface and the OT molecules are positively charged, which leads to an increase of pore size, originated from the electrostatic repulsion between functional groups with the same charge, causing lower OT transport, so that there is a minor solute flux, which is accompanied with the increase of water flux. According to all this, at pH 7–11, the OT has no net charge, but the membrane will have a negative charge, which will lead to improve the water flux, originated from the increase of pore size, and consequently, a decrease in permeate concentration.
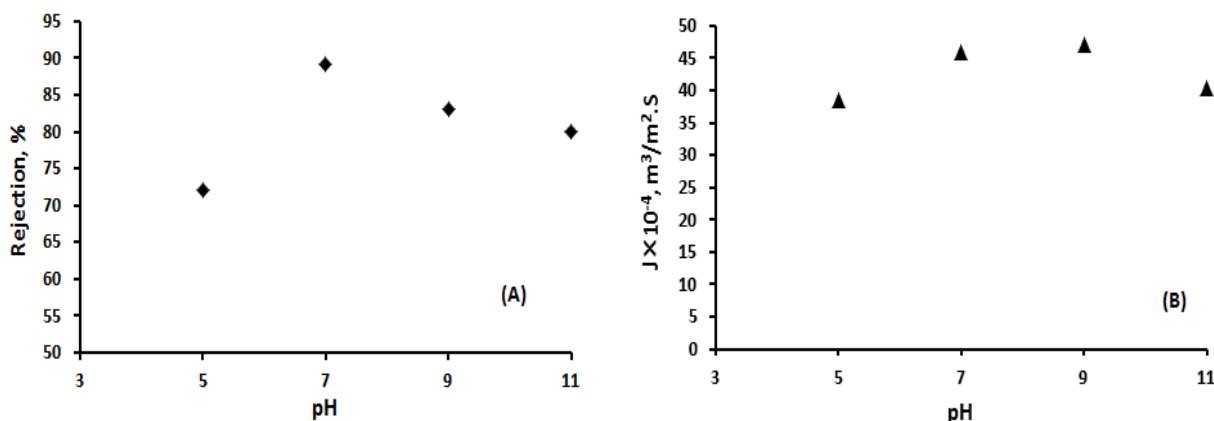

Fig.4. Influence of feed pH in rejection percentages (A) and permeate flux (B); (feed pressure $50 \times 10^5 N/m^2$, 80 mg/l OT, and feed flow rate at $2 \times 10^{-5} m^3/s$).

Effect of feed flow rate. The influence of feed flow rate on OT rejection and permeation is presented in Figs. 5 A and B. As it is obvious, the rejection is enhanced by increasing the flow rate and the permeation flux is in contrast. The influence of feed flow rate on the rejection percentage and the permeate flux was not the same. By increasing the feed flow rate from 2×10^{-5} to $8 \times 10^{-5} m^3/s$, the rejection percentage was increased from 89.2 to 98.7% and the permeation

flux decreased from $46 \times 10^4\ m^3/m^2.s$ to $38.5 \times 10^4\ m^3/m^2.s$. This effect can be described as concentration polarization. The width of the concentration polarization layer was reduced at high feed flow rates and therefore the osmotic pressure decreased. Based on Eq. (2), by reducing the osmotic pressure difference the water flux increases and the rejection of OT is improved. The maximum rejection was obtained at $8 \times 10^{-5} m^3/s$ of feed flow rate and feed concentration at 80 mg/l.
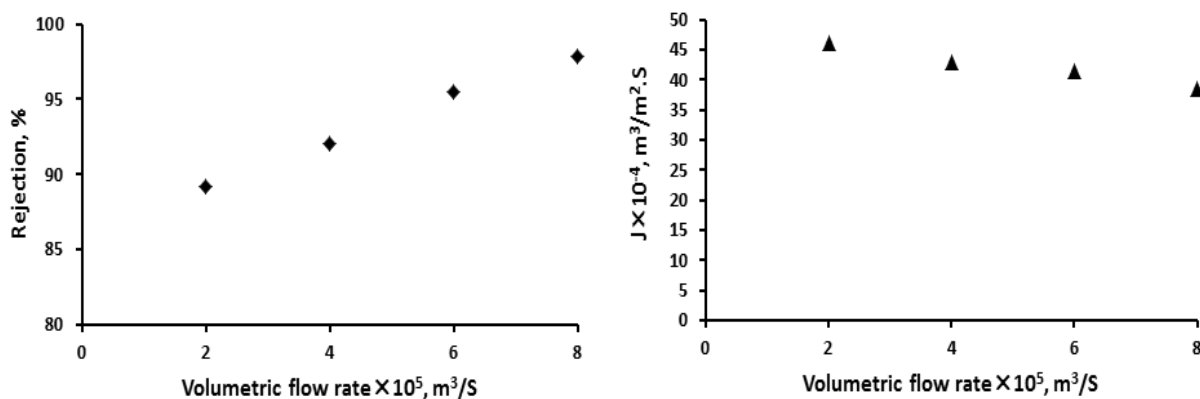
24

Fig.5. Influence of feed flow rate in rejection percentages (A) and permeate flux (B); (feed pressure $50 \times 10^5 N/m^2$, 80 mg/l OT, and pH at 7).

CONCLUSIONS

The performance of reverse osmosis for the removal of OT from aqueous solutions was explored and the effect of operational variables such as pressure, feed volumetric flow rate, feed concentration and pH on the rejection and permeate flow rate was investigated. The highest rejection (97.8%) was achieved at 80 mg/l of OT, feed pressure of $50 \times 10^5 N/m^2$, pH 7, and feed flow rate at $8 \times 10^{-5} m^3/s$. The rejection percentage was increased with an increase in pressure and feed volumetric flow rate. The permeate flux was improved with increase in pressure and decrease in volumetric flow rate of the feed. The observed changes in OT rejection with pH were related to the charge of ionizable groups in the membrane structure and the net charge of OT molecule. The maximum permeation flux ($46 \times 10^4\ m^3/m^2.s$) was achieved at optimum conditions obtained for rejection except the volumetric flow rate of feed which was $2 \times 10^{-5} m^3/s$. The influence of feed flow rate on rejection percentage and the permeate flux was not the same.

REFERENCES

1. World Health Organization (WHO), Concise International Chemical Assessment Document 7, O-Toluidine, 1998.
2. A. Shokri, K.Mahanpoor, D.Soodbar, *Desalin. Water Treat.,* **57,** 16473 (2016).
3. A.T. El-Gendi, S.A. Ahmed, H.A. Talaat, *Desalination,* **206**, 226 (2007).
4. Alturki, A.A., Tadkaew, N., Mc Donald, J.A., Khan, S.J., Price, W.E., Nghiem, L.D., *J. Membr. Sci.,* **365,** 206 (2010).
5. M.T. Ravanchi, T. Kaghazchi, A. Kargari, *Desalination,* **235**, 199 (2009).
6. N. Pena, S. Gallego, F. Del Vigo, S.P. Chesters, *Desalin. Water Treat.,* **51**, 958 (2013).
7. N. Masomboon, C. W. Chen, J. Anotai, M.C. Lu, *Sustain. Environ. Res.,* **21**(2) ,101 (2011).
8. N. Masomboon, C.W. Chen, J. Anotai, M.C. Lu, *Chem. Eng. J.,* **159**, 116 (2010).
9. A. Shokri, K. Mahanpoor, *Int. J. Ind. Chem.,* **8**, 101 (2017).
10. E. Hmani, S. Chaabane Elaoud, Y. Samet, R. Abdelhedi, *J. Hazard. Mater.,* **170**, 928(2009).
11. A. Shokri, *Desalin. Water Treat.,* **58**, 258 (2017).
12. J. Anotai, S. Singhadech, C.C. Suc, M.C. Luc, *J. Hazard. Mater.,* **196**, 395 (2011).
13. A. Bodalo, J.L. Gomez, M. Gomez, G. Leon, A.M. Hidalgo, M.A. Ruiz, *Desalination,* **223**, 323 (2008).
14. A.M. Hidalgo, G. Leon, M. Gomez, M.D. Murcia, E. Gomez, J.L. Gomez, *Desalination,* **315** 70 (2013).
15. M. Hidalgo, G. Leon, M. Gomez, M.D. Murcia, E. Gomez, C. Ginera, *J. Water Process Eng.,* **7**, 169 (2015).
16. T. Gullinkala, B. Digman, C. Gorey, R. Hausman, I.C. Escobar, *Sustainability Sci. Eng.*, **2**, 65 (2010).
17. Y. Li, J. Wei, C. Wang, W. Wang, *Desalin. Water Treat.,* **22**, 211 (2010).
18. A.L. Ahmad, L.S. Tan, S.R.A.Shukor, *J. Hazard. Mater.,* **151**, 71 (2008).
19. A. Simon, L.D. Nghiem, P. Le-Clech, S.J. Khan, J.E. Drewes, *J. Membr. Sci.,* **340**, 16 (2009).
20. A. Kulkarni, D. Mukherjee, W.N. Gill, *J. Membr. Sci.,* **114**, 39 (1996).
21. H. Ozaki, H. Li, *Water Res.,* **36**,123 (2002).

ИЗПОЛЗВАНЕ НА ОБРАТНА ОСМОЗА ЗА ОТСТРАНЯВАНЕ НА *ОРТО*-ТОЛУИДИН ОТ ОТПАДНА ВОДА

А. Шокри

Елитен клуб на младите изследователи, Клон Арак, Ислямски Азад университет, Арак, Иран

(Резюме)

орто-Толуидин (ОТ) е опасен и устойчив органичен замърсител в промишлена отпадна вода и трябва да се отстрани преди изхвърлянето й. В настоящата статия е изследвано действието на мембранна система за обратна осмоза (RO 90) за отстраняване на ОТ от водни разтвори. Изследвано е влиянието на оперативни променливи като налягане, концентрация, pH и обемна скорост на захранващия поток върху отстраняването на ОТ. Влиянието на обемната скорост на захранващия поток върху процента на очистване и преминаващия поток е различно. Установено е, че при оптималните условия (концентрация на захранване 80 mg/l, налягане на захранване $50 \times 10^5 N/m^2$, pH 7 и скорост на захранващия поток $8 \times 10^{-5} m^3/s$), процентът на очистване и преминаващият поток са съответно 97.8% и $38.5 \times 10^4 \ m^3/m^2.s$.

Using UV/ZnO process for degradation of Acid red 283 in synthetic wastewater

A. Shokri[1]*, K. Mahanpoor[2]

[1] Young Researchers and Elite Club, Arak Branch, Islamic Azad University, Arak, Iran
[2] Department of Chemistry, Faculty of Science, Arak Branch, Islamic Azad University, Arak, Iran.

In this research, the photocatalytic degradation of Acid red 283 (AR283) was investigated by the UV/ZnO process in a batch photoreactor. The experiments revealed that the ZnO nanocatalyst and UV light had a slight influence when they were used separately. The impact of various factors such as initial pH, initial dosage of dye and catalyst on the degradation efficiency was investigated. The degradation and mineralization of AR 283 were estimated by HPLC and COD tests, respectively. At optimum conditions (0.3 g/L of catalyst, pH 8 and initial concentration of AR283 25 mg/l), the removal of AR283 and COD were 99.5 and 58.5% at 60 and 120 min of reaction, respectively. The pseudo-first-order kinetics of the removal of AR283 can be explained in terms of the Langmuir–Hinshelwood model. The apparent rate constant (k_{app} $=27.2\times 10^{-3} min^{-1}$) was obtained.

Keywords: UV/ZnO process, Mineralization, Langmuir-Hinshelwood, Batch photoreactor, Acid red 283.

INTRODUCTION

The chemical industries produce wastewater containing non-biodegradable and toxic compounds that remain in the environment even after conventional treatment processes [1]. Large quantities of dyes are annually created and applied in different industries such as textile, paper, cosmetic, leather, nutrition and pharmaceutical industries [2]. The presence of even trace concentrations of dyes in the waste is highly visible and unpleasant. It can cause some severe problems to aquatic life and human health [3]. The discharge of the wastes from the textile industries contains noxious chemicals such as azo and reactive dyes which affect the natural resources such as soil fertility, aquatic organisms and the ecosystem.

There are three techniques for treatment of industrial wastewater, covering physical, chemical and biological methods. However, they are non-destructive, as they only transfer pollutants from water to another phase, thus producing secondary pollution. Therefore, costly operations such as regeneration of the adsorbent materials and post-treatment of solid wastes are needed [4]. Owing to the large quantity of aromatic matter present in dye molecules and the strength of the current dyes, conservative biological treatment methods are unsuccessful for degradation [5–7]. Accordingly, an inexpensive and easy-operated method without the creation of sludge is required [8].

Lately, advanced oxidation processes (AOPs) have offered a talented treatment choice for industrial wastewaters associated with other treatment skills. These techniques were recognized in the production of very reactive species such as hydroxyl radicals that rapidly and non-selectively oxidize a wide range of pollutants [9]. Among AOPs, semiconductor photocatalysts are a branch of AOPs that have brought up an important technology leading to the total mineralization of the pollutants [10]. This process uses a cheap, available and nontoxic semiconductor (ZnO) and leads to total mineralization of organic pollutants to CO_2, water and mineral acids. The ZnO nanocatalyst seems to be a suitable alternative to TiO_2; meanwhile its photodegradation mechanism has been confirmed to be similar to that of TiO_2 [11].

The purpose of the present work is to investigate the removal of an azo dye, Acid red 283 from synthetic wastewater in the presence of ZnO nanocatalyst by UV-C light (UV/ZnO process). The impact of UV light irradiation, pH and the amount of ZnO and AR283 was explored. A kinetic description of the process was given according to the Langmuir–Hinshelwood model whereby previous to UV irradiation, the dye molecule was pre-adsorbed on the photo catalyst surface.

EXPERIMENTAL

Materials

The azo dye, Acid red 283, was purchased from Sigma-Aldrich and used without further purification. The ZnO nanocatalyst was obtained from Merck and the average particle size was about 33 nm, the surface area was 5m^2 g^{-1}. Sulfuric acid and sodium hydroxide werepurchased from Merck. The chemical properties of AR283 are presented in Table 1. Distilled water was used throughout.

---

*) To whom all correspondence should be sent:
E-mail: aref.shokri3@gmail.com
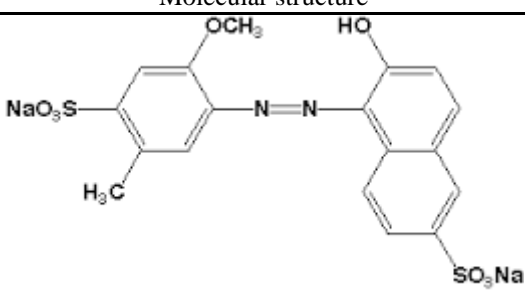
Table 1. Chemical properties of AR 283.

Pollutant	Molecular structure	λ_{max}(nm)	Molecular Mass
Acid red 283 ($C_{18}H_{14}N_2Na_2S_2O_8$)		521	496.42

Photo reactor

In this work, the tests were performed in a batch reactor with a total volume of 1 L. The schematic diagram of the experimental setup is presented in Fig. 1. The light source was a mercury lamp, Philips 15W (UV-C), which was positioned horizontally above the reactor. The reactor is made of glass and enclosed by a wooden sheet to avoid loss of UV light and equipped with a sampling system. The temperature was maintained at 25℃ in all experiments by a water-flow exchanger using an external circulating flow of a thermostatic bath (BW20G model from a Korean Company). A magnetic stirrer was used for mixing the solution in the reactor and avoiding dead zones. The air entered from the bottom of the reactor to saturate the solution with oxygen (not shown in Fig.1).
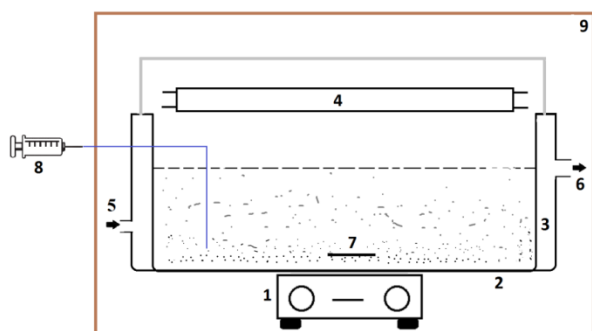

Fig. 1. Schematic diagram of the laboratory-scale experimental setup used. 1- Magnetic stirrer, 2- Batch photo reactor, 3-Jacket water, 4- UV lamp, 5- Cooling water supply from thermostat, 6- Cooling water return, 7- Magnetic bar, 8- Sampling system, 9-Dark wooden box.

Analytical Procedure

The lamp was switched on to start the reaction in the UV/ZnO process. The pH was adjusted applying a Basic pH Meter, PT-10P Sartorius Instrument, Germany by adding NaOH or H_2SO_4 (0.1 M). pH was studied in the range from 3 to 11. The tests were performed by regulating one factor, while others were held fixed.

Samples were withdrawn, centrifuged and filtered, then the concentrations of AR283 were determined by measuring the absorbance at the maximum wavelength of 521 nm by a single beam UV/Vis spectrophotometer (Agilent, 5453, U.S.A.) [12]. The mineralization of AR283 was estimated from the COD test. The COD value was obtained by dichromate closed reflux with a colorimetric method. A spectrophotometer (DR5000, Hach, USA) was applied for measuring the absorbance of COD samples at 600 nm [13]. The percentage removal of color was obtained by the difference in the absorbance values of the initial and the final samples. For further proof, samples were tested by HPLC (Knauer, Germany) equipped with spectrophotometer (Plate blue, Germany). A reverse-phase column, packed with 3 μm Separon C_{18}, was 150 mm in length and 4.6 mm in diameter. The isocratic method was used with a solvent mixture of 70% acetonitrile and 30 % deionized water with a flow rate of 1 ml/min.

The percentages of decolorization and degradation were calculated from equations 1 and 2:

$$Removal\ of\ AR283(\%) = \left(\frac{[AR283]_0 - [AR283]}{[AR283]_0}\right) \times 100 \quad (1)$$

$$Removal\ of\ COD(\%) = \left(\frac{[COD]_0 - [COD]}{[COD]_0}\right) \times 100 \quad (2)$$

where $[AR283]_0$, and $[COD]_0$ are the concentrations of $AR283$ and COD at the start of the reaction, respectively. $[AR283]$ and $[COD]$ are the concentrations of AR283 and COD at time t, respectively.

RESULTS AND DISCUSSION

Mechanism of photocatalytic degradation

As it can be seen from the following equations, when ZnO was irradiated by UV light, degradation and mineralization of AR283 occurred. The photocatalytic degradation of organic pollutant in the solution is originated by photo excitation of the semiconductor, followed by the creation of an electron–hole pair on the surface of the catalyst (Eq. 3). The high oxidative potential of the hole (h_{VB+}) in

the catalyst certificates the direct oxidation of the organic pollutant (AR283) to reactive intermediates (Eq. 4). The hydroxyl radicals can be produced by breakdown of water (Eq. 5) or by the reaction of the positive holes with hydroxide ions (Eq. 7).

$$ZnO + hv < 387 \text{ nm} \rightarrow e^-_{CB} + h^+_{vb} \qquad (3)$$
$$h^+_{vb} + AR283 \rightarrow \text{intermediates} \rightarrow CO_2 + H_2O \qquad (4)$$
$$H_2O + h^+_{vb} \rightarrow OH^\bullet_{ads} + H^+ \qquad (5)$$
$$OH^\bullet + AR283 \rightarrow \text{intermediates} + OH^\bullet_{ads} \rightarrow CO_2 + H_2O \qquad (6)$$
$$h^+_{vb} + OH^-_{ads} \rightarrow OH^\bullet_{ads} \qquad (7)$$
$$e_{CB-} + O_2 \rightarrow O_2^{\bullet-} \qquad (8)$$
$$O_2^{\bullet-} + dye \rightarrow dye - OO\bullet \qquad (9)$$
$$O_2^{\bullet-} + HO_2\bullet + H^+ \rightarrow H_2O_2 + O_2 \qquad (10)$$
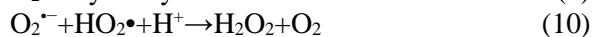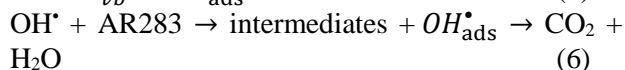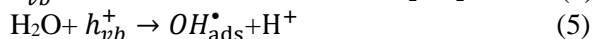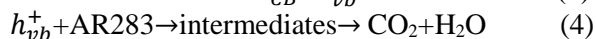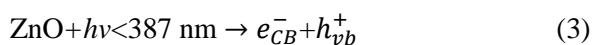
The hydroxyl radical is a very strong and non-selective oxidant that results from the degradation of organic pollutants [14]. The electron in the conduction band can reduce the molecular oxygen in the solution to form superoxide anion radicals (Eq. 8). These radicals, in the presence of organic scavengers, can form organic peroxides (Eq. 9) or hydrogen peroxide (Eq. 10). The molecular oxygen is an electron acceptor that can prevent from recombination of electron and holes.

Influence of catalyst concentration

The experiments were performed by changing the concentration of ZnO from 0.15 to 0.4 g/l, while the other variables remained fixed (Fig. 2). Experiments showed that the degradation was improved from 70.5 to 98%, with increase in ZnO concentration from 0.15 to 0.3 g/l until it reached a plateau, then it slightly decreased. Above 0.3 g/l of catalyst, the rate of AR283 disintegration was not further affected by advanced increase in ZnO concentration because of the aggregation of catalyst particles at high dosages, causing a decrease in the number of active sites on the surface of catalysts. Besides, further increase in catalyst loading may cause opacity, increase light scattering and reduction of light penetration. So the overall number of photons that can reach the surface of catalyst decreased. Consequently, the efficiency of the produced OH radicals dropped [15,16]. So, 0.3 g/l of catalyst was selected as the optimal content of photocatalyst. By an increase in the amount of catalyst to 0.4 g/l decomposition decreased to 97%.
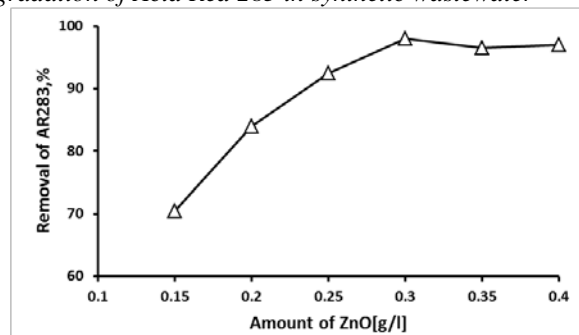

Fig.2. Effect of ZnO amounts on the removal efficiency of AR283 ([AR283]$_0$ =25 mg l^{-1}, pH= 7, 60 min of reaction)

Effect of initial pH of the solution

The effect of initial pH on the efficiency of the UV/ZnO process was investigated using solutions with different pH values from 3 to 11. The process has the highest efficiency at pH 8.0, as is illustrated in Fig. 3. The best pH for the degradation was near to the zero point of charge (ZPC) of the catalyst and this was explained with the effect of pH on the degradation rate depending on its influence on the catalyst particles.

The zero point of charge pH (pH$_{zpc}$), at which the surface charge of the ZnO is zero, was about 9.0. Thus, in acidic media, the surface of the catalyst is positively charged and this could be the most probable cause for the low efficiency of the process. These properties produced changes in the structure of dyes at various pH and adsorption on the catalyst surface [17]. In addition, low effectiveness of this process at low pH (pH=3) (54.5%) could be caused by the surface charge of the catalyst at these pH values and the corrosive properties of the solution. The degradation was improved by an increase in pH and maximum degradation (99.5%) was achieved at pH 8.

However, further increase in pH caused decrease in degradation. In alkaline conditions Coulombic repulsion between OH^- and the negatively charged surface of the catalyst particles could stop the formation of hydroxyl radicals and lessen the degradation. The removal efficiency decreased to 83% at pH 11, because the molecules of AR283 were in ionic form in the alkaline medum and could not adsorb on the ZnO surface that is negatively charged at pH higher than 9.
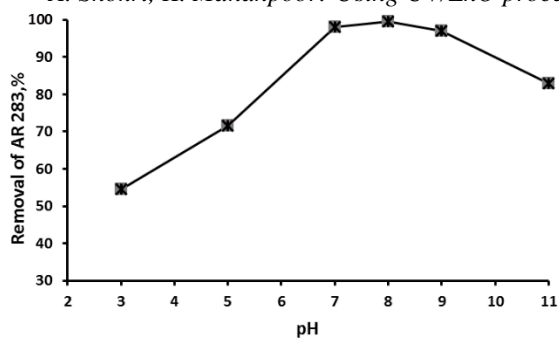
Fig. 3. Effect of pH on the degradation of AR283 ([ZnO] =0.3 g/l, irradiation time= 60 min).

Effect of initial concentration of AR283

The effect of initial concentration of AR283 on photocatalytic degradation efficiency is presented in Fig. 4. It can be seen that the color removal efficiency was reduced as the initial dosage of AR283 increased. The supposed reason is that more dye molecules are adsorbed on the surface of the ZnO catalyst when the initial concentration of AR283 was increased. The amount of adsorbed dye on the surface at different concentrations can be approximately estimated by a spectrophotometric method. The large amount of adsorbed dye has an inhibiting influence on the reaction of the dye molecules with photogenerated holes or hydroxyl radicals. When the concentration of dye is increased, it causes the dye molecules to absorb light and the photons never touch the photo catalyst surface, therefore the photo catalytic degradation efficiency decreased [18].
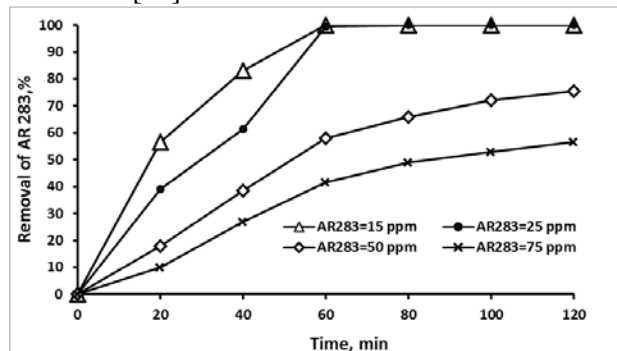

Fig. 4. Effect of initial concentration of AR283 on photo catalytic degradation efficiency ([ZnO] = 0.3 g l^{-1}, pH =8).

Effect of UV irradiation and ZnO nanoparticles

When the pollutant was irradiated with UV light for 120 min, negligible degradation (8.5%) happened. The same experiments were performed in the presence of ZnO without UV light and only 5.5% of AR283 disappeared because of adsorption of pollutant on the surface of the catalyst. Almost 99.5% of AR283 was degraded in the presence of ZnO along with UV light at 60 min of reaction. The hydroxyl radical was an extremely strong, non-

30

selective oxidant that provided the degradation of the organic pollutant [19] and this happened only on simultaneous use of catalyst and UV irradiation. As it can be seen from Fig. 5, decolorization of the AR283 solution was achieved effectively, and more than 61.5% of the dye was removed within 40 min of the reaction, although only 47% of COD were removed during 60 min of reaction. The chief mechanism for decolorization of azo dyes is the breaking of the N=N bond [20]. During the photo-assisted reactions, activated hydrogen atoms were produced which may attack the azo bond and convert it to a hydrogenated azo bond structure, which may absorb UV light at 254 nm [21].

The removal of AR283 was insignificant in the absence of ZnO nanocatalyst, which suggested that both UV light and photocatalyst were required for the effective degradation of AR283.
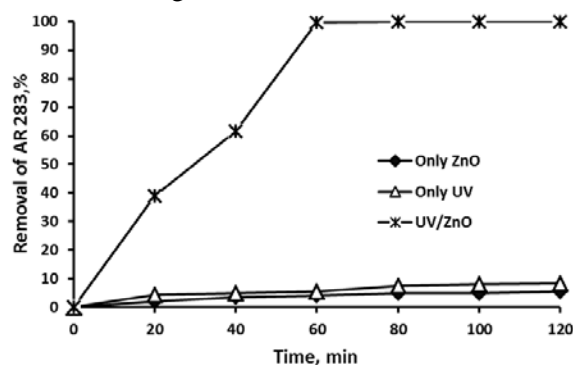
Fig. 5. Effect of various processes upon degradation of AR283 in optimum conditions ([ZnO] = 0.3 g/ l, pH = 8).

Removal of COD

As it can be seen from Fig. 6, COD decreased during the treatment process, but with a slower rate.
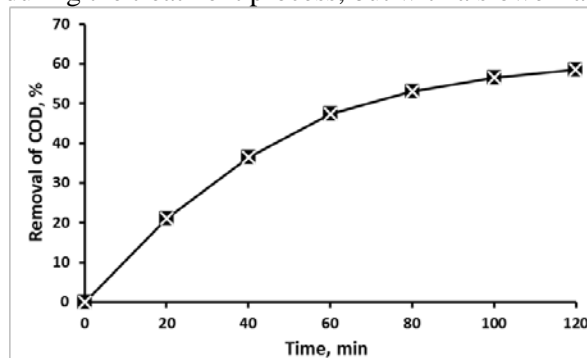
Fig. 6. Removal of COD in optimum conditions ([ZnO] = 0.3 g/ l, [AR283] =25 mg/l, pH = 8).

These values were lower (47.5% in 60 min) than the ones corresponding to the AR283 degradation (99.5% in 60 min), because intermediates were produced in the treatment process. In addition, in the first 60 min of reaction the rate of COD removal was higher, then it decreased with the progress in the treatment process because intermediates were

produced continuously and they were persistent to the photocatalytic degradation. After 120 min of reaction 58.5% of COD was removed in optimum condition for degradation of AR283.

Kinetics of Acid red 283 degradation

The relationship between the initial degradation and initial concentration of organic dyes in a heterogeneous photocatalytic degradation process was described by the Langmuir–Hinshelwood model. Usually this model was used to describe the kinetics of photocatalytic degradation in aqueous suspensions [22]. It relates the degradation rate (R_{AR283}) and the concentration of organic compound (C_{AR283}), as follows:

$$R_{AR2} = \frac{k_r K_{ad} C_{AR283}}{1 + K_{ad} C_{AR283}} \qquad (11)$$

where k_r and K_{ad} are the rate constant and adsorption equilibrium constant, respectively. In this study, the adsorption was relatively weak and the concentration of AR283 was low (25mg/l), so Eq. 11 can be simplified to pseudo first-order kinetics with an apparent rate constant, k_{app} [7]:

$$R_{AR2} = k_r K_{ad} C_{AR283} = k_{app} C_{AR283} \quad (12)$$

From the experimental results, the kinetic constant of the reaction was obtained by fitting the experimental data into pseudo first-order kinetic equation. However, when the experimental data were plotted, they looked like a first-order reaction with respect to AR283 decomposition. Therefore, an approach to this kinetic study was performed by assuming that the degradation reaction followed first-order kinetics. This methodology was in agreement with studies of several authors [23,24]. Behnajady *et al*. stated the Langmuir–Hinshelwood equation factors for decolorization of a solution containing C.I. Acid yellow 23 (40 mg l^{-1}) in the presence of ZnO to be 750 mg l^{-1} [14]. After integration, from Eq.12 the following equation was obtained:

$$ln\left(\frac{[AR283]_0}{[AR283]}\right) = K_{app} \times t \qquad (13)$$

A plot of $ln([AR283]_0/[AR283])$ *versus* time for the degradation of AR283 is shown in Fig. 7. By employing least square regression analysis the values of k_{obs} were obtained.

To evaluate these rate constants, $ln\left(\frac{[AR283]_0}{[AR283]}\right)$ *versus* reaction time was plotted, and after linear regression analysis, the first-order rate constant (k=$27.2 \times 10^{-3} min^{-1}$) and the half-life of the reaction ($t_{1/2} = 25.5 \ min$) were determined.

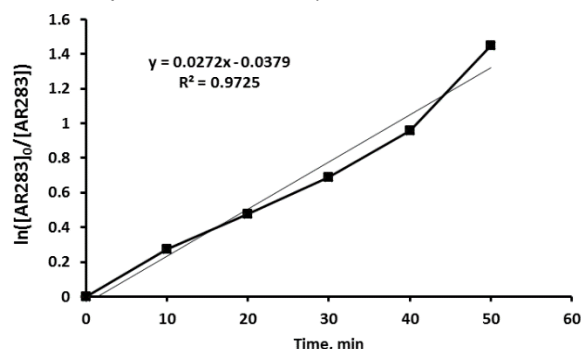**Fig. 7.** Kinetic fit for the degradation of AR283 by UV/ZnO process in optimum conditions ([ZnO] = 0.3 g/l, [AR283] =25 mg/l, pH = 8).

CONCLUSIONS

The results of this study showed that:

UV/ZnO process could be successfully used to degrade AR283 in a batch photoreactor with system light and oxygen, but UV light and ZnO had a slight effect when they were used separately. Experiments were performed to find out the optimum conditions to achieve high degradation rates needed for the photocatalytic process.

The degradation of AR283 was obviously affected by the irradiation time, initial concentration of pollutant, pH and dosage of ZnO. The optimal conditions for the degradation were: 0.3 g/l of photocatalyst, 25 mg/l of AR283 and pH 8. The removal of COD (58.5% in 120 min) was slower than the removal of AR283 (99.5% in 60 min) because of the persistent intermediates formed through degradation.

Photocatalytic degradation of AR283 in aqueous ZnO suspensions follows pseudo-first-order kinetics and the apparent rate constant (k_{app} =27.2× $10^{-3} min^{-1}$) depends on the initial concentration of AR283.

REFERENCES

1. M. I. Badawy, M. Y. Ghaly, T. A. Gad-Allah, *Desalination,* **194**, 166 (2006).
2. E. Bazrafshan, M. Ahmadabadi, A. H. Mahvi, *Fresen. Environ. Bulletin,* **22,** 584 (2013).
3. S. Parsons, *Int. Biodeter. Biodegr.,* **46**, 51 (2004).
4. A. Dalvand, R. Nabizadeh, M.R. Ganjali, M. Khoobi, S.Nazmara, A.H. Mahvi, *J. Magn. Magn. Mater.,* **404**, 179 (2016).
5. H. Jayamohan, Y. R. Smith, B. K. Gale, S. K. Mohanty, M. Misra, *J. Environ. Chem. Eng.,* **4,**657 (2016).
6. A. Shokri, K. Mahanpoor, *Int. J. Ind. Chem.,* **8,** 101 (2017).
7. A. Shokri, K. Mahanpoor, D. Soodbar, *Fresen. Environ. Bull.,* **25**, 500 (2016).

A. Shokri, K. Mahanpoor: Using UV/ZnO process for degradation of Acid Red 283 in synthetic wastewater

8. B. Cuiping, X. Xianfeng, G. Wenqi, F. Dexin, X. Mo, G. Zhongxue, X. Nian, *Desalination*, **278**, 84 (2011).
9. N. Guettai, A.H Ait, *Desalination*, **185**, 427 (2005).
10. A. Shokri, K. Mahanpoor, D. Soodbar, *J. Environ. Chem. Eng.*, **4**, 585 (2016).
11. N. Daneshvar, D. Salari, A. R. Khataee, *J. Photochem. Photobiol. A: Chem.*, **162**, 317 (2004).
12. K. Jirasripongpun, R. Nasanit, J. Niruntasook, B. Chotikasatian, *Thammasat Int. J. Sci. Technol.*, **12**, 6 (2007).
13. APHA, AWWA, WEF, Standard Methods for the Examination of Water and Wastewater, 19 th ed., APHA, Washington, USA, 1995.
14. M.A. Behnajady, N. Modirshahla, R. Hamzavi, *J. Hazard. Mater.*, **133**, 226 (2006).
15. H. Zhao, S. Xu, J. Zhong, X. Bao, *Catal. Today*, **93**, 857 (2004).
16. A. Mehrizad, P. Garbani, *Photobiol. Photochem.*, **93**, 1178 (2017).
17. H. Moradi, S. Sharifnia, F. Rahimpour, *Mater. Chem. Phys.*, **158**, 38 (2015).
18. A. Mehrizad, P. Garbani, *Water Science Technol.*, **74**, 184 (2016).
19 A. Shokri, K. Mahanpoor, D. Soodbar, *Desal. Water Treat.*, **57**, 16473 (2016).
20. N. Daneshvar, D. Salari, A.R. Khataee, *J. Photochem. Photobiol.*, **157**, 111 (2003).
21. W. Feng, D. Nansheng, H. Helin, *Chemosphere*, **41**, 1233 (2000).
22. N. Daneshvar, S. Aber, M.S. Dorraji, A.R. Khataee, M.H. Rasoulifard, *Sep. Purif. Technol.*, **58**, 91 (2007).
23. N. Barka, I. Bakas, S. Qourzal, A. Assabbane, Y. Ait-ichou, *Orient. J. Chem.*, **29**, 1055 (2013).
24. A. Shokri, *Russ. J. Appl. Chem.*, **90**, 452 (2017).

Използване на UV/ZnO процес за разграждане на Кисело червено 283 в синтетична отпадна вода

А. Шокри[1]*, К. Маханпоор[2]

[1] *Елитен клуб на младите изследователи, Клон Арак, Ислямски Азад университет, Арак, Иран*
[2] *Департамент по химия, Научен факултет, Клон Арак, Ислямски Азад университет, Арак, Иран*

(Резюме)

В настоящата статия е изследвана фотокаталитичната деградация на Кисело червено 283 (КЧ283) чрез УВ/ZnO процес в статичен фотореактор. Установено е, че използвани поотделно, нанокатализаторът ZnO и УВ светлината влияят слабо върху процеса. Изследвано е влиянието на различни фактори като изходно pH, изходни концентрации на багрилото и катализатора върху ефективността на деградацията. Деградацията и минерализацията на КЧ283 са оценени с помощта на високоефективна течна хроматография и тест за химично необходим кислород (ХНК). При оптимални условия (0.3 g/L катализатор, pH 8 и изходна концентрация на багрилото 25 mg/l), отстраняването на КЧ283 и ХНК са съответно 99.5 и 58.5% при 60 и 120 минутна реакция. Кинетиката от псевдопърви порядък на отстраняването на КЧ283 се обяснява с модела на Langmuir–Hinshelwood. Определена е привидната скоростна константа на процеса (k_{app} =27.2× $10^{-3} min^{-1}$).

Crystal structure of 4-amino-N-pyrimidin-2-ylbenzenesulfonamide

V. Gomathi*, R. Selvameena

PG and Research Department of Chemistry, Seethalakshmi Ramaswami College, Tiruchirappalli-620 002, Tamil Nadu, India

4-Amino-N-pyrimidin-2-ylbenzenesulfonamide (sulfadiazine) was recrystallised from a mixture of ethanol and N,N-dimethylformamide. The structure of sulfadiazine was confirmed by single crystal X-ray diffraction study to be monoclinic, space group $P2_1/c$, a=13.6210(9)Å, b=5.9250(3)Å, c=14.9910(9)Å, $\alpha = \gamma = 90°$, β=114.574(2)°, T=293(2)K, Z=4, F(000)= 520, Dx=1.511 mg/m^3, absorption coefficient = 0.290mm^{-1}.

INTRODUCTION

Sulfadiazine is a sulfonamide antibiotic [1,2]. The sulfa drugs, derivatives of sulfonamides, are synthetic bacteriostatic antibiotics with a wide spectrum against most gram-positive and many gram-negative organisms. Sulfa drugs are antimetabolites for the bacteria which need *p*-amino benzoic acid for the synthesis of folic acid. Sulfa drugs act as competitive inhibitors of the interaction of enzyme with normal substrate p-aminobenzoic acid.In order to grow and multiply in numbers, bacterial cells need to produce genetic material. To produce DNA they require folic acid(folate). However, bacterial cells cannot take up folic acid supplied in the diet like human cells can. Instead, they synthesize it themselves.Sulfadiazine works by preventing the bacteria from producing folate. Without folate, the bacteria cannot produce DNA and so are unable to increase in numbers. Sulfadiazine therefore stops the spread of infection. The remaining bacteria are killed by the immune system or eventually die [3,4]. Sulfadiazine is sometimes given to people who have experienced a complication of a streptococcal throat infection called rheumatic fever. Sulfadiazine is used to totally eradicate streptococcal bacteria from the body and thus prevent another episode of rheumatic fever. Repeated episodes of rheumatic fever carry an increased risk of causing permanent damage to the heart [5]. Sulfadiazine is used to treat many different types of infection, such as urinary tract infections, ear infections, burns, meningitis, malaria, toxoplasmosis [6]. Sulfadiazine is not often used these days because it can cause some serious side effects such as diarrhea, upset stomach, loss of appetite, dizziness, allergic reactions like skin rash, swelling of the face, lips or tongue, joint or muscle pain [7,8].It should not be used by people who have severe liver problems, kidney problems or porphyria [9].

MATERIALS AND MEASUREMENTS

Sulfadiazine and the solvents were obtained from a commercial supplier (Sigma-Aldrich). A crystal of dimensions 0.30 × 0.20 × 0.20 mm was mounted on a glass fibre. Measurements were performed at 293 [10] on a Bruker AXS kappa apex2 CCD diffractometer using monochromated Mo-Kα radiation [11](99.6% complete). The data were corrected for absorption using the multi-scan method of 9472 intensities, 1929 were collected. [R(int)=0.0213]. The structure was refined anisotropically using SHELX-97 [12,13]. The final wR2 was 0.0719 with a conventional R1 of 0.0281 for parameters; S=1.048.

Crystallographic study of 4-amino-N-pyrimidin-2-ylbenzenesulfonamide

Single crystals suitable for X-ray diffraction studies were obtained by evaporation from an ethanol/DMF mixture, yield 97%. Crystal data**:** $C_{10}H_{10}N_4O_2S$, monoclinic [14,15], space group $P2_1/c$, a=13.6210(9)Å, b=5.9250(3)Å, c=14.9910(9)Å, $\alpha = \gamma = 90°$, β=114.574(2)°, T=293(2)K, Z=4, F(000)= 520, Dx=1.511 mg/m^3, absorption coefficient = 0.290mm^{-1}. A white crystal of dimensions 0.30 × 0.20 × 0.20 mm was mounted on a glass fibre. The selected bond lengths and bond angles are presented in Tables 2 and 3. The atoms around the sulfonamide S atom are arranged in a slightly distorted tetrahedral configuration [16]. The angle of O(2)-S(1)-O(1)= 119.37(8)°,N(2)-S(1)-C(4)=106.20(8).

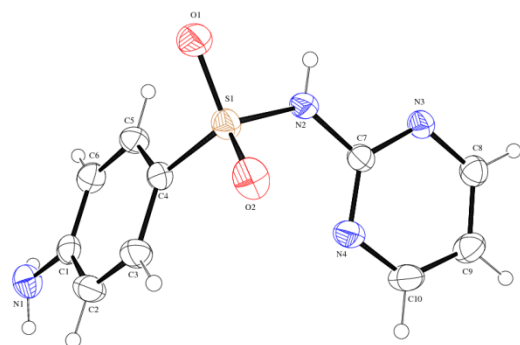*) To whom all correspondence should be sent:
E-mail: vemathi@gmail.com

Fig. 1. ORTEP diagram of 4-amino-N-pyrimidin-2-ylbenzenesulfonamide

Fig.2.Packing view of 4-amino-N-pyrimidin-2-ylbenzenesulfonamide

Hydrogenbonding

The asymmetric unit contains a sulfonamide. In this crystal structure stabilized by N---H…O and N---H…N intermolecular hydrogen bonding interactions are observed. The sulfonamide moieties are centro-symmetrically paired through

N---H…N hydrogen bonds involving N2---H2A…N3 base pairing leading to form a $R_2^2(8)$ ring motif. Further the base pairing units are connected through N---H…O hydrogen bonding interactions. These interactions are leading to the formation of a two-dimensional structure.

Table 1. Crystallographic data of 4-amino-N-pyrimidin-2-ylbenzenesulfonamide

Crystal data	4-amino-N-pyrimidin-2-ylbenzenesulfonamide
Crystal system, space group	Monoclinic, P21/c
Unit cell dimensions	
a,b,c	a = 13.6210(9) Å
	b = 5.9250(3) Å
	c = 14.9910(9)
α, β, γ	alpha = 90°
	beta= 114.574(2)°
	gamma = 90°
Volume	1100.26(11) Å^3
Calculated density	1.511 Mg/m^3
Absorption coefficient	0.290 mm^{-1}
Radiation	Mo Kα
Wavelength	0.71073 Å
Temperature	293(2) K
Crystal size	0.30 x 0.20 x 0.20 mm
Theta range for data collection	2.75 to 25.00º.
Completeness to theta	25º 99.9 %
Data / restraints / parameters	1929 / 0 / 167
Limiting indices	-16<=h<=16
	-5<=k<=7
	-17<=l<=17
T$_{min}$, T$_{max}$	0.895, 0.961
Number measured reflections / unique	9472 / 1929
Δρ$_{max}$/ Δρ$_{min}$	0.282 and -0.290 e.Å^{-3}
R1/wR2	0.0281, 0.0719
R1/wR2	0.0330, 0.0765
Molecular formula	C$_{10}$H$_{10}$N$_4$O$_2$S
CCDC No.	917049

Table 2. Selected bond distances of 4-amino-N-pyrimidin-2-ylbenzenesulfonamide

Bond distance	(Å)	Bond distance	(Å)
C(1)-C(2)	1.391(3)	C(1)-C(6)	1.396(2)
C(2)-C(3)	1.373(3)	C(3)-C(4)	1.380(2)
C(4)-C(5)	1.385(2)	C(4)-S(1)	1.7394(16)
C(5)-C(6)	1.375(2)	C(7)-N(4)	1.325(2)
C(7)-N(3)	1.338(2)	C(7)-N(2)	1.378(2)
C(8)-N(3)	1.334(2)	C(8)-C(9)	1.373(3)
C(9)-C(10)	1.368(3)	C(10)-N(4)	1.337(2)
N(2)-S(1)	1.6471(14)	O(1)-S(1)	1.4317(13)
O(2)-S(1)	1.4232(14)	C(1)-N(1)	1.377(2)

Table 3. Selected bond angles of 4-amino-N-pyrimidin-2-ylbenzenesulfonamide

Bond angle	(°)	Bond angle	(°)
N(1)-C(1)-C(6)	120.72(18)	N(1)-C(1)-C(2)	121.12(17)
C(3)-C(2)-C(1)	121.28(16)	C(2)-C(1)-C(6)	118.11(16)
C(3)-C(4)-C(5)	120.40(16)	C(2)-C(3)-C(4)	119.62(17)
C(5)-C(4)-S(1)	119.97(12)	C(3)-C(4)-S(1)	119.62(13)
C(5)-C(6)-C(1)	121.02(17)	C(6)-C(5)-C(4)	119.55(16)
N(4)-C(7)-N(2)	118.56(15)	N(4)-C(7)-N(3)	127.05(15)
N(3)-C(8)-C(9)	122.39(16)	N(3)-C(7)-N(2)	114.39(14)
N(4)-C(10)-C(9)	123.43(17)	C(10)-C(9)-C(8)	116.48(17)
C(8)-N(3)-C(7)	115.69(14)	C(7)-N(2)-S(1)	126.59(12)
O(2)-S(1)-O(1)	119.37(8)	C(7)-N(4)-C(10)	114.93(15)
O(1)-S(1)-N(2)	101.93(8)	O(2)-S(1)-N(2)	109.70(8)
O(1)-S(1)-C(4)	109.82(8)	O(2)-S(1)-C(4)	108.92(8)
N(2)-S(1)-C(4)	106.20(8)		

Table 4. Hydrogen bond geometry (Å, °) of 4-amino-N-pyrimidin-2-ylbenzenesulfonamide

D-H...A	d(D-H)	d(H...A)	d(D...A)	<(DHA)
N(1)-H(1A)...O(1)[i]	0.81(2)	2.19(2)	2.991(2)	170(2)
N(1)-H(1B)...O(2)[ii]	0.88(3)	2.52(3)	3.003(2)	115(2)
N(2)-H(2A)...N(3)[iii]	0.801(19)	2.14(2)	2.938(2)	177.5(18)

Equivalent points: (i) = x,-y-1/2,z+1/2; (ii) = x,-y+1/2,z+1/2; (iii) = -x+1,-y,-z+1

CONCLUSION

The molecular formula assigned to 4-amino-N-pyrimidin-2-ylbenzenesulfonamideby single crystal X-ray diffraction study is $C_{10}H_{10}N_4O_2S$, monoclinic, space group P21/c, a=13.6210(9)Å, b=5.9250(3)Å, c=14.9910(9)Å, α=γ=90° and β=114.574(2)°. The atoms around the sulfonamide S atom are arranged in a slightly distorted tetrahedral configuration. The angle O(2)-S(1)-O(1)=119.37(8)°, N(2)-S(1)-C(4)=106.20(8)°.

SUPPLEMENTARY DATA

Crystallographic data for the structure reported in this article are deposited at the Cambridge Crystallographic Data Centre CCDC, reference number CCDC 917049. Copies of the data can be obtained free of charge on application to CCDC 12 Union Road, Cambridge.

REFERENCES

1. The American Society of Health-System Pharmacists. Retrieved 8 December 2016.
2. www.drugs.com/mtm/sulfadiazine.
3. www.pubchem.ncbi.nlm.nih.gov.
4. P.L. Soni, H.M. Chawla, Textbook of Organic Chemistry, Sultan Chand & Sons, Reprint 2012.
5. www.Netdoctor.co.uk/medicines/infections/a7826/sulfadiazine.
6. http:/en.wikipedia.org.
7. https://medicineplus.gov.
8. http://www.healthline.com/drugs/sulfadiazine.
9. World Health Organization, **205,** 126 (2009) ISBN. 9789241547659. Retrieved 2016.
10. M. Durgun, S.P. Yalcin, H. Turkmen, M. Akkurt, E. Eroglu, *Bulg Chem Commun.*, **48**, 5 (2016).
11. Rigaku/MSC. CrystalStructure (Version3.7.0) and CrystalClear. The Woodlands, Texas, USA, 2005.
12. G.M. Sheldrick, SHELXS-97, Program for Crystal Structure solution, University of Gottingen, 1997.
13. G.M. Sheldrick, *Acta Cryst. A,***64,**112 (2008).
14. N. Colak, A.B. Gunduzalp, S. Mamas, D. Akkaya, K. Kaya, *Bulg. Chem. Commun.*,**48,** 20 (2016).
15. P. Anangamohan Panja, T. Arun, K. Mandal, *Indian J. Sec. A*, **55(A)**, 137 (2015).
16. S. Jone Kirubavathy, R. Velmurugan, R. Karvembu, N.S. P. Bhuvanesh, I.V.M.V. Inoch, P. Mosae

КРИСТАЛНА СТРУКТУРА НА 4-АМИНО-N-ПИРИМИДИН-2-ИЛБЕНЗЕНСУЛФОНАМИД

В. Гомати*, Р. Селвамеена

PG и Изследователски департамент по химия, Сееталакшими Рамасвами колеж, Тирухирапали 620 002, ТамилНаду, Индия

(Резюме)

4-Амино-N-пиримидин-2-илбинзинсулфонамид (сулфадиазин) е прекристализиран из смес на етанол и N,N-диметилформамид. Чрез рентгенов дифракционен анализ на монокристали е потвърдено, че структурата на сулфадиазина е моноклинна, пространствена група $P2_1/c$, a=13.6210(9)Å, b=5.9250(3)Å, c=14.9910(9)Å, $\alpha = \gamma = 90°$, $\beta = 114.574(2)°$, T=293(2)K, Z=4, F(000)= 520, Dx=1.511 mg/m^3, абсорбционен коефициент = 0.290 mm^{-1}.

Synthesis, characterization and biological activities of a novel Mannich base 2-[(3, 4-dimethoxyphenyl)(pyrrolidin-1-yl)methyl]cyclopentanone and its complexes with Cu(II), Co(II), Ni(II) and Fe(II) ions

M. Liaqat[1], T. Mahmud[1*], M. Imran[1], M. Ashraf[2], A. U. Haq[3], M. Muddassar[4], T. Ahmad[5]

[1]Institute of Chemistry, University of the Punjab, Lahore, Pakistan
[2]Department of Chemistry, The Islamia University of Bahawalpur, Bahawalpur, Pakistan
[3] College of Pharmacy, Gachon University of Medicinal Sciences, Incheon, South Korea
[4]Department of Biosciences, COMSATS Institute of Information Technology, Park Road, Islamabad, Pakistan
[5]Department of Chemistry, University of the Sargodha Sub-campus, Mianwali, Pakistan

One-pot, three-component Mannich reaction was carried out by condensation of 3,4-dimethoxybenzaldehyde, pyrrolidine and cyclopentanone in the presence of calcium chloride using ethanol as a solvent to afford a novel Mannich base (L). The resulting Mannich base (L) was isolated and complexed with Cu(II), Co(II), Ni(II) and Fe(II) ions. The structures of the synthesized scaffolds were confirmed by IR, ^{1}H NMR, ^{13}C NMR, mass spectroscopy, TGA and elemental analyses. The metal contents were determined by ICP-OES. All compounds showed poor antibacterial activities. The anti-enzymatic activities of the Mannich base (L) and its metal complexes were checked against jack bean urease. The Mannich base ligand (L), its nickel and iron complexes showed potent antiurease activity with IC_{50} values of 9.25±0.002, 1.42±0.003, 5.41±0.005 µM, respectively, and were superior inhibitors than the standard, thiourea (IC_{50} 21.25±0.15 µM). The probable binding mode of the most active Ni(II) complex was determined using molecular docking simulations.

Keywords: Mannich base, Metal complex, Antiurease activities, Docking studies

INTRODUCTION

The Mannich reactions are the most charming tools in the field of organic synthesis which give a quantitative approach for the production of carbon-carbon bonds in organic molecules [1−4]. These tools provide different possibilities to produce new analogues by employing various substituted derivatives of any component present in the reaction mixture. The multidisciplinary chemistry of Mannich bases offers a main role for the construction of novel species used for various commercial purposes. Mannich bases are extensively used as intermediates in the preparation of different natural and pharmaceutical products [5,6]. The growth of novel analytical routes designed for the production of β-amino carbonyl compounds has crucial significance in organic chemistry. Several chemists reported the synthesis of Mannich bases using various catalysts [7]. Chemists are trying to build up environment friendly protocols *via* nontoxic catalyst such as calcium chloride [8]. The production of metal complexes possessing certain ligands of pharmacological importance have their own place in society due to the significance of certain metal ions in several biological processes [9,10]. Transition metals play a vital biological role in association with certain metal-protein complexes [11]. The multidisciplinary applications and novel structures of Mannich bases and their complexes are responsible for their extensive investigations in the present age [12]. In view of the above potential importance of Mannich bases and in continuation of our similar recent studies [13,14] another Mannich base 2-[(3,4-dimethoxyphenyl)(pyrrolidin-1-yl)methyl) cyclopentanone (L) and its four complexes with Cu(II), Co(II), Ni(II) and Fe(II) ions were synthesized. Synthetic, structural, docking, antibacterial and antiurease activities of these compounds are part of this manuscript.

EXPERIMENTAL SECTION

3,4-Dimethoxybenzaldehyde, pyrrolidine, cyclopentanone, metal salts and solvents used were all of analytical grade and were used without further purification. Melting points were determined on a Gallen Kamp apparatus. FT-IR spectra were measured on a Perkin Elmer IR spectrometer. ^{1}H NMR and ^{13}C NMR spectra were recorded by Brucker Avance 400. Mass spectra were measured on JEOL JMS−600. Elemental analyses were performed using a EuroEA elemental analyzer. UV-visible spectra were taken using the T90+UV/VIS spectrometer PG instrument within the range of 200 – 400 nm. SDT-Q 600 V20.9
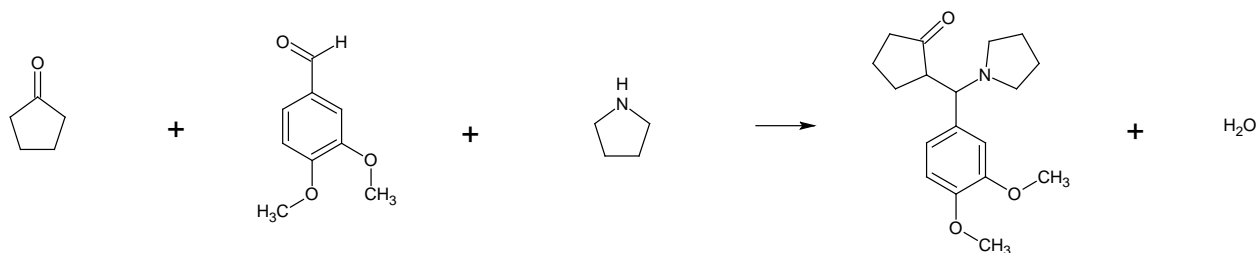
Scheme 1: Synthetic route for the synthesis of Mannich base ligand (L)

Build 20 instrument was used for TGA. Magnetic susceptibility measurements of the complexes were made by using a Gouy magnetic balance at room temperature.

Synthesis of Mannich base ligand (L):

According to a reported procedure [8], an ethanolic solution of 3, 4-dimethoxy-benzaldehyde, pyrrolidine and cyclopentanone were mixed in 1:1:1 mole ratio followed by addition of one equivalent of calcium chloride. The contents were mixed under ice cold conditions for ten min. Resulting mixture was then heated at $70-90 °C$ for 1.5 h. The mixture was then stirred at room temperature for 24 h. The progress of reaction was monitored by TLC. $NaHCO_3$ solution (5%) was added to the mixture, which resulted in a yellow precipitate, which was filtered, washed with distilled water, ethanol and finally dried.

General procedure for the synthesis of metal complexes

Hot ethanolic solution of the Mannich base and respective metal chlorides were mixed in 1:1 mole ratio. The contents were gently heated at $50 °C$ for 10 min. The resulting mixtures were then stirred at room temperature for about 2.5 h. The resulting solids formed were filtered, washed with distilled water, ethanol and finally dried under vacuum.

Characterization of ligand and its metal complexes

Mannich base (L): Molecular formula: $C_{18}H_{25}NO_3$ g/mole, yellow solid, Yield: 59%, m.p.: 188–190 °C Molecular weight: 303.35. IR (cm^{-1}): 1598 (C-N-C stretching), 1508 (C=C stretching); 1678 (C=O stretching).

Labeling of Mannich base for ^1H and ^{13}C NMR spectra

^1H NMR (400 MHz, CDCl$_3$,δ): 1.196–1.279 (6H, m, H_b, $H_{b'}$ H_f),2.060−2.130(4H,m,H_d,H_e), 2.390−2.417 (1H, t, H_C), 2.967–2.995(4H, dt, H_a, $H_{a'}$), 3.937(6H, s,oCH_3), 6.934–6.948 (1H, d, $H_{h'}$ J = 5.6 Hz), 7.134−7.137(1H, d ,H_l , J =1.2 Hz) , 7.225− 7.239(1H, d, $H_{i'}$, J = 5.6 Hz), 7.543 (1H, s, H_h). ^{13}C NMR (400 MHz, CDCl$_3$, δ): 20.15(C_d),
38

26.46(C_e), 29.02(C_b, C $_{b'}$), 30.33(C_f), 37.74(C_a, C $_{a'}$), 55.89(C_l), 55.97(OCH_3), 111(C_h), 113(C $_{h'}$), 124(C $_{i'}$), 135(C_k), 148(C_j), 150.26(C_i), not observed (C_g). EI–MS *(m/z)* (%) = 380.2 observed for $[M+ 2K-H]^+$ (100), 365.2 $[C_{17}H_{22}NO_3+2K-H]^+$ (39), 349.2$[C_{16}H_{19}NO_3+2K-H]^+$ (28).
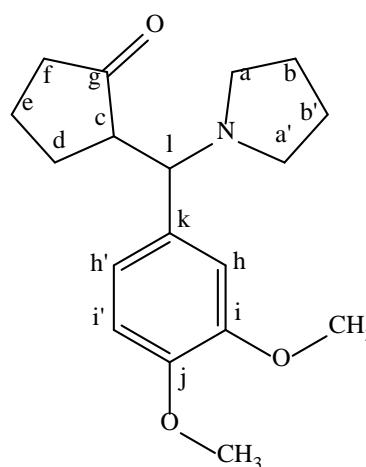
Characterization of the metal complexes

Labeling of metal complexes of L for ^1H and ^{13}C NMR spectra
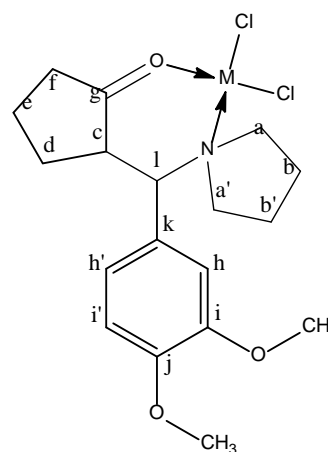
M = Cu^{+2}, Co^{+2}, Ni^{+2}, Fe^{+2}

Cu (II)-complex: Molecular formula: $C_{18}H_{25}Cl_2CuNO_3$, light green solid, yield: 51%, m.p.: decomposed above 280 °C, molecular weight: 437.85 g/mole, %age metal for MLCl$_2$:

Theoretical/experimental (14.51/13.31). IR (cm^{-1}): 1591 (C-N-C stretching), 1512 (C=C stretching); 1660 (C=O stretching), 441 (Cu−N stretching), 528(Cu-O stretching). ^{1}H NMR (CDCl$_3$, 400MHz): δ1.566 (CH$_2$, br-m, H$_a$, H$_{a'}$ H$_b$, H$_{b'}$, H$_d$, H$_e$ and H$_f$), 3.125(1H, br, s H$_c$), 3.940 (6H, s,oCH$_3$) 6.947(1H, br-s, H$_l$),7.141−7.250(2H, br-d, H$_{h'}$, H$_{i'}$), 7.550 (1H, S, H$_h$); ^{13}C NMR (400 MHz, CDCl$_3$, δ): 20.03−26.46 (CH$_2$), 55.90−55.98 (OCH$_3$), 39.16(C$_d$), 111.18−113.48 (C$_{h'}$), 114.56(C$_h$), 123.03(C$_k$), 133.68−135.40 (C$_{i'}$), 148.94 (C$_j$), 151.18 (C$_i$).

Ni (II)-complex: Molecular formula: C$_{18}$H$_{25}$Cl$_2$NiNO$_3$, greenish yellow solid, yield: 55%, m.p.: decomposed above 280oC. Molecular weight: 433.00 g/mole, %age metal for MLCl$_2$: Theoretical /experimental (13.56/13.03); IR (cm^{-1}): 1589 (C−N−C stretching), 1514 (C=C stretching); 1659 (C=O stretching), 438 (Ni−N stretching), 544(Ni−O stretching); ^{1}H NMR (CDCl$_3$, 400 MHz): δ1.260−2.172 (14H, br-m, H$_a$ H$_{a'}$ H$_b$, H$_{b'}$, H$_{d,}$ H$_e$, H$_f$) 3.122(1H, br-t, H$_c$), 3.876 − 3.941(6H, br-s,oCH$_3$), 6.951 (1H, br, d, H$_{h'}$), 7.143 (1H, br, d, H$_l$), 7.245−7.261 (1H, br-d, H$_{i'}$), 7.551(1H, s, H$_h$); ^{13}C NMR (400 MHz, CDCl$_3$, (δ): 20.26 (CH$_2$), 55.36−55.97 (OCH$_3$), 111.18(C$_{h'}$), 113.47 (C$_h$), 124.56(C$_k$), 129.03−129.41 (C$_{i'}$), 149.04−150.03 (C$_j$, C$_i$)

Co (II)-complex: Molecular formula: C$_{18}$H$_{25}$Cl$_2$CoNO$_3$, off-white solid, yield: 51%, m.p.: decomposed above 280oC, molecular weight: 433.24 g/mole, %age metal for MLCl$_2$: Theoretical/experimental (13.60/12.98); IR (cm^{-1}): 1593 (C−N−C stretching), 1515 (C=C stretching); 1661 (C=O stretching), 441(Co−N stretching), 531 (Co−O stretching); ^{1}H NMR (CDCl$_3$, 400MHz): δ1.262−1.454 (4H, br-m, H$_b$, H$_{b'}$), 1.583-2.659 (2H, br-t, H$_f$), 2.043−2.244 (4H, br−m, H$_e$, H$_d$), 2.992−3.195(1H, br-t, H$_c$), 3.812-3.857(6H, br-s,oCH$_3$), 3.939−4.015(4H,br-t, H$_a$, H$_{a'}$), 6.825−6.869(1H, br−d, H$_{h'}$), 7.013−7.140(1H, br-d, H$_l$), 7.232−7.245(1H, br-d, H$_{i'}$), 7.549−7.624(1H, br-s, H$_h$); ^{13}C NMR (400 MHz, CDCl$_3$, δ): 20.43−26.66 (CH$_2$), 55.85−55.98 (OCH$_3$), 111.17−111.86 (C$_{h'}$), 124.57(C$_h$), 133.87−133.92 (C$_k$, C$_{i'}$), 149.97−150.34 (C$_i$, C$_i$)

Fe (II)-complex: Molecular formula: C$_{18}$H$_{25}$Cl$_2$FeNO$_3$, light brown solid, yield: 56%, m.p.: decomposed above 280oC, molecular weight: 430.15 g/mole, %age metal for MLCl$_2$: Theoretical/experimental: (12.98/11.92); IR (cm^{-1}): 1595 (C−N−C stretching), 1512 (C=C stretching); 1664 (C=O stretching), 427(Fe−N stretching), 519 (Fe−O stretching);^{1}H NMR (CDCl$_3$, 400MHz): δ 1.255-2.567(14H, br- m, H$_a$, H$_{a'}$ H$_b$,H$_{b'}$ H$_d$, H$_e$, H$_f$), 3.122 (1H, br-s,

H$_c$),3.941(6H, S,oCH$_3$), 6.948 (1H, br-d, H$_{h'}$)7.143 (1H, br−d, C$_l$) , 7.248(1H, br-d, H$_{i'}$), 7.552(1H, s, H$_h$); ^{13}C NMR (400 MHz, CDCl$_3$, δ): 20.45−26.46 (CH$_2$), 55.05−55.95 (OCH$_3$), 111.11 (C$_{h'}$), 112.41 (C$_h$), 58.37(C$_f$), 123.31 (C$_k$), 133.47−133.58 (C$_{i'}$), 149.75−150 (C$_j$, C$_i$)

Biological evaluation

Antiurease activity: Measurement of antiurease activity was carried out by Berthelot assay with minor modifications [15-16]. Ten µL of 50 mM phosphate buffer (pH 7.0), 10 µL of respective test compound and 25 µL of jack beans urease (0.015 units, from Sigma) were mixed and pre-incubated at 37ºC for 10 min. Then, 40 µL of 20 mM urea was added to each well as a substrate and incubation continued at 37ºC for further 10 min followed by pre-read at 625 nm using the 96-well plate reader Synergy HT (BioTek Inc. USA). Then freshly prepared phenol hypochlorite (115 µL) reagent was added in each well (by mixing 45 µL of phenol reagent with 70 µL of alkali reagent). Incubation was further continued for another 10 min followed by the measurement of absorbance. The percentage enzyme inhibition was calculated by the formula: Inhibition (%) = 100 − [(Abs. of test sample / Abs. of control) × 100]. IC$_{50}$ values of active compounds were determined by measuring activities at further dilutions and the data were computed by using EZ-Fit Enzyme software (Perrella Inc., USA).

Molecular docking studies

Structures preparation and docking protocol: For molecular docking simulations of the most active compound, Surflex-Dock program implemented in Sybyl-X 2.12 by CARTRA Company was used under Centos-6.6 Linux operating system [17]. The structure of the most active compound was drawn by the sketching tool available in SYBYL; proper atom type for each atom in the most active compound was assigned. Compound was minimized using the Powell method until the gradient reached to 0.05 kcal/mol and the maximum iteration reached was 10000 with the Tripos force field. Similarly, the crystal structure of urease (4ubp.pdb) [18] from Protein Data Bank was retrieved. This structure was solved at the 1.5Å resolution and had all residues available in the active site. For docking simulations, the structure was refined and prepared using the protein preparation wizard. All heteroatoms were removed except the nickel ions that acted as the catalytic center for hydrolysis of urea in the active site of the enzyme. Similarly, missing hydrogen atoms were

added and protonation states were fixed at the termini of the protein. The protomol was generated near the active site residues containing Ni(II) ions and other amino acids. Surflex-Dock was employed to generate 20 docked conformers of the compound. Finally, C-Score was calculated for each conformer and the best binding pose was selected based on the best score.

In vitro antibacterial screening: The synthesized Mannich base ligand (L) and its complexes were evaluated for their antibacterial activity against *Bacillus thuringiensis* and *Escherichia coli* by the disc diffusion method [19]. Each compound was used at a concentration of 20 mg/mL in DMSO. The zone of inhibition was measured after 48 h of incubation at 37°C.

RESULTS AND DISCUSSION

The physico-analytical information of Mannich base ligand (L) and its metal complexes is given in the experimental section. All synthesized compounds are stable and coloured solids at room temperature. The ligand and its metal complexes are insoluble in common organic solvents and soluble in chloroform, DMSO and DMF. The complexes exhibited non-electrolytic nature [20].

IR spectra: In order to get meaningful information about the connecting modes of L to the metal ion in the complexes, the IR spectrum of Mannich base ligand (L) was compared with the spectral data of its metal complexes. Important peaks at 1598, 1508, 1678 cm^{-1} were attributed to C−N−C, C=C, C=O correspondingly [21-22] in agreement with our ligand. The indication of coordination through oxygen of carbonyl and nitrogen of pyrrolidine was provided by IR spectra of all complexes in which the peaks due to C=O and C-N-C were shifted to lower frequencies (1678−1659 cm^{-1}) and (1598−1589 cm^{-1}), respectively [23]. Coordination from these sites was further supported by the appearance of some new bands at 431−441 cm^{-1} and 528−544 cm^{-1} assignable to M−N and M−O bonds, respectively [24].

NMR spectra: The ^{1}H-NMR spectrum of the ligand 2-[(3,4-dimethoxyphenyl)(pyrrolidin-1-yl)methyl]cyclopentanone exhibits a multiplet 1.196−1.279 attributed to H_b, $H_{b'}$ H_f protons. The H_e and H_d protons appear as multiplet in the range δ 2.06 – 2.130 ppm. The triplet at δ 2.390 – 2.417 can be assigned to proton H_c. The protons H_a and $H_{a'}$ appear as doublet of triplet at δ 2.967 – 2.995 ppm. The methoxy protons exhibit a sharp singlet at δ 3.937 ppm. The aromatic proton $H_{h'}$ exhibits a doublet at δ 6.934 – 6.948 ppm. The doublet at δ

7.134 – 7.137 ppm is attributed to proton H_l and is in agreement with literature [25-26]. The doublet at δ 7.225 – 7.239 is attributed to the aromatic proton $H_{i'}$. The singlet at δ 7.543 is attributed to the aromatic proton H_h. These chemical shifts support well the proposed structure of L. In the metal complexes, the minor changes in chemical shift values of protons, particularly those close to C=O and C-N-C moieties support the involvement of these two groups in coordination with the metal ions [27-28].

The important chemical shifts of different carbon atoms of the ligand L and its metal complexes are also given in the experimental section. Unfortunately, chemical shift of quaternary carbon C=O could not be observed in both ligand and metal complexes, hence it is difficult to comment regarding bidentate coordination mode of ligand towards metal ion on the basis of ^{13}C NMR data. Therefore, the bidentate mode of the ligand was proposed on the basis of the IR spectra while geometry of complexes was established on the basis of %age of metal by ICP-OES, UV-Vis and magnetic moment data.

Mass spectrum (EI): The EI mass spectrum of ligand (L) was recorded. In the said spectrum the base peak was observed at 380.2 which can be attributed to [M+ 2K-H]$^+$ (100), [29]. Some other fragments at 365.2 and 349.2 were also observed and can be attributed to [C$_{17}$H$_{22}$NO$_3$+2K-H]$^+$ (39) and [C$_{16}$H$_{19}$NO$_3$+2K-H]$^+$ (28), respectively.

Thermal study (TGA): Thermal analysis was carried out in order to get knowledge about the thermal behavior of the ligand (L) and its complexes. Thermal studies were carried out by means of SDT-Q 600 V20.9 Build 20 by heating up to 1000°C. The TGA curve of the metal complexes showed an endothermic peak at 300°C which was corresponding to the elimination of chlorine coordinated to the metal ion. The organic part decomposed around 400°C. Above 600°C, there was no change in weight, the plateau observed corresponded to the oxide of the respective metal.

UV/Vis and magnetic moment data: The absorption band at 13146 cm^{-1} in the Cu (II)-L complex can be assigned to $^2T_2$ ----> ^2E transition revealing tetrahedral geometry. The magnetic moment value of 2.12 B.M. of this complex further supported its tetrahedral geometry [30]. The Ni(II)-L complex showed two absorption bands at 11675 cm^{-1}, 15421 cm^{-1} assigned to $^3T_1$(F) -----> $^3A_2$(F),$^3T_1$(F) -----> $^3T_1$(P) transitions supporting tetrahedral environment around the nickel ion. The magnetic moment value (3.21 B.M.) also favored similar environment around the nickel ion [31]. The

electronic spectrum of the Co(II)-L complex exhibited two bands at 11733 cm^{-1}, 17357 cm^{-1} assigned to $^4A_2(F)$ ------> $^4T_1(F)$ and $^4A_2(F)$ ----> $^4T_1(P)$ transitions, respectively. The appearances of these bands were in good agreement with the tetrahedral stereochemistry for Co (II) ion which was further supported by its magnetic moment value at 4.29 B.M. [31]. The electronic spectrum of the Fe(II)-L complex showed a single absorption band at 8560 cm^{-1} which was attributed to ^5E -----> $^5T_2$ transition of tetrahedral geometry. The room temperature magnetic moment (4.61 B.M.) of this complex corresponded to tetrahedral symmetry [32].

Biological activity

Antiurease assay: The synthesized scaffolds were screened for their antiurease activities and their percent inhibitions and IC$_{50}$ values were determined. The enzyme inhibition potential was observed in the following order: L−Ni(II) > L−Fe(II) > L > L−Cu(II) > with IC$_{50}$ values 1.42±0.003 > 5.41±0.005 > 9.25±0.002 > 137.52±0.58 µM, respectively, as compared with standard thiourea with IC$_{50}$ value 21.25±0.15 µM (Table 1). The lower the IC$_{50}$ value, the higher is the inhibitory potential of the compound. Complex L−Co(II) was found inactive and inhibited only 27.87% enzyme activity. This shows that the complexation of L with Ni(II) and Fe(II) improved enzyme inhibitory potential (as shown by the decreased IC$_{50}$ values in comparison with (L) while with Cu(II) antiurease activity decreased considerably (as shown by the increased IC$_{50}$ value) and with Co(II), it completely abolished inhibition. Two nickel atoms are the part of the catalytic centre of the enzyme. The highest inhibition potential of the complex L-Ni (**4**) may be attributed to the catalytic centre by Ni-bound ligand molecule though this statement needs to be justified and possible mechanism of metals in the inhibition of urease enzyme remains to be determined.

Antibacterial activity

The synthesized compounds were also evaluated for their antibacterial activity against *B. thuringiensis* and *E. coli* by the disc diffusion method. The zone of inhibition (mm) was determined as an index of antibacterial activity. These compounds exhibited poor antibacterial potential (Table 2).

Molecular docking

In order to identify the probable binding pose of the most active Ni(II) complex, it was docked in the urease crystal structure of *Bacillus pasteurii* as shown in Figure 1.
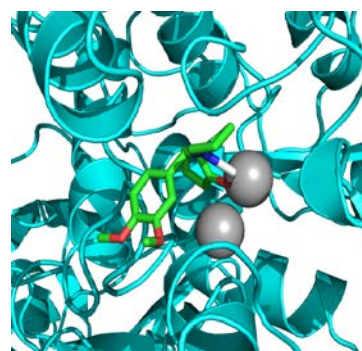

Figure 1. Predicted binding mode of the most active compound (green) in the active site (cyan) of urease enzyme. Silver spheres are Ni (II) ions.

The compound docked well in the binding site of the urease enzyme containing two Ni(II) ions, in which one is making trigonal geometries with two histidine residues (HIS137 and HIS139) and one aspartate (ASP363) while other having three coordinate covalent bonds with three histidine residues, (HIS222, His249, and HIS275). It was observed that methoxy groups on the phenyl rings were towards the solvent exposed side of the enzyme. Whereas, oxonium ion was towards one of the histidine residue (HIS222), which might give the binding stability of these compounds along with the van der Waals interactions to show biological response against the enzyme.

Table 1. Antiurease activity of L and its metal complexes

S. No.	Sample code	Inhibition (%) at 0.5 mM	IC$_{50}$ (µM)
1	L	64.87±0.07	9.25±0.002
2	L-Cu	64.53±0.92	137.52±0.58
3	L-Co	27.87±0.11	-
4	L-Ni	68.85±0.07	1.42±0.003
5	L-Fe	68.54±0.09	5.41±0.005
	Thiourea	98.45±0.87	21.25±0.15

Table 2. Antibacterial activity of ligand (L) and metal complexes

Bacteria	L (mm)	L-Cu (mm)	L-Co (mm)	L-Ni (mm)	L-Fe (mm)	Gentamycine (mm)
B. thuringiensis	3	10	11	6	5	18
E. coli	4	6	14	4	3	16

CONCLUSIONS

The present study offers a simple method for the manufacture of *β*-aminoketens. Spectroscopic techniques supported the designed structures. The synthesized scaffolds were screened for their antiurease and antibacterial activities.

Most of the compounds showed poor inhibitory activity against *B. thuringiensis* and *E. coli* and strong inhibitory potential for jack bean urease. It is noteworthy that L−Ni(II) and L−Fe(II) exhibited potent antiurease activities. The docking studies supported the binding mode of the most active compound with the enzyme which is in agreement with the previous reported studies. Additionally, the mild experimental conditions, convenient operation and simple synthetic route made it credible for the production of corresponding scaffolds which may serve as an alternative route of metal containing inhibitors against urease enzyme.

REFERENCES

1. F.F. Blicke, *Org. React.1*; Review, 303 (1942).
2. A. Cordova, *Acc. Chem. Res*., **37**, 102 (2004).
3. W.N. Speckamp, M. J. Moolenar, *Tetrahedron*, **56**, 3817 (2000).
4. S.F. Matrin, Bursk, *Tetrahedron*, **57**, 3221 (2001).
5. W. Notz, F. Tanaka, S.I. Watanable, N.S. Chowdari, J.M. Turner, R. Thayumanavan, C.F. Barbas, *J. Org. Chem*., **68**, 9624 (2003).
6. Shiozawa, K. Narita, G. Izumi, S. Kurashige, K. Sakitama, M. Ishikawa, *Eur. J. Med. Chem*., **30**, 85 (1995).
7. B. List, *J. Am. Chem. Soc*., **122**, 9336 (2000).
8. P. Kulkarni, B. Totawar, P.K. Zubaidha, *Monatsh. Chem*., **143**, 625 (2012).
9. W.G. Beyer, Manganese in Metabolism and Enzyme Function, New York: Academic Press, 1986.
10. M. Tumer, H. Koksal, M.K. Serner, S. Serin, *Transition Met. Chem*., **24**, 414 (1999).
11. M.A. A. Al−Bari, A. Khan, B.M. Rahman, M. Kudrat-E-Zahan, A.M. Mossadik, M.A.U. Islam, *Res. Agric. Biol. Sci.*, **3**, 599 (2007).
12. A. Sarika, *Transition Chem.*, **32**, 816 (2007).
13. M. Liaqat, T. Mahmud, A. Hameed, M. Ashraf, M. Shafiq, H. Asghar, *Inorganic and Nano-Metal Chemistry*, **47,** 1418 (2017).
14. M. Liaqat, T. Mahmud, M. Imran, M. Iqbal, M. Muddassar, T. Ahmad, L. Mitu, *Rev. Chim. (Bucharest)*, **68** (11), 2560 (2017).
15. M.W. Weatherburn, *Anal. Chem.*, **39**, 971 (1967).
16. S. Naureen, F. Chaudhary, N. Asif, M.A. Munawar, M. Ashraf, F.H. Nasim, H. Arshad, M.A. Khan, *Eur. J. Med. Chem.,* **102**, 464 (2015).
17. N.J. Ajay, *J. Med. Chem.,* **46**, 499 (2003).
18. S. Benini, W.R. Rypniewski, K.S .Wilson, S. Miletti, S. Ciurli, S. Mangani, *J. Biol. Inorg. Chem.*, **5,** 108 (2000).
19. A.W. Bauer, W.M. Kirby, J.C. Sherris, *Turck. Am. Clin. Pathol.*, **9**, 493 (1966).
20. W.J. Geary, *Coord. Chem. Rev.*, **7**, 81 (1971).
21. M. Simpy, S. Balgar, S. Moitha, H. N. Sheikh, B. L. Kalsotra, *Chin. J. Chem.*, **29**, 53 (2011).
22. D.T. Vendan, S. Rajeswari, S. Ilavenil, G.V. Prabhu, *Orbital Elec. J. Chem.*, **2**, 201 (2012).
23. S. Anad, *Transition Metal. Chem.*, **32**, 816 (2007).
24. J. Abdul-Ghani, M. J. Al-Jaboori, A.M. Al-Karawis, *J. Coord. Chem.*, **62**, 2736 (2009).
25. M.M. Haravi, M. Zakeri, N. Mohammadi, *Chinese Chemical Letters*, **22**, 797 (2011)
26. Q. Xu, Z. Yang, D. Yin, J. Wang, *Front. Chem. Eng. China*, **3**, 201 (2009)
27. N. Roman, S. Esthar, C. T. Raja, *Ind. Acad. Sci. J. Chem. Sci.*, **116**, 209 (2004).
28. D. Sathya, J. Senthil, S. Pria, *Int. J. Chem. Tech. Res.*, **3**, 248 (2011).
29. R. N. Grewal, H. E. Jeffrey, C. S. Christopher F. R. Alan C. Hopkinson, K. W. M. Siu, *Int. J. Mass Spect.*, **219**, 89 (2002).
30. H. Brundic, B. Kaitner, B. Kamenar, V. M. Leovac, *Inorg. Chim. Acta*, **188**, 151 (1991).
31. M.A. Sivasankaran, R. S. Joseyphus, *Spectrochimica Acta-A: Molecular and Biomolecular Spectroscopy*, **70**, 749 (2008).
32. M.Z. Chen, H. M. Sun, W. F. Li, *J. Organomet. Chem.*, **691**, 2489 (2006).

Синтез, охарактеризиране и биологична активност на нова Манихова база 2-[(3, 4-диметоксифенил)(пиролидин-1-ил)метил]циклопентанон и комплексите му с Cu(II), Co(II), Ni(II) и Fe(II) йони

М. Лиакат[1], Т. Махмуд[1*], М. Имран[1], М. Ашраф[2], А. У. Хак[3], М. Мудасар[4], Т. Ахмад[5]

[1]*Институт по химия, Пунджабски университет, Лахор, Пакистан*

[2]*Департамент по химия, Исламия университет на Бахавалпур, Бахавалпур, Пакистан*

[3] *Колеж по фармация, Гашонски университет по медицински науки, Инчеон, Южна Корея*

[4]*Департамент по бионауки, COMSATS Институт по информационна технология, Парк роуд, Исламабад, Пакистан*

[5]*Департамент по химия, Университет на Саргодха, Мианвали, Пакистан*

(Резюме)

Едностадийна трикомпонентна манихова реакция е проведена чрез кондензация на 3,4-диметоксибензалдехид, пиролидин и циклопентанон в присъствие на калциев хлорид и разтворител етанол, като е получена нова манихова база (L). Маниховата база е изолирана и са образувани комплексите й с Cu(II), Co(II), Ni(II) и Fe(II) йони. Структурите на синтезираните съединения са потвърдени чрез IR, ^{1}H NMR, ^{13}C NMR, масспектрометрия, термогравиметричен и елементен анализ. Металното съдържание е определено чрез ICP-OES. Всички съединения проявяват слаба антибактериална активност. Антиензимната активност е изследвана по отношение на бобова уреаза. Маниховата база (L), никеловият и железният комплекс проявяват силно антиуреазно действие с IC_{50} стойности съответно 9.25±0.002, 1.42±0.003 и 5.41±0.005 μM, като са по-силни инхибитори от стандарта тиоуреа (IC_{50} 21.25±0.15 μM). Възможният начин на свързване на най-активния никелов комплекс е определен чрез молекулни докинг симулации.

QSAR study on the physico-chemical parameters of barbiturates by using topological indices and MLR method

E. Esmaeili[1], F. Shafiei[2]*

Department of Chemistry, Science Faculty, Arak Branch, Islamic Azad University, Arak, Iran

In this study the relationship of the Randic' (^1X), Balaban (J), Szeged (Sz), Harary (H), Wiener (W), Hyper-Wiener (WW) and Wiener polarity (Wp) with the polarizability (POL), molar refractivity (MR) and octanol/water partition coefficient (logP) of barbiturates is studied. The chemical structures of the molecules were optimized using *ab initio* 6-31G basis sets method and Polak-Ribiere algorithm with conjugated gradient within Hyper Chem 8.0 environment. The multiple linear regressions (MLR) and backward methods (with significance at the 0.05 level) were employed to give the QSAR models. After MLR analysis, we studied the validation of linearity between the molecular descriptors in the best models for the used properties. The predictive powers of the models were discussed by using the method of cross-validation. The results have shown that the combination of two descriptors (Wp, W) is excellent for predicting the polarizability, and the descriptor (WW) is useful for modeling and for predicting the molar refractivity and octanol/water partition of the corresponding barbiturates.

Keywords: Barbiturates; QSAR; Polarizability; Molar refractivity; Octanol/water partition coefficient; Multiple linear regressions (MLR); Validation

INTRODUCTION

Barbiturates are a category of compounds that are focal nervous system depressants. Barbiturates overdose leads to weakness of the central nervous system, respiratory and cardiovascular depression and eventual death [1-4]. Barbituric acid derivatives act as central nervous system depressors and are used in medicine as sedative, hypnotic and anticonvulsant drugs with hypnotic or sedative properties depending on the dose administered [5]. Drug therapy is mainly used to reduce the symptoms of acute insomnia while their role in the management of chronic insomnia remains unclear [6,7]. Attention to sleep hygiene is the most important line of treatment and should be tried before any pharmacological approach is considered [8]. The relative activity in a series of barbituric acid substitution derivatives and their lipophilicity has been studied [9]. Quantitative structure – activity relationship (QSAR) has been known as a quantum chemical technique in connection with the biological activity of compounds by their molecular structure and has been used as a predictive tool in drug design [10]. A QSAR analysis of 21 molecules of 1, 2, 3-oxadiazole-2-thiones has been performed using multiple linear regression model [11]. Calculation of the volume distribution of certain pharmaceutical compounds from their structural descriptors has been considered [12]. QSAR studies on the benzylidenebarbiturate derivatives inhibiting the activity of the mushroom tyrosinase have been investigated [13]. QSAR models have been developed to determine the penetration coefficients of barbiturates in biological membranes [14]. 3D QSAR technique has been used to predict biological properties such as toxicity of chemicals [15-18]. The structure-activity relationship in barbiturates and its similarity to other drugs has been traditionally developed to the estimation and prediction of biological activity [19-21]. The aim of this study is to provide reliable QSAR models for predicting the polarizability (POL), molar refractivity (MR) and octanol/water partition coefficient (logP) of barbiturates.

MATERIALS, MATHEMATICAL METHOD AND GRAPHS

The barbiturates discussed in this study consist of 17 derivatives with substitution at 3, and 5, 5 positions. Figure 1 shows the template structure of barbiturates used in the present study.
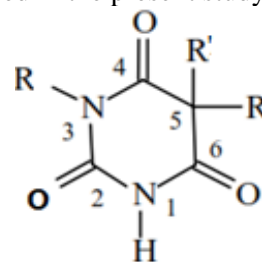

Figure 1. The structural template of barbiturates

*) To whom all correspondence should be sent:
E-mail: f-shafiei@iau-arak.ac

Table 1. Barbiturates and their polarizability, molar refractivity and octanol/water partition coefficient

Compound No	Name of compound	POL	MR	Log P
1	Barbituric acid	11.1	23.23	-1.6
2	1,3-Dimethylpyrimidine-2,4,6-trione	14.22	34.52	-1.4
3	5,5-Dimethylpyrimidine-2,4,6-trione	14.77	32.31	-0.37
4	5-Ethyl-5-methylpyrimidine-2,4,6-trione	16.6	36.91	-0.03
5	5-Ethyl-1-methylpyrimidine-2,4,6-trione	16.6	38.18	-0.37
6	5-Ethyl-5-isopentylpyrimidine-2,4,6-trione	23.14	58	1.86
7	5-sec-Butyl-5-ethyl-1-methylpyrimidine-2,4,6-trione	23.94	56.43	1.42
8	5-Ethyl-5-(pentan-2-yl)pyrimidine-2,4,6-trione	23.94	55.26	1.55
9	5-sec-Butyl-5-ethylpyrimidine-2,4,6-trione	22.11	52.4	1.19
10	5-(Hexan-2-yl)pyrimidine-2,4,6-trione	22.11	50.76	0.88
11	5-Ethyl-5-(Hexan-2-yl)-1,3-dimethylpyrimidine-2,4,6-trione	29.45	69.65	2.44
12	5-Allyl-5-(pentan-2-yl)pyrimidine-2,4,6-trione	25.58	59.9	1.73
13	5-sec-Butyl-5-allylpyrimidine-2,4,6-trione	21.91	50.7	0.94
14	5-Cyclohexenyl-1,5-dimethylpyrimidine-2,4,6-trione	24.01	61.95	1.17
15	5-Ethyl-5-phenylpyrimidine-2,4,6-trione	24.43	57	1.25
16	5-Ethyl-1-methyl-5-phenylpyrimidine-2,4,6-trione	26.26	62.77	1.51
17	5-Ethyl-1,3-dimethyl-5-phenylpyrimidine-2,4,6-trione	27.55	66.8	1.74

The polarizability, molar refractivity and octanol/water partition coefficient of barbiturates is taken from the quantum mechanics methodology with ab initio 6-31G basis sets method and Polak-Ribiere algorithm with APHS.

TOPOLOGICAL INDICES

A topological index is a numeric quantity that is mathematically derived in a direct and unambiguous manner from the structural graph of a molecule. The topological indices (TIs) used for the QSAR analysis were Wiener (W) [22], Szeged (Sz) [23], first order molecular connectivity (^{1}X) [24], Balaban (J) [25], Hyper-Wiener (WW) [26], Wiener polarity (Wp) [27] and Harary (H) [28] indices. All used topological indices were calculated using hydrogen suppressed graph by deleting all carbon-hydrogen, as well as heteroatomic hydrogen bonds from the structure of the barbiturates. The calculations of topological indices used in this paper are well documented. The descriptors were calculated with the chemicalize program [29]. Seven topological indices tested in the present study are listed in Table 2.

REGRESSION ANALYSES

In the present work, linear regression analyses were performed using SPSS-16 (SPSS Inc., Chicago, IL, USA)). The polarizability (POL), molar refractivity (MR) and octanol/water partition coefficient (logP) were used as dependent variables and ^{1}X, J, H, W, Wp, WW and Sz indices as independent variables. Criteria for selection of the best multiple linear regression model were the statistics: squared multiple correlation coefficient (R^2), adjusted correlation coefficient (R^2_{adj}), Fisher ratio (F), root mean square error (RMSE), Durbin-Watson value (DW) and significance (Sig).

Table 2. Barbiturates and their topological indices used in the present study

No.	^{1}X	J	H	W	WW	Wp	Sz
1	4.18	2.08	19.5	84	159	9	144
2	5.04	2.39	27.32	140	281	17	230
3	4.94	2.43	27.57	138	274	17	226
4	5.5	2.73	31.43	177	372	20	279
5	5.57	2.65	31.05	181	388	19	287
6	7.42	2.74	47.51	418	1115	26	576
7	7.41	3.05	49.44	379	903	32	549
8	7.48	2.9	48.43	398	1005	29	556
9	6.98	2.74	44.39	324	761	28	468
10	7.06	2.34	41.92	374	1040	21	518
11	8.84	2.9	63.25	632	1761	38	866
12	7.98	2.77	52.83	472	1233	30	644
13	7.48	2.96	48.65	391	961	29	549
14	7.98	2.2	54.63	458	1179	32	770
15	8.11	2.2	54.4	458	1172	31	756
16	8.54	2.15	59.76	526	1363	35	863
17	8.96	2.11	65.37	598	1564	39	976

RESULTS

Several linear QSAR models involving three-seven descriptors were established and the strongest multivariable correlations were identified by the backward stepwise regression routine implemented in SPSS used to develop the linear model for the prediction of polarizability, molar refractivity and octanol/water partition coefficient.

QSAR models for molar refractivity (MR)

The best linear model for molar refractivity contains four topological descriptors, namely, Hyper Wiener (WW), Szeged (Sz), Harary (H) and Wiener (W) indices. The model is presented below:

Model 1

MR =-14.096-0.037(Sz)+ 0.118(WW)-
0.464(W)+3.224(H)   (1)
N=17,   R=0.991, R^2=0.983, R^2_{adj} = 0.977,
RMSE= 26.346, F=172.333, Sig=0.000, DW=2.102

QSAR models for the polarizability (POL)

The best linear model for polarizability contains four topological descriptors, namely, Wiener polarity (Wp), Hyper Wiener (WW), Randic (^1X) and Szeged (Sz) indices.

The regression parameters of the best four descriptors correlation model are gathered in equation (2):

Model 2

POL= -0.676+2.653(^1X)+0.179(Wp)-
0.011(Sz)+0.005(WW)   (2)
N=17,   R=0.996, R^2=0.992, R^2_{adj} = 0.989,
RMSE=10.248, F=351.311, Sig=0.000, DW=1.959

QSAR models for octanol/water partition coefficient (logP)

The best linear model for the octanol/water partition coefficient contains three topological descriptors, namely, Hyper Wiener (WW), Szeged (Sz) and Harary (H) indices. The model is presented below:

Model 3

logP =-3.706-0.008(Sz)+0.002(WW)+0.154(H) (3)
N =17, R=0.968, R^2=0.937, R^2_{adj}=0.922,
RMSE=2.594, F=64.046, Sig=0.000, DW=1.978.

These models produced a squared correlation coefficient close to 1, and the results of other statistical parameters are also very satisfactory.

DISCUSSION

We studied the relationship between the topological indices and the polarizability, molar refractivity and octanol/water partition coefficient of 17 barbiturates. In this study, to find the best

model to predict the parameters mentioned, we will use the following sections.

Multicollinearity: Multicollinearity test is a basis of the variance inflation factor (VIF) value of multicollinearity test results using SPSS. If the VIF value lies between 1 and 10, then there is no multicollinearity; if the VIF<1 or >10, then there is multicollinearity. In all our final models there is multicollinearity, because the values of the correlations between independent variables are close to 1 and the VIF value does not lie between 1 and 10.

Validation: The success of any QSAR model depends on the accuracy of the input data, selection of appropriate descriptors, statistical tools and validation of the developed model. In this section, for verification and validity of the regression models, we will focus on Durbin-Watson statistics and unstandardized predicted and residual values. The Durbin-Watson statistics ranges in value from 0 to 4. A value near 2 indicates non-autocorrelation. In all our models, the value of Durbin-Watson statistics are close to 2 (see eqs.1, 2 and 3) and hence the errors are uncorrelated.

Results and discussion of validation: Multiple linear regression method was used for all QSAR analyses. A good QSAR model should have both suitable relativity and good predictability. We studied the validation of linearity between the molecular descriptors in the models 1, 2 and 3. We obtained by SPSS the Pearson (2) coefficient correlation and collinearity statistics as follows (see Tables 3, 4 and 5). For model 1 the Pearson correlations (WW, W), (WW, H) and (W, H) are near 1, and VIF (WW, H, W, Sz) >10, therefore there is linearity between these descriptors. After removing W and H from this model, we corrected model 1 as follows:

MR=26.298+0.027(WW)   (4)

N=17, R=0.968, R^2=0.936, R^2_{adj} = 0.932,
RMSE= 51.4242, F=219.944, Sig=0.000, DW=1.560, Q^2=0. 88.

Similarly to model 1 we obtained the corrected models 2 and 3 as follows:

POL=8.822+0.265(Wp)+0.006(WW)   (5)

N=17, R=0.986, R^2=0.973, R^2_{adj}= 0.969, RMSE= 14.353, F=248.454, Sig=0.000, DW=0.950, Q^2=0.86.

logP=-1.22+0.002(WW)   (6)

N=17, R=0.915, R^2=0.837, R^2_{adj} = 0.826, RMSE= 4.246, F=76.787, Sig=0.000, DW=0.836, Q^2=0.88.

Further we computed Q^2 (Eq. 7) by 50% of the data, randomly, that are positive and less than 1:

$$Q^2 = 1 - \frac{\sum (Y_i - \bar{Y}_{i|i})^2}{\sum (Y_i - \bar{Y})^2} \quad Q^2 \leq 1 \qquad (7)$$

where the notation indicates that the response is predicted by a model estimated when the ith sample was left out from the data set.

Regular residuals: The residual is the difference between the observed and predicted values. Comparison between predicted and observed values

of polarizability, molar refractivity and octanol/water partition coefficient of the barbiturates is shown in Table 6. Figures 2-4 show the linear correlation between the observed and the predicted polarizability, molar refractivity and octanol/water partition coefficient of barbiturates values obtained using equations (4-6), respectively

Table 3. Correlation between the molecular descriptors (model 1) for molar refractivity (MR)

	Pearson correlations (model 1)			Collinearity statistical		Corrected model	
	H	WW	Sz	W	Tolerance	VIF	VIF	VIF
H	1	0.960	-0.521	-0.974	0.001	698.821	35.953	-
WW		1	-0.405	-0.996	0.000	2.15×10^3	19.135	1
Sz			1	0.381	0.027	37.541	32.103	-
W				1	0.000	4.784×10^3	-	-

Table 4. Correlation between the molecular descriptors (model 2) for the polarizability (POL)

	Pearson correlations (model 2)				Collinearity statistical		Corrected model	
	Wp	WW	^{1}X	Sz	Tolerance	VIF	VIF	VIF
Wp	1	0.425	-0.682	-0.258	0.058	17.097	9.152	6.283
WW		1	-0.663	-0.427	0.036	27.833	15.60	6.283
^{1}X			1	-0.209	0.019	52.583	-	-
Sz				1	0.042	23.718	22.681	-

Table 5. Correlation between the molecular descriptors (model 3) for octanol/water partition coefficient (logP)

	Pearson correlations (model 3)			Collinearity statistical		Corrected model
	Wp	WW	Sz	Tolerance	VIF	VIF
Wp	1	-0.432	0.718	0.028	35.953	-
WW		1	0.298	0.052	9.135	1
Sz			1	0.031	2.103	-

Table 6. Comparison between predicted and observed values of models calculated validation of POL, MR and logP of the corresponding barbiturates.

| No.	Observed MR	Predicted MR	Residual	No.	Observed POL	Predicted POL	Residual	No.	Observed logP	Predicted logP	Residual
1	23.23	30.59	-7.36	1	11.10	12.21	-1.11	1	-1.60	-0.86	-0.74
2	34.52	33.89	0.63	2	14.22	15.10	-0.88	2	-1.40	-0.59	-0.81
3	32.31	33.70	-1.39	3	14.77	15.06	-0.29	3	-0.37	-0.61	0.24
4	36.91	36.35	0.56	4	16.60	16.47	0.13	4	-0.03	-0.39	0.37
5	38.18	36.78	1.40	5	16.60	16.31	0.29	5	-0.37	-0.35	-0.02
6	58.00	56.43	1.57	6	23.14	22.74	0.40	6	1.86	1.27	0.59
7	56.43	50.70	5.73	7	23.94	23.00	0.94	7	1.42	0.79	0.63
8	55.26	53.46	1.80	8	23.94	22.87	1.07	8	1.55	1.02	0.53
9	52.40	46.86	5.54	9	22.11	21.04	1.07	9	1.19	0.48	0.71
10	50.76	54.40	-3.64	10	22.11	20.94	1.17	10	0.88	1.10	-0.22
11	69.65	73.89	-4.24	11	29.45	30.00	-0.55	11	2.44	2.71	-0.27
12	59.90	59.62	0.28	12	25.58	24.55	1.03	12	1.73	1.53	0.20
13	50.70	52.27	-1.57	13	21.91	22.57	-0.66	13	0.94	0.92	0.02
14	61.95	58.16	3.79	14	24.01	24.74	-0.73	14	1.17	1.41	-0.24
15	57.00	57.98	-0.98	15	24.43	24.43	0.00	15	1.25	1.39	-0.14
16	62.77	63.13	-0.36	16	26.26	26.69	-0.43	16	1.51	1.82	-0.31
17	66.80	68.56	-1.76	17	27.55	29.02	-1.47	17	1.74	2.27	-0.53
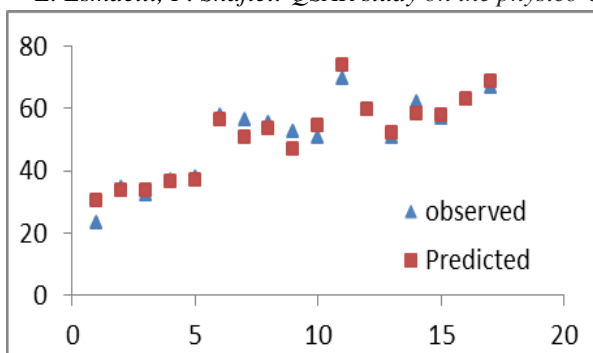
Fig. 2. Comparison between observed and predicted values of molar refractivity (MR) calculated by the MLR method.
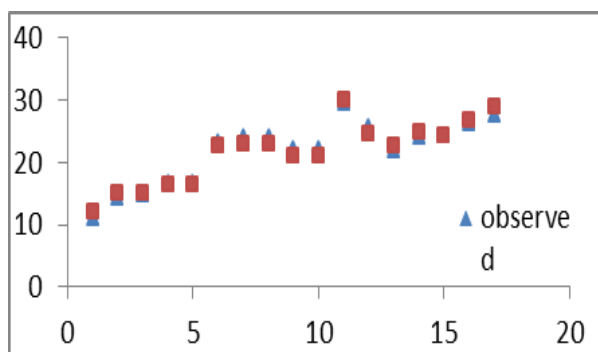

Fig. 3. Comparison between observed and predicted values of polarizability calculated by the MLR method.
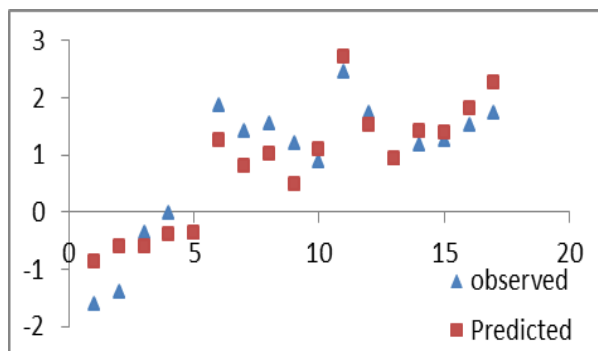

Fig. 4. Comparison between predicted and observed values of logP calculated by the MLR method.

CONCLUSIONS

QSAR models for prediction of the polarizability (POL), molar refractivity (MR) and octanol/water partition coefficient (log P) for a training set of barbiturates using MLR based on topological descriptors calculated from molecular structure alone were developed. MLR model proved to be a useful tool in the prediction of POL, MR and log P. Cross-validation as the evaluation technique was designed to evaluate the quality and predictive ability of the MLR model. The obtained results showed that two topological indices (WW and Wp) could be used successfully for predicting POL, and Hyper-Wiener index (WW) is a good topological index for modeling logP and MR.

REFERENCES

1. N. Kiyosawa, K. Tanaka, J. Hirao, K. Ito, N. Niino, K. Sakuma, M. Kanbori, T. Yamoto, S. Manabe, N. Matsunuma, *Arch.Toxicol*., **78**, 435 (2004).
2. R. Lal, S. Faiz, R.K. Garg, K.S. Baweja, J. Guntupalli, K.W. Finkel, *Am. J. Kidney Dis.,* **48**, 13 (2006).
3. B.J. Pleuvry, *Anaesth. Intensive. Care*, **5**, 252 (2004).
4. M. Fryer, *Anaesth. Intensive Care,* **5**, 317 (2004).
5. E.A. Mamina, V.V. Bolotov, *Pharm. Chem. J.,* **38**, 53 (2004).
6. C. M. Morin, *Psychosom. Med*., **62**, 483 (2000).
7. M. Hirshkowitz, Essentials of neuropsychiatry and clinical neurosciences (4 ed.). In: S. C. Yudofsky, R. E. Hales, eds., Arlington, Virginia, USA, American Psychiatric Publishing, p. 315, 2004.
8. H.E. Flamer. *Med. J. Aust.,* **162**, 603 (1995).
9. R. Ray, J.D. Sharma, S.N. Limaye, *Asian J. Chem.,* **19**, 3382 (2007).
10. M.J.S. Dewar, E.G. Zoebisch, E.F. Healy, J.J.P. Stewart, *J. Am. Chem. Soc*., **107**, 3902, (1985).
11. Z. Almi, S. Belaidi, T. Lanez, N. Tchouar, *Int. lett. Chem. Phys. Astron.,* **37**, 113 (2014).
12. M.H. Fatemi, Z. Ghorbannezhad, *J. Serb. Chem. Soc.,* **76**, 1003 (2011).
13. R.L. Sawant, G.D. Jadhav, P.D. Lanke, J.B. Wadekar, *Drug Design & Discovery,* **4**, 1077 (2013).
14. C. Hansch, A.R. Steward, S.M. Anderson, D. Bentley, *J. Med. Chem*., **11**, 1 (1967).
15. R.D. Crammer III, D.E. Paterson J.D. Bunce, *J. Am. Chem. Soc.,* **110**, 5959 (1988).
16. G. Klebe, U. Abraham, T. Mietzner, *J. Med. Chem*., **37**, 4130 (1994).
17. A.N. Jain, K. Koile, D. Chapman, *J. Med. Chem.,* **37**, 2315 (1994).
18. B.D. Silverman, D.E. Platt, *J .Med. Chem*., **39**, 2129 (1996).
19. G. Bravi, E. Gancia and A. Zaliani, *J. Comput-Aided. Mol. Des*., **11**, 62 (1997).
20. C. Hansch, A. Kurup, R Garg, H. Gao, *Chem.Rev*., **101**, 619 (2001).
21. S.C. Basak, Topological Indices and Related Descriptors in QSAR and QSPR in: J. Devillers, A. T. Balaban (eds.), Gordon and Breach, Amsterdam. 563, 1999.
22. P.V. Khadikar, N.V. Deshpande, P.P. Kale, A. Dobrynin, I. Gutman, G. Dömötör, *J. Chem. Inf. Comput. Sci*., **35**, 547 (1995).
23. I. Gutman, S. Klavžar, *J. Chem. Inf. Comput. Sci.* **35**, 1011 (1995).
24. M. Randić, *J. Math. Chem*., **7**, 155 (1991).
25. A. T. Balaban, *Chem. Phys. Lett.,* **89**, 399 (1982).
26. I. Gutman, *Croat. Chem. Acta*, **77**, 61 (2004).
27. M. Liu, B. Liu, *MATCH. Commun. Math. Comput. Chem.* **66**, 293 (2011).
28. C. K. Das, B. Zhou, N. Trinajstic, *J. Math. Chem*., **1**, 1369 (2009).
29. Web search engine developed by ChemAxon; software available at http:// www.Chemicalize.Org.

QSAR ИЗСЛЕДВАНЕ НА ФИЗИКОХИМИЧНИТЕ ПАРАМЕТРИ НА БАРБИТУРАТИ С ИЗПОЛЗВАНЕ НА ТОПОЛОГИЧНИ ИНДЕКСИ И МЕТОДА НА МНОГОКРАТНАТА ЛИНЕЙНА РЕГРЕСИЯ

Е. Есмаейли, Ф. Шафией*

Департамент по химия, Научен факултет, Клон Арак, Ислямски Азад университет, Арак, Иран

(Резюме)

В настоящата статия е изследвана зависимостта на топологичните индекси Randic (^{1}X), Balaban (J), Szeged (Sz), Harary (H), Wiener (W), Hyper-Wiener (WW) и Wiener полярност (Wp) от поляризуемостта (POL), моларния коефициент на пречупване (MR) и разпределителния коефициент между октанол и вода (logP) на барбитурати. Химичните структури са оптимизирани с помощта на *ab initio* 6-31G базисен метод и алгоритъма на Polak-Ribiere със спрегнат градиент в Hyper Chem 8.0 обкръжение. За получаване на QSAR моделите са използвани методите на многократна линейна регресия и обратните методи (със значимост на 0.05 ниво). След анализ чрез многократна линейна регресия е изследвана линейността при молекулните дескриптори в най-добрите модели. Прогнозната сила на моделите е обсъдена по метода на кръстосаното валидиране. Резултатите показват, че съчетанието от два дескриптора (Wp, W) е подходящо за предсказване на поляризуемостта, а дескрипторът (WW) е подходящ за моделиране и предсказване на моларния коефициент на пречупване и разпределителния коефициент между октанол и вода на барбитуратите.

Stability of gold complex based on mercaptotriazole in acid and neutral media

S. Dimitrijević*[1], M. Rajčić Vujasinović[2], St. Dimitrijević[3], B. Trumić[1], A. Ivanović[1]

[1]Mining and Metallurgy Institute Bor, Zeleni bulevar 35, 19210 Bor, Serbia
[2]Technical faculty in Bor, University of Belgrade VJ 12, 19210 Bor, Serbia
[3] Innovation Center Faculty of Technology and Metallurgy, University of Belgrade, Belgrade, Serbia

Stability of the gold complex based on mercaptotriazole in two acid electrolytes with different pH values and in a neutral medium was investigated in this work. Investigation was performed by visual monitoring and electrochemical characterization of the electrolytes in a period of one year or until first visible signs of complex decomposition. Electrochemical characterization of the gold complex based on mercaptotriazole was performed by open circuit potential measurement, cycling voltammetry method and by recording the polarization curves. The pH values of the electrolytes were measured before and after each electrochemical experiment. These tests were performed at different starting pH values: 2, 4 and 7 at optimal concentration of gold in the electrolyte of 2.5 g/dm^3. For electrolytes with pH values of four and seven, the first visible signs of the complex decomposition appeared tree months after synthesis. Electrolyte with pH value of two was visually stable for a period of one year.

Keywords: stability, gold complex, mercaptotriazole, non-cyanide gold electrolyte, electrochemical characterization

INTRODUCTION

Cyanide-based electrolytes for gold and gold alloys are the most used and reliable ones, especially in industrial applications. Cyanide electrolytes are exceptionally stable; the stability constant of $[Au(CN)_2]^-$ is about 10^{38}. However, with regard to the safety and disposal of wastewater, there is increasing concern on the application of cyanide-based processes [1, 2]. Furthermore, cyanide is classified as a hazardous chemical and gold plating from cyanide-based baths, is known as a high-risk technology from the general ecological point of view. The main disadvantages of using cyanide complexes are [3 - 7]:

• The presence of cyanide in solutions, wastewater and atmosphere raises the issues on ecology, occupational health and safety at work.

• Compliance with strict regulations may increase the production costs.

• A negative redox potential may lead to hydrogen evolution during plating and hinders the formulation of chemical baths.

• Incorporation of cyanide in the coatings.

• Low limiting cathode currents of cyanide complexes limit the rate of deposition.

• Incompatibility with the photoresist materials used in the lithographically patterned electrodeposition of gold.

The baths with high pH are often used to prevent undesirable evolution of hydrogen cyanide. Therefore, these alkaline baths contain an excess of cyanide in order to maintain their concentration constant. This excess cyanide moves the redox potential to more negative direction, which requires a reducing agent with a very negative redox potential. These drawbacks of electrolytes with gold cyanide have motivated the research on alternative gold complexes. Non-cyanide electrolyte for the production of decorative coatings are based mainly on the complex of gold with an organic compound. However, their use has not found satisfactory industrial application due to the low stability constants, manifested by decomposition of the complex and precipitation of elemental gold from the electrolyte [5, 8-12].

A general and significant problem for most non-cyanide baths is their low stability. This characteristic limits their usability. Instability of these compounds is most often manifested by their decomposition and precipitation of elemental gold, usually as colloid gold. The formation of colloidal gold is attributed to the disproportionation reaction of Au (I) ions in solution [5, 13−20]:

$$3Au^+ \leftrightarrow 2Au^0 + Au^{3+}$$

Formation of colloidal gold is an undesirable occurrence in the plating process due to the tendency to increase the roughness of surface, stimulating the formation of nodules, and other defects [21]. The surface of golden particles can cause additional autocatalytic deposition of gold, which accelerates the decomposition of the bath [1]. In extreme cases, deposition of gold on the surfaces of galvanizing cell was also observed.

Other models of gold decomposition have also been identified. For example, oxidation of ligands

---

(e.g. sulfite into sulfates) leads to an increase in the concentration of other less stable Au (I) complexes and reduction in the overall stability of the bath. Similarly, the hydrolysis or exchange of ligands and protonation reactions may lead to the formation of unstable gold species which may adversely affect the stability of the bath [21, 22].

EXPERIMENTAL PART

The aim of this work was to investigate the stability of the gold complex based on mercaptotriazole in acid and neutral medium for electrolytes with pH value 2, 4 and 7.

All electrolytes investigated in this research were synthesized according to the procedure described elsewhere [8].

This investigation was performed by open circuit potential measurement, cycling voltammetry method and recording the polarization curves, with pH values of the electrolyte measured before and after each electrochemical experiment for a period of one year or until the first visible signs of decomposition of the complex have been noticed by visual monitoring.

Electrochemical studies were carried out in a system consisting of an electrochemical cell and hardware interface for computerized control and data acquisition. In a standard three-electrode electrochemical cell, the working electrode was a gold-plated platinum electrode (active surface of 4.52 mm^2), whose potential was controlled against a saturated calomel reference electrode (SCE). Platinum foil (1×2 cm) served as a counter electrode. All potentials are given *versus* SCE.

The computerized control (National Instruments card, NI-6251) and data acquisition software (LabVIEW 8.2 platform and applications specifically developed for the electrochemical measurements), fully developed by the Technical Faculty in Bor [8, 23], were used to run the electrochemical experiments. The hardware consisted of a PC, AD/DA converter (PCI-E 20 428 produced by Burr-Brown), and an analog interface developed at the University of Belgrade, Technical Faculty in Bor.

The electrolyte volume used in the experiments was 100 ml. All experiments were carried out at a temperature of 25 ± 0.5 °C.

The pH values of the electrolytes were measured before and after each electrochemical measurement. The pH values were measured with a WTW pH 3110 instrument.

The open circuit potential was monitored for a period of 60 s. A relatively short time interval was chosen because no significant differences were observed for a period of 600 s in the initial series of measurements.

Cyclic voltammograms were recorded with a scan rate of 100 mV/s, in the following potential ranges:

a) for pH 2: (from +1.6 to -0.6) V
b) for pH 4: (from +1.6 to -1.5) V
c) for pH 7: (from +1.5 to -1.3) V

Polarization curves were recorded with a scan rate of 5 mV/s in the potential ranges: for pH 2: (from +0.2 to -0.6) V; for pH 4: (from +0.2 to -1.1) V and for pH 7: (from +0.2 to -1.2) V. The potential ranges were ordered by the start of gaseous hydrogen (bottom limit) and gaseous oxygen (upper limit) evolution.

RESULTS AND DISCUSSION

Visual monitoring of electrolyte

Fresh synthesized electrolyte [8] with gold concentration of 2.5 g/dm^3 and pH = 2 is colorless. No visual changes were observed by monitoring the electrolyte with this pH value for a period of one year.

The gold complex with mercaptotriazole with pH = 4 is almost colorless. After one month, the appearance of precipitate in a form of yellow flakes was observed in this electrolyte at room temperature (25 °C). After two months, a small amount of reduced elemental gold was observed in the precipitate. After three months, the electrolyte was decomposed. The solution was almost colorless with a significant amount of yellow needle-shaped crystals which were mixed with a greater amount of elemental gold.

The gold complex with mercaptotriazole with pH = 7 is pale yellow (the color is more intense than the color of the cyanide electrolyte). After a month at room temperature (25 °C) it was noted that the complex of gold at this pH value was almost colorless with the appearance of a white precipitate. Two months after the synthesis, the electrolyte solution was transparent with a pale violet precipitate. The electrolyte after three months was almost colorless with a significant amount of violet precipitate mixed with reduced elemental gold.

Open circuit potential

Table 1 shows the measured values of the open circuit potential (monitored over 60 s) of the electrolyte with starting pH = 2 and pH values of the same electrolyte before and after electrochemical measurements after 1 h, 24 h, 1 month, and then every month until 12 months from the moment of synthesis.

Table 1. Open circuit potential and pH value of electrolyte before and after electrochemical measurements for different standing time from the moment of synthesis of the electrolyte with pH=2

Time	pH = 2		
	E *vs*. SCE (V)	pH (before)	pH (after)
1 h	+0.206	1.85	1.95
24 h	+0.163	1.90	1.96
7 days	+0.158	1.95	1.99
1 month	+0.160	2.03	2.06
2 months	+0.155	2.05	2.10
3 months	+0.166	2.09	2.11
4 months	+0.197	2.09	2.11
5 months	+0.201	2.10	2.12
6 months	+0.206	2.10	2.12
7 months	+0.173	2.12	2.14
8 months	+0.178	2.13	2.16
9 months	+0.169	2.14	2.17
10 months	+0.198	2.15	2.19
11 months	+0.197	2.18	2.20
12 months	+0.202	2.17	2.21

Table 2. Open circuit potential and pH value of electrolyte before and after electrochemical measurements for different standing times from the moment of synthesis of the electrolytes with pH = 4 and pH = 7

Time	pH = 4			pH = 7		
	E *vs*. SCE (V)	pH (before)	pH (after)	E *vs*. SCE (V)	pH (before)	pH (after)
1 h	-0.028	4.20	4.40	-0.029	7.10	7.05
24 h	-0.179	4.30	4.35	-0.030	7.08	7.06
7 days	-0.169	4.33	4.35	-0.029	7.07	1.10
1 month	-0.173	4.35	4.37	-0.022	7.14	7.12
2 months	-0.180	4.35	4.40	-0.023	7.20	7.15
3 months	-0.179	4.38	4.45	-0.026	7.25	7.18

Table 2 shows the measured values of the open circuit potential (monitored over 60 s) and pH values of electrolytes with pH value = 4 and 7 before and after electrochemical measurements after 1 h, 24 h, 1 month and then every month until three months or until first visible signs of decomposition of the complex.

Open circuit potential (OCP) of the electrolyte with pH = 2, measured in a period of 1 h to 12 months from the moment of synthesis was in the ranges from +0.206 V to +0.155 V. The most positive value of the OCP (+0.206 V) was measured after 1 h from the moment of electrolyte synthesis. The same value was measured after 6 months. The value of +0.202 V after 12 months may be considered as the same value as at the start of the experiment. Even the most negative value of +0.155 V (after two months) was not significantly lower than the former ones. The most positive value of the open circuit potential indicates the most unstable structure. However, the change of the open circuit potential value over a period of one year was not large, which indicates very high stability of the electrolyte with pH = 2.

The electrolyte with a pH value of four had the most positive value of the open circuit potential (-0.028 V) after 1 h from the moment of synthesis. After 24 h, a significantly more negative value of

the open circuit potential of -0.179 V was measured which indicated that in the first 24 h changes occurs and establish a stable structure within the complex. Further changes of OCP are insignificant (values after 24 h and after three months are nearly the same).

The electrolyte with pH = 7 had the most negative values of the open circuit potential: -0.029 V and -0.030 V after 1 h and 24 h from the moment of synthesis, respectively. A slightly more positive open circuit potential of -0.022 V was measured after 48 h from the moment of electrolyte synthesis. Changes in the values of OCP, in the period from 1 h to 3 months were very small. These values of OCP indicated that a stable structure is established within the first hour after synthesis.

The pH value of the electrolyte increases after each electrochemical measurement for electrolytes with pH values of 2 and 4, and decreased for the electrolyte with pH = 7, as shown in Table 2. These changes are small and the pH values may be considered as stable, especially for the unbuffered electrolytes in this research.

Cyclic voltammetry

The cathode parts of cyclic voltammograms are shown in Figure 1. They are recorded at pH value of 2 for different elapsed time after the electrolyte
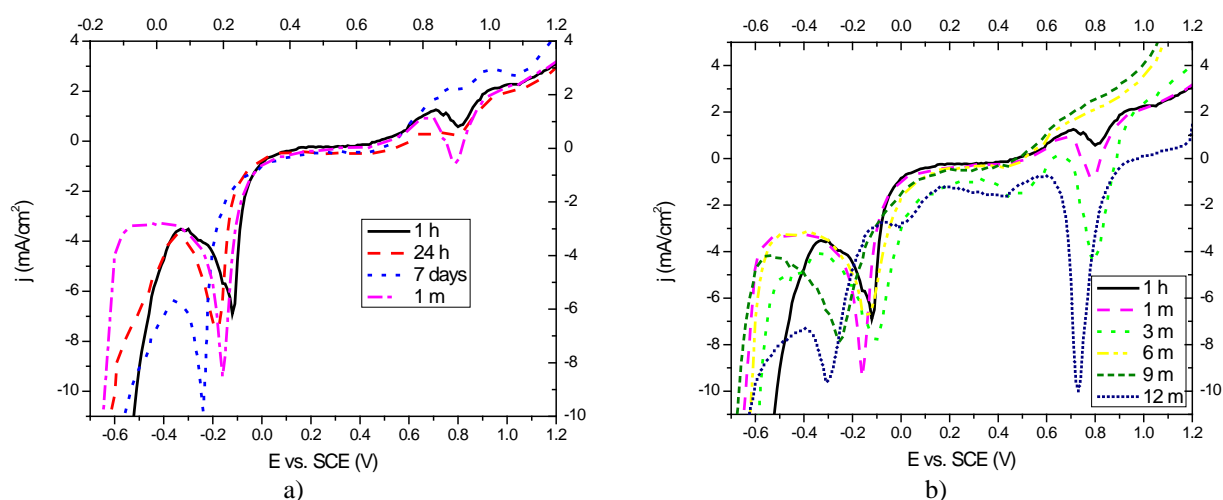
Fig. 1. Cyclic voltammograms (cathodic part) recorded for the gold complex based on mercaptotriazole at pH = 2 for different elapsed time after the electrolyte synthesis: a) 1 h, 24 h, 7 days and 1 month; b) 1 h, 1 month, 3 months, 6 months, 9 months and 12 months
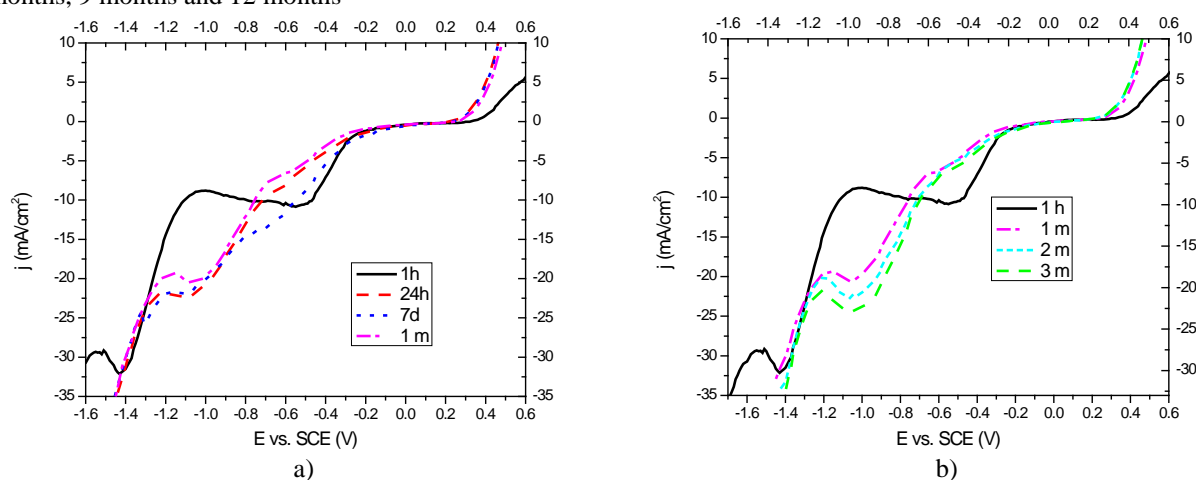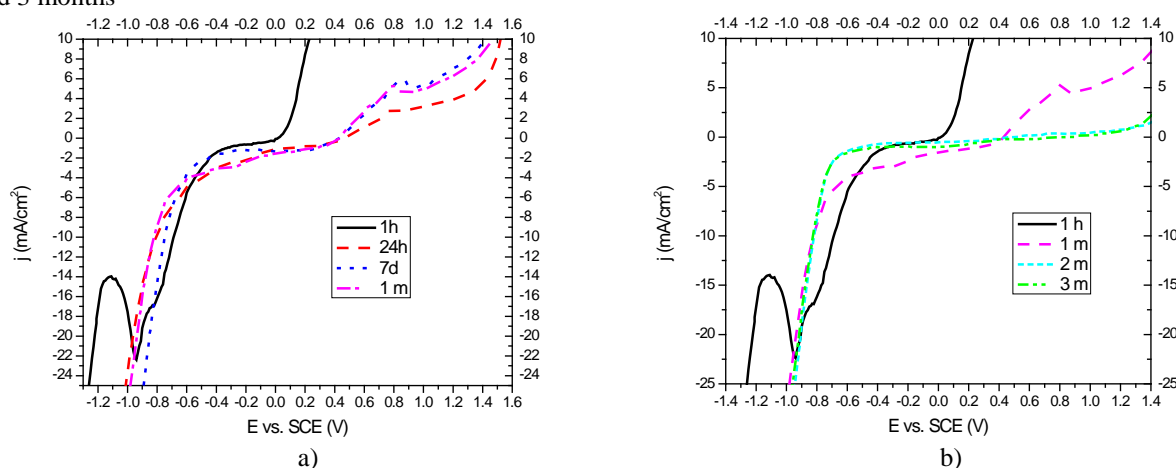

Fig. 2. Cyclic voltammograms (cathode part) recorded for the gold complex based on mercaptotriazole at pH = 4 for different elapsed time after the electrolyte synthesis: a) 1 h, 24 h, 7 days and 1 month; b) 1 h, 1 month, 2 months and 3 months

Fig.3. Cyclic voltammograms (cathode part) recorded for the gold complex based on mercaptotriazole at pH = 7 for different elapsed time after the electrolyte synthesis: a) 1 h, 24 h, 7 days and 1 month b) 1 h, 1 month, 2 months and 3 months

synthesis: 1 h, 24 h, 7 days, 1 month, 3 months, 6 months, 9 months and 12 months.

Cyclic voltammograms for different elapsed time after the electrolyte synthesis: 1 h, 24 h, 7 days, 1 month, 2 months and 3 months are presented in Figure 2 (pH = 4), and Figure 3 (pH = 7). From the cyclic voltammograms for the

electrolyte with pH = 2, (Fig. 1 a and b), it can be noted that the voltammograms recorded after 1 h and 24 h are similar in shape with two current peaks. At the potential of +0.80 V, a sharp current peak appears on the voltammogram recorded after 24 h from the synthesis as well as after one hour, but with less current intensity. On both

53

voltammograms, sharp current peaks were observed at the potential of -0.12 V on the voltammogram recorded after 1 h, and at the potential of -0.18 V for the voltammogram recorded after 24 h.

The voltammogram recorded after seven days, shown in Figure 1 a, is slightly different from the former two, because it has only one sharp current peak at the potential of -0.24 V. At the potential value of +0.80 V, at which the former two voltammograms have small peaks, on the cathodic part of the voltammograms recorded after seven days, no clear current peak appears, only a fold in the location corresponding to the reaction of gold reduction. Cathodic current density begins to rise sharply at the same potential value as the former two voltammograms (-0.35 V).

Voltammogram recorded after a month is similar to voltammograms recorded after 1 h and 24 h. On this voltammogram, in addition to two current peaks, the first at a value of potential of +0.78 V, and the other at -0.16 V, a fold can be observed at the potential value of +0.45. The sharp increase in the cathode current density starts from -0.50 V.

Two current peaks appear in the voltammogram recorded after three months. The first peak appears at nearly the same potential value (+0.79 V). The second peak occurs at the same potential value in relation to the voltammograms recorded after 1 h (-0.12 V). The sharp increase in the cathode current density starts from the same value of the potential as for voltammograms recorded after 1 h and 24 h, and the fold is at the same potential value. All these features indicate similar behavior in the first three months.

The voltammograms recorded after 6 and 9 months to the potential value of 0 V are similar in shape with folds at the same potential value (+0.43 V). Current peak on voltammogram recorded after 6 months appears at the potential value of -0.14 V and on the voltammogram recorded after 9 months at the more negative potential value of -0.25 V. On these two voltammograms, a sharp rise of cathode current density starts at nearly the same value potential (-0.50 V and -0.55 V respectively). On voltammograms recorded after 12 months, there are two current peaks. The first is at the potential value of +0.73 V, and the second at -0.31 V with the appearance of two folds at potential of +0.40 V and -0.02 V. The sharp increase in the cathode current density starts at the potential of -0.40 V. These two cyclic voltammograms are very similar and have the same basic features as the others, but with more prominent first cathode peak

at +0.8 and +0.7 V, respectively for the electrolytes after six and twelve months.

Voltammogram recorded after 1 h in the electrolyte with pH 4 is different from the others recorded at this pH value. Two peaks appear on this voltammogram, the first, wide, at a potential value of -0.50 V, and the other at -1.43 V. At -1.55 V cathode current density starts to rise rapidly, indicating the start of hydrogen evolution leading to the reduction of current efficiency. On all other voltammograms (Figure 2a), folds at the potential of -1.08 V can be observed, and the sharp increasing of the cathode current density starts at the potential of -1.25 V.

Voltammograms recorded after one, two and three months are very similar, the current peaks appear at the same value potential (-1.05 V), as well as a sharp increase in the cathode current density (-1.2 V). It can be concluded from the voltammograms recorded for the electrolyte with pH = 4 that the major changes in a structure of electrolyte occur in the first 24 hours. After that, all changes are almost negligible.

On the voltammogram recorded after 1 h for the electrolyte with pH = 7 (Figure 3) at the potential of -0.78 V, a fold appears and on the potential of -0.95 V – a sharp current peak. The sharp increase of the cathode current density starts at -1.15 V. On the voltammograms recorded after 24 h, 7 days and one month, the folds occur at the same potential value of +0.40 V, while a sharp increase of cathode current density starts from the potential of -0.60 V. On the voltammograms recorded after one, two and three months, the folds appear at the same potential value (+0.40 V) as the voltammograms recorded after seven days. The sharp increase in the cathode current starts from a less negative value of potential (-0.68 V). As for the electrolyte with pH = 4, the major changes in the structure of electrolyte occur in the first 24 hours, and the electrolyte is stable during a three-month interval.

Polarization curves

Polarization curves for the electrolyte with gold concentration of 2.5 g/dm³, recorded at different pH values with a potential scan rate of 5 mV/s, are presented in Figure 4 for the electrolyte with pH = 2, in Figure 5 for the electrolyte with pH = 4, and in Figure 6 for the electrolyte with pH = 7 for different elapsed time after electrolyte synthesis.

On the polarization curves, recorded for the electrolyte with pH = 2 (Figure 4) after 1 h and 24 h, two wide plateaus appear and the current peaks are at the same current density, and have the same
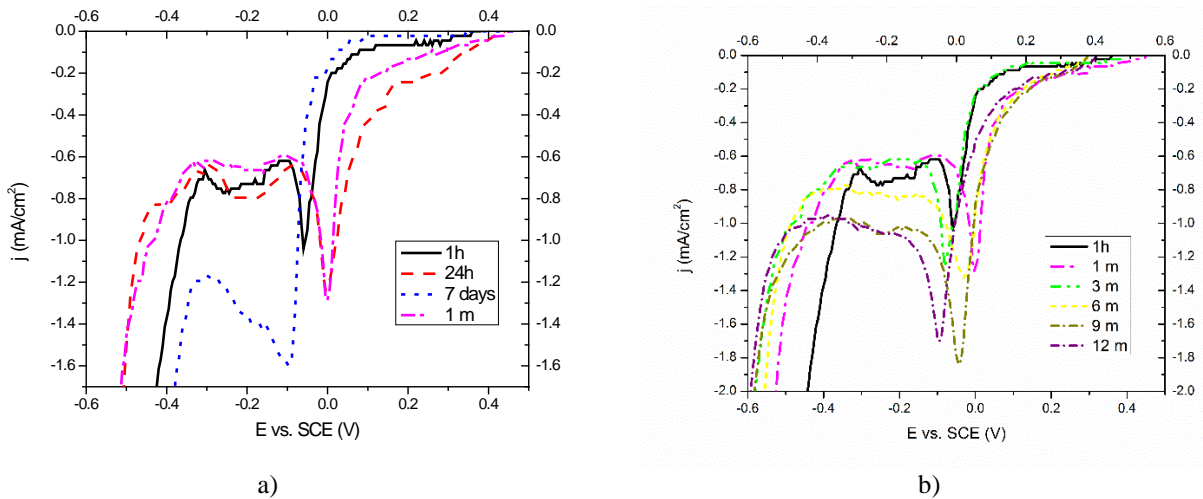
a)   b)

Fig. 4. Polarization curves recorded for the gold complex based on mercaptotriazole at pH = 2 for different elapsed time after electrolyte synthesis: a) 1 h, 24 h, 7 days and 1 month; b) 1 h, 1 month, 3 months, 6 months, 9 months and 12 months
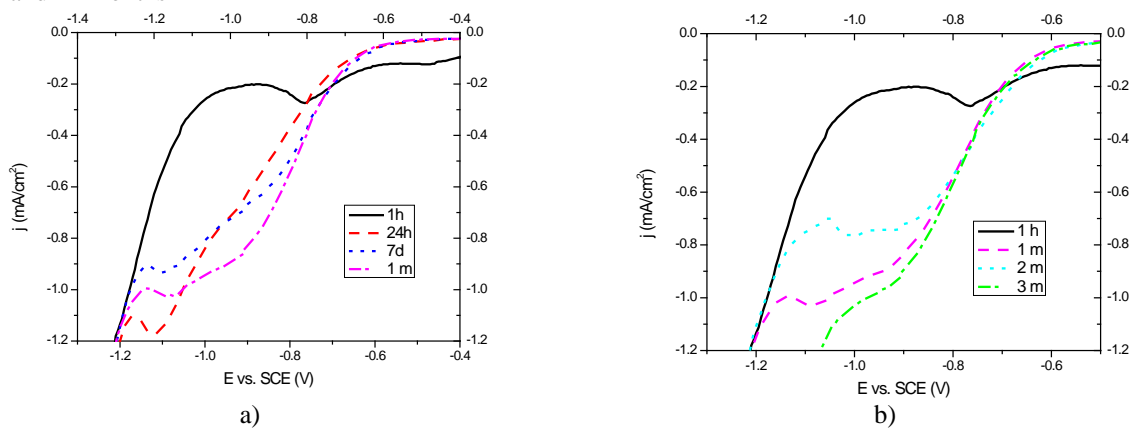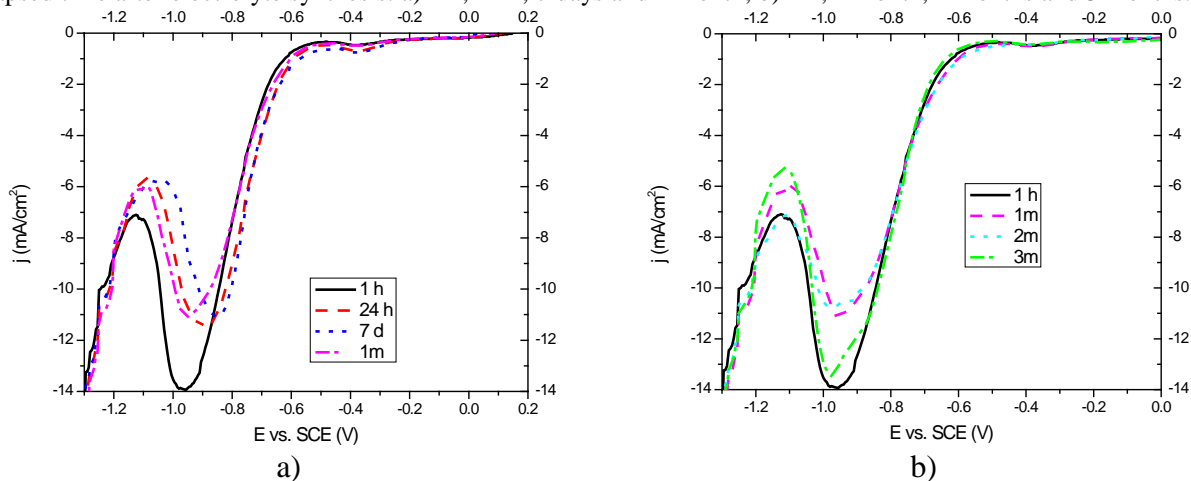

a)   b)

Fig. 5. Polarization curves recorded for the gold complex based on mercaptotriazole at pH = 4 for different elapsed time after electrolyte synthesis: a) 1 h, 24 h, 7 days and 1 month; b) 1 h, 1 month, 2 months and 3 months.

a)   b)

Fig. 6. Polarization curves recorded for the gold complex based on mercaptotriazole at pH = 7 for different elapsed time after electrolyte synthesis: a) 1 h, 24 h, 7 days and 1 month; b) 1 h, 1 month, 2 months and 3 months

potential value. The first plateau occurs at a current density of 0.02 mA/cm^2, and the other at 0.80 mA/cm^2.

On the polarization curve recorded after seven days, one wide and one short plateau appear at the same current density, and at the same potential value as on the former two curves. On the polarization curves recorded after one month and three months, two plateaus appear with the same

current densities, the first with a current density of 0.04 mA/cm^2, and the other with 0.64 mA/cm^2. On the polarization curves recorded after 6, 9 and 12 months, the first plateau appears with the same current density of 0.08 mA/cm^2, while the second plateau of the recorded polarization curve after 6 months occurs with a current density of 0.82 mA/cm^2. The second plateau on the polarization

55

curves recorded after 9 and 12 months appears with a current density of 1.06 mA/cm^2.

Similarity between all voltammograms, except that after one hour is obvious and indicates high stability of the complex within the full period of 12 months. It confirms the results for the other two methods.

For the electrolyte at pH = 4 presented in Figure 5 it can be seen that on the polarization curve recorded after 1 h the first plateau occurs at a current density of 0.12 mA/cm^2 while no plateaus for polarization curves, recorded after 24 h and 7 days, can be identified. The first plateaus for polarization curve, recorded after 1 month, 2 months and 3 months, appear with the same current densities, while the other plateaus on these curves have got different current densities (after 1 month 1.03 mA/cm^2, after 2 months 0.75 mA/cm^2 and after 3 months 1.27 mA/cm^2). Similarity between the polarization curves from 24 h to 3 months was higher than for the electrolyte with pH = 2.

The polarization curves, recorded for the electrolyte of pH = 7 (Fig. 6) after 1 h, 24 h and 7 days, are of similar shape. Wide plateaus appear on all curves at potential values close to the open circuit potential values until the potential value of -0.6 V. The sharp power peaks appear on all polarization curves at similar values of the potential. On the polarization curve recorded after 1 h, the current peak occurs at -0.97 V. After 24 h from moment of synthesis, a current peak occurs at a more positive potential (-0.95 V). Current peak at polarization curve recorded after 7 days appears at the potential of -0.85 V. On the polarization curves recorded after one month, two months and three months, a wide plateau appears with the current density of 0.33 mA/cm^2 and in the potential region from the open circuit potential until -0.5 V. All polarization curves have sharp current peaks at the potential of about -0.95 V.

The similarity of the polarization curves including the one after one hour after synthesis was the highest of all investigated electrolytes.

CONCLUSION

Investigation of the influence of pH value on the stability of electrolytes with the optimal concentration of gold of 2.5 g/dm^3 in acidic and neutral media over a period of one year, or until the first visible signs of the complex decomposition, showed that in the electrolytes with pH = 4 and 7, the first visible signs of the complex decomposition appeared after three months.

No visual changes were noticed for the electrolyte with pH = 2 for a period of one year with a slight change of electrochemical properties after six months. For this electrolyte, the OCPs and polarization curves were similar in the full period of one year, and cyclic voltammograms for six and twelve months have shown slightly different characteristics.

The open circuit potential for the electrolyte with pH = 4 had a little bit larger changes than for the other two electrolytes. However, all other electrochemical measurements have shown similar results for the three-month period. Electrolyte with pH = 7 had the most similar results for all measurements, which indicates a high stability within three months.

The results of all methods in all investigated electrolytes differ significantly only for the periods of time shorter than 24 hours. This indicates that the major changes in the structure of the complex occur during this period of time.

REFERENCES

1. S. Roy, *ECS Trans.*, **16**, 667 (2009).
2. M.J. Liew, S. Roy and K. Scott, *Green Chem.*, **5,** 376 (2003).
3. S. Đorđević, Metalne prevlake, Tehnička knjiga, Beograd 1990.
4. S. Đorđević, M. Maksimović, M. Pavlović, K. Popov, Galvanotehnika, Tehnička knjiga, Beograd, 1998.
5. S. Dimitrijević, Z. Stević, M. Vujasinović, V. Grekulović, S. Dimitrijević, B. Trumić, S. Alagić, *Metall. Mater. Engin.*, **2**, 269 (2015).
6. P.A. Kohl, Electrodeposition of gold, Modern Electroplating, Fifth Edition, Wiley & Sons, Inc., 2010.
7. A.R. Halpern, R.M. Corn, *ACS Nano*, **7,** 1755 (2013).
8. S. Dimitrijević, M. Rajčić-Vujasinović, S. Alagić, V. Grekulović, V. Trujić, *Electrochim. Acta*, **104**, 330 (2013).
9. S.B. Dimitrijević, M.M. Rajčić-Vujasinović, R.M. Jančić-Hajneman, J.B. Bajat, V.K. Trujić, D. D. Trifunović, *Int. J. Mater. Res.*, **105**, 271 (2014).
10. S.B. Dimitrijević, M.M. Rajčić-Vujasinović, D.D. Trifunović, B.T. Trumić, Z.M. Stević, S.P. Dimitrijević, *Int. J. Mater. Res.*, **107,** 624 (2016).
11. S. Dimitrijević, M. Rajčić-Vujasinović, R. Jancic-Hajneman, D. Trifunović, J. Bajat, V. Trujić, S. Alagić, Proceedings, International Scientific and Professional Meeting Eco-Ist'12, 194, (2012).

12. S.B. Dimitrijevic, M.M. Rajcic-Vujasinovic, R.M. Jancic-Hajneman, J.B. Bajat, V.K. Trujic, D.D. Trifunovic, Proceedings ,44th International October Conference on Mining and Metallurgy, Bor, Serbia, 321, 2012.

13. Y. Okinaka, M. Hoshino, *Gold Bull.*, **31**, 3 (1998).

14. Y. Okinaka, *Gold Bull.*, **33**, 117 (2000).

15. T. Osaka, A. Kodera, T. Misato, T. Homma, Y. Okinaka, *J. Electrochem. Soc.,* **144**, 3462 (1997).

16. H. Honma, K. Hagiwara, *J. Electrochem. Soc.*, **142**, 81 (1995).

17. H. Honma, Y. Kagaya, *J. Electrochem. Soc.*, **140**, L135 (1993).

18. M. Kato, Y. Okinaka, *Gold Bull.,* **37,** 37 (2004).

19. M. Kato, J. Sato, H. Otani, T. Homma, Y. Okinaka, T. Osaka, O. Yoshioka, *J. Electrochem. Soc.*, **149**, C164 (2002).

20. M. Kato, Y. Yazawa, Y. Okinaka, Proceedings of the AESF, Annual Technical Conference, Baltimor MD, 'SUR/FIN'95', 805, 1995.

21. D.R. Gabe, *Trans. Inst. Met. Finish.,* **75**, B131 (1997).

22. T.A. Green, *Gold Bull.,* **40**, 105 (2007).

23. Z. Stević, M. Rajčić-Vujasinović, *Hem. Indus.*, **61**, 1 (2007).

СТАБИЛНОСТ НА ЗЛАТЕН КОМПЛЕКС С МЕРКАПТОТРИАЗОЛ В КИСЕЛА И НЕУТРАЛНА СРЕДА

С. Димитриевич*[1], М. Райчич Вуясинович[2], Ст. Димитриевич[3], Б. Трумич[1], А. Иванович[1]

[1]*Институт по минно дело и металургия в Бор, Зелени бул. 35, 19210 Бор, Сърбия*

[2] *Технически факултет в Бор, Белградски университет VJ 12, 19210 Бор, Сърбия*

[3] *Иновационен център, Факултет по технология и металургия, Белградски университет, Белград, Сърбия*

(Резюме)

В настоящата статия е изследвана стабилността на златен комплекс с меркаптотриазол в два кисели електролита с различно pH и в неутрална среда. Изследването е проведено чрез визуално проследяване и електрохимично охарактеризиране на електролитите за период от една година или докато се забележат първи видими белези за разлагане на комплекса. Електрохимичното охарактеризиране на комплекса е извършено чрез измерване на потенциала в отворена верига, циклична волтамметрия и регистриране на поляризационни криви. pH стойностите на електролитите са измервани преди и след всеки електрохимичен експеримент. Тестовете са проведени при различни изходни pH стойности: 2, 4 и 7 при оптимална концентрация на злато в електролит с обем от 2.5 g/dm^3. За електролитите с pH 4 и 7, първите видими белези на разлагане на комплекса се появяват три месеца след синтеза. Електролитът с pH 2 е видимо стабилен в продължение на една година.

Nanosized Zn₂SnO₄ powders synthesized by coprecipitation and consecutive hydrothermal treatment in two different alkaline media

V. Blaskov[1]*, I Stambolova[1], L. Dimitrov[2], M. Shipochka[1], D. Stoyanova[1], A. Eliyas[3]

[1] *Institute of General and Inorganic Chemistry, Bulgarian Academy of Sciences, Acad. G. Bonchev, bl. 11, Sofia 1113, Bulgaria*
[2] *Institute of Mineralogy and Crystallography "Acad. Ivan Kostov", Bulgarian Academy of Sciences, Acad. G. Bonchev, bl. 107, Sofia 1113, Bulgaria*
3- *Institute of Catalysis, Bulgarian Academy of Sciences, Acad. G. Bonchev, bl. 11, Sofia 1113, Bulgaria*

A two-step method has been applied to the synthesis of zinc orthostannate, Zn₂SnO₄. As a first step X-ray amorphous hydroxide precursor had been obtained by coprecipitation of Zn(NO₃)₂ and SnCl₂ solutions using Na₂CO₃. In the second step the precursor was subjected to hydrothermal treatment (HT) in the presence of sodium hydroxide or ammonium hydroxide. The samples have been characterized by X-ray diffraction (XRD), X-ray photoelectron spectroscopy (XPS), scanning electron microscopy (SEM) and UV-Vis spectroscopy. The precursor powder showed absorption edge at about 423 nm, while the absorption band of the HT samples, obtained in NH₄OH and NaOH, is shifted to 441 nm and 471 nm, respectively. The treatment of the amorphous precipitate in the presence of sodium hydroxide leads to a higher degree of crystallization, smaller sizes of the crystallites and higher photocatalytic activity for discoloration of the textile dye Methylene Blue (MB).

Keywords: zinc stannate, nanometer size, hydrothermal, photocatalyst, visible absorption

INTRODUCTION

The zinc orthostannate Zn_2SnO_4, is a stable phase in the system ZnO-SnO_2 having inverse spinel structure. Recently, Zn_2SnO_4 has been intensively investigated with the view to its thermodynamic stability, high electrical conductivity, high electron mobility and low visible light absorption [1]. These properties of zinc ortho-stannate make it a suitable material with potential applications as anode in Li ion batteries [2], gas sensors [3, 4], in photoluminescence [5] and as photocatalysts [6].

However it is difficult to obtain Zn_2SnO_4 by conventional solid state reaction. Hashemi et al. [7] have revealed that a single phase of zinc stannate is being formed during calcination at 1280°C for 12 h. Zinc ortho-stannate have been obtained by mechanical activation of the starting ZnO and SnO_2 powders, followed by sintering at 1300°C, by Nikolic et al. [8]. The high temperature sintering at 1300 °C is undesirable and it be avoided by calcination of the co-precipated with NaOH amorphous precursor of mixed zinc and tin hydroxides [9]. Another way to prepare zinc stannate at low temperature is the hydrothermal method. This method allows the obtaining of a homogeneous and well crystallized compound at much lower temperatures than the classical treatment. Therefore the deterioration of the properties as a result of undesirable sintering and agglomeration processes is avoidable. Fang and et al. [10] have synthesized spinel Zn_2SnO_4 via hydrothermal method at 220°C using aqueous solutions of $Zn(CH_3COO)_2 \cdot 2H_2O$ and $SnCl_4 \cdot 5H_2O$ and NaOH solution serving as mineralizer. Also, nanosized Zn_2SnO_4 has been synthesized by the hydrothermal process in water/ethylene glycol mixed solutions [11].

Recently we have carried out coprecipitation of Zn and Sn hydroxides with Na_2CO_3 from an aqueous solution mixture of $Zn(NO_3)_2$ and $SnCl_2$ and subsequent mechanical activation in order to prepare nanosized zinc stannate [12]. The advantage of natrium carbonate as precipitating agent is that the decomposition of the precursor is complete at lower temperatures (about 350°C).

Recently it has been demonstrated that Zn_2SnO_4 exhibits high activities and durabilities for photodegradation of water soluble textile dyes [11, 13]. The methylene blue (MB), a typical textile dye, has been used as the model water pollutant to evaluate the photocatalytic activity of the hydrothermally prepared zinc stannate spinel powders.

To our best knowledge there are no available data on the preparation of Zn_2SnO_4 powders by hydrothermal treatment of co-precipitate in basic media.

In this paper we are prepared crystalline Zn_2SnO_4 powders by a two - step procedure: co-precipitation with Na_2CO_3 of hydroxide precursor and consecutive hydrothermal treatment of the

---

* To whom all correspondence should be sent.
E-mail: vblaskov@abv.bg

precipitate in different basic media (NaOH and NH₄OH). Also the effect of the nature of basic media on the particles structure, morphology and activity in discoloration of textile dye as model waste water contaminant over the zinc stannate samples.

EXPERIMENTAL

Aqueous solutions of 0.5 mol/l $Zn(NO_3)_2.6H_2O$ and 0.3 mol/l $SnCl_2.2H_2O$ (acidified to avoid hydrolysis) were prepared. The two solutions were mixed at component ratio corresponding to the stoichiometric molar ratio between the oxides participating in the Zn_2SnO_4 (ZnO : SnO$_2$ = 2:1). Sodium carbonate solution was used as a precipitating agent. In order to obtain a homogeneous precipitate, the sodium carbonate solution (0.5 mol/l) was added drop-wise, under intensive stirring. The final pH of the solution was 7.5. The obtained precipitate was being aged for 4 h, and then it was washed several times to until negative reaction for chloride (Cl⁻) anions was achieved. After that the precipitate was dried 12 h at 60°C. Two samples of precursor material, prepared by co-precipitation, were treated hydrothermally (HT) in basic media. Two samples of 1.5 g from the precursor material were treated hydrothermally 24 h at 200 ^{0}C in 15 mL of 0.4 mol/l solution of NaOH or in 25 % wt. NH₄OH. The samples were filtered, then washed with distilled water and dried at 100 ^{0}C.

The phase composition of the samples obtained was studied by X-ray diffraction (XRD) on Dron 3M diffractometer with CoK$_\alpha$ radiation, applying accelerating voltage and current intensity of 40 kV and 40 mA respectively. The scan step was 0.02 degrees and acquisition time on each step was 1 second. The crystalline sizes of the samples were calculated based on X-ray peak profile broadening by using analysis program that applies Debye-Scherrer's equation. The particle morphology of the samples was observed by scanning electron microscope (SEM) JEOL-5510 at 10 kV accelerating voltage. The DR UV-Vis spectra were recorded on a Thermo Evolution 300 UV-Vis, equipped with a Praying Mantis device. BaSO₄ is applied as a reference sample. The X-ray photoelectron spectroscopy (XPS) studies were performed in a VG Escalab II electron spectrometer using AlK$_\alpha$ radiation with energy of 1486.6 eV under base pressure 10^{-7} Pa and a total instrumental resolution 1eV. The binding energies (BE) were determined utilizing the C1s line (from an adventitious carbon) as a reference with energy of 285.0 eV. The accuracy of measuring the BE values was 0.2 eV.

The photocatalytic activities of the samples were measured using an UV lamp with light intensity of 5.10^{-5} W/cm², located in the centre of the reactor. The latter contained aqueous solution (5 ppm) of Methylene Blue (MB) dye. This solution was homogenized with a magnetic stirrer at 400 rpm. The photocatalytic activity was evaluated by measuring the residual dye concentration at regular time intervals using Jenway 6400 spectrophotometer. The actual dye concentration was calculated by comparing the absorbance of the collected sample, measured at the wavelength of spectral maximum of the MB, based on calibration curve.

RESULTS AND DISCUSSION

The X-ray diffraction patterns revealed that the starting precursor material, having Zn_2SnO_4 composition, is X-ray amorphous, while both hydrothermally treated (HT) samples are crystalline (Fig.1). The crystalline sizes of the samples are calculated by the Debye-Scherrer's equation. The HT sample, prepared in the presence of NaOH, showed higher degree of crystallization and smaller crystallites size (25 nm) than that of the sample, prepared in the presence of NH₄OH (39 nm). The advantage of the two-step synthesis procedure (consisting of precipitation with Na₂CO₃ and consecutive hydrothermal treatment) is the formation of nano-sized crystallites (24-70 nm) of zinc stannate. The conventional sintering process leads to bigger size of the crystallites of zinc stannate with dimensions higher than 100 nm [8].

Figure 2 represents the UV–Vis spectra of Zn_2SnO_4 precursor powder and HT prepared samples.

The UV-Vis spectra show red-shifting of the absorption band edge for the samples prepared in the presence of NH₄OH and NaOH respectively (Fig. 2), comparing with the precursor material. The vertical line at about 450 nm in Fig. 2 schematically represents the value of the end of ultraviolet part and the beginning of the blue part of the visible spectra. The precursor powder showed absorption band edge at about 423 nm, which is shifted to 441 nm and 471 nm for the hydrothermally prepared zinc stannate in the presence of NH₄OH and NaOH, respectively. The shift in the absorption band edge to the visible part of spectra proved that the hydrothermal treatment in basic media of precipitated amorphous Zn_2SnO_4 is a promising method for the preparation of photocatalysts, potentially active under solar light irradiation.
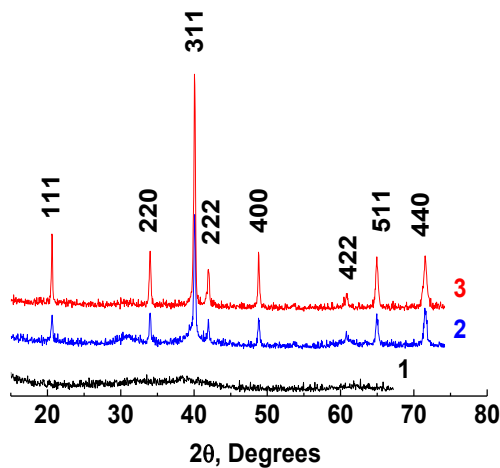
Fig.1. XRD patterns of the samples. 1-precursor material, 2 - HT prepared in the presence of NH4OH, 3 – HT prepared in the presence of NaOH. For a better observation, the X-ray patterns are shifted upwards.
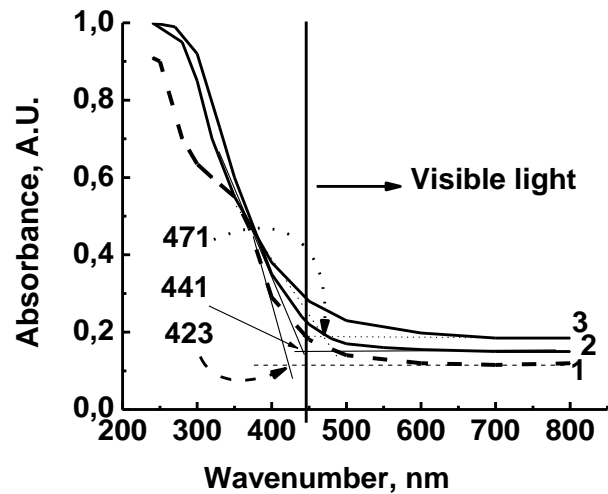
Fig.2. UV-Vis spectra of starting precursor - 1, and HT prepared samples in the presence of NH4OH - 2 and in the presence of NaOH - 3. The values of absorption band edges are indicated.
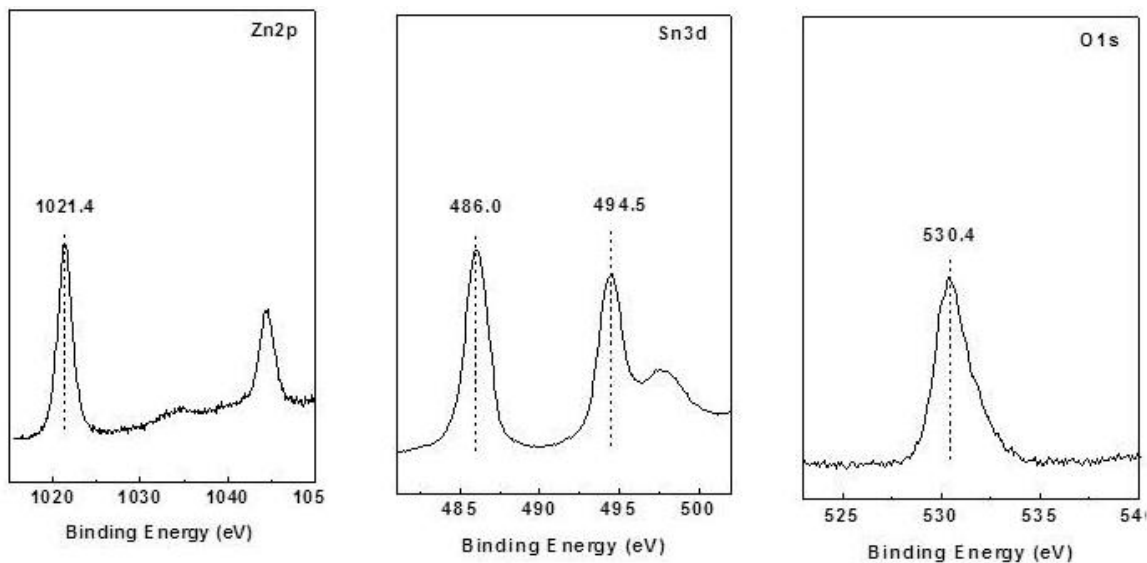

Fig.3. Zn2p (a), Sn3d (b) and O1s (c) core level XPS spectra of HT- Zn_2SnO_4 in NH_4OH.

The XPS spectra of the samples are shown in Fig. 3. The characteristic peak of $Zn2p_{3/2}$ is located at 1021.4 eV, which is typical of ZnO (Fg 3). The binding energies of Sn $3d_{5/2}$ and Sn $3d_{3/2}$ core electrons are located at 486.0 and 494.5 eV, respectively. The position of the O1s peak at 530.4 eV corresponds to the state of the oxygen atom O^{2-} in the zinc stannate. The XPS spectra of the sample, prepared in the presence of NH_4OH, did not display N1s peak at binding energy of about 399.8 eV, showing that nitrogen is not incorporated in the sample during the hydrothermal treatment.

The SEM micrographs of the hydrothermally treated powders are shown in Fig. 4. The general morphology of HT synthesized products consists of aggregates, which are not distinguishable from one another. The size of the particles depends on the type of the basic media. It has to be noted that the samples treated in NH_4OH possess large aggregates with non-uniform sub-micron and micron-sized particles (Fig. 4a), while in NaOH the aggregates are smaller. Thus the treatment in NaOH leads to the formation of smaller particles with size within the range 100 - 300 nm (Fig. 4b).

60

a   b
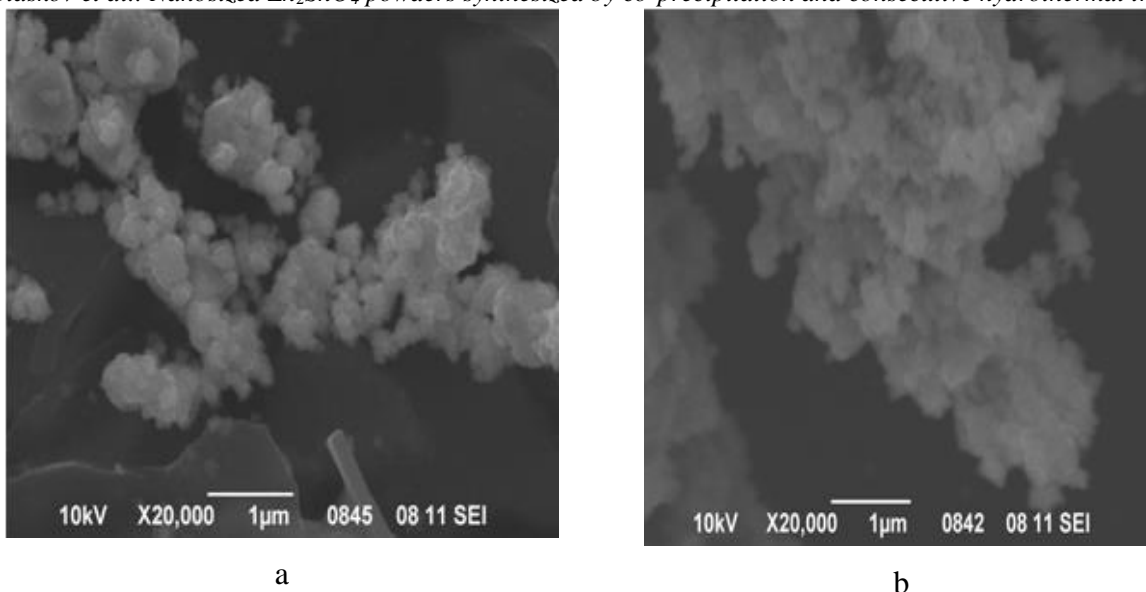
Fig.4. SEM micrographs of Zn₂SnO₄ powders HT treated in NH₄OH (a) and NaOH (b)
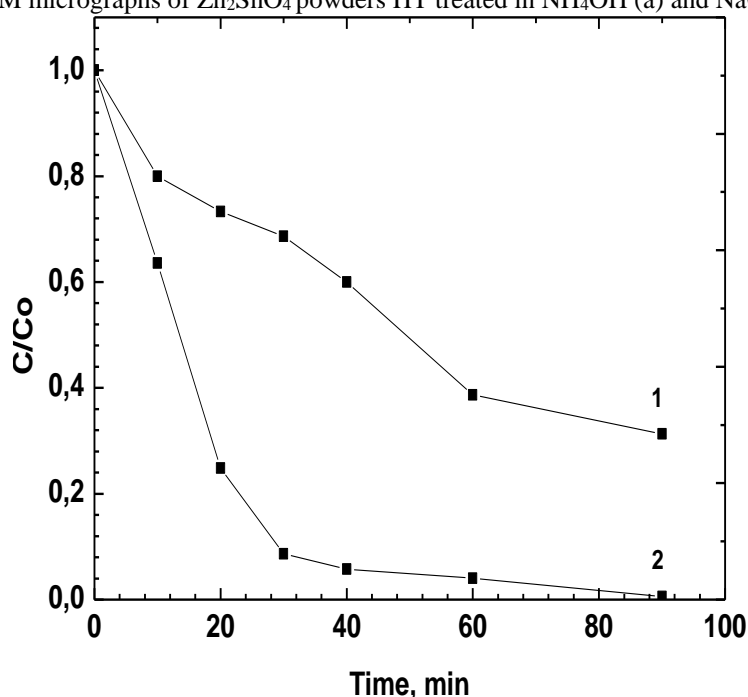
Fig.5. Photocatalytic discoloration of MB by Zn₂SnO₄-HT prepared in the presence of NH₄OH (1) and NaOH (2).

The photocatalytic activity of Zn₂SnO₄ powder was followed based on the change in the relative concentration C/C_0 (where C_0 is initial concentration of MB dye) with the time under UV illumination (Fig. 5). When the Zn₂SnO₄ is being irradiated, electrons in the valence band (VB) are being excited to the conduction band (CB). Simultaneously holes are being generated in the VB, which are reacting immediately with the dye or interacting with the surface-bound H_2O or OH to produce the OH^- radical species – a strong oxidant for the mineralization of MB. Generally, the overall photocatalytic activity of semiconductors is primarily depending on its adsorption capacity, on the specific surface area, the structure and morphology. Therefore the high photocatalytic activity of the nanocrystalline Zn₂SnO₄ could be attributed to the smaller crystallites size and respectively to the higher specific surface area, which is more favorable for the mass transfer reactions in the liquid phase. Another factor influencing the activity is the particles aggregates [14]. The size and distribution of particle aggregates in the samples obviously influence the light absorption and light scattering, which are determining the degree of photon interaction with the catalyst surface. The intensity of the light scattered from the surface of ammonia treated

powders is probably stronger due to the presence of larger aggregates. Another reason for the lower photocatalytic activity of ammonia treated samples is the larger crystallite sizes, resp. lower specific surface area. The HT samples, prepared in the presence of NaOH, showed very fast discoloration of MB dye- about 90% conversion for a period of half an hour.

CONCLUSIONS

Nano-sized Zn_2SnO_4 powders have been obtained by two-step synthesis procedure, consisting of co-precipitation of mixed zinc stannate - amorphous hydroxi-carbonates and their consecutive hydrothermal treatment in basic media (NaOH or NH_4OH). The samples, prepared in NaOH, showed higher degree of crystallinity and smaller size crystallites, than those of the powders, prepared in the presence of NH_4OH. The photocatalytic activity in methylene blue discoloration of Zn_2SnO_4, hydrothermally prepared in the presence of NaOH, reaches almost 90% degradation degree of the dye within 30 min under UV irradiation. Both HT samples showed red shift in the UV-Vis spectra. The samples prepared by this two-step synthesis method showed absorption at visible wavelengths, which proves that they are promising materials for the preparation of photocatalysts active under visible light.

REFERENCES

1. W.W. Coffen, *J. Amer. Ceram. Soc*., **36**, 207 (1953).
2. F. Belliard, P. A. Connor, J. T. S. Irvine, *Solid State Ionics*, **135**, 163 (2000).
3. I. Stambolova, K. Konstantinov, M. Khristova, P. Peshe , *Phys. Stat. Solidi (a),* **167**, R11 (1998).
4. I. Stambolova, K. Konstantinov, D. Kovacheva, P. Peshev, T. Donchev, *J. Solid State Chem*., **128**, 305 (1997).
5. Q.R. Hu, P. Jiang, H. Xu, Y. Zhang, S.L. Wang, X. Jia, *J. Alloys Comp.,* **484**, 25 (2009).
6. Y. Lin, S. Lin, M. Luo, J. Liu, *Mater. Lett*., **63**, 1169 (2009).
7. T. Hashemi, H.M. Al-Allak, J. Illingsworth, A.W. Brinkman, J. Woods, *J. Mater. Sci. Lett*., **9**, 7765 (1990).
8. M.V. Nikolic, T. Ivetic, D.L. Young , K.M. Paraskevopoulos, T.T. Zorba, V. Blagojevic, P.M. Nikolic, D. Vasiljevic-Radovic, M.M. Ristic, *Mater. Sci. Eng*., **138**, 7 (2007).
9. W. Cun, W. Xinming, Z. Jincai, M. Bixian, S. Guoying, P. Ping'an, F. Jiamo, *J. Mater. Sci*., **37**, 2989 (2002).
10. J. Fang, A. Huang, P. Zhu, N. Xu, J. Xie, J. Chi, S. Feng, R. Xu, M. Wu, *Mater. Res. Bull*., **36**, 1391 (2001).
11. X. Fu, X Wang, J. Long, Z Ding, T Yan, G. Zhang, Z. Zhang, H. Lin, X Fu, *J. Solid State Chem*., **182**, 517 (2009).
12. I. Stambolova, V. Blaskov, D. Radev, Ya.Tsvetanova, S.Vassilev, P.Peshev, *J.Alloys Comp*., **391**, L1 (2005).
13. X. Lou, X. Jia, J. Xu, Sh. Liu, Q. Gao, *Mater. Sci. Eng. A,* **432**, 221 (2006).
14. A. C. Dodd, A.J. McKinley, M. Sanders, T. Tsuzuki, *J. Nanopart. Res*, **8**, 43 (2006).

НАНО-РАЗМЕРНИ ПРАХОВЕ ОТ Zn₂SnO₄, СИНТЕЗИРАНИ ЧРЕЗ СЪ-УТАЯВАНЕ И ПОСЛЕДОВАТЕЛНО ХИДРОТЕРМИЧНО ТРЕТИРАНЕ В ДВЕ РАЗЛИЧНИ АЛКАЛНИ СРЕДИ

В. Блъсков[1]*, И. Стамболова[1], Л. Димитров[2], М. Шипочка[1], Д. Стоянова[1], Ал. Елияс[3]

[1] Институт по обща и неорганична химия, Българска академия на науките, 1113 София, България

[2] Институт по минералогия и кристалография, Българска академия на науките, 1113 София, България

[3] Институт по катализ, Българска академия на науките, 1113 София, България

(Резюме)

Цинковият ортостанат Zn₂SnO₄ беше получен посредством двустадиен метод. Първоначално беше синтезиран рентгеноаморфен хидроксид чрез съутаяване от разтвори на Zn(NO₃)₂ и SnCl₂ и утаител Na₂CO₃. На втория стадий полученият прекурсор беше обработен хидротермално (XT) в среда на натриев хидроксид или амониев хидроксид. Така получените образци бяха охарактеризирани чрез ренгенофазов анализ (РФА), ренгенова фотоелектронна спектроскопия (РФС), сканираща електронна микроскопия (СЕМ) и UV-Vis спектроскопия. За прахообразния изходен образец беше регистриран абсорбционен ръб при 423 nm, докато при образците, получени хидротермално XT в среда от NH₄OH и NaOH той се измества съответно към 441 nm и 471 nm. Обработката на аморфната утайка в среда на натриев хидроксид води до по-добра кристализация, по-малки размери на кристалитите и по-висока фотокаталитична активност при окислително обезцветявяането на текстилното багрило метиленово синьо (MB).

Effect of controlled volume variation on the osmotic rate in aqueous solutions

I. L. Minkov[1, 2,*], E. D. Manev[2], S. V. Sazdanova[2], K. H. Kolikov[3]

[1]*Sofia University "St. Kliment Ohridski" , Faculty of Medicine, Department of Chemistry and Biochemistry, Physiology and Pathophysiology, 1 Kozyak Str., 1407 Sofia, Bulgaria*
[2]*Sofia University "St. Kliment Ohridski", Faculty of Chemistry and Pharmacy, Department of Physical Chemistry, 1 James Bourchier Blvd., 1164 Sofia, Bulgaria*
[3]*Plovdiv University "Paisii Hilendarski", Faculty of Mathematics and Informatics, 24 Tzar Assen Str., 4000 Plovdiv, Bulgaria*

The evolution of the osmotic pressure in aqueous solutions was studied experimentally as a function of time in two different regimes: of constant and variable solution volume. Quantitative dependence of the solvent osmotic rate on the relative solution volume variation was established as well. Glucose, a biologically active substance, was chosen as a reference solute for the complex tests. A custom made osmotic cell was used. A novel operative experimental approach, employing controlled limited variation of the solution volume was developed and applied for the purpose. First of all, the obtained kinetic dependencies reveal strong divergence in the rates of the process at the two experimental regimes. The rise of pressure is much faster at constant solution volume, while the solvent influx is many times greater in the regime of variable volume. Moreover, the rate of the osmotic process is being modified by varying the solution volume. We consider the effects established here by means of an artificial semipermeable membrane to be of relevance for the processes taking place in the real living cells and tissues.

Keywords: membrane permeability, semipermeable membrane, osmotic kinetics

INTRODUCTION

Osmosis, i.e. the passage of fluid (usually water) through a semipermeable membrane, has been known for almost two centuries. Although always being on the agenda, for rather long time it seems not to have drawn largely the attention of the researchers. Yet, it needs not be surprising that in the latest years, with the discovery of the role of aquaporins as selective pores in water transport, the interest to this phenomenon has undergone genuine revival. As K. Alleva *et al.* have formulated the issue in their excellent review paper (Aquaporins: Another piece in the osmotic puzzle) [1]: "The elucidation of osmotic phenomena will help to understand central issues such as the identification of the causes of previously identified syndromes ….. and could also aid in finding adequate therapies for various pathologies, the comprehension of water management by plants, and the development of efficient methods for water purification. Therefore, unveiling the osmotic process is important both at the biological and technological level".

The driving force of the osmotic process is the concentration difference between two solutions separated by a semipermeable membrane. It creates pressure difference across the membrane (*osmotic pressure*). Solvent transport takes place from the more diluted solution to that of higher concentration, until equilibrium is reached. J. H.

van't Hoff was the first [2] to propose a theory and a formula, named the *van't Hoff law*, for the (equilibrium) osmotic pressure, Π, resulting from the transfer of solvent through the membrane:

$$\Pi = cRT , \qquad (1)$$

where c (mol/m^3) is the molar concentration of the dissolved substance, R (8.314 J/mol K) is the universal gas constant, T (K) is the absolute temperature. This equation is still in use, along with a number of more complex formulae for Π that have been produced since as well [3-8]. Although we are aware of the supposedly more precise formulae, we have found the original van't Hoff law to be entirely sufficient for the tasks considered here, as discussed further.

Equilibrium studies of osmosis, whether theoretical or experimental, predominate in the literature, but the interest to the kinetic aspects of the process has persisted through the years [9-12]. Osmotic equilibrium is considered to be well understood from thermodynamic viewpoint and does not pose serious ambiguities. In contrast, the dynamic aspects of the process frequently exhibit new and even surprising effects, which are difficult to explain within the frames of the traditional kinetic models.

The aim of our present investigation was to examine in detail the specific features of the osmotic process in an aqueous solution under dynamic conditions as a function of time, while applying two different experimental regimes: of

---

* To whom all correspondence should be sent.
E-mail: minkov.ivan@gmail.com

constant and variable solution volume. In the case of confined volume, Krustev, Kolikov *et al.* [13] have introduced the term 'confined osmosis', defined as "…osmosis at which practically constant solution volume is maintained by external mechanical influence, resulting in an increase of the hydrostatic pressure in this volume".

The specific tasks of the present investigation required a novel approach and modification of the classical experimental setup. In the classical membrane osmometry Π is directly determined by the hydrostatic pressure value established in an "open mode" – through the rise of the liquid level in the solution compartment. Of course, such an approach is only suitable at moderate elevation – of the order of decimeters – which, accordingly, means small concentration differences: up to a few tens of millimoles per liter (see Eq. 1). An alternative mode, without such limitations, is conducting the process in a closed constant volume [4, 5, 8] and determining Π by means of an appropriate pressure sensor. Here we put forward an operative hybrid method, which combines the advantages of the two above: it comprises controlled variation of the solution volume, which permits measuring much higher pressure levels, when subjected to the "open mode".

For the complex tests we have chosen glucose: a low molecular mass compound that is a popular biological agent, already used elsewhere as a reference in osmotic studies [8].

MATERIALS AND METHODS

Glucose Braun G-5 (5% glucose of high purity; B. Braun Melsungen AG, Germany) was employed in all experiments. Polyamide composite semipermeable Koch RO (reverse osmosis) membranes were used within the prescribed ranges (pH = 4-11; temperature < 50°C). All solutions were prepared with Elga Labwater (model PURELAB Option-Q7) deionized water. The membrane osmometer employed in our experiments was specially designed and built for the purpose [14]. It consists of two cylindrical plastic shells: for solvent and solution, respectively. A semipermeable membrane of 5.0 cm diameter was sealed between the shells and was supported against deformations by two additional perforated Plexiglas disks on either side. The operative area of the membrane (the integral surface area of orifices) was ca. 5 cm^2, Fig. 1. Such a kind of a membrane osmometer, with solution compartment of constant volume, has been employed already in our preceding study of equilibrium osmotic pressure [15].
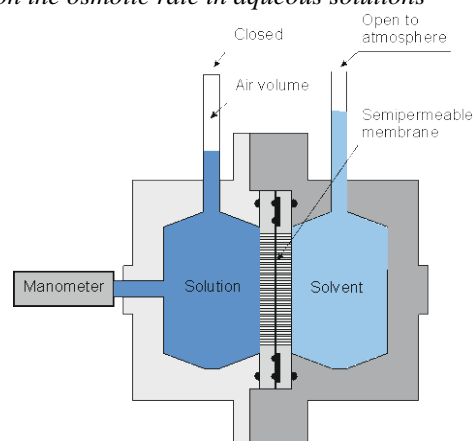
Fig. 1. Schematic of the membrane osmometer (osmotic cell).

However, the specific tests of the present investigation, primarily, the comparison between osmotic rates at variable and constant solution volume, required further refinement. We applied here our novel "hybrid" modification of the cell with limited variation of the solution volume. Thin graduated 1.3 m long transparent plastic tubing of 2 mm radius was attached to the solution chamber to provide control over the liquid and air amount, and measure the solution level rise at variable volume. Thus, with initial capacity of the solution compartment of 60 cm^3, the attached tube provided variable additional volume of ca. 16 cm^3, that is, a possibility of volume change by up to some 25 %. We consider this sufficient for our present purpose. Of course, we could have supplied even larger span of volume variation, but such a step would have brought further complication, due to the substantial dilution of the studied solution upon time.

A unique and promising feature of this novel modification is its potential to control the rate of pressure rise. As pointed out by a reviewer of our work: „This is relevant not only for an understanding of biological systems but may have interesting technical applications, as potentially damaging abrupt pressure changes can be avoided".

Of course, as required by the gas laws, in the case of (limited) volume variation the 'solvent influx *vs*. pressure' dependence is not linear: the liquid flux per unit pressure steadily decreases upon building osmotic pressure, as illustrated by Fig. 2. Yet, for the purpose of our comparison here such non-linearity does not create any problems. The ultimate solution concentrations were derived by means of the amount of solvent passed through the membrane. The corresponding osmotic pressure was registered by a 16-bar electronic pressure sensor (reading ±0.01 bar). All experiments were conducted at a temperature of 22$^{\text{O}}$C.
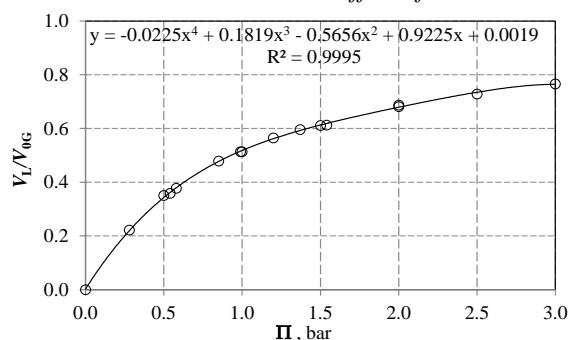
Fig. 2. Solvent influx V_L, relative to the vacant initial (gas) volume V_{0G}, as a function of the osmotic pressure Π in the regime of limited variation of the solution volume.

RESULTS AND DISCUSSION

The solute concentration as chosen for the comparison of the osmotic rates for processes at constant and variable solution volume was 5% = 0.278 mol/L glucose. We shall remind here that, at such a level of solute concentration, we have found that the use of the original van't Hoff law as a reference for the equilibrium osmotic pressure values proved entirely sufficient for the tasks considered here. The results of the extensive study of Grattoni *et al.* [8] have clearly shown, that the divergencies between the equations describing the equilibrium osmotic pressure in the references cited above [2-8] become significant at solute concentrations above ca. 0.5 mol/L, corresponding (at room temperature) to maximal (equilibrium) osmotic pressure values of the order of 12 bar. At our chosen concentration of solute $c = 0.278$ mol/L, we have operated in the range of moderate levels of osmotic pressure values below 7 bar. In this range, the deviations between all the above cited equations are well within the limits of the experimental scatter, as established in ref. [8] for a number of nonionic, low-molecular solutes, including glucose.

The obtained experimental results are presented in Figs. 3-6 and Table 1.

The juxtaposition of the obtained kinetic dependences, as presented in Fig. 3, demonstrates the drastic differences in the rates of osmotic pressure rise for the two regimes.

With variable cell volume, the osmotic pressure rise occurs at much slower rate. However surprising at first sight, this finding can be regarded as a quite natural result. The amount of solvent, which has to pass into the solution compartment of the cell, in order to lift the osmotic pressure, differs dramatically in the two regimes.
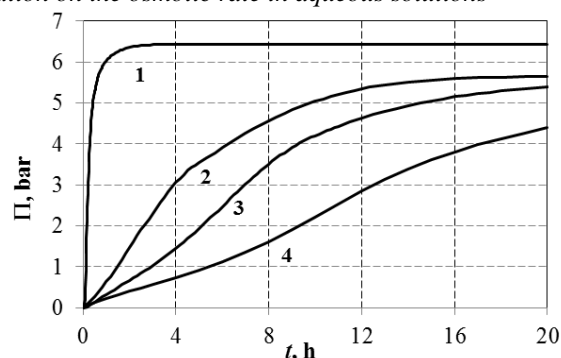
Fig. 3. Osmotic pressure Π vs. time t dependence for the two experimental regimes: (1) Constant volume); (2) Variable volume (+ 4 cm^3); (3) Variable volume (+ 8 cm^3); (4) Variable volume (+ 16 cm^3).

For example, employing the value for the coefficient of compressibility of pure water of 4.6×10^{-5} bar^{-1}, one estimates that for a closed cell of solution volume of 60 cm^3 the amount of solvent needed to raise the pressure by one atmosphere is 2.76×10^{-3} cm^3 (= 1.53×10^{-4} moles of H_2O). Concurrently, in our case of limited solution volume variation, even by the addition of as little as 4 cm^3 to the initial 60 cm^3, the amount of solvent necessary to lift the pressure up to a level of $\Pi = 1.0$ bar will be *ca.* 2.08 cm^3 (= 0.115 moles of water; conf. Fig. 2). The latter amount is some 750 times larger than that at constant volume and, of course, will definitely require longer time for transport. For the sake of comparison we can also employ the classical case of unlimited solution volume variation. For an osmotic cell connected to an open tube of radius as small as 2 mm (= 0.2 cm), the amount of solvent necessary to lift the solution level by 10.2 m (in order to impose hydrostatic pressure of 1 atmosphere) would be $4\pi \times 10^{-2}$ (cm^2) $\times 1.02 \times 10^3$ (cm) = 128 cm^3 (= 7.1 moles of H_2O)!

The '$d\Pi/dt$ *vs. t*' dependences, as derived from the data of Fig. 3 and presented in Fig. 4 (a,b), exhibit marked differences in the kinetic behaviour of the studied systems at the two regimes:

Firstly, the rate of pressure increase reaches many times greater values at the regime of constant volume and the temporal dependence passes through a sharp maximum.

Secondly, one can observe distinct differences in the $d\Pi/dt$ pattern at different volume expansion. At the lowest level of 4 cm^3, a well-defined maximum in the temporal dependence is still present. However, as the additional volume increases, the maximum becomes shallower, and at the largest level of volume variation (of 16 cm^3) it turns into a wave-shaped dependence, exhibiting first a shallow minimum, followed by a shallow maximum.

Thirdly, the maximal values of the rate of osmotic pressure rise, $d\Pi/dt$, steeply decrease with the volume expansion: from ca. 25 bar/h at constant volume (Fig. 4a) down to 0.32 bar/h at $\Delta V = 16$ cm^3 (Fig. 4b).
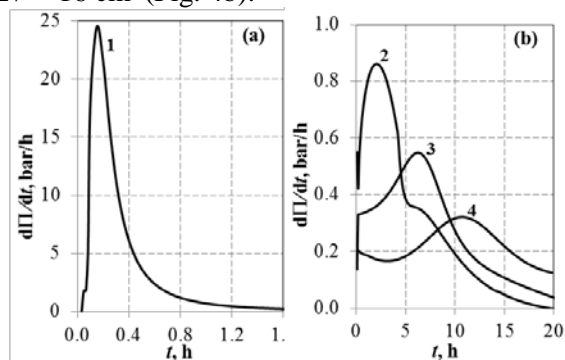

Fig. 4. Rates of osmotic pressure increase, $d\Pi/dt$ *vs. t* for the two experimental regimes: (a) Constant volume regime (1); (b) Variable additional volume regime: (2) 4 cm^3; (3) 8 cm^3; (4) 16 cm^3.

The integral temporal dependences for the amount of solvent transfer, ' Δn_L *vs. t* ', presented in Fig. 5 (a,b) depict yet another remarkable finding. While the osmotic pressure rise is always faster at constant volume, the flow through the membrane is much faster in the regime of variable volume. As it must be noted, the scales for Δn_L in the two sections of Fig. 5 differ by three orders of magnitude! Thus, the solvent influx rates at variable regime turn to be practically by two orders of magnitude larger practically in all studied cases.

The above conclusion is reinforced by the differential temporal dependences, ' dn_L/dt *vs. t* ', presented in Fig. 6. At constant volume the osmotic process appears to start at a slower rate and sharply accelerate with time to pass through an expressed maximum, beyond which the rate of solvent transfer rapidly declines. The picture is rather different in the regime of varied solution volume. Almost from the very start of the process the solvent transfer rates uniformly diminish with time at all such cases of different level of volume expansion.

All these results are outlined in Table 1, which presents the osmotic characteristics, as estimated in SI-units for the two different regimes: maximal total solvent influx values (Δn_L) at the final $t = 20$ h, maximal rates of osmotic pressure rise at constant volume $(d\Pi/dt)_{con}$, at variable volume $(d\Pi/dt)_{var}$ and their ratios for the different volume expansions; the corresponding values of the solvent transfer rates $(dn_L/dt)_{con}$ at constant volume, at

variable volume $(dn_L/dt)_{var}$ and their ratios for the different volume expansions $\frac{(dn_L/dt)_{var}}{(dn_L/dt)_{con}}$; the times corresponding to the maximal pressure increase rates (τ_p) and maximal solvent influx rates (τ_n), and the ratios of instant to equilibrium pressure values at the solvent influx maxima ($\Pi_{(\tau_n)}/\Pi_{eq}$). The solvents influx rates were computed using an estimated value for the active membrane area of 4.65 cm^2.
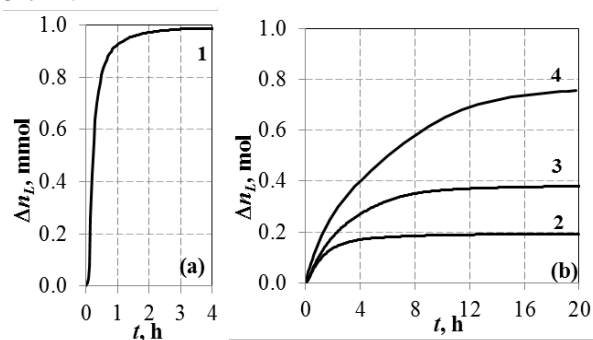
Fig. 5. Total solvent influx Δn_L as a function of elapsed time *t* dependences for the studied variations of solute volume: (a) Constant volume regime (1): Δn_L *is shown in millimoles*; (b) Variable additional volume regime: (2) 4 cm^3; (3) 8 cm^3; (4) 16 cm^3 (Δn_L *is shown in moles*).
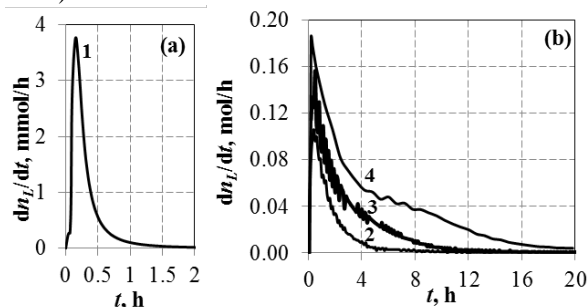

Fig. 6. Solvent rates of transfer differential dependences dn_L/dt as a function of lapsed time *t* for the two regimes. (a) constant volume regime (1); (b) Variable additional volume regime: (2) 4 cm^3; (3) 8 cm^3; (4) 16 cm^3.

Among the obtained results some are quite surprising and far from easy to interpret at once. For instance, we would have rather expected fairly steady pressure and liquid transfer rates, especially in the initial stages, away from equilibrium. Nevertheless, the initial increase may be attributed to a delayed response of the semipermeable membrane to the early impact of solvent, to which it needs time to adjust.

Table 1. Comparison of the kinetic characteristics of the osmotic process in aqueous glucose solutions at the two different regimes (subscripts 'var' and 'con' indicate *variable* and *constant* solution volume. Active area of the semipermeable membrane $S_M = 4.65$ cm³

	Constant volume	Varied volume		
	$V_{0G} = 0$ cm³	$V_{0G} = 4$ cm³	$V_{0G} = 8$ cm³	$V_{0G} = 16$ cm³
Δn_L [mol] (t=20h)	1.53×10^{-4}	0.19	0.38	0.75
dp/dt (*maximal*) [mbar/s]	6.80	0.239	0.153	0.089
$\dfrac{(dp/dt)_{con}}{(dp/dt)_{var}}$	-----	28.5	44.5	76.5
dn/dt (*maximal*) [mmol/m²s]	1.97	65.7	95.6	113.5
$\dfrac{(dn/dt)_{var}}{(dn/dt)_{con}}$	-----	33.3	48.5	57.6
τ_p [s]	0.54×10^3	6.48×10^3	21.24×10^3	38.88×10^3
τ_n [s]	0.54×10^3	2.52×10^3	2.16×10^3	0.72×10^3
$p(\tau_n)/p_{eq}$ [%]	26.7	6.37	2.79	1.09

In any case, the onset of the decline beyond the maxima appears to occur too early to be interpreted in terms of the decreasing difference between equilibrium and instant osmotic pressure values (the driving force of the osmotic process toward equilibrium). The pressure value at the maximum is still sufficiently far from the respective upper limit of Π.

Besides those already observed in Figs. 3-6, there are more tendencies to note in Table 1 for the determined characteristics upon changing the experimental conditions. Such are e.g. the reverse trends in the time-span of reaching the maximal pressure ascent rate, τ_p, and the maximal solvent influx rate, τ_n. Concurrently, the pressure level at which the maximal influx rates, $\Pi_{(\tau_n)}$, are reached noticeably declines when the additional solution volume is enlarged and are definitely lower than those reached at the respective maximal pressure ascent rates, $\Pi_{(\tau_p)}$.

We can summarize in brief the present findings as follows:
- The novel approach of limited variation of solution volume applied here has proved efficient and productive for the osmotic experiments.
- The obtained 'pressure *vs.* time' dependences attest that the rise of pressure is much faster at constant solution volume.
- Inversely, the solvent influx through the semipermeable membrane toward the solution is many times greater in the regime of variable volume.
- The values of flow rate at constant solution volume pass through expressed and well defined maxima, while at variable volume they exhibit a steady decline with time, starting practically from the onset of the process. The latter effect may be principally attributed to the applied technique of limited variation of solution volume. Concurrently, the dilution of the operative solution in the progress of the process can only account for a small fraction of the decline.

CONCLUSIONS

The set off here study of aqueous solutions under different osmotic regimes employs a new experimental approach of limited solution volume variation. The results obtained demonstrate the applicability and the advantages of the new method when comparing the osmotic behaviour at different regimes. Most remarkably, the kinetic rate values for the two regimes are very different. Qualitatively speaking, the fact that the pressure increase at constant solution volume occurs at much faster rate is a natural result, considering the amount of solvent transferred into the solution compartment. In fact, the picture in terms of solvent flow rates is exactly the reverse: transfer of liquid is much faster in the case of variable volume.

Summing up, we consider the effects established here for the osmotic process by means of an artificial semipermeable membrane to be of

relevance for processes taking place in nature and technology. For instance, our present results are in accord with the recognized now vision about the feasible mechanism of self-maintained cell homeostasis. The living cells rapidly achieve osmotic equilibrium in confined volumes upon changes in the environment mostly by means of protein channels in the lipid membranes, despite osmosis being considered a slow process in general.

The data generated in the present investigation have allowed our deriving definite qualitative and semi-quantitative conclusions about the distinctions in the kinetics of the osmotic process under the different regimes (of constant and variable solution volume). In stricter quantitative terms, the interpretation of the obtained differences is much more complex and would demand additional considerations. This, however, is beyond the scope of the present initial investigation and is meant to be a subject of further studies of ours.

REFERENCES

1. K. Alleva, O. Chara, G. Amodeo, *FEBS Letters*, **586**, 2991 (2012).
2. J.H. van't Hoff, *Z. Phys. Chem.*, **1**, 481 (1887).
3. H.N. Morse, J.C.W. Frazer, F.M. Rogers, *J. Am. Chem.*, **38**, 175 (1907).
4. J.C.W. Frazer, R.T. Myrick, *Am. Chem. J.*, **38**, 1907 (1916).
5. P. Lotz, J.C.W. Frazer, *Am. Chem. J*, **43**, 2501 (1921).
6. D. Stigter, *J. Chem.*, **651**, 118 (1960).
7. V.T.Granik, B.R.Smith, S.C.Lee, M.Ferrari, *Biomedical Microdevices*, **4**, 309 (2002).
8. A.Grattoni, M. Merlo, M. Ferrari, *J. Phys. Chem.B*, **111**, 11770 (2007).
9. J.H. Northrop, *J. Gen. Physiology*, **10**, 883 (1927).
10. M. H. Jacobs, Modern Trends in Physiology and Biochemistry, New York, Academic Press, 149, 1952.
11. C.V. Paganelli, A.K. Solomon, *J. Gen. Physiol.*, **4**, 259 (1957).
12. H.C. Longuet-Higgins, G. Austin, *Biophysical J.*, **6**(2), 217 (1966).
13. G.A. Krustev, K.H. Kolikov, D.D. Hristozov, E.I. Peeva, *Annual Session of the Union of Scientists in Bulgaria, Plovdiv*, **23**, 11 (2007).
14. K.H. Kolikov, Device for Membrane Separation and Selective Purification of Industrial Fluids and Biological Objects, *Patent Application № 110-149*, 29.05.2008.
15. I. Minkov, E. Manev, S. Sazdanova, K. Kolikov, Proc. IV International Conference of Young Scientists – Plovdiv, 23-24 June 2011, **XIII**, 97, (2012).

ВЛИЯНИЕ НА КОНТРОЛИРАНАТА ПРОМЯНА НА ОБЕМА ВЪРХУ СКОРОСТТА НА ОСМОЗАТА ВЪВ ВОДНИ РАЗТВОРИ

И. Л. Минков[1, 2,*], Е. Д. Манев[2], С. В. Сазданова[2], К. Х. Коликов[3]

[1] Софийски университет "Св. Климент Охридски", Медицински факултет, Катедра по химия и биохимия, физиология и патофизиология, ул. Козяк 1, 1407 София, България
[2] Софийски университет "Св. Климент Охридски", Факултет по химия и фармация, Катедра по физикохимия, бул. Дж. Баучер 1, 1164 София, България
[3] Пловдивски университет „Паисий Хилендарски", Факултет по математика и информатика, ул. Цар Асен 24, 4000 Пловдив, България

(Резюме)

Изменението на осмотичното налягане във водни разтвори е изследвано експериментално като функция от времето при два различни режима: на постоянен и променлив обем на разтвора. Установена е количествена зависимост на скоростта на осмозата в разтворителя от относителната промяна на обема на разтвора. Глюкозата, като биологично активно вещество, е избрана като референтен разтворен компонент в комплексните изследвания. За целта е изработена специална осмотична клетка. Разработен е нов експериментален подход, използващ контролирана ограничена промяна на обема на разтвора. Получените кинетични зависимости показват съществени различия в скоростта на процеса при двата експериментални режима. Повишаването на налягането е много по-бързо при постоянен обем на разтвора, докато притокът на разтворител е много по-голям в режим на променлив обем. Освен това, скоростта на осмозата се променя при промяна на обема на разтвора. Ние считаме, че зависимостите установени в настоящата статия с помощта на изкуствена полупропусклива мембрана са от значение и за процесите, протичащи в реалните живи клетки и тъкани.

Quercetin content and ratios to total flavonols and total flavonoids in Bulgarian fruits and vegetables

S. Tsanova-Savova[*], F. Ribarova, V. Petkov

Medical University – Sofia, Medical College "Yordanka Filaretova"
3, Yordanka Filaretova Str., Sofia 1606, Bulgaria

Flavonoids as bioactive compounds in vegetable foods have been the subject of numerous research projects. Quercetin, with its powerful antioxidant activity, has also been and is currently in the focus of studies on plant species identification, and on its role in healthy nutrition. The current literature sources provide diverse information on its content in particular plant species but there are almost no data on its ratios to other flavonoids representatives. The aim of this survey was to provide information about quercetin analysis and content as a major flavonols representative and quercetin ratios to total flavonols, expressed as a sum of myricetin, quercetin and kaempferol and to total flavonoids in Bulgarian fruits and vegetables. The survey covered 17 fruit and 13 vegetable samples, complying with the current sampling requirements, with a view to food composition assessment. Quercetin and other flavonols analysis by High Performance Liquid Chromatography (HPLC) method; Total flavonoid content was determined by the aluminum chloride colorimetric assay. Evidence is presented on quercetin content in fruits and vegetables and on its ratio to total flavonols and total flavonoids content. The results demonstrate that quercetin is most frequently the major flavonol representative in the majority of the analyzed samples. There is, though, an interesting exception, presented by the representatives of the *Cruciferae* family - broccoli and Brussels sprouts - where the quercetin ratio to total flavonoids is very high, reaching up to almost 50%. In fruits, quercetin in strawberries is only 44.0% of the total flavonols, thus demonstrating once again the need for a complex approach in the analysis of the data for flavonoids content. The supplementation of the flavonoids composition and content data with evidence about their ratios will enable more correct identification of the biodiversity and will allow to compensate, though to only a certain extent, the effect of the biological variation on the accuracy of the analysis, and will enrich the information needed to build up a data base for flavonoids in foods.

Key words: flavonoids, quercetin, flavonols, fruits, vegetables

INTRODUCTION

The Food Composition Tables are an indispensable part of the food information system that, together with the criteria for the biological role of the food and its nutrients, is involved in the building up and establishment of the food policy. Food, as a basic environmental compartment sets the need of knowledge on its composition to enable its nutritional value and safety. Currently there are huge data arrays containing information about macro- and micronutrients and on the bioactive compounds content in foods as well. An example in this aspect is supplied by the US Department of Agriculture that has developed data bases for phytonutrients, carotenoids, flavonoids, isoflavonoids, anthocyanines in addition to the major food composition data base [1]. The present survey was focused on the content of the flavonoid quercetin in foods, because of its confirmed bioactivity in the prevention of oxidative stress in the organism [2, 3], as well as against the development of a number of degenerative diseases [4-6]. Quercetin attracted our attention as it is the most comprehensively studied flavonoid of the flavonols group and all data bases for this class of polyphenolic compounds contain any information on it.

Criteria for judging the quality of food composition data and databases have long been established. In 2002 those criteria have been formalized by Holden et al. [7] assessing food data quality. Whether generating new analytical data or assessing existing data, quality criteria are fundamentally related to the following stages: the number of food samples collected, the number of samples prepared for analysis, the number of discrete samples analyzed, the number of analytical replicates, the number that represents the best value and the variability and the quality of analytical procedure used [8].

In this relation, in spite of the variety of data on flavonoids content in foods, they either do not comply with the requirements for a database or the biovariety of the selected plant species is very large, or no relationships have been searched for between the particular representatives in the flavonoids groups. Striving for stability of the results for flavonoids content in plant species used for food purposes, we support that it is appropriate

---

* To whom all correspondence should be sent.
E-mail: silvia.tsanova.savova@gmail.com

to analyze not only the real numerical value of the quantity of the individual representatives of flavonoids classes per unit of plant tissue but also to establish the ratio between the compounds themselves, building up the content of each individual plant species. The aim of this survey was to provide information for analysis and content of quercetin as a major flavonols representative and quercetin ratios to total flavonols expressed as a sum of myricetin, quercetin and kaempferol and to total flavonoids in Bulgarian fruits and vegetables.

MATERIALS AND METHODS

Sampling plan

This survey covered the analysis of 17 fruit and 13 vegetable samples. Each analyzed individual sample of fresh fruits and vegetables was an aggregate sample of three *single* samples purchased at three different premises in one and the same day. The amount of the purchased single samples was as follows: not less than 0.5 kg for berries (raspberries, blueberries, blackberries), not less than 1 кg for the other fruits and vegetables and three pieces for vegetables that are sold either in pieces (cabbage) or bunches (leeks) (BNS ISO 874: 1996) [9]. A sampling protocol was elaborated for each single sample, describing its origin. The single samples were aggregated in a common sample (*aggregate sample*). After a careful check fruits and vegetables with infringed integrity and freshness were pulled out of the aggregate sample. A s*ubsample* was made of the aggregate sample, through random selection of fruits and vegetables, that was lyophilized. It was weighed before and after the sublimation drying with the task to determine its dry fraction that was necessary for the precise calculation of the results. When preparing the subsample all non-edible parts of the fruits and vegetables were removed. The lyophilized subsample was stored in hermetically vacuum sealed packs at temperature of 4°C until the time of the analysis. Before the analysis the lyophilized subsample was ground, sieved through a sieve with pore size 0.5 mm and homogenized. Part of the lyophilized subsample was taken, representing the analytical sample [10].

Methods for determination of flavonols in fruits and vegetables
Extraction and hydrolysis

The lyophilized subsamples were ground to fine powder. The analytical sample was weighed in a 200 ml Erlenmeyer flask with ground glass joints and water, solution of tertiary butylhydroquinone

(TBHQ) (2 mg/ml MeOH), and hydrochloric acid (10 M) were added to it as follows (Table 1):

Table 1 Sample preparation for flavones and flavonols analysis

Sample	Weight (g)	TBHQ (ml)	H$_2$O (ml)	HCl (ml)
Lyophilizate	0.500 – 1.500	25	19	6

Each analytical sample was completed with 500 μl internal standard morin in a way that the final morin concentration in the sample would reach 2.5 μg/ml.

The extraction and hydrolysis of the sample in this survey was performed at 1.2 M HCl in 50% MeOH in a water bath at 90^{0}C for 2 h under a reverse condenser. After the hydrolysis period had expired, the sample was allowed to cool down for about 5 min, and after that 1 ml solution of ascorbic acid was added to it (1 mg/ml). The sample was transferred to a 100 ml graduated flask and the marked volume was made up by adding methanol. The sample was subjected to an ultrasound bath for 3 min and, after that, if necessary, the volume was again adjusted to the mark. The extract was homogenized and an aliquot part of it was ultracentrifuged for 5 min at 14000 rpm. The supernatant was filtered through a membrane filter (HV-Millipore) with pore diameter 0.45 μm.

High performance liquid chromatographic analysis

The separation was performed by an Alltima column (100 × 4.6 mm i.d., 3 μm) C18, Alltima Associates, Inc., connected to a pre column packed with the same filling. The elution was isocratic with c 28 % acetonitrile in 2% acetic acid (Eluent I). The flow rate was 0.9 ml/min, with working pressure 11.5 – 12 MPa.

The amount of flavonols and flavones in the samples was determined by the method of the internal standard. For this purpose a linear correlation equation of the relationship between the ratio of the signals of the standard solutions to the internal standard and the concentration of the determinable compounds in the calibration standard solutions was constructed. The results were listed in mg/100 g fresh weight.

Since by the present HPLC analysis only 3 individual flavonols may be determined, we have decided to refer the quercetin content, as their main representative, to total flavonoids load in fruits and vegetables.

Total flavonoids assay

Total flavonoid content was determined by the aluminum chloride assay [11]. All samples were analyzed in duplicates. In brief an aliquot of 1 ml of

extracts or standard solution of catechin (20-100 mg/l) was added to 10 ml volumetric flask containing 4 ml H_2O, and after that 0.3 ml 5% $NaNO_2$ was added. After 5 min, 0.3 ml 10% $AlCl_3$ was added and at 6th min, 2 ml 1M NaOH was added and the total volume was made up to 10 ml with H_2O. The absorbance of the solution was measured against the reagent blank at 510 nm. Total flavonoids content was expressed as mg catechin equivalents CE/100 g fresh mass [12].

RESULTS AND DISCUSSION

The results for quercetin and total flavonols content (expressed as a sum of myricetin, quercetin and kaempferol) in Bulgarian fruits, determined by HPLC method were presented in Table 2 in mg/100 g fresh weight. All results complied with the requirements for food data representativeness as they were a mean value of duplicate analyses of a pool of 3 market samples. In addition, each value was an average result of at least three aggregated (pool) samples, which meant at least 9 individual samples. In this relation, the presented data were among the most precise data, available in the literature sources, concerning the sampling plan [13, 14].

The table also contains the quercetin ratios to total flavonols (sum of myricetin, quercetin and kaempferol) determined by HPLC method, and to total flavonoids determined by a colorimetric method, expressed in percents (%).The results shown in Table 2 revealed that the data obtained by HPLC analytical methods were normally lower than those provided by non-specific colorimetric spectrophotometry and, in some cases, for example with sour cherries, only 1% of the total flavonoids were on the account of the flavonol quercetin. This could be explained by the fact that the total flavonoids assay reported also other classes of phenolic compounds which, in fruits, were most frequently anthocyanins, catechins and their forms associated with gallic acid.

In all cases it should be taken into account that it was possible that the colorimetric method for analysis of total flavonoids and other phenolic compounds, and even some tannins would provide positive results. That was the cause for the inclusion in data bases for flavonoid content in foods only of results from chromatographic quantitative analysis.

The results showed that most often quercetin was the major flavonol representative and in many fruit samples it was the only representative of this flavonoids class. Generally the content of the other two flavonols representatives - myricetin and

Table 2. Quercetin content in fruits and ratios to total flavonols and total flavonoids

Fruit	Quercetin mg/100g	Quercetin/ Total Flavonols[1] %	Quercetin/ Total Flavonoids[2] %
Apple, red (peeled)	0.0	0.0	0.0
Apple, red (unpeeled)	1.59	100.0	3.0
Apple, green (peeled)	0.0	0.0	0.0
Apple, green (unpeeled)	1.39	100.0	1.0
Blackberry	2.70	84.4	5.0
Blueberry	9.92	72.9	5.0
Cherry	2.52	100.0	13.0
Fig	0.87	100.0	4.0
Grape, black	2.32	91.3	3.0
Grape, white	1.56	85.7	4.0
Peach	3.41	100.0	23.0
Pear (peeled)	0.0	0.0	0.0
Pear (unpeeled)	0.59	100.0	1.0
Plum	2.34	100.0	2.0
Raspberry	1.60	100.0	6.0
Sour cherry	1.08	100.0	1.0
Strawberry	1.02	44.0	1.0

[1]Total flavonols as sum of myricetin, quercetin and kaempferol, determined by HPLC analysis;

[2] Total Flavonoids, determined by $AlCl_3$ colorimetric assay and expressed as mg catechin equivalents CE/100g fresh weight; determined by HPLC methods and expressed as mg/100 g fresh weight

kaempferol - was very small and was detected only in samples of grapes, blackberries and blueberries.

There was, though, a notable exception of the general rule – in strawberries quercetin was only 44.0% of the total flavonols that once again emphasized the need of a complex approach to analysis of data for flavonoids content.

The data also showed that the highest ratio quercetin/total flavonoids belonged to peaches – 23%, followed by cherries – 13.0% and raspberries – 6.0%.

The results for quercetin content in samples of Bulgarian vegetables, presented in mg/100 g fresh weight as well as the ratio quercetin/total flavonols and quercetin/total flavonoids (%) were listed in Table 3.

It is obvious that quercetin is the main flavonol in Bulgarian vegetables. Our previous studies have shown that myricetin was not detected in vegetable samples and kaempferol did not exceed amounts of 0.8 mg/100 g. In this sense quercetin ratio to total flavonoids in vegetables was not a surprise and the results were equal or close to 100 % in many of the tested samples. An interesting exception, though, were the results of the representatives of the *Cruciferae* family – broccoli and Brussels sprouts. Only those two vegetable species had a very high quercetin to total flavonoids ratio, reaching up to almost 50% in Brussels sprouts.

Table 3. Content of quercetin in Bulgarian vegetables and its ratio to total flavonols and total flavonoids

Vegetable	Quercetin mg/100g	Quercetin/ Total Flavonols[1] %	Quercetin/ Total Flavonoids[2], %
Okra	20.03	100.0	41.0
Tomato	1.42	88.2	11.0
Red pepper	1.49	100.0	11.0
Green pepper	10.27	100.0	37.0
Lettuce	15.39	100.0	16.0
Brussels sprouts	2.63	49.8	8.0
Broccoli	2.94	36.6	16.0
Red onion	45.25	100.0	(241.9)
White onion	20.41	100.0	-
Spring onion	10.32	87.60	65.0
Leek	0.0	0.0	0.0
Beans green	2.13	100.0	52.0
Beans yellow	2.29	100.0	28.0

[1]Total flavonols as a sum of myricetin, quercetin and kaempferol, determined by HPLC analysis;
[2]Total Flavonoids, determined by $AlCl_3$ colorimetric assay and expressed as mg catechin equivalents CE/100g fresh weight; determined by HPLC methods and expressed as mg/100 g fresh weight

The results for quercetin content and its ratio to total flavonols in samples of representatives of the family *Liliaceae* – leeks, spring, red and white onions showed that quercetin was not detected in leeks which complied with literature evidence [15]. The data for spring and mature onions were interesting, demonstrating the importance of botanical maturity for the quercetin/flavonols ratio in vegetables. For example, in fresh spring onions quercetin was 87.6 %, while in the mature white and red onions it was 100% of the studied amount of total flavonols. In this group of samples the results for the ratio quercetin/total flavonoids was also interesting. It was established that in spring onions quercetin accounted for 65% of all flavonoids – the highest determined value. Unfortunately we could not provide data for quercetin/total flavonoids ratio in white onions as total flavonoids were not determined for those samples. The results for red onions were startling – formally they were 241.9%, which was an unreal value. That was the only sample we tested where quercetin, determined by HPLC methods exceeded the total amount of flavonoids, determined by spectrophotometry. This result could be explained by the excessively high biological variation of flavonoids in food samples or by an analytical mistake in the determination of high amounts of total flavonoids by spectrophotometric methods. This once again supports the importance of a good sampling plan and assessment of the data quality and emphasizes on critical interpretation of results obtained from analysis of single food samples.

The importance of the presented quercetin/total flavonoids ratios to the greatest extent was outlined by the results for green and yellow beans. The data showed that, while quercetin content in the two types of foods was very close, its percentage rate in green beans was about two times higher than that in yellow beans.

CONCLUSION

The rich plant biodiversity requires a broad spectrum of indicators for its identification. The analysis implemented in this survey showed that the inclusion of ratios between individual representatives of the flavonols group provided a more comprehensive and reliable assessment of the flavonols representation in the target plant species and could predict a value for their bioactivity that was closer to the real one. The completion of the data for composition and content of flavonoids with their ratios values will enable more correct identification of the biodiversity and compensation, though to a certain extent, for the effect of biological variation on the accuracy of the analysis and will enrich the information necessary for building up data bases for flavonoids in foods.

REFERENCES

1. S. Bhagwat, D.B. Haytowitz, J.M. Holden (Ret.), USDA Database for the Flavonoid Content of Selected Foods, Release 3.1. U.S. Department of Agriculture, Agricultural Research Service (2014). Nutrient Data Laboratory Home Page: http://www.ars.usda.gov/nutrientdata/flav
2. D. Amić, V. Stepanić, B. Lučić, Z. Marković, J.M. Dimitrić Marković, *J. Mol. Model.* **19**, 2593 (2013).
3. R. Sokolová, I. Degano, S. Ramešová, J. Bulíčková, M. Hromadová, M. Gál, J. Fiedler, M. Valášek, *Electrochim. Acta*, **56**, 7421 (2011).
4. M.-L. Hertog, P.M. Sweetnam, A.M. Fehilly, P.C. Elwood, D. Kromhout, *Am. J. Clin. Nutr.*, **65**, 1489 (1997).
5. I.-W. Arts, D.R. Jacobs, L.J. Harnack, M. Gross, A.R. Folsom, *Epidemiology*, **12**, 668 (2001).
6. M.K. Hossain, A.A Dayem, J. Han, Y. Yin, K. Kim, S.K. Saha, G.M. Yang, H.Y. Choi, S.G. Cho, S.G., *Int. J. Mol. Sci.*, **17**, 569 (2016).
7. J. M. Holden, S.A. Bhagwat, K.Y. Patterson, *J. Food Compds. Anal.,* **15**, 339 (2002).
8. B. Burlingame, *J. Food Compds. Anal.,* **17**, 251 (2004).
9. БДС ISO 874. Fresh Fruits and Vegetables - Sampling. (1986).
10. S. Tsanova-Savova, F. Ribarova, M. Gerova, *J. Food Compos. Anal.,* **18**, 691 (2005).

73

11. L.-L. Soares, V. L. Bassani, G. González Ortega, P. R. Petrovick, *Acta Farmaceutica Bonaerense*, **22**, 203 (2003).
12. D. Marinova, F. Ribarova, M. Atanassova, *J. Uni. Chem. Technol. Metallur.*, **40**, 255 (2005).
13. S.A. Bhagwat, K.Y. Patterson, J.M. Holden, *J. Food Compos. Anal.*, **22**, 366 (2009).
14. S. H. Nile, S.H. Kim, E.Y. Ko, S.W. Park, Biomed Res Int. doi:10.1155/2013/718065, 718065 (2013).
15. C. Kevers, M. Falkovski, J. Tabart, J.-O. Defraigne, J. Dommes, J. Pincemail, *J. Agric. Food Chem.,* **55**, 8596 (2007).

СЪДЪРЖАНИЕ НА КВЕРЦЕТИН И СЪОТНОШЕНИЯТА МУ КЪМ ОБЩИТЕ ФЛАВОНОЛИ И ОБЩИТЕ ФЛАВОНОИДИ В БЪЛГАРСКИ ПЛОДОВЕ И ЗЕЛЕНЧУЦИ

С. Цанова-Савова[*], Ф. Рибарова, В. Петков

Медицински университет-София, Медицински колеж „Йорданка Филаретова“, ул. Йорданка Филаретова, София 1606, България

(Резюме)

Флавоноидите, като биоактивни съединения в растителните храни, са обект на голям брой изследвания. С мощната си антиоксидантна активност кверцетинът е във фокуса на изследванията върху идентифицирането на растителните видове и ролята му в здравословното хранене. В литературата има разнообразна информация относно съдържанието му в различните видове растения, но почти няма данни за съотношенията му с други представители на флавоноидите. Целта на настоящия преглед е да се събере информация относно анализа на кверцетин, съдържанието му като основен представител на флавонолите и съотношението му към общите флавоноли, изразени като сума от мирицетин, кверцетин и кемпферол, както и към общите флавоноиди в български плодове и зеленчуци. В прегледа са включени проби от 17 плодове и 13 зеленчуци, взети в съгласие със съвременните изисквания за пробоподготовка с оглед оценка на състава им. Анализът на кверцетин и други флавоноли е извършен с високоефективна течна хроматография; тоталното съдържание на флавоноиди е определено чрез колориметричен метод с алуминиев хлорид. Определено е съдържанието на кверцетин в плодове и зеленчуци и съотношението му към общите флавоноли и общите флавоноиди. Показано е, че кверцетинът е основният представител на флавонолите в повечето от изследваните проби. Има едно иинтересно изключение при представителите на сем. *Cruciferae* – броколи и брюкселско зеле, където съотношението на кверцетин към общите флавоноиди е много високо – почти 50%. В плодовете, например в ягодите, кверцетинът е само 44% от общите флавоноли. От получените резултати следва, че е нужен комплексен подход при анализа на данните за съдържанието на флавоноиди. Допълването на данните за състава и съдържанието на флавоноиди с данни за техните съотношения ще даде възможност за по-коректна идентификация на биоразнообразието, за компенсация, макар и частична, на влиянието на биологичната вариация върху точността на анализа и ще обогати информацията, необходима за създаване на база данни за флавоноиди в храни.

Coffee grounds as low-cost adsorbent for the removal of copper (II) and lead (II) from aqueous solutions

J. Seniūnaitė, R. Vaiškūnaitė*, D. Paliulis

Department of Environmental Protection and Water Engineering, Vilnius Gediminas Technical University, Saulėtekio al. 11, Vilnius, Lithuania, LT-10223

This work aims to study the removal of Cu (II) and Pb (II) from aqueous solutions with commercial coffee wastes (coffee grounds). Materials with no further treatment such as coffee residues from café may act as adsorbents for the removal of Cu (II) and Pb (II). Coffee ground fraction <200 μm was used in the experimental research. The effect of pH (2.0, 3.0, 4.0 and 5.0), contact time (15, 30, 60, 90, 120, 150, 180, 300, 480 and 720 min) and initial concentration of Cu(II) and Pb(II) (10 mg/L, 20 mg/L, 30 mg/L, 40 mg/L, 50 mg/L) on the adsorption was studied. The optimum values of the process variables were: contact time, 120-720 minutes; pH, 5.0; initial Cu(II) and Pb(II) concentration 20 mg/L. Equilibrium data fitted well to Langmuir and Freundlich models for Pb (II) and Cu (II) with high R^2 values. Studies have shown that coffee grounds are a suitable adsorbent for heavy metals removal from water.

Keywords: coffee grounds, adsorption, copper, lead, heavy metals, Freundlich isotherm, Langmuir isotherm

INTRODUCTION

Water pollution due to the disposal of heavy metals continues to be a great worldwide problem. Heavy metals pollution occurs in industrial wastewater that is emitted by metal plating facilities, mining operations, battery-manufacturing processes, production of paints and pigments, and ceramic and glass industries [1]. This wastewater commonly includes ions of copper, lead, etc. [2]. Heavy metals are "eternal pollutants" – they tend to accumulate and migrate from one place to another and are never destroyed Not only impact of individual heavy metals. is dangerous, but also their combined synergistic effect.

Copper (Cu) ions can be found in many wastewater sources including printed circuit board manufacturing, electronics plating, plating, wire drawing, copper polishing, paint manufacturing, use of wood preservatives and printing operations. Typical concentrations vary from several thousand mg/l from plating bath waste to less than 1 mg/L from copper cleaning operations [3]. It has been proved that high concentration of copper ion could be a reason for the relatively common diarrhoea, abdominal cramps and nausea [3,4]. High excess of Cu can cause autoimmune reactions that damage the central nervous system, liver, kidneys, cause gastritis, peptic ulcer disease, lung disease or liver cirrhosis [5].

Lead (Pb) has environmental importance due to its well known toxicity and intensive use in industries such as storage-battery manufacture, printing, pigment manufacturing, petrochemicals, fuel combustion and photographic materials [6]. Assimilation in the human body of relatively small amounts of Pb (II) over a long period of time can lead to malfunctioning of certain organs and chronic toxicity. Children exposed to lead are at risk for impaired development, lower IQ, shortened attention span, hyperactivity, and mental deterioration, children under the age of six being at a more substantial risk. Adults usually experience decreased reaction time, loss of memory, nausea, insomnia, anorexia, and weakness of the joints when exposed to lead. Lead can cause serious injury to the brain, nervous system, red blood cells, and kidneys [4–6]. Copper and lead have a negative impact on ecosystems and living organisms, therefore, the removal of these heavy metal ions from wastewater is important from the perspectives of human health. Several techniques for heavy metals removal have been developed, including filtration, precipitation (electrochemical), electrocoagulation, membrane filtration [1]. Although the above-mentioned methods are widely used, they require high exploitation costs or application of complex technical solutions, so a cheaper and adaptable technology for removal of heavy metals from water is needed. Because of its low cost, simplicity of design, and ease of operation, the adsorption technique has been the most extensively used one of these techniques. Adsorption is a recognized method for the removal of heavy metals from wastewater having low concentration of heavy metal. The adsorption process offers flexibility in design and operation and in many cases produces high-quality treated

---

* To whom all correspondence should be sent.
E-mail: rasa.vaiskunaite@vgtu.lt

effluent. Moreover, this adsorption is reversible and adsorbents can be regenerated by suitable desorption techniques [7].

Activated carbon is widely used in the world for heavy metal adsorption. Due to the lengthy and costly preparation of adsorbents, its price is high, which limits its use for water treatment. Recently, the use of organic waste (tea sludge, sawdust, rice husks, etc.) is gaining popularity for heavy metals biosorption. The most important advantage of these sorbents is the low cost. However, there is a lack of literature dealing with the possible application of coffee residues as adsorbents (i.e. for metals). In general, "coffee residues" are generally called the solid wastes discarded from the extraction process of instant coffee manufacturing, and the final residues originated from cafeterias. In the last years, the instant coffee industry has experienced a constant growth, as instant coffee has become one of the most popular kinds of coffee drinks by millions of people around the world. As a consequence, large amounts of coffee grounds, which are the solid residues obtained during the processing of coffee powder with hot water or steam to prepare instant coffee, have been generated worldwide (in the order of 6 mln tones/year) [8]. The annual amount of coffee consumed by a Lithuanian inhabitant is about 5.5 kg according to data of Lithuanian Consumer Institute (2012), therefore a big amount of coffee grounds are generated in Lithuania as waste every year. Coffee waste as adsorbent was tested for adsorption of various metals – lead, cadmium, nickel, indium, strontium, etc. [9-17]. Coffee grounds are also used for adsorption of dyes [18-20]. Also coffee pulp was tested as adsorbent for adsorption of organic compounds [21].

In this study, we investigated the application of the coffee grounds and measured the amount of copper (II) and lead ions (II) adsorbed onto the coffee grounds from synthetic wastewater. Moreover. impact of pH and contact time with adsorbent on he adsorption efficiency was evaluated.

METHODOLOGY

Preparation of adsorbents. The low-cost commercial medium-roasted ground coffee (Arabica variety) was used as an adsorbent. Coffee grounds were untreated coffee residues collected from coffee machines of local cafeterias. Sieve analysis was used to divide the coffee residues into two size fractions (<200 μm and >200 μm) with a vibratory sieve shaker Retsch AS 200 [22]. According to our research results, the fraction of coffee grounds < 200 μm was selected for further experimental research. These residues were untreated, only washed with deionized water (Demiwa 3 roi system) until a pH close to 6.0 was achieved. Finally the grounds were oven-dried (SNOL 3.5) at 100–105 °C for 24 h, cooled to room temperature and were suspended in a plastic container in order to protect against adverse environmental impact [23].

Elemental analysis of adsorbent. The thermal field emission scanning electron microscope JEOL JSM-7600F with energy dispersive X-ray spectroscopy detector was used for elemental analysis of <200 μm coffee ground.

Determination of dry bulk density. Determination of dry bulk density of coffee ground sized smaller than 200 μm was carried out applying standard ISO 567:1995.

Adsorbate. Lead and copper atomic spectroscopy standard solutions of 1000 mg/L ± 2 mg/L (2% HNO_3) (ROTI®STAR) were used as the source of Cu (II) and Pb (II) in the synthetic wastewater. The aqueous solutions containing Cu^{2+} and Pb^{2+} cations of concentration 10 mg/L, 20 mg/L, 30 mg/L, 40 mg/L, 50 mg/L were prepared by diluting the standard metal solutions (Cu(II) and Pb(II)) in a measuring flask to the 100 mL mark with deionized water. All chemical reagents were of analytical grade and were used in the experiments as received without further purification. Deionized water used in experiments meets the requirements of standard LST EN ISO 3696:1996 (Water for analytical laboratory use – specification and test methods). All volumetric flasks used in the experiments were of an accuracy class.

Effect of sorption time on the removal of heavy metals. The sorption time is assessed by analyzing the static heavy metals sorption from the aqueous solution. The aim of these experiments was to determine the time when the equilibrium of adsorption is achieved. Durations of 15, 30, 60, 90, 120, 150, 180, 300, 480 and 720 min were selected for adsorption research. The experiments of static heavy metals adsorption from aqueous solution were performed by mixing an adsorbent sample with the heavy metal solution in a 1:100 ratio of adsorbent and solution mass (i.e., 1 g of adsorbent and 100 ml of aqueous solution) using capped bottles (200 ml). The suspensions were shaken at 21±1 °C at 20 rpm for the mentioned contact time applying Rotoshake RS12. The samples were filtered (using glass filter with 0.45 μm pores) and the heavy metal concentrations in the filtrate were measured applying AAS method [1].

Batch mode adsorption studies (Effect of pH on the removal of heavy metals). The maximum allowable concentration (MAC) of lead and copper in wastewater to be discharged to wastewater collection system is 0.5 and 2.0 mg/L, respectively (Regulation on wastewater management, *Official Gazette,* No. 110-4522, 2007). The influence of different pH values was studied in the range of 2.0*,* 3.0*,* 4.0 and 5.0) (10 mg/L Cu (II) and Pb (II) solution). The effect of pH was followed by mixing 1 g of adsorbent with 100 mL of metal single-component solution. The pH value, ranging between 2.0 and 5.0, was kept constant throughout the adsorption process by micro-additions of HNO_3 (0.1 M) or NaOH (0.1 M). pH was measured with Mettler Toledo seven Multi pH meter. The suspension was shaken at 20 rpm at constant temperature (21±1 °C) for selected contact time (from 15 to 720 min) with Rotoshake RS12. Calibration curves were prepared before each sample measurement.

Effect of concentration. The concentration of Cu(II) and Pb(II) was assessed by analyzing the static heavy metals sorption from the aqueous solution. The aim of these experiments was to determine the concentration of metal when the equilibrium of adsorption is achieved. Concentrations of 10, 20, 30, 40 and 50 mg·L^{-1} were selected for Freundlich and Langmuir adsorption isotherm creation.

Freundlich isotherm is widely applied in heterogeneous systems [24]. The slope ranging between 0 and 1 is a measure of the adsorption intensity or surface heterogeneity, becoming more heterogeneous as its value gets closer to zero.

Freundlich isotherm is expressed as:

$$q_e = K_F C_e^{1/n}, \qquad (1)$$

or in linear form:

$$\log qe = \log K_F + \frac{\log C_e}{n}, \qquad (2)$$

where *qe* - amount of adsorbate in the adsorbent at equilibrium (mg/g); K_F - Freundlich isotherm constant (mg/g); C_e - equilibrium concentration (mg/L); *n* - adsorption intensity.

Langmuir isotherm

Langmuir adsorption isotherm, originally developed to describe gas–solid phase adsorption onto activated carbon, has traditionally been used to quantify and compare the performance of different bio-sorbents. In its formulation, this empirical model assumes monolayer adsorption (the adsorbed layer is one molecule in thickness); adsorption can only occur at a finite (fixed) number of definite localized sites, which are identical and equivalent, with no lateral interaction and steric hindrance between the adsorbed molecules, even on adjacent sites.

Langmuir isotherm is expressed as:

$$qe = \frac{Q_0 b C_e}{1 + b C_e}, \qquad (3)$$

or in linear form:

$$\frac{1}{q_e} = \frac{1}{Q_0} + \frac{1}{b Q_0 C_e}, \qquad (4)$$

where *qe* - amount of adsorbate in the adsorbent at equilibrium (mg/g); Q_o - maximum monolayer coverage capacity (mg/g); *b* - Langmuir isotherm constant (L/mg); C_e - equilibrium concentration (mg/L).

Percent adsorption decreased while metal uptake per unit weight of adsorbent increased as the initial Cu(II) and Pb(II) concentration increased from 10 to 50 mg·L^{-1} and after that percentage adsorption became constant.

Analytical method. Lead and copper concentrations were determined using atomic absorption spectrophotometer (AAS model Buck Scientific 210 VGP) operated with an air-acetylene flame, a slit of 0.7 mm at 283.2 and 324.7 nm wavelength, accordingly.

Evaluation of adsorption capacity. The adsorption capacity (Q) of the adsorbent was calculated by the following equation [2, 18]:

$$Q = \frac{(C_i - C_f) \cdot V}{m}, \ mg/g; \qquad (5)$$

where C_i – the concentration of metal ion before adsorption, mg/L; C_f – the concentration *of* metal ion after adsorption at the equilibrium state, mg/L; *V* – the volume of solution l; *m* – the sorbent mass, g.

Statistical analysis. Each analysis was prepared and analysed in triplicate. The average of the results and the standard deviation values were calculated.

RESULTS AND DISCUSSION

Determination of chemical composition of coffee ground. Elemental analysis provided the complete elemental composition of adsorbent as shown in Table 1.

Table 1. Composition of coffee grounds

Chemical element	Composition (weight %)
Carbon	68.80
Nitrogen	5.46
Oxygen	25.42
Silicon	0.09
Other elements	0.23
Total	100.00

It can be assumed that the carbon content in coffee grounds is affected by the coffee roasting. Average-roasted coffee grounds were used in the experimental studies. The effective parameter on molecules adsorption is the particle size of the adsorbent. Pollution uptake in adsorption process is a function of specific surface or external surface of adsorbent. According to our experimental results, it could be concluded that coffee grounds size has no significant impact on the adsorption of copper and lead, therefore only the smaller fraction (<200 µm) was selected for research. Similar results were observed in case of cadmium adsorption on coffee grounds. A series of experiments were performed in the range of particle size [225–800 µm] as a function of contact time [9]. It was observed that the rate of cadmium adsorption was not remarkably affected by the change in the particle size (change in surface area) of the coffee grounds. This statement can indicate that the adsorption takes place at the surface of the adsorbent and the functional groups are probably responsible for the adsorption of metal ions on the coffee grounds. It was found that bulk density of coffee grounds was 0.53 g/cm^3.

Effect of contact time. In order to define the kinetics of copper and lead adsorption, the parameters of the adsorption process were studied for contact time ranging between 15 and 720 min at room temperature (21±1°C) by monitoring the percent removal of copper and lead by the adsorbent. Figure 1 depicts the effect of contact time on the adsorption of Cu (II) onto coffee grounds.

Results presented in Fig. 1 show that the removal rate of Cu (II) ions was rapid in the first few minutes. The sorption equilibrium was achieved in 120 min. Figure 2 depicts the effect of contact time on the adsorption of Pb (II) onto coffee grounds.

Equilibrium experiments were conducted to study the effects of contact time and initial pH on the adsorption of copper and lead. Using the >200 µm fraction of coffee grounds for copper removal the treatment efficiency was 85.9% when the metal concentration was 0.5 mg/L, while the removal efficiency of lead was 87.2% [25]. According to Agwaramgbo *et al.* [28] 88.0% Pb removal efficiency was achieved by applying coffee grounds (initial lead concentration was 1300 mg/L). The maximum Pb removal efficiency according to our experimental data was about 84.5%. According to Gupta *et al.* [30] maximum adsorption capacity for Pb (II) onto coffee modified with ZnCl$_2$ solution was 63 mg/g. According to Rafiq *et al.* [33] coffee husk adsorption capacity for Cu (II) was 7.5 mg/g. Kyzas found maximum adsorption capacity of 70 mg/g for Cu (II) [31]. The maximum adsorption capacities were 0.845 mg/g for lead (II) and 0.657 mg/g for copper (II), which was considered high for untreated material.

Fig. 1. Effect of contact time on the adsorption of Cu (II) onto coffee grounds (pH = 5.0, 10 mg/L ion concentration, adsorbent: solution ratio 1:100 w:v, T = 21±1 °C, 15–720 min contact)
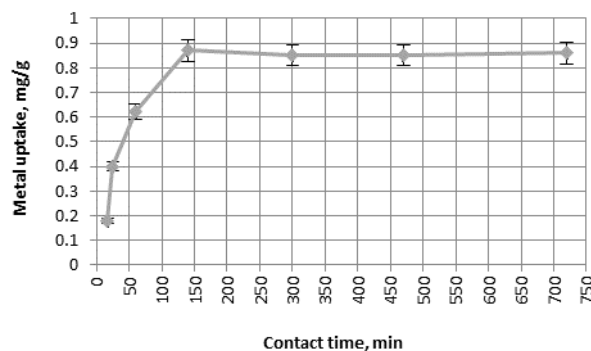
Fig 2. Effect of contact time on adsorption of Pb (II) onto coffee grounds (pH = 5.0, 10 mg/L ion concentration, adsorbent solution ratio 1:100 w:v, T = 21±1 °C, 15–720 min contact)

The plots could be split in three distinct regions: (i) 0–30 min, indicating the instantaneous adsorption of ions, suggesting rapid external diffusion and surface adsorption; (ii) 30–120 min, showing a gradual equilibrium; (iii) 120–720 min, indicating the equilibrium state.

According to Kyzas data [27] Cu (II) adsorption equilibrium onto coffee waste was achieved after 120 min, but according to Dutta *et al.* (2015) equilibrium conditions of cadmium adsorption onto coffee grounds were achieved in less than 30 min [18,25]. The adsorption equilibrium time depends on metal concentration and absorbent dose. It can be seen that the adsorbed amount of Pb (II) and Cu (II) ions increases with contact time up to 120 min, after that maximum removal is attained. Due to the not so quick adsorption rate (120 min), it can be

inferred that physi-sorption is predominant in this adsorption process. 120 min was selected as the optimum contact time for all further experiments.

The effect of solution pH. Aqueous phase pH governs the speciation of metals and also the dissociation of active functional sites on the sorbent. It has been identified as the most important variable affecting metal adsorption onto adsorbent, this partly because hydrogen ions themselves are strongly competing with adsorbate. To characterize the effect of pH on Cu (II) and Pb (II) adsorption using coffee grounds, a set of equilibrium adsorption experiments were conducted by modifying the pH from 2.0 to 5.0. The pH of the aqueous medium not only affects the solubility of the metal ions but also the ionic form in which they will be present in the solution and the type and ionic state of the functional groups at the biosorbent surface. The choice of pH range (2.0–5.0) in the present study was based on the fact that

approximately at pH 5.5 precipitation of Cu and Pb starts in aqueous solution [18, 26]. According to our research data at lower pH levels (<2.0) desorption of adsorbed metals from coffee grounds starts. Fig. 3 shows the effect of pH on the removal of Cu (II) ions onto coffee grounds from aqueous solutions.

The amount of copper ions sorbed by coffee grounds increases with the increase in pH from 2.0 to 5.0. Copper is mainly present in the form of Cu (II), with smaller amounts of CuOH between pH 2.0 and 5.0 [33]. At pH = 2.0 the removal of Cu (II) percentage was 3.5%. After pH 3.0 the uptake of Cu (II) increases sharply up to pH = 5 – metal uptake increases from 0.223 to 0.657 mg/g. No pH values over 5.0 were studied since precipitation of Cu (II) ions starts. Fig. 4 shows the effect of pH on the removal of Pb (II) ions onto coffee grounds from aqueous solutions.

Fig. 3. Effect of pH on adsorption of Cu (II) onto coffee ground from single metal solution (10 mg/L ion concentration, adsorbent solution ratio 1:100 w:v, T = 21±1 °C, 720 min contact)

Fig. 4. Effect of pH on adsorption of Pb (II) onto coffee ground from single metal solution (10 mg/L ion concentration, adsorbent solution ratio 1:100 w:v, T = 21±1 °C, 720 min contact)

The pH of solution was identified as the most important variable governing metal adsorption on the adsorbent. The amount of Pb (II) ions adsorbed by coffee grounds increased with the increase in pH from 2.0 to 5.0. The heavy metal-removal capacity increased very sharply with an increase in pH from 3.0 to 5.0. The low metal adsorption at pH 3.0 was attributed to the competition that metal ions face from hydrogen ions for the available adsorption sites. The results showed that pH is an important parameter affecting the adsorption of heavy metals. No adsorption of metal ions was observed for pH less than 2.0 according to our research data.

The hydrolysis reactions of divalent metal cations can be represented by the general reaction:

$$M^{2+} + nH_2O \leftrightarrow M(OH)_n^{2-n} + nH^+ \quad (6)$$

However, based on the equilibrium constants, only the first hydrolysis reaction (n=1) is considered significant for lead ions [23]:

$$Pb^{2+} + H_2O \leftrightarrow PbOH^+ + H^+ \quad (7)$$

At pH = 2.0 the percentage removal of Pb (II) was 4.4%. After pH 3.0 the uptake of Pb (II) increased sharply up to pH = 5.0 – Pb uptake increased from 0.255 to 0.845 mg/g. No pH values over 5.0 were studied since precipitation of Pb (II) ions starts. In all cases, the adsorption of Pb (II) ions onto coffee grounds presented higher metal removal percentages than Cu (II). The optimum pH selected was pH = 5.0 both for Cu (II) and Pb (II). According to Dávila Guzmán *et. al.* [11] optimum pH for Cu^{2+} adsorption is 4.5–5.0. Maximum adsorption capacity of adsorbent depends on the initial concentration of metal; due to the low initial concentration, the achieved maximum adsorption capacity was lower than that determined by other researches [11].

Coffee is composed of cellulose and alkaloids such as trigonelline, quinolinic acid, tannic acid,

nicotinic acid, and caffeine [18]. Adsorption mechanism of coffee grounds could be easily explained. In the case of cations (as copper or lead), the possible hypotheses are clear enough. The coffee materials primarily contain weak acidic and basic functional groups. It follows from the theory of acid-base equilibria that at 2.0<pH<7.0 the binding of heavy metal cations is determined primarily by the state of dissociation of the weak acidic groups. Carboxyl groups (–COOH) are the important (but not the only) groups for metal uptake by these materials. At pH = 7, there are lower numbers of competing hydrogen ions and higher numbers of ligands are exposed with negative charges, resulting in higher copper or lead adsorption. The minimal adsorption at low pH may be due to the higher concentration and high mobility of H^+, which are preferentially adsorbed rather than metal ions. Increasing the pH of the solution, the lower number of H^+ (with higher negative surface charge) results in higher copper or lead adsorption [27-30]. Nevertheless, at higher pH values determination of metal sorbed is overvalued because of metal precipitation [36].

This pH value depends on metal concentration in solution. It can be seen that the adsorption percentages are very low in strong acidic medium for the untreated coffee ground. Metal ions are not adsorbed at low pH, opening up the possibility for these adsorbents to be used repeatedly for adsorption of metal ions with stripping in acid solution.

The pH selected as optimum for adsorption experiments was pH = 5, where the adsorbents presented the maximum removal just before the pH-zone of 5.5 where precipitation and hydrolysis phenomena dominate. Desorption of heavy metals could be carried out at low pH values. According to Kyzas [18] the optimum pH found for desorption was pH = 2.0 for Cu (II) [31-35].
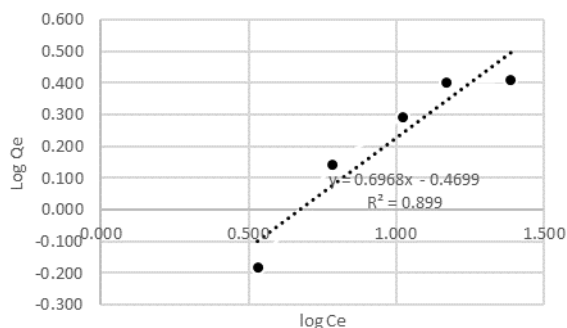
Fig. 5. Freundlich plots for Cu (II) adsorption at pH 5.0 on coffee grounds, adsorbent solution ratio 1:100 w:v, T = 21±1 °C, 720 min contact, Freundlich isotherm parameters: n=1.435, K_F=0.339

Figures 5-8 show the Freundlich and Langmuir adsorption isotherms of Cu(II) and Pb(II), for an initial pH 5, by coffee grounds. The physical parameters for the adsorption of Cu(II) and Pb(II) are determined from the linear Freundlich (Figures 5, 6) and Langmuir isotherms and are tabulated in figures 5, 6, 7 and 8.

Results presented in Figs. 5 and 6 show that the removal rate of Cu(II) and Pb(II) ions can be described with Freundlich isotherm.
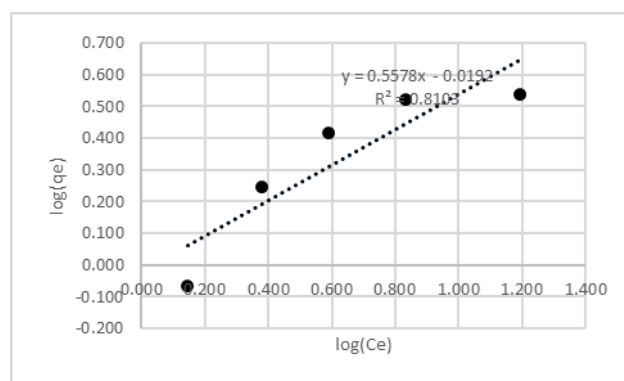
Fig. 6. Freundlich plots for Pb (II) adsorption at pH 5.0 on coffee grounds, adsorbent solution ratio 1:100 w:v, T = 21±1 °C, 720 min contact, Freundlich isotherm parameters: n=1.793, K_F=0.957
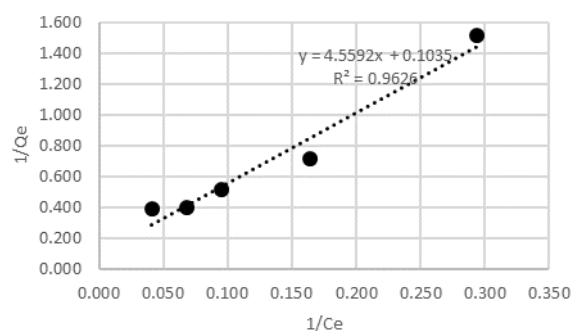
Fig. 7. Langmuir plots for Cu(II) adsorption at pH 5.0 on coffee grounds, adsorbent: solution ratio 1:100 w:v, T = 21±1°C, 720 min contact, Langmuir isotherm parameters: Q_o=9.662, b=0.023.

The values of the Freundlich isotherm parameters as well as the correlation coefficient (R^2) of the Freundlich equations are given in Figs. 5 and 6.

The Freundlich constant, K_F unlike the Langmuir constant, Q_o does not predict the saturation of the solid surface by the monolayer coverage of the adsorbate but it gives a relative measure of the adsorption capacity and estimates bond strength. The value of "n" discloses the adsorption pattern. The favorable adsorption is understood from the values of 1<n < 10 while irreversible adsorption is noticed from n>10 and unfavorable adsorption from n<1. Favorable

adsorption was registered, because n was in the range $1 < n < 10$ in both cases (Cu(II) and Pb(II)). Results presented in Figs. 7 and 8 show that the removal rate of Cu(II) and Pb(II) ions can be described with Langmuir isotherm. The values of the Langmuir isotherm parameters, as well as the correlation coefficient (R^2) of the Langmuir equations are given in Figs. 7 and 8.
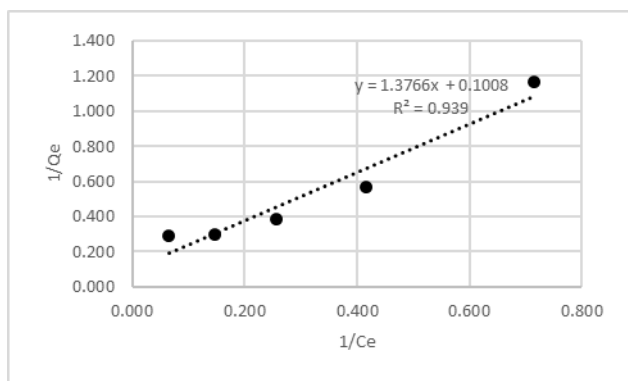
Fig. 8. Langmuir plots for Pb (II) adsorption at pH 5.0 on coffee grounds, adsorbent solution ratio 1:100 w:v, T = 21±1 °C, 720 min contact, Langmuir isotherm parameters: Qo=9.921, b=0.073

The separation factor (R_L) can be used to determine whether or not the adsorption process will be favorable [37]. The parameter predicts that the type of isotherm could to be irreversible (RL=0), favorable ($0 < R_L < 1$) or unfavorable ($R_L > 1$). For the present study, the values of R_L obtained at different initial heavy metal (Cu(II) and Pb(II)) concentrations are presented in Table 2. These values are between zero and one indicating that the adsorption was favorable.

The Langmuir model is an indication of surface homogeneity of the adsorbent.

Table 2. R_L values and type of isotherm

Initial Cu (II) concentration, mg/L	R_L value
10	0.813
20	0.685
30	0.592
40	0.521
50	0.465
Initial Pb (II) concentration, mg/L	R_L value
10	0.578
20	0.407
30	0.313
40	0.255
50	0.215

Even though the comparison of the results obtained shows that the Langmuir equation yielded a higher R^2 value than the Freundlich equation, the closeness of both R^2 values to unity suggests that both equations could readily be used to represent the equilibrium conditions of the system. Therefore, it is assumed that adsorption involves direct contact of metal ions onto the surface of coffee ground and thus proceeds up to monolayer coverage.

Studies have shown (Figs. 1–8) that the efficiency of the adsorption process of copper and lead ions onto coffee grounds depends not only on contact time and concentration, but also on pH of the solution. The remarkable results obtained in this study prompt us to use the coffee waste as an adsorbent for the treatment of wastewater polluted with heavy metals.

CONCLUSIONS

1.   Metal uptake increases with an increase in contact time. On increasing contact time from 15 to 720 min, adsorption efficiency of Cu (II) and Pb (II) increases from 15.30 to 65.7% and from 18.40 to 84.5%, accordingly. The adsorption equilibrium of the investigated metals was achieved in 120 min, when single metal ion concentration in solution was 10 mg/L.

2.   Experimental studies showed that pH of the solution has an impact on adsorption process efficiency. Copper (II) and lead (II) adsorption from aqueous solutions is most effective when the solution is weakly acidic, i.e., pH = 5.0. Maximum adsorption capacity for Cu (II) onto coffee ground was 0.657 mg/g and maximum adsorption capacity for Pb (II) onto coffee ground was 0.845 mg/g, when single metal ion concentration in solution was 10 mg/L.

3.   The sorption of Pb (II) ions onto coffee grounds was by 14–30% better than the adsorption of Cu (II) ions. There are many factors having impact on the efficiency of the adsorption process such as different ion species, polarity and ionic radius.

4.   This study showed that both Freundlich and Langmuir equations can be used to describe the adsorption phenomena for Pb(II) and Cu(II) onto coffee grounds.

REFERENCES

1. O. E. A. Salam, A. N. Reiad, M. M. ElShafei, *J. Adv. Res.,* **2**, 297 (2011).
2. M. E. Argun, S. A. Dursun, *Bioresource Technol.,* **99** (7), 2516 (2008).
3. M. H. Salmani, M. H. Ehrampoush, S. Sheikhalishadi, M. Dehvari, *J. Health Res.,* **1** (1), 11 (2012).
4. R. A. Wuana, F. E. Okieimen, ISRN Ecol., 1, 2011.
5. A. Naudžiūnaitė, Heavy metals migration in diferent soil types profiles, in: Lithuanian: Sunkiųjų metalų

migracija skirtingų tipų dirvožemių profiliuose, Akademija, Kaunas, 2009.

6. N. Zahra, *J. Anal. Environ. Chem.*, **13** (1), 11 (2012).
7. M. Bilal, J. A. Shah, T. Ashfaq, S. M. H. Gardazi, A. A. Tahir, A. Pervez, Q. Mahmood, *J. Hazard. Mater.*, **263**, 322 (2013).
8. S. I. Mussatto, Ballesteros, S. Martins, J. A. Teixeira, *Sep. and Purif. Technol.*, **83**, 173 (2011).
9. N. Azouaou, Z. Sadaoui, A. Djaafri, H. Mokaddem, *J. Hazard. Mater.*, **184** (1), 126 (2010).
10. W. L. Chou, C. T. Wang, K. Y. Huang, Y. C. Chang, C. M. Shu, *Int. J. Phys. Sci.*, **7**, 16, 2445 (2012).
11. N. E. Davila-Guzman, F. J. Cerino-Córdova, J. R. Rangel-Mendez, P. E. Diaz-Flores, AIChE Annual Meeting: Conference Proceedings, 2011.
12. D. Imessaoudene, S. Hanini, A. Bouzidi, *J. Radioanal. Nucl. Chem.*, **298** (2), 893, (2013).
13. X. Liu, D. J. Lee, *Bioresource Technol.*, **160**, 24 (2014).
14. H. B .S. Muhammad, K. B. A. Mohammad, H. Z. Toh, The Singapore Public Service: Integrity, Service, Excellence, 2012.
15. H. D. Utomo, *Nat. Resour.*, **6** (3), 152 (2015).
16. H. Y. Yen, C. P. Lin, *Desalin. Water Treatm.*, **1**, 11154 (2015).
17. H. Y. Yen, S. L. Huang, *Desalin. Water Treatm.*, **1**, 21328 (2015).
18. G. Z. Kyzas, *Mater.*, **5** (10), 1826 (2012).
19. J. Roh, H. N. Umh, C. M. Yoo, S. Rengaraj, B. Lee, Y. Kim, *Korean J. Chem. Eng.*, **29** (7), 903 (2012).
20. K. Shen, M. A. Gondal, *J. Saudi Chem. Soc.*, **1**, 120 (2013).
21. M .Gonçalves, M. C. Guerreiro, P. H. Ramos, L. C. A. de Oliveira, K. Sapag, *Water Sci. Technol.*, **68** (5), 1085 (2013).
22. A. H. Mahvi, D. Nagipour, F. Vaezi, S. Nazmara, *Am. J. Appl. Sci.*, **2** (1), 372 (2005).
23. P. Dalal, *Int. J. Plant, Anim. Environ. Sci.*, **2** (4), 109 (2012).
24. K. Y. Foo, B. H. Hameed, *Chem. Eng. J.*, **156** (1), 2, (2010).
25. M. S. Rajput, A. K. Sharma, S. Sharma, S. Verma, *Int. J. Chem. Sci.*, **3** (1), 9 (2015).
26. A. Dutta, Y. Diao, R. Jain, E. R. Rene, S. Dutta, *J. Environ. Eng.*, 5001 (2015).
27. K. B. Payne, T. M. Abdel-Fattah, *J. Environ. Sci. Health.*, **39** (9), 2275 (2004).
28. G. Z. Kyzas, N. K. Lazaridis, A. C. Mitropoulos, *Chem. Eng. J.*, **189**, 148 (2012).
29. L. Agwaramgbo, N. Lathan, S. Edwards, S. Nunez, *J. Environ. Protect.*, **4**, 741 (2013).
30. N. E. Dávila-Guzmán, F. de Jesús Cerino-Córdova, E. Soto-Regalado, J. R. Rangel-Mendez, P. E. Díaz-Flores, M. T. Garza-Gonzalez, J. A. Clean, *Soil Air Water*, **41** (6), 557 (2013).
31. V. K. Gupta, A. Nayak, S. Agarwal, *Environ. Eng. Res.*, **20** (1), 1 (2015).
32. R. Lafi, A. ben Fradj, A. Hafiane, B. H. Hameed, *Korean J. Chem. Eng.*, **31**, 12, 2198 (2014).
33. W. E. Oliveira, A. S. Franca, L. S. Oliveira, S. D. Rocha, *J. Hazard. Mater.*, **152** (3), 1073 (2008).
34. S. Rafiq, M. K. Ali, M. Sakari, J. Sulaiman, S. M. Yasir, *Int. J. Environ. Bioenerg.*, **7** (2), 91 (2013).
35. F. Barbier, G. Duc, M. Petit-Ramel, *Physicochem. Eng. Asp.*, **166** (1), 3, 153 (2000).
36. M. Minamisawa, H. Minamisawa, S. Yoshida, N. Takai, *J. Agr Food Chem.*, **52** (18), 5606 (2004).
37. F. Aisien, N. Amenaghawon, O. Urhobotie, *J. Eng. Sci. Tech.*, **10** (12) 1641 (2015).

УТАЙКА ОТ КАФЕ КАТО ЕВТИН АДСОРБЕНТ ЗА ОТСТРАНЯВАНЕ НА МЕД (II) И ОЛОВО (II) ОТ ВОДНИ РАЗТВОРИ

Й. Сенюнайте, Р. Вайшкунайте*, Д. Палиулис

Департамент по опазване на околната среда и хидро-инженерство,

Вилнюс Гедиминас технически университет, Саулетекио ал. 11, Вилнюс, Литва, LT-10223

(Резюме)

В настоящата статия е изследвано отстраняването на Cu (II) и Pb (II) от водни разтвори с утайка от кафе от търговски обекти. Утайката е използвана като адсорбент без допълнителна обработка. В експериментите е използвана фракцията с размер на частиците <200 μm. Изследвано е влиянието на pH (2.0, 3.0, 4.0 и 5.0), контактното време (15, 30, 60, 90, 120, 150, 180, 300, 480 и 720 min) и началната концентрация на Cu(II) и Pb(II) (10 mg/L, 20 mg/L, 30 mg/L, 40 mg/L, 50 mg/L). Оптималните стойности на параметрите на процеса са: време на контакт 120-720 min; pH 5.0; начална концентрация на Cu(II) и Pb(II) 20 mg/L. Равновесните данни съответстват на моделите на Langmuir и Freundlich за Pb (II) и Cu (II) с високи R^2 стойности. Установено е, че утайката от кафе е подходящ адсорбент за отстраняване на тежки метали от води.

The selective catalytic reactions for improvement of characteristics of gasolines

L. R. Sassykova[1*], Zh. T. Basheva[2], M. K. Kalykberdyev[2], M. Nurakhmetova[2,3], A. T. Massenova[1,2], K. S. Rakhmetova[2]

[1]al-Farabi Kazakh National University, Almaty, Kazakhstan
[2]D.V.Sokolsky Institute of Fuel, Catalysis & Electrochemistry, Almaty, Kazakhstan
[3]Kazakh-British Technical University, Almaty, Kazakhstan

The aim of the research is the development of selective catalysts for the processes improving service performance of gasolines: catalytic hydrogenation of gasoline fractions and production of octane-increasing component of fuel additives – diisopropyl ether (DIPE). The data on the content of organic compounds in the gasoline fractions after the reaction of catalytic hydrogenation show that benzene was absent, the content of aromatic compounds was reduced from 55.12% (wt.) to 32.5% (wt.). The olefins content was reduced from 0.23% (wt) to 0.11% (wt), and the paraffins content - from 12.41% (wt.) to 11.99% (wt), whereas the iso-paraffins content increased from 30.08% (wt) to 34.09% (wt). The content of naphthenes increased from 2.12% (wt.) to 10.14% (wt.). The developed catalytic method of DIPE synthesis from iso-propanol and propane under mild conditions allowed production at a yield of 30.5-68.5%. The most active and stable catalysts for synthesis of DIPE from iso-propanol are molybdenum- and nickel-containing catalysts. The maximum DIPE yield in the optimal temperature range (250-300 °C) was 62.0-68.5%.
Keywords: catalysts, gasoline, hydrogenation, additives, diisopropyl ether, metal blocks

INTRODUCTION

Today the production of gasolines is one of the major processes in the oil refining industry and largely determines not only the development of the industry, but also the strategic potential of a country [1,2].

Catalytic hydrogenation of straight-run gasoline distillates in the presence of efficient catalysts allows hydrogenation of benzene and polycyclic aromatic hydrocarbons - one of the most perspective and relevant methods of improvement of the operational properties of fuels [3-6]. The increased content of aromatic hydrocarbons, especially bicyclic ones, leads to reduction of speed and completeness of combustion of fuel, promotes carbonizing in the combustion system of the engine and worsens the ecological situation in the world. Thus, the development of highly effective catalysts for catalytic hydrogenation (hydrodearomatization) providing hydrogenation of benzene and polycyclic aromatic hydrocarbons in gasoline fractions improves the composition and ecological characteristics of gasoline - a prospective urgent task. The development of gasoline production is connected with the desire to improve the basic operational properties of the fuel – knock resistance, estimated octane number, as well as reduction of the toxic effects of gasoline, i.e. improvement of the sustainability of the used fuels. Such issues can be solved either by changing the chemical composition (conversion of gasoline compounds) or by application of fuel additives. The use of various fuel additives worldwide allows production of fuels which release minimal amount of nitrogen oxides, carbon oxides, and various organic substances into the atmosphere during combustion and exploitation. Diisopropyl ether (DIPE) is a promising substitute for MTBE due to non-toxicity, lower volatility and lower production costs [7-9]. The aim of this research was to develop catalysts for the two processes that improve the operational properties of gasoline: (1) catalytic hydrogenation of gasoline fractions (hydrodearomatization) and (2) synthesis of octane-enhancing component of additives – DIPE.

EXPERIMENTAL

In the research two types of catalysts were used: in order to study the hydrogenation of the aromatic ring in gasoline fractions supported catalysts based on platinum group metals with additives were synthesized; whereas for DIPE synthesis research catalysts on metal blocks were prepared. Synthesis methodology for both types of catalysts was developed earlier by the authors of this article [10-17]. For the preparation of the supported hydrogenation catalysts the following carriers were used: aluminum oxide γ-Al_2O_3, SiO_2 and activated carbon. The catalysts were prepared by deposition of the respective active metal compounds on the carrier by impregnation. Two-component catalysts (based on Pd-Pt, Rh-Pt, Pd-Rh) were prepared by joint impregnation of the support with the solutions

---

*) To whom all correspondence should be sent:
E-mail: larissa.rav@mail.ru

of the corresponding compounds. For the Pd-Pt samples 2% solution of Na_2CO_3 was also used. The dripping of Na_2CO_3 solution was performed after termination of support impregnation with the solutions of the compounds containing the active component. Before each experiment, the catalysts were reduced in a solvent medium in hydrogen for 30 min in the conditions required for the experiment.

The preparation of the catalysts on the metal blocks for the synthesis of DIPE was conducted according to the methodology comprising several successive steps: (i) preparation of metal blocks, (ii) impregnation of blocks with secondary support (based on aluminum), and (iii) application of active metal compounds on the metal blocks impregnated with a secondary carrier [10-14]. For the preparation of metal blocks a heat-resistant foil of 50 µm thickness and required length and width was used, which was corrugated by folding of the superimposed smooth foil and corrugated tape into a cylindrical block (Figure 1). For the preparation of the catalysts on the metal blocks the corresponding salts of the active metals (acetates, nitrates, etc.) were applied. Catalysts with molybdenum, tungsten, manganese, vanadium, nickel and niobium as the active phase were synthesized using the compounds of the base metals. The metal compounds were applied on the secondary carrier by impregnation of alumina and zeolites NaY, ZSM-5 with different silicate modules (30 and 80). The metal concentrations ranged from 3% to 7 %.

As a method for the synthesis of nano-sized complex-oxide catalysts the pyrolysis of polymer-salt compositions was used. This method is versatile, flexible, simple to implement, and allows production of catalysts with sufficient surface area and adhesion [11, 14, 18-20]. For introduction of the complex-oxide compounds of such metals as vanadium and tungsten, oxygen-containing ammonium salts were used, e.g. tungstic acid, ammonium metavanadate. As polymer components the nonionic water-soluble polymers polyvinyl alcohol, polyethylene glycol, which form stable aqueous solutions with the salt forms, were applied. The metal block carrier was impregnated with the polymer-salt solutions followed by heat treatment. As a result, nanosized particles of vanadium, tungsten and nickel oxides (15-20 nm size) were obtained.

For the qualitative and quantitative analyses of the starting compounds and reaction products the following methods were used: gas-liquid chromatography (GLC), iodometric titration and aniline point method. Chromatographic analysis of the starting compounds and products was carried out by GLC on different devices: "Crystal 2000M" with capillary column Zebron ZB-1 30 ml × 0.53 mm ID × 5.00 µm with 100% dimethylsiloxane liquid phase (gas-carrier – helium, detector – flame-ionization); "Crystal 4000M Lux" with capillary column Zebron ZB-1 30 ml × 0.53 mm ID × 5.00 µm with 100% dimethylsiloxane liquid phase (gas-carrier – helium, detector – flame-ionization), "Chrom-5" with a packed column with a stationary phase of 15% Carbowax-1500, and gas-liquid chromatograph 3700 with a packed column (stationary phase of 15% Carbowax-1500). GLC analysis of the gasoline fractions was conducted according to the standard GOST R 52714-2007 [21, 22]. The total time of GLC analysis was 15-20 min for the DIPE synthesis and 90-120 min for the hydrogenation of gasoline fractions. The determination of octane number was performed by motor and research methods.

RESULTS AND DISCUSSIONS
Hydrogenation of gasoline fractions

The liquid phase hydrogenation of the aromatic ring in gasoline fractions was carried out at elevated pressure of hydrogen on a high-pressure kinetic installation (HPKI) and on a pulp digester – the apparatus for the processes at elevated pressure with heating was from Amar Equipment Ltd [16, 17].

a   b

Fig.1. The metal blocks for the laboratory samples of catalysts: a - perspective view; b - cross-sectional view

The process was carried out in compliance with the isobaric-isothermal mode. The results of experiments on the reduction of hydrocarbons and gasoline fractions were documented in the form of curves in a Cartesian coordinate system, where the horizontal axis represented the duration of the experiment in min (τ), and the vertical axis - the amount of absorbed hydrogen in cm^3.

In this paper the hydrogenation of two gasoline fractions was studied: the stable catalysate LG (benzene content – 0.37%) and straight-run gasoline AVT (benzene content – 3.18%), both obtained from Atyrau Oil Refinery LLP. The reactions were carried out with electrolytic hydrogen from a cylinder (99.8%), whereas, for the GLC helium (99.992%) from a cylinder was used. As the solvents iso-propanol and "reagent grade" hexane were applied.

It was found that during the first minutes of the reactions the hydrogen absorption was much higher on the Rh-Pd and Rh-Pt catalysts than on the catalysts of other composition. The results of the final samples showed that the content of benzene and other aromatics decreased (in total). The hydrogenation of gasoline fractions at various hydrogen pressures on the most active and stable catalyst Rh-Pt (9:1)/Al$_2$O$_3$ was studied. With an increase in hydrogen pressure in the range of 0.5-5.0 MPa the reaction time was reduced by a factor of 2. Benzene content of 0.06% was observed only at a pressure of 3.0 MPa, whereas at other hydrogen pressure levels benzene was absent in the final samples. After the hydrogenation of gasoline fractions the aromatics content in the final samples was within 32.5-34.6%. According to the bilogarithmic dependence of velocity on pressure the reaction order as per hydrogen after absorption of 1.0 mole of hydrogen was close to 1.0.

Tables 1, 2 present data on the hydrogenation of gasoline fractions on different catalysts. Data on quantitative and qualitative composition of the initial gasoline fractions and after hydrogenation are shown. Fig. 2 shows the chromatogram of the initial sample of gasoline stable catalyst LG.

The data on the group composition of organic compounds in gasolines showed (fig.3) that after the catalytic hydrogenation benzene was absent, the aromatics content decreased from 32.5 to 55.12% (wt.), the olefins content - from 0.23 to 0.1 % (wt.), and the paraffins content - from 12.41 to 11.99% (wt.), whereas the content of isoparaffins increased from 30.08 to 34.09% (wt.) and of naphthenes – from 2.12 to 10.14% (wt.).

Table 1. Hydrogenation of gasoline fractions of Atyrau Oil Refinery LLP on various catalysts at P$_{H2}$ = 4.0 MPa, T=25°C in hexane. V$_{gasoline fraction}$ =30.0 ml, V$_{solvent}$=10.0 ml.

Catalyst	Gasoline fraction	Component content, % wt.			
		Benzene		Aromatics (in total)	
		initial sample	after hydrogenation	initial sample	after hydrogenation
2% Rh-Pt/ HY (80)	stable catalysate LG	3.18	0.2	55.12	37.2
	straight-run gasoline AVT	0.37	0.1	9.93	5.25
5% Rh-Pt/Al$_2$O$_3$	stable catalysate LG	3.18	0.0	55.12	32.8
	straight-run gasoline AVT	0.37	0.0	9.93	4.8
2% Pt HZSM-5 (30)	stable catalysate LG	3.18	1.2	55.12	42.0
	straight-run gasoline AVT	0.37	0.0	9.93	5.4
2 % Pt/HZSM-5 (80)	stable catalysate LG	3.18	1.0	55.12	40.9
	straight-run gasoline AVT	0.37	0.05	9.93	5.1
0.5% Rh-Pd/ Al$_2$O$_3$	stable catalysate LG	3.18	1.5	55.12	40.0
	straight-run gasoline VT	0.37	0.2	9.93	6.1
2% Pd-Cu/C	stable catalysate LG	3.18	2.0	55.12	42.0
	straight-run gasoline AVT	0.37	0.3	9.93	6.4

Table 2. Group composition of hydrocarbons in the gasoline fraction stable catalysate LG before and after the hydrogenation on 0.5% Rh-Pt / Al_2O_3

Gasoline fraction	Hydrocarbons content, % wt. / % vol.					
	Paraffins	Iso-paraffins	Olefins	Naphthenes	Aromatics (in total)	Benzene
Before hydrogenation	12.41/14.78	30.08/34.09	0.23/0.25	2.12/2.30	55.12/56.76	3.18/2.78
After hydrogenation	11.99/10.55	34.09/37.45	0.11/0.12	10.14/8.21	32.51/33.47	0/0
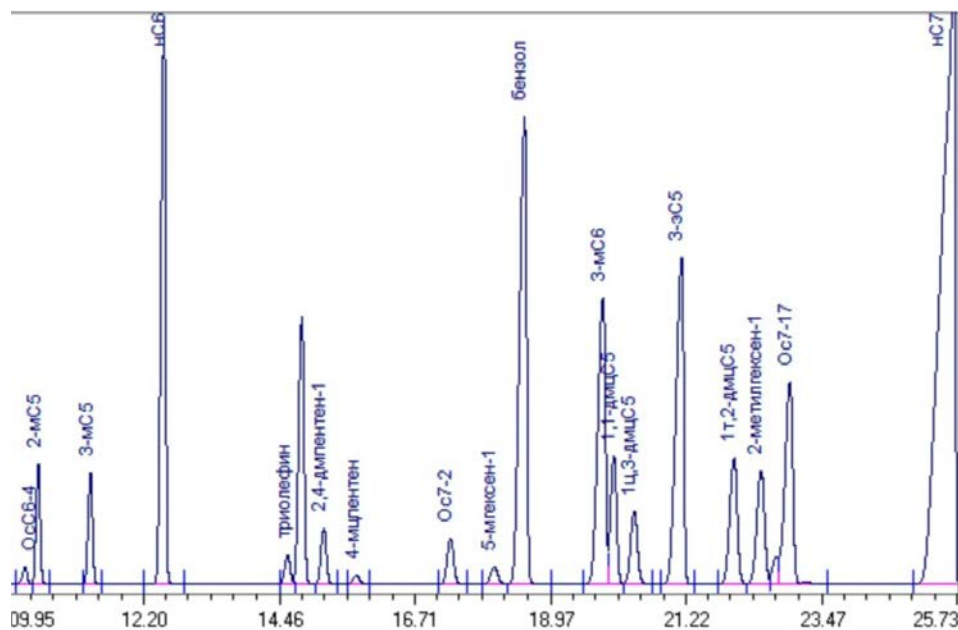
Fig. 2. Chromatogram of initial sample of gasoline stable catalysate LG (a peak of benzene at 18.2)
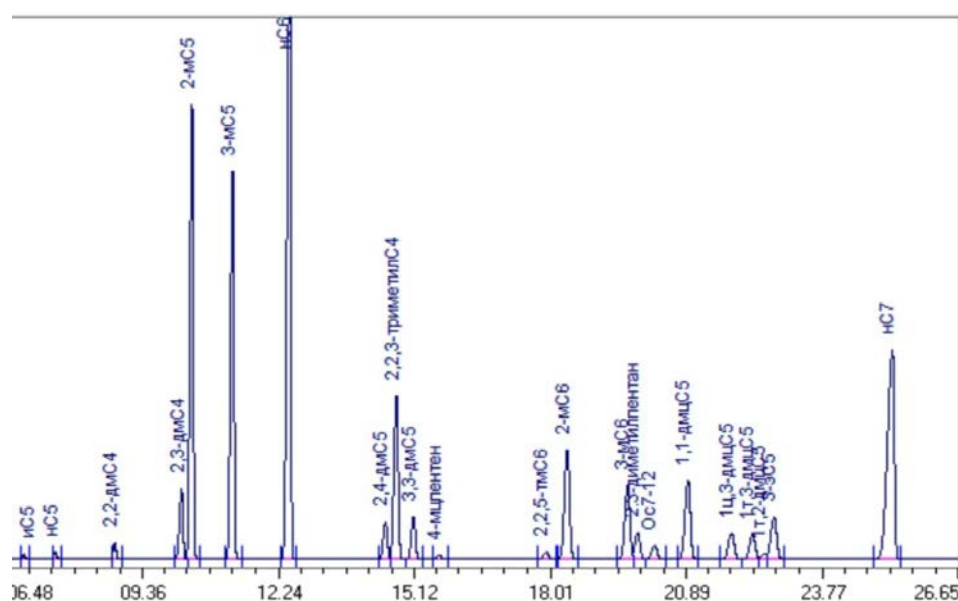
Fig 3. Chromatogram of a sample of gasoline stable catalysate LG after hydrogenation (no peak of benzene)

The octane numbers of the gasoline fractions before and after hydrogenation were determined by the Independent Centre of Expertise of oil products ORGANIC LLP (Almaty, Kazakhstan). The rated octane number of the stable catalysate did not change both before and after the hydrogenation and was equal to 94 units; whereas the motor octane number before the hydrogenation was 82.6 and after – 82.7. The octane number of the straight-run gasoline fraction AVT before and after the experiment was 60, whereas the motor octane number was 50. The octane number data confirmed that the process of hydrodearomatization of gasoline fractions did not reduce their octane number.

DEVELOPMENT OF THE CATALYTIC METHOD FOR DIPE PRODUCTION

The DIPE synthesis reaction from iso-propanol or propane was carried out in a flow-through installation on a metal block catalyst which was placed in a quartz reactor. The reactor with an internal diameter of 10 mm was heated by an electric furnace (Fig. 4). The reactor temperature varied from 150 to 600°C and was measured by a chromel-alumel thermocouple.
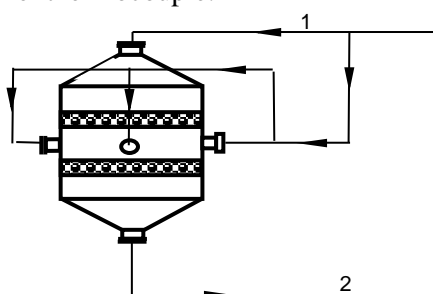
Fig. 4. Scheme of the catalytic reactor P2601 for DIPE synthesis. 1 - initial reagent (iso-propanol); 2 – reaction product (DIPE).

The isopropyl alcohol (or propane from a cylinder) was fed to the reactor via the plunger pump, where the catalyst was placed beforehand. The amount of the metal block catalyst was 3 ml.

The activity of the catalysts in the synthesis of DIPE was determined by iso-propanol (propane) conversion and DIPE yield. The catalytic conversion of isopropyl alcohol into DIPE was examined on various catalysts of various acidity within the temperature range of 150-300°C (Table 3). It was found that the process should be carried out at temperatures not exceeding 300°C, as the catalyst selectivity and DIPE yield decreased because of the formation of a by-product – propylene (Fig.5).

By partial oxidation of propane on the catalyst based on vanadium and molybdenum, WO_3-V_2O_5/Al_2O_3, iso-propanol was formed with a yield of 80-82.1%, and DIPE – 2.5-2.95%. On the WO_3/ZrO_2 catalysts at 300-500°C propanol was formed with a yield of 59.9%-72%. When 0.1% of Pd was added to the WO_3/ZrO_2 catalyst the conversion of propane to DIPE increased to 76.4-80.1% at 500°C.
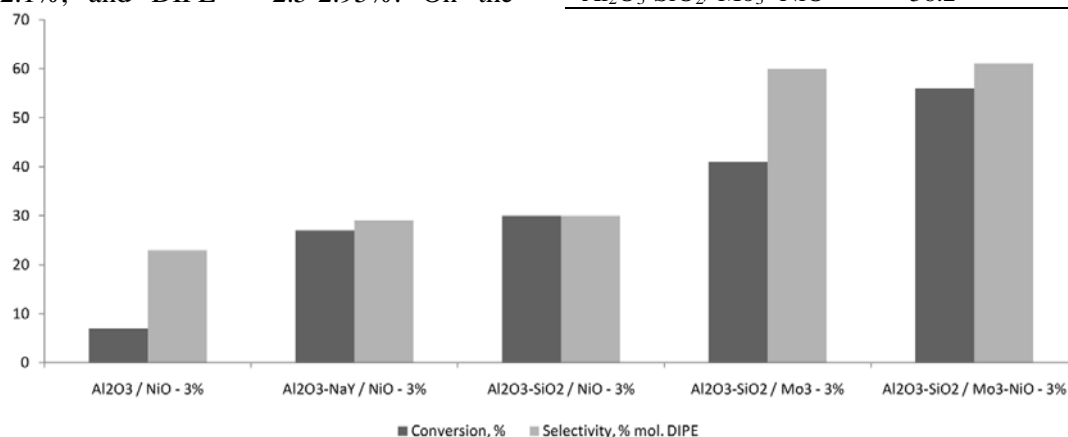
Physical and chemical properties of the synthesized catalysts were determined by various physical and chemical methods of analysis: BET, TPD, electron microscopy (EM), XRD. The analysis of the carriers and catalysts by XRD showed that in case of a catalyst on a metal carrier based on V_2O_5-WO_3 there were peaks at 4.38, 3.4, 2.8Å and orthorhombic lattice. In the active phase no NiO-crystal lattice was formed.

The electron microscopy of the samples was performed on EM-125K by the one-stage replicas method with extraction using microdiffraction (magnification of 160K), as well as on a focused beam microscope Jeol JSM-6610 (Japan). On the nickel-tungsten-vanadium and nickel-copper catalysts on the metal carriers accumulation of solid particles that did not coalesce into aggregates and were dispersed on the carrier surface was observed. The particle size was mainly 20-15 nm. As an example, the results of the scanning electron microscopy analysis of a carrier Al_2O_3 of the catalysts (Fig. 6) and some catalysts applied onto it for the hydrogenation of gasoline fractions are shown (Fig.7). The EM data obtained in this work indicated that the Al_2O_3 carrier structure consisted of needle-like crystalline formations of a size of 200-300Å with specific surface area S = 117.9 m²/g and pore size of 400Å.

Table 3. Synthesis of DIPE on 3%-catalysts of different compositions at 200ºC

Catalyst	Conversion, %	Selectivity, % mol. DIPE
Al_2O_3 / NiO	6.2	24.0
Al_2O_3 -NaY / NiO	26.3	28.2
Al_2O_3-SiO_2/ NiO	29.8	29.7
Al_2O_3-SiO_2/ Mo_3	40.1	60.0
Al_2O_3-SiO_2/ Mo_3- NiO	56.2	60.8

■ Conversion,% ■ Selectivity, % mol. DIPE

Fig.5. Dependence of the activity and selectivity of the catalysts on their composition in the reaction of DIPE synthesis from iso-propanol.
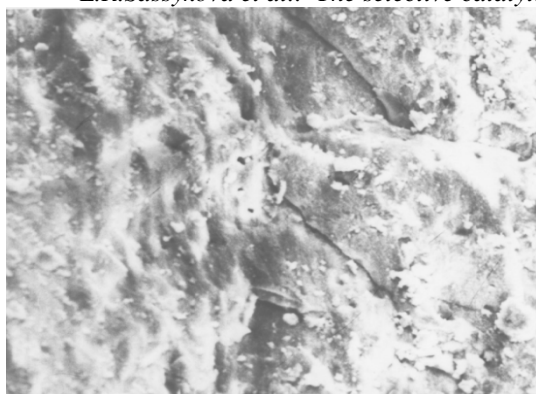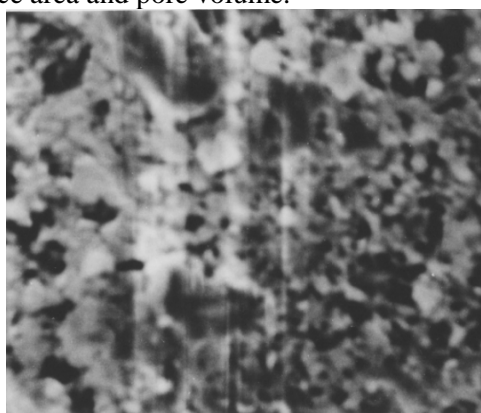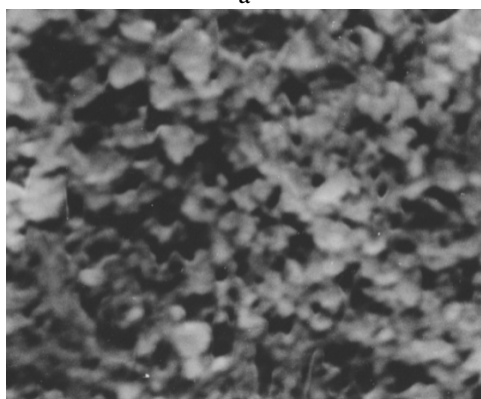
Fig.6. EM image of γ-Al₂O₃

The results of the analyses of the physical and chemical characteristics of the catalysts showed that the synthesized catalysts had a considerable surface area and pore volume.

a

b

Fig.7. EM images of different supported catalysts used for the hydrogenation of gasoline fractions: a - 5% Pd-Pt/γ-Al₂O₃, b - 2%-Pd-Cu/γ-Al₂O₃

The strength and concentration of acid sites of the Ni-Mo catalysts supported on the metal blocks after reaction and regeneration cycles were determined by the method of thermal desorption of ammonia. It was found that with the increase in the duration of the reaction a gradual decrease of catalyst acidity took place, presumably due to the blocking of the active sites by hydrocarbon deposits that resulted in a decrease of their catalytic activity.

CONCLUSION

Catalyst systems for the processes for improving the quality of gasolines were synthesized: for the catalytic hydrogenation of gasoline fractions and the synthesis of octane-enhancing component of additives – diisopropyl ether (DIPE). The data on the group composition of organic compounds in gasolines showed that after the catalytic hydrogenation benzene was absent, the aromatics content decreased from 32.5 to 55.12% (wt.), the olefins content - from 0.23 to 0.1 % (wt.), the paraffins content - from 12.41 to 11.99% (wt.), whereas the content of isoparaffins increased from 30.08 to 34.09% (wt.) and that of naphthenes – from 2.12 to 10.14% (wt.). The octane number of the gasoline fractions after hydrogenation remained almost unchanged, while the benzene content decreased from 3.18 % (starting samples) to total absence in the final samples. It was found that the optimum catalyst composition for the synthesis of DIPE from iso-propanol under the experimental conditions was based on molybdenum and nickel compounds. On the catalysts of the following compositions 3% Al₂O₃/NiO and 3%Al₂O₃-NaY/NiO soot formation was observed, and the activity of the catalysts decreased. DIPE yield within the optimal temperature range (250-300ºC) was 62.0-68.5%.

REFERENCES

1. A.M. Danilov, V.E. Emelyanov, High-octane gasoline: how to do? // http://www.newchemistry.ru
2. V.Ph. Tretyakov, T.N. Burdeynaya, V.A. Matyshak, L.S. Glebov, *Environmental Catalysis: Achievements and Prospects, 17 Mendeleevskii Congress on General and Applied Chemistry*, Kazan, September 21-26, 2003. Abstracts, Kazan, 2003, p. 469.
3. O.V. Yurkina, Y.L. Krayev, *Refining and Petrochemicals*, **11**, 8 (2002).
4. M.I. Temkin, D. Yu. Murzin, N.V. Kul'kova, *Kinetics & Catalysis*, **30** (3), 637 (1989).
5. O.V. Yurkina, Y.L. Krayev, A.V. de Vecchi, *Refining and Petrochemicals*, **1**, 24 (2003).
6. L.B. Galperin, A.P. Fedorov, G.N. Maslyansky, *Chemistry and Technology of Fuels and Oils*, **1**, 42 (1974).
7. A.Y. Rozovskii, G.I. Lin, *Izv.RAN, ser.khim*, **11**, 2352 (2004).
8. C. Sundar Raj, S. Sendilvelan, *International Journal of Automotive and Mechanical Engineering*, **2**, 144 (2010).
9. S. A. Karpov, Features of oxygenates in gasoline, PhD Thesis, Ufa, 2012, p. 46.
10. L.Sassykova, Sh. Gil'mundinov, A. Nalibayeva, I. Bogdanova, *Revue Roumaine de Chimie*, **62(2),** 107-114(2017).
11. Sh.A. Gilmundinov, L.R. Sassykova, A.M. Nalibayeva, *International Symposium on Metastable*

L.R.Sassykova et al.: The selective catalytic reactions for improvement of characteristics of gasolines

and Nano Materials, *ISMANAM*, Greece, Corfu, 2007, p.168.

12. L.R. Sassykova, A.T. Massenova, Sh.A. Gilmundinov, V.N. Bunin, K.S. Rakhmetova, *DGMK*, *Tagungsbericht*, **3**, 181 (2014).

13. L.R. Sassykova, A. Ussenov, A. T. Massenova, Sh. A. Gil'mundinov, K.S. Rakhmetova, V.N. Bunin, Zh.T. Basheva, M.K. Kalykberdiyev, *Int. J. Chem. Sci.*, **14**(1), 206 (2016).

14. L.R. Sassykova, A. Nalibayeva, Sh.A. Gil'mundinov, *Bul. Chem. Comm.*, **49**(3), 583 (2017).

15. D.A. Baiseitov, Sh.E. Gabdrashova, A.N. Magazova, O. Dalelkhanuly, Zh.B. Kudyarova, M.I. Tulepov, L.R. Sassykova, Z.A. Mansurov, *Int. J. Chem. Sci.*, **14**(1), 244 (2016).

16. O.A. Frolova, A.T. Massenova, L.R. Sassykova, Zh.T. Basheva, E. Baytazin, A. Ussenov, *Int. J. Chem. Sci.*, **12**(2), 625 (2014).

17. L.R. Sassykova, M.K. Kalykhberdyev, Zh.T. Basheva, A.T. Massenova, N.A. Zhumabai, K.S. Rakhmetova, *News of National Academy of RK*, series of Chemistry and Technology, 1, 64 (2016).

18. B. Kathirvelu, S. Subramanian, *Environmental Engineering Research*, **22**(3), 294 (2017).

19. S. Sendilvelan, K. Bhaskar, *Oriental Journal of Chemistry*, **33**(4), 2111 (2017).

20. B. Kathirvelu, S. Subramanian, N. Govindan, S. Santhanam, *Sustainable Environment Research*, **27**(6), 283 2017).

21. GOST P 52714-2007, 2007.

22. ASTM D 4057:95, Guide to manual sampling of oil and oil products, 2000.

СЕЛЕКТИВНИ КАТАЛИТИЧНИ РЕАКЦИИ ЗА ПОДОБРЯВАНЕ НА ХАРАКТЕРИСТИКИТЕ НА ГАЗОЛИНИ

Л. Р. Сасикова[1*], Ж. Т. Башева[2], М. К. Каликбердиев[2], М. Нурахметова[2,3], А. Т. Масенова[1,2], К. С. Рахметова[2]

[1] *ал-Фараби Казахски национален университет, Алмати, Казахстан*
[2] *Институт по горива, катализ и електрохимия „Д.В. Соколски", Алмати, Казахстан*
[3] *Казахско-британски технически университет, Алмати, Казахстан*

(Резюме)

Целта на изследването е да се разработят селективни катализатори за процесите, подобряващи действието на газолините: каталитично хидрогениране на газолиновите фракции и получаване на компонент, повишаващ октана в горивните добавки – диизопропилов етер (ДИПЕ). Данните за съдържанието на органични компоненти в газолиновите фракции след каталитично хидрогениране показват отсъствие на бензен, намаляване на съдържанието на ароматни съединения от 55.12% (тегл.) на 32.5% (тегл.), на олефини от 0.23% (тегл.) на 0.11% (тегл.) и на парафини – от 12.41% (тегл.) на 11.99% (тегл.), докато съдържанието на изопарафини се повишава от 30.08% (тегл.) на 34.09% (тегл.) и това на нафтени – от 2.12% (тегл.) на 10.14% (тегл.). Разработеният каталитичен метод за синтез на ДИПЕ от изопропанол или пропан при меки условия позволява получаването на добиви от 30.5-68.5%. Най-активни и стабилни катализатори за синтеза на ДИПЕ от изопропанол са молибден- и никел-съдържащите катализатори. Максималният добив в оптималния температурен интервал (250-300 ℃) е 62.0-68.5%.

Laboratory system for artificial fog generation with controlled number and size distribution of droplets

O. D. Ivanov[1*], Y. I. Ralev[1], P. V. Todorov[1], I. P. Popov[1], K. N. Angelov[1], J. L. Pérez-Díaz[2], M. K. Kuneva[1]

[1] *Georgi Nadjakov Institute of Solid State Physics, Bulgarian Academy of Sciences, 72 Tzarigradsko Chaussee blvd., 1784 Sofia, Bulgaria*

[2] *Universidad de Alcalá, EPS, Campus externo N-II km 33,600, Alcalá de Henares 28805, Spain*

In this article a system for generation of fogs is presented, which can be used in testing equipment and experiments that require control of the amount and size distribution of aerosol particles. The main goal of the system development is to eliminate the human error and to improve the results on producing artificial fog with predictable parameters.

Key words: artificial fog, spraying techniques, droplet size distribution, aerosols

INTRODUCTION

Fog is an aggregation of microscopic water droplets, spread in the air. The average size of natural fog droplets is of about 10-15 µm, but can vary between 1 and 100 µm. According to the droplet size distribution, fogs could be divided in two main groups: composed of relatively small droplets – few microns in diameter (typical for radiation fogs) and composed of bigger droplets – above 45 µm in many cases (typical for advection fog). Fog is widely used as a cleaning agent for contaminated areas in a number of applications: industrial processing, defense, aerospace, automotive, (e.g. corrosion test chambers and salt fog cabinets), power generation, telecommunications, for medical purposes (e.g. nebulizers), etc. These applications require precise control on the amount and properties of the used fog. Further research for gaining the required insight into fog formation and dynamics is needed in order to develop different devices such as fog sensing elements (sensors), etc.

For the development, testing and calibration of fog sensors based on the SPCE (surface photo-charge effect) [1] a specialized installation for producing artificial fog under laboratory conditions is needed. The process of natural fog formation involves a number of physical processes (thermo-dynamic and microphysical ones) which cannot be completely reproduced in a laboratory environment. The main problem in the case of artificial fog generation is to produce droplets of desired amount and size distribution to simulate fogs with parameters close to those of the natural ones. Such setups have been developed in the industry, in cases when different features of spray nozzles had to be investigated [2]. For example, numerous scientific papers exist, in which the variation in the size distribution of droplets was experimentally determined [3-5]. In these studies, the fluid pressure of nozzles and the proportion of fluids were varied [4, 5]. Various methods for fog generation have been reported - vibro-acoustic and acoustic generators for aerosols [6], vortex sprayers [7], pneumatic nozzles [8], electro-sprayers [9], and others. In a number of studies the relationship between the geometrical features of nozzles and the amount and size of the droplets they produce, is analyzed [9-11]. Since the size distribution and the droplets number density are the most important parameters of fog, they play a crucial role in the investigation and the development of fog sensors. Therefore, for the purpose of fog sensors development, a flexible system is needed, which allows to precisely control the number density and the size distribution of the droplets, as well as to be capable of generating droplets with predefined parameters. During our literature and market survey, we could not find any existing system satisfying all our experimental requirements. The main requirements to fog simulator for our sensor tests include: (i) producing fogs with controllable number density and size distribution of droplets and (ii) producing fogs with variable and controllable chemical composition. The second one will be a subject of a separate paper.

---

* To whom all correspondence should be sent.
E-mail: ogi124@yahoo.com

EXPERIMENTAL SETUP OF THE AUTOMATED SYSTEM FOR FOG GENERATION

Since controlling the number density and the diameter distribution of the droplets is the main requirement to a system for producing artificial fog, the first part of the setup designed by us and described here is intended to provide control on these parameters. The main parts of our setup are the fog generation unit (Fig. 1A) and the control unit (Fig.1B).

A

B
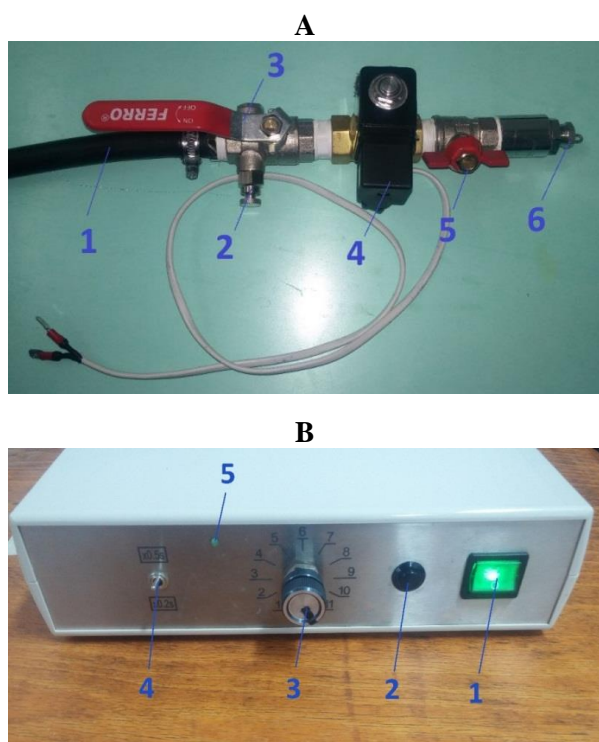
Fig. 1. Main parts of the system for fog generation: **A.** System unit for fog generation working with tap water: (1) hose fluid inlet; (2) bleeding valve; (3) inlet shut-off valve; (4) electromagnetic valve; (5) outlet shut-off valve; (6) nozzle; **B.** Control unit: (1) power button; (2) pulse initiation button; (3) knob for setting the timer (seconds); (4) switch for selection of time multiplier; (5) LED indicator for operation

Fig. 1A shows the water dispensing system of the fog generation unit. The system is fed with tap water through hose (1) and is bled *via* valve (2) when filling. After fixation of the device, taps (3) and (5) are successively opened. The fog generation is accomplished by the valve (6) and by passing a pulse with a specific duration, which comes from the control unit to the electromagnetic valve (4).

The fog generating unit is put in action by the control unit through an electromagnetic valve. The control unit generates uniform pulses with duration

varying from 0.2 to 0.5 seconds, selected by the switch (4) and multiplied by the multiplier (3). When the desired values for the pulse duration are set, button (2) is used to initiate fog generation.

Fig. 2 depicts the block diagram of the experimental setup for measuring the diameters of droplets produced by the system. It is set to the desired position, so that the generated fog falls in the working area of the measuring equipment - a laser particle size analyzer (1). The system uses the pressure from the water dispensing system (5) and - *via* the nozzle (3) - fog with desired characteristics is produced. The control unit (2) sends regular pulses to the electromagnetic valve (4), so that the same amount of water is fed each time.
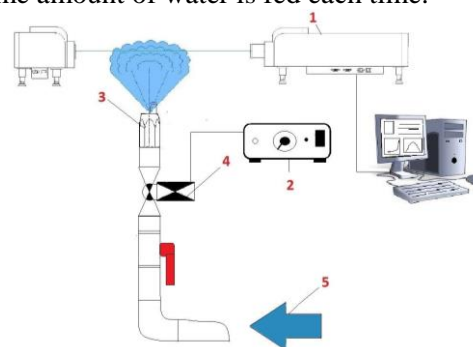
Fig. 2. Block diagram of the experimental setup for measuring the size of droplets generated by the system working with tap water: (1) laser particle size analyzer; (2) control unit; (3) nozzle; (4) electromagnetic valve; (5) source of water at a pressure of 6 bar.

A laser particle size analyzer *(JNWINNER, model 319A)* was used to analyze the droplet distribution and their microphysical characteristics in order to clarify how the nozzle orifice diameter influences the parameters of fog. The nozzle (4) is positioned at a certain distance from the measuring equipment (1).

A manometer and valves were mounted on the pressurized gas tank, which allow to control precisely the feeding pressure of nitrogen, so that fogs with variable characteristics, such as number density and size distribution of the generated fog droplets, to be produced.

EXPERIMENTAL RESULTS ON THE OPERATION OF THE AUTOMATED SYSTEM FOR FOG GENERATION

Since fog depends on the mass flow of pulverized water which is determined by the type of nozzle used, we conducted experiments to examine the effect of nozzles with different orifice diameters on fog formation at a constant gas pressure of 6 bar and by using tap water. The device has a set of eight nozzles [12] and each of them creates fog

with specific parameters (number of droplets, diameter distribution, etc.), so that it is possible different types of fog to be investigated. Three of these nozzles (Fig. 3) were chosen to be studied in this experiment: PJ6 with orifice diameter of 0.152 mm (1); PJ10 with orifice diameter of 0.254 mm (2), and P54 with orifice diameter of 1.37 mm (3). One hundred measurements were taken for each nozzle. The spraying distance was kept constant for all experiments – 65 cm. Fig. 4 represents the amount and diameter distribution of droplets sprayed by nozzles PJ6, PJ10 and P54.

The summarized results from the measurements of the droplets produced by the three nozzles of the system operating with tap water are shown in Table 1 and graphically represented in Fig. 5.

Fig. 3. Three of the tested BETE nozzles (http://www.bete.com/pdfs/BETE_PJ.pdf): PJ6 with orifice diameter of 0.152 mm (1); PJ10 with orifice diameter of 0.254 mm (2), P54 with orifice diameter of 1.37 mm (3).
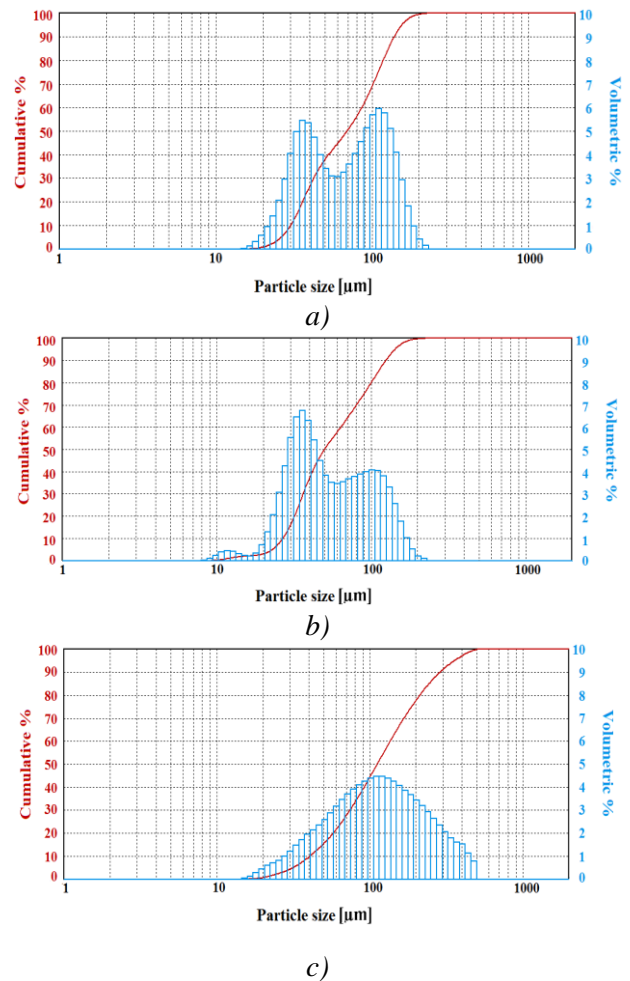
Fig.4. Diameter distribution and amount of droplets produced by a nozzle: a) PJ6; b) PJ10; c) P54

Table 1. Summarized results from measurements of droplets produced by the automated spraying system, and nozzles with varying orifice diameters.

Nozzle	PJ6	PJ10	P54
Modality of the distribution	Bimodal	Multimodal	Monomodal
Peak(s) [µm]	36 110	12 36 100	120
Averaged diameter by surface area [µm]	55.164	44.899	83.298
Averaged diameter by volume [µm]	77.179	64.434	139.791
Surface area-to-volume ratio [cm^2/cm^3]	1087.674	1336.332	720.305
Fit error × 100 [%]	0.006	0.005	0.028
Min. diameter [µm]	16	9	16
Max. diameter [µm]	230	230	500

The experimental results show that the investigated nozzles generate droplets with different size distributions and within different size ranges. 55% of the droplets, produced by nozzle PJ6, have diameters between 60 and 230 µm, and 45% of them are in the range 16-230 µm. Nozzle PJ10 generates droplets, which are predominantly within the same size interval as those produced by PJ6, but also a small amount of tiny droplets between 9 and 20 µm are present.

The other difference is that about 55% of the droplets from nozzle PJ10 are between 20 and 60

91

μm, and only 42% of all generated droplets have diameters between 60 and 230 μm. Nozzle P54, on the other hand, produces significantly larger droplets than the other two nozzles – 55% of them are in the range 100-500 μm, and only 45% are between 16 and 100 μm.

The other difference is that about 55% of the droplets from nozzle PJ10 are between 20 and 60 μm, and only 42% of all generated droplets have

diameters between 60 and 230 μm. Nozzle P54, on the other hand, produces significantly larger droplets than the other two nozzles – 55% of them are in the range 100-500 μm, and only 45% are between 16 and 100 μm.

These results show that the system working with tap water has the capability of generating different kinds of fogs with specific predefined parameters.
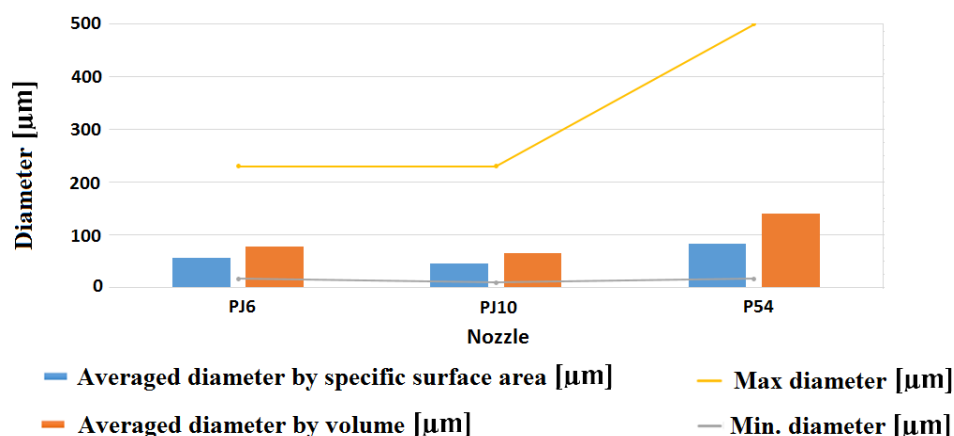
Fig. 5. Summarized results for the diameter distribution and the amount of droplets, generated by the system working with tap water and nozzles PJ6, PJ10 and P54

CONCLUSIONS

A simple, innovative laboratory system for producing artificial fog is designed and described. It allows improved control of water spraying, control of droplet amount and size distribution, stable parameters of the fog. The droplet diameters vary in the range of the real fog ones.

The system was developed for the purpose of eliminating the human factor, when conducting experiments, and also to increase the efficiency of our investigations by achieving high functionality. Our system is able to generate fog with predefined parameters, and it also gives the freedom to precisely control these parameters (amount and diameter distribution of droplets), thus producing fogs with great predictability and repeatability. The established setup can be used in research projects to study different aerosol generators and could also find application in other testing equipments and experiments which require control of the number, density and size distribution of aerosol particles.

REFERENCES

1. N. Vankova, O. Ivanov O, I. Yordanova, *Spectroscopy Letters,* **30** (2), 257 (1997).
2. W. Schäfer, S. Rosenkranz, F. Brinckmann, C. Tropea, *Particuology,* **29** (12), 80 (2016).
3. J. Majewski, *Przegląd Elektrotechniczny,* **89** (3), 300 (2013).
4. M. Ochowiak, *Chemical Engineering and Processing,* **109** (11), 32 (2016).
5. X. Liu, R. Xue, Y. Ruan, L. Chen, X. Zhan, Y. Hou, *Cryogenics,* **83** (4), 59, (2017).
6. W. Yuen, S. Fu, C. Chao, *Journal of Aerosol Science,* **104** (2), 79 (2017).
7. K. Park, S. Heister, *International Journal of Multiphase Flow,* **36** (1), 1 (2010).
8. P. Andreussi, L. Tognotti, M. Graziadio, G. De Michele, *Aerosol Science and Technology,* **13** (1), 35 (1990).
9. O. Lastow, W. Balachandran, *Journal of Electrostatics,* **65** (8), 490 (2007).
10. M. Ochowiak, L. Broniarz-Press, S. Rozanska S, M. Matuszak, S. Wlodarczak, *Chemical Engineering and Processing: Process Intensification,* **98** (12), 52 (2015).
11. M. Altimira, A. Rivas, G. Larraona, R. Anton, J. Ramos, *International Journal of Heat and Fluid Flow,* **30** (2), 339 (2009).
12. http://www.bete.com/pdfs/BETE_PJ.pdf/

ЛАБОРАТОРНА СИСТЕМА ЗА ГЕНЕРИРАНЕ НА ИЗКУСТВЕНА МЪГЛА С КОНТРОЛИРАНИ БРОЙ И ДИАМЕТЪР НА КАПКИТЕ

О. Д. Иванов[1*], Я. И. Ралев[1], П. В. Тодоров[1], Й. П. Попов[1], К. Н. Ангелов[1], Х.Л. Перес-Диас [2], М. К. Кънева[1]

[1] *Институт по физика на твърдото тяло „Акад. Г. Наджаков", Българска академия на науките, бул. „Цариградско шосе" 72, 1784 София, България*
[2]*Университет на Алкала, Алкала де Енарес, Мадрид, Испания*

(Резюме)

Представена е система за генериране на мъгла в лабораторни условия, която може да се използва при експерименти, изискващи контрол върху количеството и разпределението по големина на аерозолни частици. Основната цел на системата е елиминирането на възможна човешка грешка и подобряване на резултатите при получаване на изкуствена мъгла с предварително зададени параметри.

System for generation of fogs with controlled impurities

O. D. Ivanov[1*], Y. I. Ralev[1], P. V. Todorov[1], I. P. Popov[1], J. L. Pérez-Díaz[2], M. K. Kuneva[1]

[1] *Georgi Nadjakov Institute of Solid State Physics, Bulgarian Academy of Sciences, 72 Tzarigradsko Chaussee blvd., 1784 Sofia, Bulgaria*

[2] *Universidad de Alcalá, EPS, Campus externo N-II km 33,600, Alcalá de Henares 28805, Spain*

In this article a system for generation of fogs is presented, which can be used for testing fog sensors under laboratory conditions. Our prototype is able to generate fogs with various chemical composition (up to 6 kinds of fluids), amount, diameters and size distribution of droplets with spraying driven by pulses of different duration (0.2 to 5.5 seconds). Thus, sensors for use in different areas can be tested, for example: control of attacks with CBRN (Chemical, Biological, Radiological, and Nuclear) agents, measurements of industrial pollutants, dust pollution, detection of poisonous gases, etc. The main goal of the system development is to eliminate the human error and to improve the results of producing artificial fog with predictable parameters. An important advantage of this system is that it allows the amount of impurities in fog to be precisely controlled.

Keywords: Artificial fog, Spraying techniques, Droplet size distribution, Air pollution

INTRODUCTION

Fog is a natural phenomenon which is a subject of observation and scientific research. This phenomenon is usually harmless to living organisms, but, when polluted, it could also be dangerous and harmful. In 1952 a dense fog covered London for five days and caused death of 12000 people and thousands of animals in the region due to chemical processes leading to a deadly mix of fog and pollution (sulfur dioxide (SO_2), dust and others) [1,2]. The same events nowadays often occur in China and other locations. According to a recent study [3], environmental pollution was the reason for one of every six premature deaths in the world in 2015 and is killing more people every year than all wars and violence in the world. There are different sources emitting chemicals to the atmosphere and ambient fog could also contain a number of potentially toxic substances [4-6]. Often fog interacts with pollutants physically, chemically or biologically, thus increasing their toxic effect. Water droplets in fog may concentrate soluble toxic air pollutants and, when inhaled, or fall on the skin, droplets deliver very high doses of toxicants. Effects of exposure to chemical pollutants under foggy conditions are of great interest since fog droplets penetrate easily into the lower respiratory tract, especially droplets of less than 10 μm in diameter [7].

Fog is widely used as a cleaning agent for contaminated areas in a number of applications: industrial processes, defense, aerospace, automotive, (e.g. corrosion test chambers and salt fog cabinets), power generation, telecommunications, for medical purposes (e.g. nebulizers), etc. [8]. These applications require precise control of the amount and properties of the used fog. That is why further research in this field is needed in order to gain the required insight into fog formation and dynamics, as well as to develop fog-sensing elements for detection and identification of harmful biological and chemical aerosols in natural fogs being of special interest. Fog studies more often are performed by using theoretical simulations of fog formation through a number of models [9], resulting in slightly overestimated droplet numbers [10]. Theoretical simulations have been also used to predict the chemical behavior of polluted fog [11, 12].

Fog generation technology is currently widely available [13-16] and experimental simulators (test chambers/cabinets) of polluted fog are used in industry for corrosion tests investigation in atmosphere of salt or acidic impurities. However, there is still lack of laboratory simulators of chemically polluted fog.

For development of gas sensors based on the SPCE (surface photo-charge effect) [17, 18] we needed a laboratory fog simulator for their laboratory testing and calibration. Since the size distribution and the number density of droplets are the most important parameters of fog, they play a crucial role in the investigation and the development of fog sensors. That is why we need a flexible system, which produces fogs with controllable/predictable amount and size distribution of droplets, being also able to produce

* To whom all correspondence should be sent.
E-mail: ogi124@yahoo.com

fog with variable and controllable chemical composition. The system should easily switch between different solutions with varying chemical composition, in order to study interactions between fog and different kinds of impurities. During our literature and market survey, we could not find any existing system satisfying all of our experimental requirements. We have already reported the first version of an experimental laboratory system for generation of fog with predictable droplet amount and parameters, working with tap water elsewhere [19]. Here, the second version of the system is presented, which generates fogs with different impurities and varying parameters.

EXPERIMENTAL SETUP OF THE AUTOMATED SYSTEM FOR FOG GENERATION

Figure 1 shows the automated system for fog generation: the pulverizing unit having the ability of simultaneous water and impurity spraying and the pulse control unit, respectively.
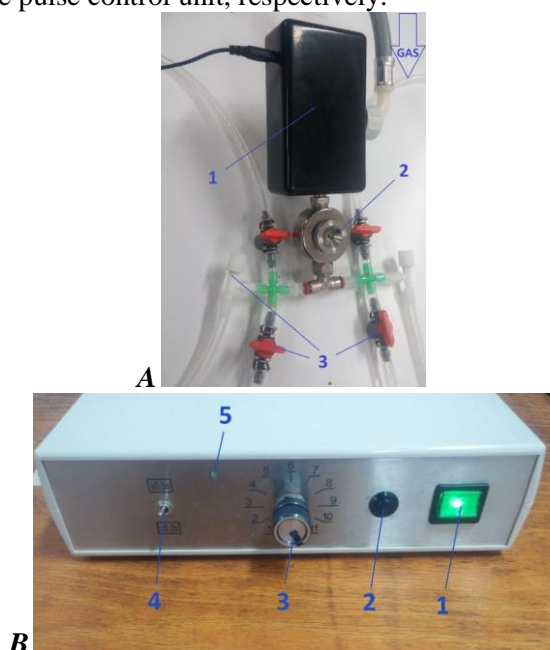
Fig. 1. A. Fog spraying unit: (1) electromagnetic valve; (2) fog generating nozzle (orifice diameter of 0.4 mm); (3) valves; **B.** Control unit: (1) power button; (2) pulse initiation button; (3) knob for setting the timer (seconds); (4) switch for selection of time multiplier; (5) LED indicator for operation

The control unit developed by us was described elsewhere [18]. It generates uniform pulses with duration of 0.2 or 0.5 seconds, selected by the switch (4) and multiplied by the multiplier (3). When the desired values for the pulse duration are set, button (2) is used to initiate fog generation.

Fig. 2 depicts the block diagram of the part of the system intended for generation of fogs with varying chemical composition. Working liquid is atomized by means of a pneumatic atomizing nozzle [19] which works on a siphon principle. The system operates in the following way: pressurized gas (nitrogen) is fed from the tank (5) to the atomizing nozzle (4), which draws water from one of the containers (7) and fogs the working area with the operating liquid. The supply of pressurized gas to the atomizer is regulated by an electromagnetic valve (3). The supply of operating liquid to be fogged (tap or distilled water and contaminating medium) is regulated by corresponding valves (6). Depending on the impurity, which is to be included in the generated fog, the corresponding container is used. The prototype has six branches with six valves, so that switching between different containers can be done easily and quickly. The electromagnetic valve (3) between the source of pressurized gas and atomizing nozzle is controlled by a specially developed pulse generator (2) (shown in Fig. 2) and supplies pressurized gas to the atomizing nozzle in response to an output signal coming from the pulse generator (controller). Different settings can be used, in order to achieve desired durations of fog spraying.
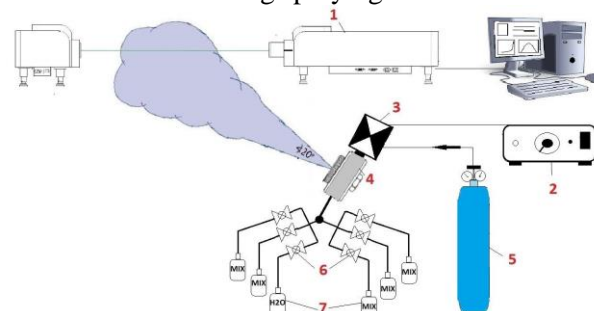
Fig. 2. Block diagram of the automated system for generation of fog with impurities – (1) laser particle size analyzer; (2) spray duration control unit; (3) electromagnetic valve; (4) nozzle; (5) pressurized gas tank; (6) valves; (7) fluid containers

To analyze the distribution and microphysical characteristics of droplets and clarify how the feeding gas pressure influences the parameters of fog, a laser particle size analyzer *(JNWINNER, model 319A)* was used. The nozzle (4) is positioned at a certain distance from the measuring equipment (1). The control unit (2) generates pulses with durations varying from 0.2 to 5.5 seconds, and passes them to the electromagnetic valve (3), so that uniform and identical sprayings can be achieved. As mentioned above, with the aid of the pressurized gas from tank (5) and thanks to the special construction of the nozzle, only the fluid from the chosen container (7) is used. It should be noted that for investigating specific chemical

solutions additional valves (6) are used, which allow convenient sprayings with different duration for each kind of fluid.

A manometer and valves were mounted on the pressurized gas tank, which allow precise control of the feeding pressure of nitrogen, so fogs with variable characteristics, such as number and size distribution of the generated fog droplets, can be produced.

EXPERIMENTAL RESULTS ON THE WORK OF THE AUTOMATED SYSTEM FOR FOG GENERATION

Investigation on fog parameters at different gas pressures

Research on droplets generated by the automated pulverizing system which uses a gas-liquid (nitrogen and distilled water) mixing nozzle, was performed at four different feeding gas pressures of 1, 2, 3, and 4 bar, with nozzle orifice diameter of 0.4 mm. One hundred measurements were taken for each of the four gas pressures. The spraying distance was kept constant for all experiments – 65 cm. The purpose of the study was to find out how the number density and the diameter of the droplets vary with the gas pressure.

Fig. 4 compares the average results for the amount and the diameter distribution of droplets for each gas pressure. The graphs represent the distribution of the diameter of the measured particles – on the X-axis the different sizes are given, so, according to the height of a certain blue bar, the volumetric percentage for the respective size can be detected on the right Y-axis. The red curve, on the other hand, gives information about the percentage of particles, with smaller than each size marked on the X-axis, and its values can be detected on the left Y-axis. The variation of general fog characteristics with atomizing gas pressure can be easily seen in the figure.

Table 1 shows the summarized results from measurements of microphysical characteristics and distribution of droplets generated by the automated system: modality of the distribution (i.e. the number of peaks – monomodal, when there is only one peak in the spectrum; bimodal, when there are two peaks; and multimodal, when there are more than two peaks); the values of the local peaks of the distribution; average diameters, calculated by surface area and by volume; surface area-to-volume ratio; fit error.
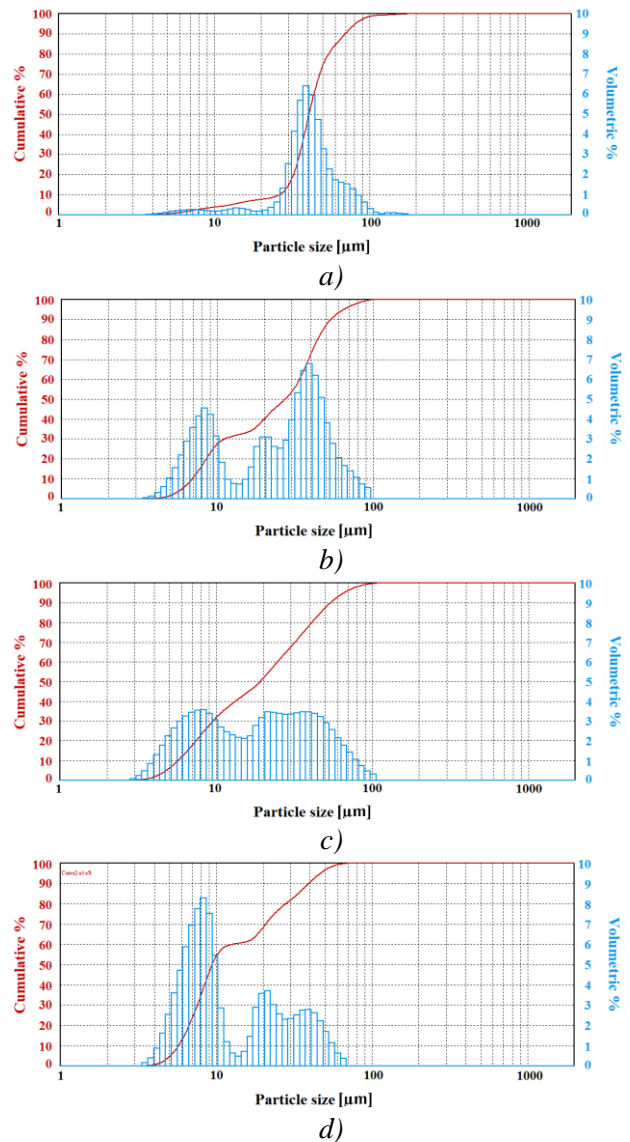
Fig. 3. Diameter distribution and amount of droplets, generated at different gas pressures: a) 1 bar; b) 2 bar; c) 3 bar; d) 4 bar

The summarized results of testing the automated system for fog generation are represented graphically in Fig. 5.

The observed overall tendency is that the values of the average diameters calculated by surface area and by volume decrease with increasing gas pressure. At the highest gas pressure of 4 bar, these values are the lowest. Also, the difference between the maximum and the minimum diameter is the smallest in that case – 65 μm, which means that the width of this diameter distribution is the narrowest one.

The widest size distribution spectrum, on the other hand, is observed at gas pressure of 1 bar, where the difference between the maximum and the minimum diameter is about 170 μm, and the values of the average diameters are highest.

Table 1. Summarized results from measurements of droplets, produced by the automated spraying system at varying gas pressures

Gas pressure [bar]	1	2	3	4
Modality of the distribution	Multimodal	Multimodal	Multimodal	Multimodal
Peak(s) [μm]	7 15 40	8 20 40	8 20 38	8 20 40
Averaged diameter by surface area [μm]	32.867	15.643	12.65	10.103
Averaged diameter by volume [μm]	44.061	28.587	24.806	16.875
Surface area-to-volume ratio [cm^2/cm^3]	1825.552	3835.695	4742.945	5938.751
Fit error ×100 [%]	0.009	0.008	0.010	0.008
Min. diameter [μm]	3.979	3.65	3.071	3.65
Max. diameter [μm]	177.477	96.993	105.737	68.675
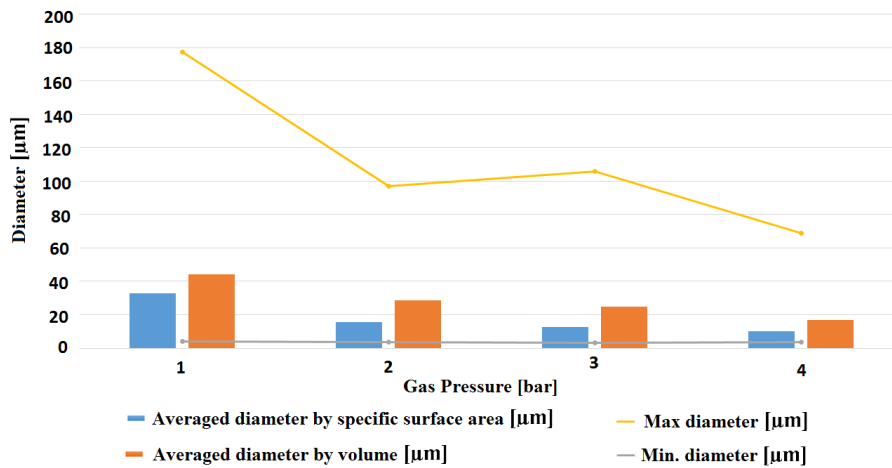
Fig. 4. Summarized results for the minimum and the maximum diameters detected, averaged diameters by specific surface area and by volume, for different gas pressures (1-4 bar), for the automated system for fog generation, at a spraying distance of 65 cm

At gas pressure of 4 bar the automated system produces the smallest droplets and they have similar sizes, while at 1 bar the generated droplets are relatively big, but a small amount of tiny ones is also present. At gas pressures of 2 and 3 bar the size ranges are almost identical, but while at 3 bar the diameter distribution is relatively smooth and the amounts of droplets of different sizes are similar, at pressure of 2 bar only 10% of all droplets have sizes between 10 and 20 μm.

The experimental results for the automated system for fog generation show that the parameters of the produced fog can be precisely controlled, as well as the way they change when varying the gas pressure, fed to the nozzle.

Investigation on fog parameters with added impurities

We have performed tests which show how impurities influence the parameters of fog. Figure 9 compares the change in the number and the diameter distribution of droplets of pure distilled water, when 5% of KH_2PO_4 are added. The droplets were produced by the automated system at gas pressure of 2 bars for both cases and the measurements were taken at 65 cm distance from the nozzle.

There is a notable change in the fog parameters when 5% of KH_2PO_4 are added to distilled water. The percentage of small droplets between 3 and 10 μm increases significantly, while larger droplets (above 80 μm) disappear.

Figure 6 shows the deviation of the sensor's spraying of seven solutions with varying concentrations of tetracycline. One capsule of tetracycline was dissolved in different amounts of distilled water – 400, 200, 100, 80, 60, 40 and 20 ml.

It can be seen from the graph that the increase in the content of tetracycline leads to higher deviations of the signal from our sensor.

CONCLUSIONS

A simple, innovative laboratory simulator of chemically polluted fog is designed and studied. It allows improved control of water spraying, control of droplet amount and size distribution, stable parameters of the fog and introducing different kind of pollutants in it. The fog density and droplet size are in the range of the real fog ones. The system makes possible the production of fogs with great predictability and repeatability. At the same time, impurities with variable concentrations can be

a)

b)
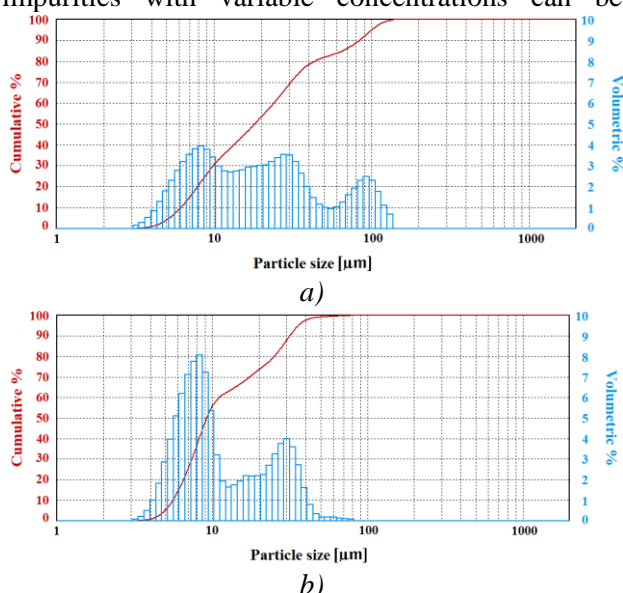
Fig.5. Diameter distribution and amount of droplets of: a) pure distilled water; b) distilled water + 5% KH$_2$PO$_4$.
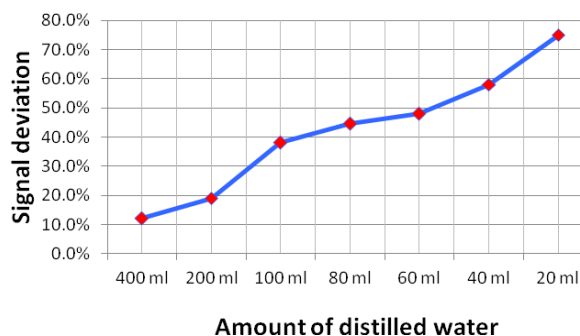
Fig.6. Sensor's signal deviation in response to spraying by fog of distilled water and varying amounts of Tetracycline.

signal from its initial indication after included to the generated fog easily and quickly, thus allowing convenient study of the interactions between fog and different kinds of impurities.

The conducted experiments show that the system functions properly and satisfies all requirements for successful development of fog sensors. Tests in a controlled environment allow precise calibration of sensors, adjustment of their working characteristics and evaluation of their work with different pollutants.

Although the system was developed for testing SPCE-based gas sensors, it can be included in research projects for studying atmospheric chemistry, different aerosol sources, industrial pollutants, chemical and biological weapons and their disposal. The system could also find application in other testing equipments and experiments which require control of the number density, size distribution of aerosol particles and pollutant concentrations.

REFERENCES

1. D. T. Mage, E. M. Donner, *Medical Hypotheses,* **45** *(5),* 481 (1995).
2. J. M. Waldman, J. W. Munger, D. J. Jacob, R. C. Flagan, J. J. Morgan, M. R. Hoffmann, *Science*, **218**, 677 (1982).
3. P. Landrigan et al. (38 nmbs.), *The Lancet*, **390** (10105), 1811 (2017).
4. M. R. Hoffmann, *Environ. Sci. Technol*, **18**, 61 (1984).
5. D. Grosjean, B. Wright, *Atmos. Environ*. **17**, 2093 (1983).
6. P. S. Gill, T. E. Graedel, C. J. Wechslery, *Rev. Geophys. Space Phys*., **21**, 903 (1983).
7. J. D. Hackney, W. S. Linn, E. L. Avol, *Environmental Health Perspectives*, **63**, 57 (1985).
8. P. R. Phipps, I. Gonda, *Chest*, **97** (6), 1327 (1990).
9. Draft for discussion at *DHS/NIST Workshop on Homeland Security Modeling & Simulation*, June 14-15, 16 (2011).
10. J. Rangognio, P. Tulet, T. Bergot, L. Gomes, O. Thouron, M. Leriche, *Atmospheric Chemistry and Physics Discussions*, **9**, 17963 (2009).
11. D. J. Jacob, M. R. Hoffmann, *Journal of Geophysical Research*, **88** (11), 6611 (1983).
12. L. Li, D.-J. Liu, *Int. J. Environ. Res. Public Health*, **11** (9), 8909 (2014).
13. W. Yuen, S. Fu, C. Chao, *Journal of Aerosol Science,* **104** (2), 79 (2017).
14. K. Park, S. Heister, *International Journal of Multiphase Flow,* **36** (1), 1 (2010).

15. P. Andreussi, L. Tognotti, M. Graziadio, G. De Michele, *Aerosol Science and Technology,* **13** 35 (1990).
16. O. Lastow, W. Balachandran, *Journal of Electrostatics,* **65**, 490 (2007).
17. N. Vankova, O. Ivanov O, I. Yordanova, *Spectroscopy Letters,* **30**, 257 (1997).
18. J.L. Pérez-Díaz, M. Kuneva, in *Advances in Biosensors: Reviews, Vol. 1*, S. Y. Yurish (ed.), International Frequency Sensor Association (IFSA) Publishing, S. L., p. 121, 2017
19. O. Ivanov, Y. Ralev, P. Todorov, I. Popov, K. Angelov, J.L. Pérez-Díaz, M. Kuneva, *Bulg. Chem. Commun.*, 2017, in print.
20. https://www.hennlich.hu/fileadmin/user_upload/KATEGORIEN/Pneumatikzerstaeuber_Duesen/Dokumente/en_136.pdf

СИСТЕМА ЗА ГЕНЕРИРАНЕ НА МЪГЛА С КОНТРОЛИРАНИ ПРИМЕСИ

О. Д. Иванов[1*], Я. И. Ралев[1], П. Тодоров[1], Й. П. Попов[1], Х. Л. Перес-Диас[2], М. К. Кънева[1]

[1] *Институт по физика на твърдото тяло „Акад. Г. Наджаков", Българска академия на науките, бул. „Цариградско шосе" 72, 1784 София, България*
[2]*Университет на Алкала, Алкала де Енарес, Мадрид, Испания*

(Резюме)

В статията е представена система за генериране на мъгла, която може да се използва за тестване в лабораторни условия на датчици за мъгла. Нашият прототип може да генерира мъгли с различен химичен състав (до 6 вида флуиди), количество, диаметър и разпределение по размери на капчиците при различна продължителност на импулсите на пулверизиране. С помощта на тази система могат да се тестват сензори за различни цели, като например за проверка при атака с химични, биологични, радиологични или ядрени агенти, за измерване на промишлени замърсявания, замърсяване с прах, детектиране на отровни газове и др. Основна цел на системата е елиминирането на човешката грешка и подобряване на резултатите при получаване на изкуствена мъгла с предварително зададени параметри. Важно предимство на тази система е, че тя позволява прецизен контрол върху количеството примеси, добавяни към мъглата.

HNO₃ immobilized on nano SiO₂: A novel efficient heterogeneous catalytic system for the synthesis of 2-substituted oxazolines, imidazolines, thiazolines, and 2-aryl-1*H*-benzimidazoles under solvent-free conditions

K. Nikoofar*, Sh. Moazzez Dizgarani

Department of Chemistry, Faculty of Physics and Chemistry, Alzahra University, Vanak, Tehran 1993893973, Iran.

HNO₃ immobilized on nano SiO₂ (HNO₃@nano SiO₂) was examined for the synthesis of 2-substituted oxazolines, imidazolines, thiazolines and 2-aryl-1*H*-benzimidazole derivatives under solvent-free conditions. The results confirmed its excellent efficiency in the preparation of the mentioned heterocycles. The method proved to be simple, green, and convenient; the synthesized nanocatalyst was efficient in a vast domain of substrate transformations to the corresponding products in good yields. The recovery and reusability of the synthesized nanocatalyst was investigated in 4 runs without registering activity loss. The mechanism of the transformations is proposed.

INTRODUCTION

In recent years developing new and efficient methods for the synthesis of heterocyclic biologically active natural compounds has received considerable attention in organic chemistry. This importance is due to their wide application in medicine. Oxazolines, imidazolines and thiazolines are important substructures in a large number of biologically active natural products [1,2]. Many derivatives of these heterocycles have shown anti-hypertensive [3], anti-depressive [4], anti-hypercholesterolemic [5], anti-diabetic [6], anti-tumor [7], and anti-inflammatory [8] properties. In addition to these important features, they are also known as valuable intermediates in organic transformations [9]. Several publications have been described for the synthesis of 2-substituted oxazolines, imidazolines and thiazolines from different precursors such as carboxylic acids [10], esters [11], nitriles [12, 13], amides [14], aziridines [15], and aldehydes [16].

Benzimidazole motif plays very important roles in numerous pharmaceutical molecules possessing anti-HIV [17], anti-fungal [18], anti-cancer [19], antihelminthic [20], anticoagulant [21], and proton pump inhibitor properties [22]. Benzimidazoles are a component of vitamin B12 and are related to the DNA base purine and the stimulant caffeine [23]. Methods for synthesis of benzimidazoles include the condensation reaction of *o*-phenylenediamines with aldehyde [24], carboxylic acids [25], and orthoester derivatives [26]. Various reaction conditions and a variety of homogeneous and heterogeneous catalysts such as S/Co(NO₃)₂ [27], sulfuric acid {[3-(3-silicapropyl)sulfanyl]propyl}ester (SASPSPE) [28], zeolite [29], Fe(HSO₄)₃ [30], silica supported tungstosilicic acid [31], trichloroisocyanuric acid (TCCA) [32], and tribromomelamine [33] have also been applied for the preparation of these *N*-containing heterocycles.

A variety of oxidants and catalysts have been used for the synthesis of imidazoline, thiazoline, oxazoline and benzimidazole derivatives. Although these methods worked nicely in many cases, however, some of them suffer from one or more limitations such as low yields, use of volatile or toxic organic solvents, requirement of excess amounts of catalysts or reagents, special apparatus and harsh reaction conditions. Consequently, development of a convenient, high yield environmentally benign procedure for synthesis of imidazoline, thiazoline, oxazolines, and benzimidazoles is still a challenging research.

In continuation of our research interest in nanochemsitry [34-38] in this article we proposed a new protocol for the synthesis of oxazolines, imidazolines and thiazolines *via* the reaction of nitriles with 2-aminoethanol, ethylenediamine, and 2-aminoethanethiol in the presence of catalytic amount of HNO₃@nano SiO₂ under solvent-free conditions. In addition, the preparation of benzimidazoles under solvent-free conditions by the reaction of *o*-phenylenediamines with aldehydes or carboxylic acids in the presence of HNO₃@nano SiO₂ was reported.

RESULTS AND DISCUSSION

The nanocatalyst was synthesized *via* a simple procedure reported by our group [36] and was characterized by FI-IR and SEM techniques. The H⁺

---

*) To whom all correspondence should be sent:
E-mail: kobranikoofar@yahoo.com

Table 1. Optimization the reaction conditions for the synthesis of **3a**.

Entry	Conditions[a]	Yield (%)	Time (h)
1	HNO₃@nano SiO₂ (0.01 g)/ solvent-free/ r.t.	20	12
2	HNO₃@nano SiO₂ (0.01 g)/ solvent-free/ 60 °C	45	7.30'
3	HNO₃@nano SiO₂ (0.01 g)/ solvent-free/ 80 °C	60	5
4	HNO₃@nano SiO₂ (0.01 g)/ solvent-free/ 90 °C	85	2.30'
5	HNO₃@nano SiO₂ (0.01 g)/ solvent-free/ 100 °C	85	2.30'
6	HNO₃@nano SiO₂ (0.01 g)/ H₂O/ reflux	20	12
7	HNO₃@nano SiO₂ (0.01 g)/ CH₃CN/ reflux	_ [b]	12
8	HNO₃@nano SiO₂ (0.01 g)/ EtOH/ reflux	_ [b]	12
9	HNO₃@nano SiO₂ (0.01 g)/ CH₂Cl₂/ reflux	_ [b]	12
10	HNO₃@nano SiO₂ (0.01 g)/ EtOH:H₂O (1:1)/ reflux	_ [b]	12
11	HNO₃@nano SiO₂ (0.01 g)/ CHCl₃/ reflux	_ [b]	12
12	HNO₃@nano SiO₂ (0.01 g)/ CH₃OH/ reflux	_ [b]	12
13	HNO₃@nano SiO₂ (0.008 g)/ solvent-free/ 90 °C	75	3.30'
14	HNO₃@nano SiO₂ (0.012 g)/ solvent-free/ 90 °C	85	2.30'
15	Catalyst-free/ solvent-free/ r.t.	10	24
16	Catalyst-free/ solvent-free/ 90 °C	15	24

[a] The molar ratio of **1a**/ **2a** was 1/1; 5 mL of each solvent was used; [b] The substrates remained intact.

1a: X = CH, R = H
1b: X = CH, R = Me
1c: X = N, R = 1
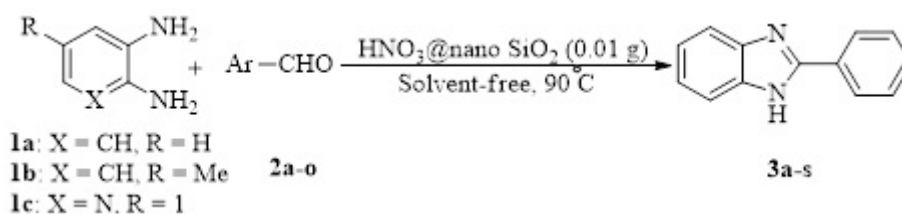
Scheme 1. Synthesis of 2-aryl-1*H*-benzimidazoles by HNO₃@nano SiO₂.
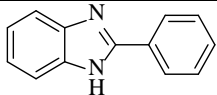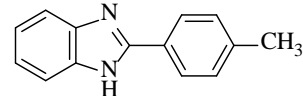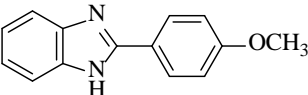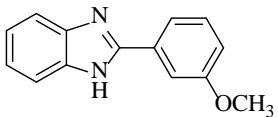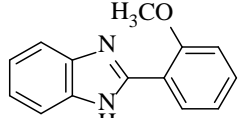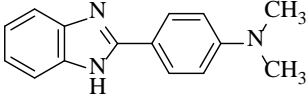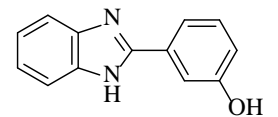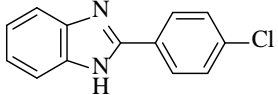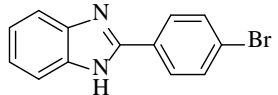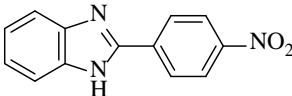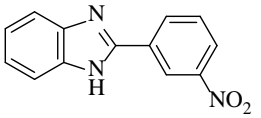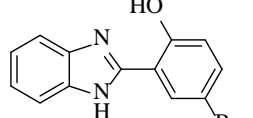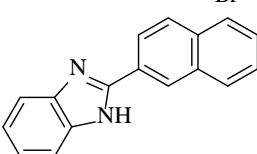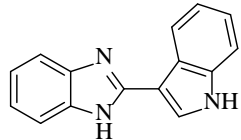
concentration on the surface of the catalyst, which was determined by titration of 0.1 g of the solid with NaOH (0.1 N), was equal to 4.3 meq/g.

To evaluate the catalytic activity of HNO₃@nano SiO₂, the condensation of *o*-phenylenediamine and benzaldehyde to prepare 2-phenyl-1*H*-benz-imidazole was chosen as model reaction (Table 1). Screening the temperature effect in the presence of 0.01 g of the nanocatalyst exhibited that the best results were obtained at 90 °C (entries 1-5). Performing the model reaction in different solvents did not lead to satisfactory results (entries 6-12). Investigating the nanocatalyst amount demonstrated that the best yield was obtained with 0.01 g of the catalyst (entries 4 and 13). Increasing the catalyst amount up to 0.012 g didn't affect the reaction progress (entry 14). In order to confirm the catalyst efficacy in preparation of **3a**, the model reaction was also examined in the absence of nanocatalyst at room temperature and 90 °C with low yields (entries 15,16).

In the next step the reaction of different aldehydes with 1,2-phenylenediamines was performed under the optimal conditions (Scheme 1). The results are summarized in Table 2.

As can be seen in Table 2, the reaction of *o*-phenylenediamine (**1a**) with benzaldehyde and its various electron-donating and electron-withdrawing substituents was performed successfully (entries 1-12). The condensation of **1a** with 2-naphthaldehyde, with a sterically-hindered construction, eventuated to the corresponding benzimidazole **3a** in 71% yield (entry 13). The heteroaromatic massive indole-3-carbaldehyde (**2n**) gave its **3n** analogue in moderate yield (entry 14). Terephthalaldehyde, as a bifunctional aldehyde system, reacted with 2 mmol of **1a** in the presence of 0.02 g of HNO₃@nano SiO₂ to prepare 2-(4-(1*H*-benzimidazol-2-yl)phenyl)-1*H*-benzimidazole. This observation confirmed the selective operation of the nanocatalyst, that no mono-adduct was obtained as by-product. The prosperous condensation of 4-methyl-*o*-phenylenediamine (**2a**) with benzaldehyde and 4-methylbenzaldehyde affirmed the efficacy of the nanocatalyst (entries 16,17). 2,3-Diaminopyridine (**1c**) also generated the corresponding benzimidazoles in the reaction with **2b** and **2h,** respectively (entries 18,19)

Table 2. Synthesis of 2-aryl-1*H*-benzimidazoles using HNO$_3$@nano SiO$_2$ (0.01 g) at 90 °C under solvent-free conditions.

Entry	Diamine	Ar		Product		Time (h)	Yield (%)	M.p., Ref. (°C)[a]
1	**1a**	C$_6$H$_5$	**2a**		**3a**	2.50'	85	285-289, 286-288 [29]
2	**1a**	4-CH$_3$C$_6$H$_4$	**2b**		**3b**	2.30'	86	268-272, 269-273 [39]
3	**1a**	4-OCH$_3$C$_6$H$_4$	**2c**		**3c**	5.10'	75	223-225, 224-225 [39]
4	**1a**	3-OCH$_3$C$_6$H$_4$	**2d**		**3d**	4.30'	72	223-227, 223-227 [39]
5	**1a**	2-OCH$_3$C$_6$H$_4$	**2e**		**3e**	4.10'	65	133-135, 133-135 [30]
6	**1a**	4-N(CH$_3$)$_2$C$_6$H$_4$	**2f**		**3f**	3.15'	84	292-294, 288-290 [40]
7	**1a**	3-OHC$_6$H$_4$	**2g**		**3g**	3.15'	74	273-275, 277 [41]
8	**1a**	4-ClC$_6$H$_4$	**2h**		**3h**	2.45'	83	283-285, 284-286 [29]
9	**1a**	4-BrC$_6$H$_4$	**2i**		**3i**	3.20'	77	282-285, 283-284 [29]
10	**1a**	4-NO$_2$C$_6$H$_4$	**2j**		**3j**	5.55'	75	318, 317 [41]
11	**1a**	3-NO$_2$C$_6$H$_4$	**2k**		**3k**	5.25'	60	206-207, 207-208 [29]
12	**1a**	2-OH-5-BrC$_6$H$_3$	**2l**		**3l**	2.20'	88	255-257, 256-257 [29]
13	**1a**	2-Naphthyl	**2m**		**3m**	3.30'	71	217-219, 218-219 [42]
14	**1a**	3-Indolyl	**2n**		**3n**	4.20'	69	195–197, 196-198 [24]

15	**1a**	Terephthalyl	**2o**		**3o**	4.20'	67	245-246, 245-247 [43]
16	**1b**	C_6H_5	**2a**		**3p**	3.10'	89	239-241, 240-242 [39]
17	**1b**	$4\text{-}CH_3C_6H_4$	**2b**		**3q**	2.55'	80	101-103, 100-104 [39]
18	**1c**	$4\text{-}CH_3C_6H_4$	**2b**		**3r**	2.15'	86	243-247
19	**1c**	$4\text{-}ClC_6H_4$	**2h**		**3s**	3.25'	75	260-264

[a] Reference of known compounds; [b] The reaction was performed with **1a** (2 mmol) and HNO₃@nano SiO₂ (0.02 g).
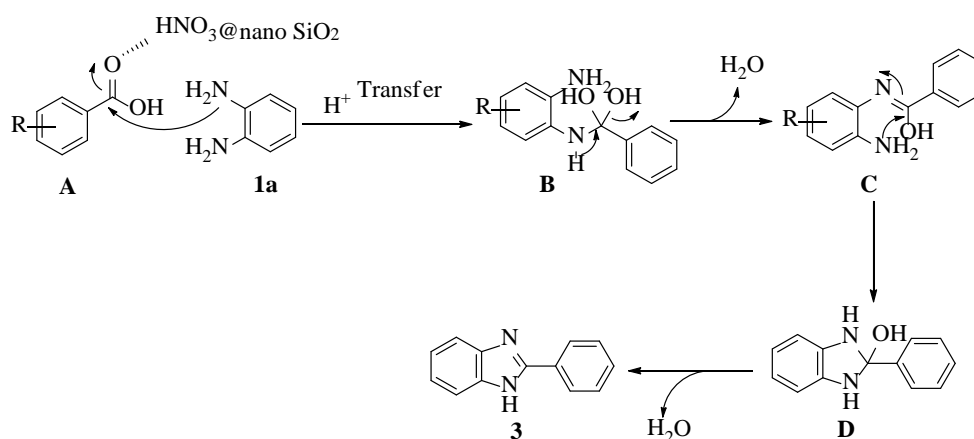
Scheme 2. Plausible mechanism for the synthesis of 2-aryl-1*H*-benzoimidazoles using HNO₃@nano SiO₂.

In order to investigate the high efficacy of the nanocatalyst, in the next step the benzimidazoles were obtained *via* the reaction of *o*-phenylenediamine and carboxylic acids in the presence of 0.02 g of HNO₃@nano SiO₂ at 100 °C under solvent-free conditions. Results are summarized at Table 3. Different types of organic benzoic acids condensed with *o*-phenylenediamine (entries 1-8). Acetic acid as an aliphatic candidate also successfully created the 2-methyl-1*H*-benzimidazole (**3v**) (entry 9). No significant substituent effect was observed. According to the data, the electron-donating substituents at para-position of benzoic acid, such as 4-methyl, 4-methoxy, and 4-hydroxy substituents carried out the condensation better than benzoic acid (entries 2-4); while the electron-withdrawing 4-nitrobenzoic acid performed the reaction in a longer period than benzoic acid (entry 6). Comparison of data in Tables 2 and 3, demonstrated that aldehydes are better candidates than carboxylic acids in the condensation with diamines.

Although the real reaction route is not obvious, a plausible mechanism for the synthesis of 2-aryl-1*H*-benzimidazoles was proposed *via* the condensation reaction of *o*-phenylenediamine with carboxylic acids in the presence of HNO₃@nano SiO₂ (Scheme 2). The nucleophilic attack of *o*-phenylenediamine (**1a**) to activated carboxylic acid **A** produced the intermediate **B**, which by water release gave the imine-alcohol intermediate **C**. The intramolecular Michael addition of the amine group in **C** to C=N bond led to **D** which dehydrated to form the products **3**.

In the next step, to evaluate the best efficiency of the nanocatalyst, we report a simple, efficient and eco-friendly approach for the synthesis of 2-oxazolines, 2-imidazolines, and 2-thiazoline derivatives using HNO₃@nano SiO₂ (Table 4). In each case a model reaction was chosen for screening the best reaction conditions. The results are summarized in Table 4.

Table 3. Synthesis of 2-aryl-1*H*-benzimidazoles *via* the reaction of carboxylic acids with *o*-phenylenediamine in the presence of HNO₃@nano SiO₂ (0.02 g) at 100 °C under solvent-free conditions.

$$\text{1a} \;(\text{o-}C_6H_4(NH_2)_2) \;+\; R-CO_2H \xrightarrow[\text{Solvent-free, 100 °C}]{\text{HNO}_3@\text{nano SiO}_2 \;(0.02\ g)} \;\text{3}$$

4a-i

Entry	R		Product		Yield (%)	Time (h)	M.p., Ref. (°C)[a]
1	C₆H₅	4a	2-phenyl-benzimidazole	3a	75	5	285-289, 286-288 [29]
2	4-CH₃C₆H₄	4b	2-(4-CH₃-phenyl)-benzimidazole	3b	82	4.45'	268-272, 269-273 [39]
3	4-CH₃C₆H₄	4c	2-(4-OCH₃-phenyl)-benzimidazole	3c	78	4.20'	223-225, 224-225 [39]
4	4-OHC₆H₄	4d	2-(4-OH-phenyl)-benzimidazole	3t	81	4.35'	228-230, 229-230 [40]
5	3-OHC₆H₄	4e	2-(3-OH-phenyl)-benzimidazole	3g	73	5.10'	273-275, 277 [41]
6	4-NO₂C₆H₄	4f	2-(4-NO₂-phenyl)-benzimidazole	3j	74	8.10'	318, 317 [41]
7	3-NO₂C₆H₄	4g	2-(3-NO₂-phenyl)-benzimidazole	3k	65	8	206-207, 207-208 [29]
8	2-NO₂C₆H₄	4h	2-(2-NO₂-phenyl)-benzimidazole	3u	67	8.20'	264–265, 264-266 [29]
9	CH₃	4i	2-methyl-benzimidazole	3v	64	9	176–177, 176-178 [44]

[a] Reference of known compounds.

Table 4. Screening the reaction conditions for preparation of 2-phenyl-4,5-dihydro-1*H*-imidazole (**7a**), 2-phenyl-4,5-dihydro-1,3-oxazole (**9a**), and 2-phenyl-4,5-dihydro-1,3-thiazole (**11a**).

A: 5a (PhCN) + 6 (H₂N–CH₂CH₂–NH₂) → 7a (2-phenyl-4,5-dihydroimidazole)
B: 5a (PhCN) + 8 (HO–CH₂CH₂–NH₂) → 9a (2-phenyl-4,5-dihydrooxazole)
C: 5a (PhCN) + 10 (HS–CH₂CH₂–NH₂) → 11a (2-phenyl-4,5-dihydrothiazole)

Entry	Solvent (5 mL)/ HNO₃@nano SiO₂ (g)/ temperature (°C)/ **6** (mmol)	Time (h)	Yield (%)	Solvent (5 mL)/ HNO₃@nano SiO₂ (g)/ temperature (°C)/ **8** (mmol)	Time (h)	Yield (%)	Solvent (5 mL)/ HNO₃@nano SiO₂ (g)/ temperature (°C)/ **10** (mmol)	Time (h)	Yield (%)
1	-/ 0.006/ 100/ 4	4.30'	30	-/ 0.005/ 90/ 6	6.20'	30	-/ 0.005/ 100/ 3.5	4.30'	55
2	-/ 0.012/ 100/ 4	4.20'	60	-/ 0.01/ 90/ 6	5.20'	50	-/ 0.008/ 100/ 3.5	3.30'	70
3	-/ 0.015/ 100/ 4	3.30'	65	-/ 0.02/ 90/ 6	4.50'	60	-/ 0.01/ 100/ 3.5	3	75
4	-/ 0.02/ 100/ 4	3.30'	65	-/ 0.024/ 90/ 6	4	70	-/ 0.012/ 100/ 3.5	3	75
5	-/ 0.015/ r.t./ 4	12	-	-/ 0.02/ r.t./ 6	12	-	-/ 0.01/ r.t./ 3.5	12	-
6	-/ 0.015/ 90/ 4	3.45'	55	-/ 0.02/ 60/ 6	5.10'	50	-/ 0.01/ 80/ 3.5	4	65
8	-/ 0.015/ 110/ 4	3.30'	65	-/ 0.02/ 100/ 6	4	70	-/ 0.01/ 110/ 3.5	3	75
9	H₂O/ 0.015/ reflux/ 4	12	-	H₂O/ 0.02/ reflux/ 6	12	-	H₂O/ 0.01/ reflux/ 3.5	12	-
10	EtOH/ 0.015/ reflux/ 4	12	-	EtOH/ 0.02/ reflux/ 6	12	-	EtOH/ 0.01/ reflux/ 3.5	12	-
11	CH₃CN/ 0.015/ reflux/ 4	12	-	CH₃CN/ 0.02/ reflux/ 6	12	-	CH₃CN/ 0.01/ reflux/ 3.5	12	-
12	-/ 0.015/ 100/ 2	6.10'	52	-/ 0.02/ 90/ 3	6.20'	54	-/ 0.01/ 100/ 3	3.20'	63
13	-/ 0.015/ 100/ 5	3.30'	65	-/ 0.02/ 90/ 7	4	70	-/ 0.01/ 100/ 4	3	70

Various parameters such as catalyst amount, solvent, temperature, and substrates molar ratio was examined. The best results for 2-phenyl-4,5-dihydro-1*H*-imidazole (**7a**) synthesis were obtained in the presence of 0.015 g of nanocatalyst under solvent-free conditions at 100 °C using 4 mmol of ethylenediamine (Table 2, column A, entry 3). 2-Phenyl-4,5-dihydro-1,3-oxazole (**9a**) was prepared using 6 mmol of ethanolamine at 90 °C under solvent-free conditions using 0.02 g of HNO₃@nano SiO₂ (Table 2, column B, entry 3). The data for entry 3 of column C confirmed that 2-phenyl-4,5-dihydro-1,3-thiazole (**11a**) was obtained at 100 °C in the presence of 0.01 g of nanocatalyst under solvent-free conditions *via* the reaction of 3.5 mmol of amino ethanethiol (**10**).

Under these optimized conditions, a variety of aromatic and heteroaromatic nitriles were reacted with ethylenediamine to generate the corresponding 2-imidazolines (Table 5, entries 1-8). According to the data in Table 5, electron-withdrawing nitriles such as 4-chloro and 4-bromo benzonitriles carried out the reaction in shorter duration than electron-donating nitriles such as 4-methyl and 4-methoxy derivatives. 2-Cyanopyridine (**5f**), as a heteroaromatic nitrile, gave the 2-(4,5-dihydro-1*H*-imidazol-2-yl) pyridine very successfully (entry 6). Another interesting observation was with isophthalonitrile (**5g**) where using **5g**/ **6** with the molar ratio 1/ 4 in the presence of 0.015 g of

nanocatalyst gave 3-(4,5-dihydro-1*H*-imidazol-2-yl)benzonitrile as the only product. No bis-cyclization was seen under these conditions.
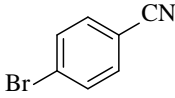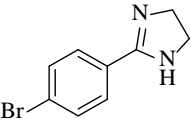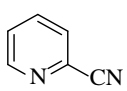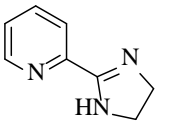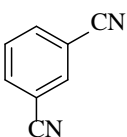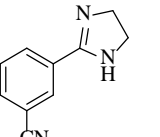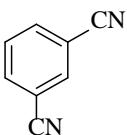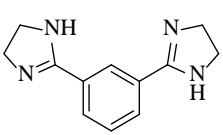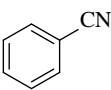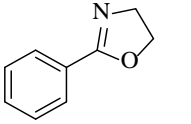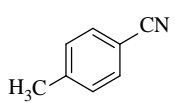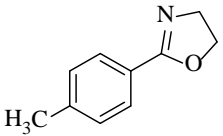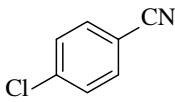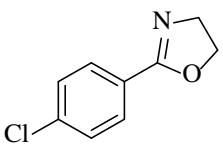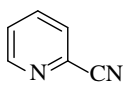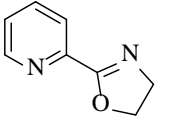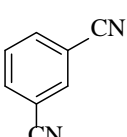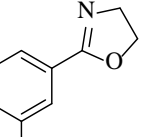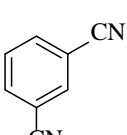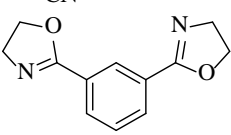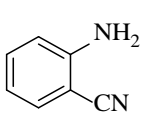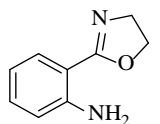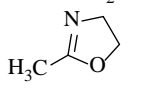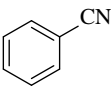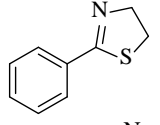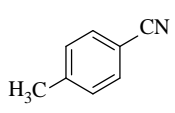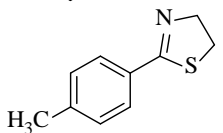
Changing the molar ratio of **5g**/ **6** to 1/8 in the presence of 0.03 g of HNO₃@ nano SiO₂ yielded the 1,3-bis(4,5-dihydro-1*H*-imidazol-2-yl) benzene as the only product. Based on these facts, the chemoselectivity of the procedure was confirmed. Under the optimized reaction conditions different oxazolines and thiazolines were also prepared. Manufacturing of mono- and bis-oxazolines (entries 13 and 14) and bis-thiazoline (entry 23) also validated the chemoselectivity of the procedure. The suggested mechanism for the synthesis of 2-imidazolines, 2-oxazolines, and 2-thiazolines is given in Scheme 3. The nanocatalyst activated the nitrile **5** to form the activated analogue **A**. The nucleophilic attack of **6, 8, 10** to **A** generated **B**. Intramolecular attack of NH₂ to C=N bond gave **C** which released NH₃ to produce the desired products **7, 9** and **11**. In order to show the efficient activity of the nanocatalyst, the reaction of *o*-phenylenediamine and benzaldehyde in a molar ratio of 1/1 was chosen as a model. After completion of the reaction (2.50', Table 2, entry 1), methanol (10 mL) was added to the mixture and the catalyst was filtered. The filtrate was washed with methanol (5 mL). The residue was heated at 100 °C for 30 min and used for another run. The catalyst could be recovered and reused for 4 runs without activity loss (Fig. 3).
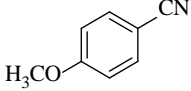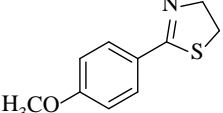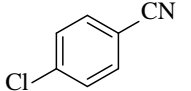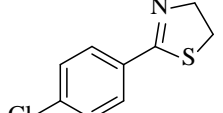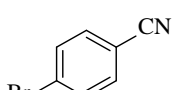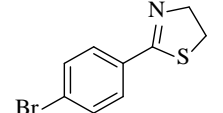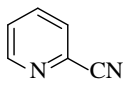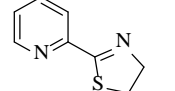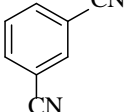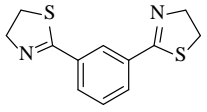
Table 5. Synthesis of imidazolines, oxazolines, and thiazolines in the presence of HNO₃@nano SiO₂.

Entry	Nitrile		Product		Time (h)	Yield (%)	M.p., Ref. (°C)[a]
1	(phenyl-CN)	**5a**	(2-phenyl imidazoline)	**7a**	3.30'	65	100-101, 100-101 [31]
2	(4-methylphenyl-CN)	**5b**	(4-methylphenyl imidazoline)	**7b**	9	67	176-179, 177-179 [31]
3	(4-methoxyphenyl-CN)	**5c**	(4-methoxyphenyl imidazoline)	**7c**	8	65	138-140, 139-140 [31]
4	(4-chlorophenyl-CN)	**5d**	(4-chlorophenyl imidazoline)	**7d**	6.30'	74	187–188, 186–188 [32]

5		5e		7e	4.10'	64	243–245, 242-246 [32]
6		5f		7f	2.50'	84	102-103, 101-102 [31]
7		5g		7g	3.25'	78	132–134, 133–134 [32]
8[b]		5g		7h	4.30'	83	243-244, 242-243 [31]
9		5a		9a	4	70	Oil, Oil [32]
10		5b		9b	9	64	72-73, 71-73 [27]
11		5d		9c	5.45'	69	78-79, 77-79 [32]
12		5f		9d	4.30'	89	67-69, 68-69 [27]
13		5g		9e	4.30'	83	97-100, 98-100 [32]
14[c]		5g		9f	5.30'	74	136-140, 137–139 [32]
15		5h		9g	9.10'	68	52-56, 53-55 [27]
16	CH₃CN	5i		9h	12	57	107-109, 108-109 [45]
17		5a		11a	3	70	126–129, 126-128 [32]
18		5b		11b	10	55	39-41, 40-41 [33]

106

19	H₃CO—C₆H₄—CN	**5c**	thiazoline (H₃CO-phenyl)	**11c**	8	56	52-54, 53-55 [32]
20	Cl—C₆H₄—CN	**5d**	thiazoline (Cl-phenyl)	**11d**	7	70	52–55, 53-55 [32]
21	Br—C₆H₄—CN	**5e**	thiazoline (Br-phenyl)	**11e**	8	75	59-61, 60-62 [32]
22	pyridine-2-CN	**5f**	thiazoline (pyridin-2-yl)	**11f**	8	85	92–93, 92-94 [32]
23[d]	benzene-1,3-dicarbonitrile	**5g**	bis-thiazoline	**11g**	4.45'	80	110-113, 111-113 [32]

[a] Reference of known compounds; [b] Reaction conditions: ethylenediamine (8 mmol) and HNO₃@nano SiO₂ (0.03 g); [c] Reaction conditions: ethanolamine (12 mmol) and HNO₃@nano SiO₂ (0.02 g); [d] Reaction conditions: aminoethanthiol (7 mmol) and HNO₃@nano SiO₂ (0.02 g).
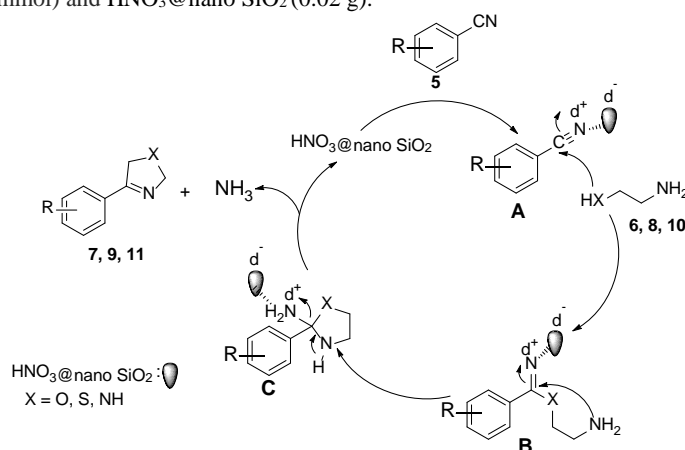
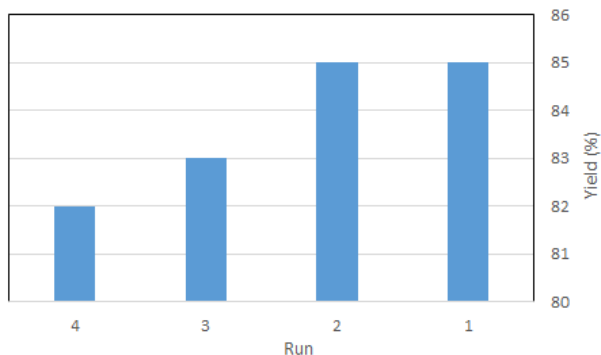**Scheme 3.** Suggested mechanism for the preparation of 2-imidazolines, 2-oxazolines, and 2-thiazolines.

Fig. 3. Recovery and reusability of HNO₃@nano SiO₂ in the reaction of *o*-phenylenediamine and benzaldehyde.

EXPERIMENTAL

Materials and methods

All chemicals were purchased from Merck, Aldrich and Alfa Aesar and were used without further purification. The amorphous nano silica with average particle size of 20-30 nm and specific surface area of 180-270 $m^2 g^{-1}$ was purchased from Tecnan Company. IR spectra were recorded in KBr disks using FT-IR Bruker Tensor 27 instrument. Melting points were determined on a Shimadzu DSC-50 thermal analyzer and are uncorrected. ^{1}H NMR spectra were recorded with a Bruker drx (400 MHz) machine. Elemental analyses were performed using a Thermo-Finnigan Flash EA 1112 Series. Progress of the reaction was monitored by thin layer chromatography (TLC) techniques using commercial available silica gel sheets. Preparative layer chromatography (PLC) was carried out on 20×20 cm^2 plates coated with a 1 mm layer of Merck silica gel PF$_{254}$, by applying the silica as slurry and drying in air. The products were characterized by their melting points, FT-IR, ^{1}H NMR, and CHN analysis.

Preparation of HNO₃@nano SiO₂ [36]

In a round-bottom flask, concentrated HNO₃ (1 mL) was added to a mixture of commercial nano SiO₂ (2.5 g) in 10 mL of dry CHCl₃ and stirred at room temperature for 180 min. CHCl₃ was evaporated at atmospheric pressure and the obtained solid was placed in an oven for 2 h at 100°C to get the HNO₃@nano SiO₂ as pale yellow solid.

General procedure for synthesis of benzimidazoles 3a-s via the reaction of diamines and aldehydes

A mixture of diamines **1a-c** (1 mmol) and aldehydes **2a-o** (1 mmol) in the presence of HNO₃@nano SiO₂ (0.01 g) at 90 °C was stirred for appropriate time (Table 2, 2.15'-5.55'). The progress of the reaction was monitored by TLC. After completion, methanol (10 mL) was added to the mixture. The nanocatalyst was filtered and the filtrate was washed with methanol (5 mL). The crude products were purified by PLC (eluent: *n*-hexane/ethyl acetate, 2/1) to obtain 3a-s in 60-89 %.

General procedure for synthesis of benzimidazoles via the reaction of o-phenylenediamine and carboxylic acids

A mixture of *o*-phenylenediamine (**1a**) (1 mmol) and carboxylic acids **4a-i** (1 mmol) in the presence of HNO₃@nano SiO₂ (0.02g) at 100 °C was stirred for appropriate time (Table 3, 4.20'-9 h). The progress of the reaction was monitored by TLC. After completion, methanol (10 mL) was added to the mixture. The nanocatalyst was filtered and the filtrate was washed with methanol (5 mL). The crude products were purified by PLC (eluent: *n*-hexane/ethyl acetate, 2/1) to obtain the corresponding benzimidazoles in 64-82 %.

General procedure for synthesis of 2-substituted imidazolines 7a-h

A mixture of the nitriles **5a-h** (1 mmol), ethylenediamine (**6**) (4 mmol), and HNO₃@nano SiO₂ (0.015 g) was stirred at 100 °C under solvent-free conditions for appropriate time monitored by TLC (Table 5, 2.50'-9 h). After completion, methanol (10 mL) was added to the mixture. The nanocatalyst was filtered and the filtrate was washed with methanol (5 mL). The crude products were purified by PLC (eluent: *n*-hexane/ethyl acetate, 2/1) to obtain the corresponding imidazolines (Table 5, entries 1-8) in 64-84 %.

General procedure for synthesis of 2-substituted oxazolines 9a-h

A mixture of a nitrile (1 mmol), ethanolamine (**8**) (6 mmol), and HNO₃@nano SiO₂ (0.01 g) was stirred at 90 °C under solvent-free conditions for appropriate time monitored by TLC (Table 5, 4-12 h). After completion, methanol (10 mL) was added to the mixture. The nanocatalyst was filtered and the filtrate was washed with methanol (5 mL). The crude products were purified by PLC (eluent: *n*-hexane/ethyl acetate, 2/1) to obtain the pure products **9a-h** (Table 5, entries 9-16) in 57-89 %.

General procedure for synthesis of 2-substituted thiazolines 11a-g

A mixture of nitriles **5a-g** (1 mmol), aminoethanthiol (**10**) (3.5 mmol), and HNO₃@ nano SiO₂ (0.01 g) was stirred at 100 °C under solvent-free conditions for appropriate time monitored by TLC (Table 5, 3-10 h). After completion, methanol (10 mL) was added to the mixture. The nanocatalyst was filtered and the filtrate was washed with methanol (5 mL). The crude products were purified by PLC (eluent: *n*-hexane/ethyl acetate, 2/1) to obtain the pure products **11a-g** (Table 5, entries 17-23) in 55-85 %.

2-(4-Methylphenyl)-3H-imidazo[4,5-b]pyridine (3r): M.p. 243-247 °C. IR (KBr) v/ cm^{-1} 3444, 3028, 2962, 1698, 1620, 1108, 648. ¹H NMR (DMSO-d_6) δ 2.48 (s, 3H, Me), 7.20 (dd, J = 7.95 Hz, J = 4.76 Hz, 1H), 7.36 (d, J = 8.08 Hz, 2H), 7.74 (d, J = 7.65 Hz, 1H), 7.96 (d, J = 7.84 Hz, 1H), 8.12 (d, J = 8.08 Hz, 2H), 8.29 (d, J = 4.6 Hz, 1H). Anal. calcd. for $C_{13}H_{11}N_3$: C 74.62, H 5.29, N 20.08 %, found: C 74.43, H 5.16, N 19.96 %.

2-(4-Chlorophenyl)-3H-imidazo[4,5-b]pyridine (3s): M.p. 260-264 °C. IR (KBr) v/ cm^{-1} 3469, 1613, 11452, 1082, 766, 672. ¹H NMR (DMSO-d_6) δ 6.56 (dd, J = 7.57 Hz, J 4.94 Hz, 1H), 7.40 (d, J = 7.5 Hz, 1H), 7.56 (d, J = 8.4 Hz, 2H), 7.84 (d, J = 6.05 Hz, 1H), 8.03 (d, J = 8.44 Hz, 2H), 8.69 (br s, 1H). Anal. calcd. for $C_{12}H_8N_3Cl$: C 62.75, H 3.51, N 18.29 %, found: C 62.55, H 3.41, N 18.07 %.

CONCLUSION

In conclusion, in this work we have synthesized a simple nanocatalyst *via* embedding HNO₃ on nano SiO₂ and characterized it by titration, FT-IR, and SEM techniques. Its catalytic activity was examined in the synthesis of benzimidazoles, imidazolines, oxazolines, and thiazolines under solvent-free conditions. The simple work-up procedure, the absence of hazardous and non-green solvents, good yields, mild reaction conditions, chemoselectivity, and recyclability of the catalyst are highlighted features of this new procedure.

REFERENCES

1. B.S. Davidson, *Chem. Rev.*, **93**, 1771 (1993).
2. C. Dardonville, I. Rozas, *Med. Res. Rev.*, **24**, 639 (2004).
3. G.A. Head, S. L. Burke, C.K.S. Chan, *Clin. Exp. Hypertens.*, **19**, 591 (1997).
4. E.S. Vizi, *Med. Res. Rev.*, **6**, 431 (1986).
5. H.Y. Li, S. Drummond, I. Delucca, G.A. Boswell, *Tetrahedron*, 52, 11153 (1996).
6. L. Crane, M. Anastassiadou, S. El Hage, J.L. Stigliani, G. Baziard-Mouysset, M. Payard, J.M. Leger, J.G. Bizot-Espiard, A. Ktorza, D.H. Caignard, P. Renard, *Bioorg. Med. Chem.,* **14**, 7419 (2006).
7. L.T. Vassilev, B.T. Vu, B. Graves, D. Carvajal, F. Podlaski, Z. Filipovic, N. Kong, U. Kammlott, C. Lukacs, C. Klein, N. Fotouhi, E.A. Liu, *Science,* **303**, 844 (2004).
8. M. Ueno, K. Imaizumi, T. Sugita, I. Takata, M. Takeshita, *Int. J. Immunopharmacol.,* **17**, 597 (1995).
9. T.G. Gant, A.I. Meyers, *Tetrahedron*, **50**, 2297 (1994).
10. A. Cwik, Z. Hell, A. Hegedus, Z. Finta, Z. Horvath, *Tetrahedron Lett.*, **43**, 3985 (2002).
11. P. Zhou, J.E. Blubaum, C.T. Burns, N.R. Natale, *Tetrahedron Lett.*, **38**, 7019 (1997).
12. I. Mohammadpoor-Baltork, A.R. Khosropour, S.F. Hojati, *Synlett.*, **18**, 2747 (2005).
13. V. Mirkhani, M. Moghadam, S. Tangestaninejad, H. Kargar, *Tetrahedron Lett.*, 47, 2129 (2006).
14. C.T. Brain, A. Hallett, S.Y. Ko, *Tetrahedron Lett.*, **39**, 127 (1998).
15. M.K. Ghorai, K. Ghosh, K. Das, *Tetrahedron Lett.*, **47**, 5399 (2006).
16. H. Fujioka, K. Murai, O. Kubo, Y. Ohba, Y. Kita, *Tetrahedron,* **63**, 638 (2007).
17. T. Roth, M.L. Morningstar, P.L. Boyer, S.H. Hughes, R.W. Buckheit, C.J. Michejda, *J. Med. Chem.*, **40**, 4199 (1997).
18. J.S. Kim, B. Gatto, Ch.Yu, A. Liu, L.F. Liu, E.J. LaVoie, *J. Med. Chem.,* **39**, 992 (1996).
19. L.I. Kruse, D.L. Ladd, P.B. Harrsch, F.L. McCabe, S.M. Mong, L. Faucette, R. Johnson, *J. Med. Chem.*, **32**, 409 (1989).
20. L. Veerakumari, N. Munuswamy, *Vet. Parasitol.*, **91**, 129 (2000).
21. W.K.R. Mederski, D. Dorsch, S. Anzali, J. Gleitz, B. Cezanne, C. Tsaklakidis, *Bioorg. Med. Chem. Lett.*, **14**, 3763 (2004).
22. C.C. McGowan, T.L. Cover, M.J. Blaser, *Gastroenterol.*, **107**, 1573 (1994).
23. K.L. Brown, *Chem. Rev.,* **105**, 2075 (2005).
24. M.A. Chari, D. Shobha, T. Sasaki, *Tetrahedron Lett.*, **52**, 5577 (2011).
25. S. Salahuddin, M. Shaharyar, A. Mazumder, M.J. Ahsan, *Arab. J. Chem.*, **7**, 418 (2014).
26. B. Karami, Sh. Nikoseresht, S. Khodabakhshi, *Chinese J. Catal.*, **33**, 298 (2012).
27. H. Ge, P. Liu, X. Li, W. Sun, J. Li, B. Yang, Zh. Shi, *Tetrahedron*, **69**, 6591 (2013).
28. N. Iravani, N. Safikhani Mohammadzade, Kh. Niknam, *Chinese Chem. Lett.*, 22, 1151 (2011).
29. A. Mobinikhaledi, N. Foroughifar, M. Zendehdel, M. Jabbarpour, *Synth. React. Inorg.*, **38**, 390 (2008).
30. H. Eshghi, M. Rahimizadeh, A. Shiri, P. Sedaghat, *Bull. Korean Chem. Soc.*, **33**, 515 (2012).
31. M.N-Esfahani, M. Montazerozohori, M. Moghadam, P. Akhlaghi, *ARKIVOC*, **X**, 97 (2010).
32. S.F. Hojati, S.A. Nezhadhosiny, *J. Serb. Chem. Soc.*, **77**, 1181 (2012).
33. L. Wu, *E. J. Chem.,* 9, 1035 (2012).
34. Kh. Ghanbari, K. Nikoofar, *Monatsh. Chem.*, **145**, 1867 (2014).
35. K. Nikoofar, Kh. Ghanbari, *Monatsh. Chem.*, **146**, 2021 (2015).
36. K. Nikoofar, Sh. Moazzez Dizgarani, *J. Suadi Chem. Soc.*, **21**, 787 (2017).
37. K. Nikoofar, S. Gorji, *J. Sulfur Chem.*, **36**, 178 (2015).
38. M. Haghighi, K. Nikoofar, *J. Saudi Chem. Soc.,* **20**, 101 (2016).
39. F. K. Behbahani, A. Lotfi, *Eur. Chem. Bull.*, **2**, 694 (2013).
40. V. Prabhakar, K.S. Babu, L.K. Ravindranath, J. Latha, *World J. Pharm. Phar. Sci.*, 4, 553 (2015).
41. A.T. Khan, T. Parvin, L.H. Choudhury, *Synth. Commun.*, **39**, 2339 (2009).
42. Y. Venkateswarlu, S.R. Kumar, P. Leelavath, *Org. Med. Chem. Lett.*, **3**, 7 (2013).
43. V.A.S. Sontakke, P.P. Ghosh, B.A. Lawande, V.S. Shinde, *Org. Chem.*, 45, 3682 (2013).
44. H. Thakuria, G. Das, *RKIVOC*, **XV**, 321 (2008).
45. Aldrich, Catalog Handbook of Fine Chemicals, 1988-1989. P 1038.

HNO₃ ИМОБИЛИЗИРАНА ВЪРХУ НАНО SIO₂: НОВА ЕФЕКТИВНА ХЕТЕРОГЕННА КАТАЛИТИЧНА СИСТЕМА ЗА СИНТЕЗ НА 2-ЗАМЕСТЕНИ ОКСАЗОЛИНИ, ИМИДАЗОЛИНИ, ТИАЗОЛИНИ И 2-АРИЛ-1*H*-БЕНЗИМИДАЗОЛИ В ОТСЪСТВИЕ НА РАЗТВОРИТЕЛ

К. Никоофар*, Ш. Моазез Дизгарани

Департамент по химия, Факултет по физика и химия, Алзахра университет, Ванак, Техеран 1993893973, Иран

(Резюме)

HNO₃ имобилизирана върху нано SiO₂ (HNO₃@нано SiO₂) е изследвана за синтез на 2-заместени производни на оксазолини, имидазолини, тиазолини и 2-арил-1*H*-безцимидазол в отсъствие на разтворител. Резултатите потвърждават отличната ефективност на катализатора за получаване на споменатите хетероцикли. Доказано е, че синтезираният нанокатализатор е ефективен в широка област от трансформации на субстрата, даващи съответните продукти с добри добиви. Възстановяването и повторната употреба на катализатора са изследвани в 4 цикъла без загуба на активността. Предложен е механизъм на трансформациите.

Effect of LXR agonist T0901317 and miR-33inhibitor on SIRT1-AMPK and circulating HDL-C levels

A. Mohammadi[1,2], H. Fallah[1], B. Shahouzehi[1]*, H. Najafipour[3]

[1]Department of Clinical Biochemistry, Afzalipour School of Medicine & Physiology Research Center, Kerman University of Medical Sciences, Kerman, Iran
[2]Sirjan School of Medical Sciences, Sirjan, Iran

[3]Department of Physiology, Afzalipour School of Medicine & Physiology Research Center, Kerman University of Medical Sciences, Kerman, Iran

Cardiovascular diseases (CVD) are still the leading cause of mortality and morbidity worldwide. Liver X receptors (LXRs) and sterol regulatory element binding proteins (SREBPs) play an important role in lipid homeostasis. LXRs affect SREBPs and promote lipid synthesis and reverse cholesterol transport (RCT). MicroRNA-33 down regulates AMPK, ABCA1 and CPT1 mRNA. Sirt1 also affects LXR and SREBP activity through deacetylation. We assessed the effect of LXR agonist and miR-33 inhibitor on Srebp-2, Sirt1, AMPK expression, and lipid profile. Twenty four mice were divided into four groups (n=6) and the study duration was 7 days. Group I, the control group, did not receive any treatment, group II received 30 mg/kg/48 h LXR agonist (T0901317) through i.p. injection, group III received 1 mg/kg/48 h antagomiR-33 by i.p. injection and group IV received a combination of T0901317 and antagomiR-33. miR-33, AMPK, Sirt1, Srebf-2 and Srebf1c gene expression were quantified by real time PCR, and AMPK, Sirt1 and Srebp-2 protein expression by western blotting. T0901317 administration increased miR-33 and srebf-2 expression. Co-administration of T0901317 and antagomiR-33 reduced srebf-2 and miR-33 levels and increased HDL-c levels. AMPK was reduced in those groups which received T0901317. Sirt1 gene and protein expression remained unchanged. In spite of progress in drug discovery for atherosclerosis and metabolic diseases, these disorders are not fully controlled. It seems that there is a synergistic effect between T0901317 and antagomiR-33 which reduce intracellular sterol levels and increase cholesterol transport to hepatocytes, therefore this can be considered as a therapeutic alternative in atherosclerosis and cardiovascular diseases.

Key words: LXR agonist, miR-33, T0901317, AMP-activated protein kinase

INTRODUCTION

Lipid homeostasis imbalance results in complications such as atherosclerosis, diabetes mellitus and metabolic syndrome [1, 2]. There are networks of genes which orchestrate lipid metabolism; including Sterol Regulatory Element-Binding Factor (SREBF) family, Liver X receptor (LXRs), AMP-activated Protein Kinase (AMPK). Recently, microRNA-33 (miR-33) family also was linked to lipid metabolism regulation [3-6].

MicroRNAs are short, endogenous, non-coding RNAs which emerged as regulators of gene expression and are implicated in many biological processes [7, 8]. MiRNAs bind to their specific mRNA targets in 3' UTR (untranslating region) and cause mRNA degradation or translational inhibition [2]. MicroRNA-33 is located in the intronic region of SREBF family genes. In humans, there are two isoforms of miR-33, miR-33a and miR-33b. miR-33a is located in intron 16 of the SREBF-2 gene and miR-33b is located in intron 17 of the SREBF-1 gene. However there is only one miR-33 isoform in mice which is located within intron 15 of the mouse Srebf-2 gene. MiR-33 is highly conserved and seed sequence of miR-33 family is identical in human and mouse [9-11]. The SREBPs are DNA binding transcription factors and there are two SREBPs, designated as SREBP-1 and SREBP-2. Also, there are two different isoforms of SREBP-1, SREBP-1a and 1c [9, 11]. SREBPs are the regulators of sterol and lipid homeostasis [2]. SREBPs act *via* regulating the expression of many genes involved in cholesterol, lipid and phospholipid metabolism [2, 8]. LXRs consist of two subtypes, LXR-α and LXR-β which are encoded by two separate genes. LXRs are a superfamily of nuclear receptors which control metabolism of glucose, lipid and cholesterol. LXR-α is expressed in tissues such as liver, intestine, kidney, adipose tissue and certain immune cells, while LXR-β is expressed in all tissues [6, 12]. Some of the target genes for LXRs target genes consist of SREBF-1c, SREBF-2, ABCA1, ABCG1, ABCG5 and CYP7A1 (CYP enzyme cholesterol 7α-hydroxylase) [13-17]. LXRs ability to promote SREBP-1c gene expression resulted in FAS

activation and lipogenesis [6]. Also, LXRs are known as cholesterol sensors and are involved in cholesterol transport and metabolism. T0901317 up-regulates SREBP-1c expression, however, data on its effects on SREBP-2 are controversial. LXR activation also affects reverse cholesterol transport (RCT) by elevation of ABCA1 gene expression [6, 17].

Silent mating type information regulation 2 homolog 1 (sirtuin1; SIRT1) is a member of NAD$^+$ dependent histone deacetylase family which regulates the targets by deacetylation. SIRT1 targets include LXRs, SREBP-1c and peroxisome-proliferated activated receptor c co-activator (PGC)-1 α [5, 18]. SIRT1 activates LXR by deacetylation and subsequently LXR promotes SREBF-1c gene expression and elevated lipid synthesis. But SIRT1 also deacetylates the SREBP-1c protein, reduces its activity and inhibits lipogenesis [5]. AMPK enhances NAD$^+$ levels which activates SIRT1 resulting in modulation of downstream SIRT1 targets [4, 5]. AMPK can suppress SREBP-1c gene expression by LXR suppression. SIRT-1 and AMPK signaling increase fatty acid oxidation and suppress lipogenesis. Therefore, SIRT1 and AMPK are intriguing therapeutic targets in treatment of metabolic disease [4].

MiR-33 inhibits HDL synthesis and controls lipids metabolism by targeting AMPK, ABCA1, and ABCG1 [3, 19, 20]. Rayner *et al.* evaluated miR-33 inhibition therapeutic effects on atherosclerosis [21]. Data about LXRs effect on SREBP-2 and co-expression of miR-33 are rudimentary [10, 22-27]. It has been reported that LXR deficient mice showed higher expression of SREBP-2 while other study showed that T0901317, LXR agonist, caused elevation of SREBP-2 expression [23]. In this study, the therapeutic activation of LXR along with inhibition of miR-33 and their impact on SIRT1-AMPK and some other genes and proteins involved in lipid and cholesterol metabolism were assessed.

MATERIALS AND METHODS

Materials

LXR synthetic agonist T0901317 was purchased from Cayman Chemical (71810, Ann Arbor, MI, United States), *in vivo* LNA™ miR-33 inhibitor was purchased from Exiqon (Woburn, MA, United States), miRCURY RNA isolation kit-tissue (300111-Exiqon),miRCURY LNA universal cDNA synthesis kit (203301, Exiqon), LNA PCR primer set for miR-33 (205690, Exiqon), LNA PCR primer set for U6 (203907, Exiqon), ExiLENT SYBR green master mix (203403, Exiqon), EZ-10 Spin column total RNA mini-prep super kit (BS584, Bio Basic Inc., Ontario, Canada), Prime script RT reagent kit (RR037A, Takara Bio Inc., Otsu, Japan), SYBR premix EX taq II Tli RNaseH plus (RR820L, Takara, Otsu, Japan). All antibodies were purchased from Santa Cruz.

Materials description and preparation: LXR agonist T0901317 is hardly soluble in aqueous buffers; therefore, it was dissolved in DMSO and diluted with PBS (pH 7.2) according to the manufacturer's instruction. The *in vivo* LNA™ microRNA inhibitors are designed as short (14-16mer) sequences which easily are taken up with fully modified PS backbone to minimize toxicity. The *in vivo* LNA™ microRNAs-33 inhibitor was dissolved in PBS according to supplier's instruction. Both LXR agonist and the *in vivo* LNA™ microRNA inhibitor were prepared daily and administered by intraperitoneal injection to mice every two days.

Animals: Twenty four male mice weighing 22±2 g were obtained from Kerman Physiology Research Center's Animal Care Center and were fed with standard diet and water *ad libitum*. Mice were housed at a temperature of 22°C, with 12 h light/12 h darkness cycle and allowed 7 days for acclimatization. Mice were randomly divided in 4 groups (n=6) as follows: Group I (control, received chow diet), Group II (LXR agonist, received 30mg/kg T0901317), Group III (anti miR-33, received 1mg/kg LNA miR-33 inhibitor), Group IV (received LXR agonist & LNA miR-33 inhibitor). Mice received 3 intraperitoneal injections of T0901317 or *in vivo* miR-33 LNA inhibitor according to their designated groups every two days in a six-day period (days 1, 3 and 6). At the end of the treatment period (day seventh) and after 10 hours fasting overnight, mice were sacrificed, blood samples were collected and serum was separated. Liver tissue was excised and washed with cold saline and was immediately frozen in liquid nitrogen. Finally, serum and tissues were moved to a -80°C freezer till further examination. All procedures were approved by the Animal Research Ethics Committee of Kerman University of Medical Sciences (Ethic committee permission No IR.KMU.REC. 1394.319).

MicroRNA-33 quantification: In order to quantify miR-33 according to microRNA extraction protocol, about 15 mg of liver tissue was excised and total RNA (including small RNA <200 nt) was extracted by miRCURY RNA isolation kit. First-strand cDNA for microRNAs were synthesized by miRCURY LNA universal cDNA synthesis kit. Synthesized cDNA was diluted 1:80 and 5

μl/reaction were used for real time-PCR as follows: 95°C for 10 min, then 40 cycles of 95°C for 10 s and 60°C for 1 min using ExiLENT SYBR green master mix (Exiqon) by ABI step one plus instrument. Real-time PCR reaction was performed in triplicate. U6 was used as housekeeping gene and values were normalized to U6 [13, 28].

Real-time PCR: about 75 mg of liver tissue was removed from storage and total RNA was extracted using EZ-10 spin column total RNA mini preps super kit (Bio Basic). 250 ng of total RNA was transcribed and cDNA synthesized by Prime Script RT reagent kit for real-time PCR (Takara) using oligo dT primer and random 6mer according to the kit instructions. Real-time PCR reaction (20 μl) contained 2X SYBR Premix Ex Taq II RNaseH plus (Takara), ROX, primers of the target gene, sterile water and cDNA template (100 ng cDNA). Real time PCR was performed on ABI Step One Plus instrument as follows: stage 1 denaturation, 95°C for 10 min, then 40 cycles of 95°C for 20 s and 60°C for 30 s. A melt curve analysis was performed which started from 60°C and increased by 0.3°C increments up to 95°C. Real-time PCR reactions were performed in duplicate. Amplicons of each target gene were examined by agarose gel electrophoresis (2% agarose gel, 90V) in order to confirm the presence of a specific band. Specific primers for target genes were purchased from MACROGEN (MACROGEN Inc., Seoul, South Korea) as listed in Table 1. The expression level was determined by the $2^{-\Delta\Delta Ct}$ method [23, 24].

Western blotting: liver tissue (50 mg) was homogenized on ice-cold protein extraction RIPA buffer (containing protease inhibitor cocktail, 1 mM phenylmethylsulfonyl fluoride [PMSF] and 1 mM sodium orthovanadate, pH 7.4). The homogenate was centrifuged at 15,000 rpm at 4 °C for 20 min and the supernatant was removed for further study. Total protein concentration was determined by the Bradford method. An equal volume of 2× sample buffer was added to each sample and incubated at 95°C for 5 min. 100 μg of proteins were loaded on a 12.5 % SDS-PAGE gel and the separated proteins (120 volts, 80 min) were transferred to a polyvinylidene difluoride (PVDF) membrane. Blocking was performed by overnight incubation of the membrane at 4°C with 5 % skim milk in tris-buffered saline and Tween 20. The membrane was

incubated with primary antibodies (Santa Cruz) in TBST buffer for 1 h, and then washed 4 times for 5 min in TBS-T, followed by incubation with goat-anti-rabbit secondary antibody for 1 h at room temperature. All antibodies were diluted with 2% blocking buffer prepared by TBS-T. The PVDF membrane was incubated with a substrate (Western Lightening Plus ECL, Perkin-Elmer) for 1 min. Antibody–antigen complex was detected using an enhanced chemiluminescence detection film in a dark room. After development, the band densities were analyzed by the ImageJ software. β-Actin immunoblotting was used as a control for loading [29].

Lipid profile: In order to evaluate the lipid profile of mice, total cholesterol, high-density lipoprotein (HDL-c) and triglyceride (TG) levels were measured.

Statistical analysis: Data from real time-PCR, western blotting and serum parameters were expressed as mean ± SEM. Data were analyzed by SPSS v.16 (SPSS Inc., Chicago, IL). In order to compare groups, one-way ANOVA was used and for pair-wise comparison the post hoc Tukey's test was used. P-values ≤ 0.05 were considered as statistically significant.

RESULTS

Real time-PCR analysis showed that miR-33 expression is up-regulated following T0901317 administration (p=0.047). AntagomiR-33 reduced miR-33 and this reduction was attenuated by T0901317 (Fig. 1).
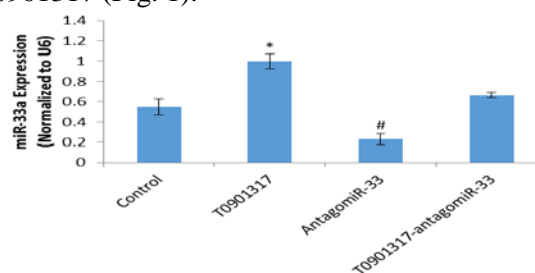

Fig 1. Evaluation of miR-33 expression shown by real-time PCR in liver tissue of 4 groups of mice, I. untreated control group, II. LXR agonist (T0901317), III. antagomiR-33 (miR-33 inhibitor), and IV. combination of T0901317 and antagomiR-33. All data are expressed as mean ± SEM (n = 6 mice/group). * statistically significant compared to the control group, # statistically significant compared to the T0901317 group (p < 0.05 considered as significant).

Table 1. Sequences of real-time PCR primers

Genes name	Forward primer 5' to 3'	Reverse primer 5' to 3'	Product size (bp)
Ampk	CTCAGTTCCTGGAGAAAGATGG	CTGCCGGTTGAGTATCTTCAC	174
Beta-actin	CAACGAGCGGTTCCGATG	GCCACAGGATTCCATACCCA	90
Sirt1	GCAGGTTGCAGGAATCCAA	GGCAAGATGCTGTTGCAAA	80
Srebf-1c	GGAGCCATGGATTGCACATT	GCTTCCAGAGAGGAGGCCAG	190
Srebf-2	CCAAAGAAGGAGAGAGGCGG	CGCCAGACTTGTGCATCTTG	130

Gene expression experiment revealed that T0901317 causes up regulation of Srebf-2, Srebf-1c and sirt1, of those, sirt1 elevation was not significant. Inhibition of miR-33 significantly up regulates AMPK. Interestingly, co-administration of antagomiR-33 and LXR agonist down regulated Srebf-2 expression (Fig. 2). Srebp2 protein levels were reduced by antagomiR-33 and combination of antagomiR-33 and T0901317. AMPK protein levels were upregulated by antagomiR-33 and combination of antagomiR-33 and T0901317 (Fig. 3). T0901317 significantly increased TG levels compared to control group. HDL-c increased in the three other groups compared to control (p=0.01) (Table 2).

DISCUSSION

Cardiometabolic diseases such as atherosclerosis and associated cardiac complications are considered as major public health problems and cardiovascular diseases (CVD) are the leading cause of mortality worldwide.

Even with drugs such as statins, beta blockers, and other medications, the risk of cardiometabolic diseases is still increasing [1, 2]. Therefore, the major goal is finding strategies to reduce the risk of cardiometabolic diseases.

For this reason, the focus is on HDL elevation and improvement of RCT. MiR-33 is located in introne of SREBFs gene family and affects mRNA of target genes [3]. It was documented that miR-33 inhibits Abca1 and AMPK, and as a result potentially reduces serum HDL levels and also RCT [3, 30]. Thus, it seems that miR-33 is a good potential therapeutic target for finding new approaches in order to reduce risk of cardiometabolic diseases. LXR agonists activate LXR and SREBPs as downstream targets of LXRs [23, 31], so they have beneficial effects on lipid metabolism and showed some advantageous effects such as HDL elevation, promotion of RCT and increase cholesterol excretion as bile salts.

It has been reported that miR-33 is co-expressed with SREBF family of transcription factors [26]. There is however a controversy over co-expression of Srebf-2 and miR-33 following LXR agonists' administration. Previously, some studies have confirmed co-expression of Srebf-2 and miR-33 [6, 19, 28] while some other studies have reported that there is no relationship between Srebf-2 and miR-33 expression under different conditions [15, 23, 24, 26, 27].
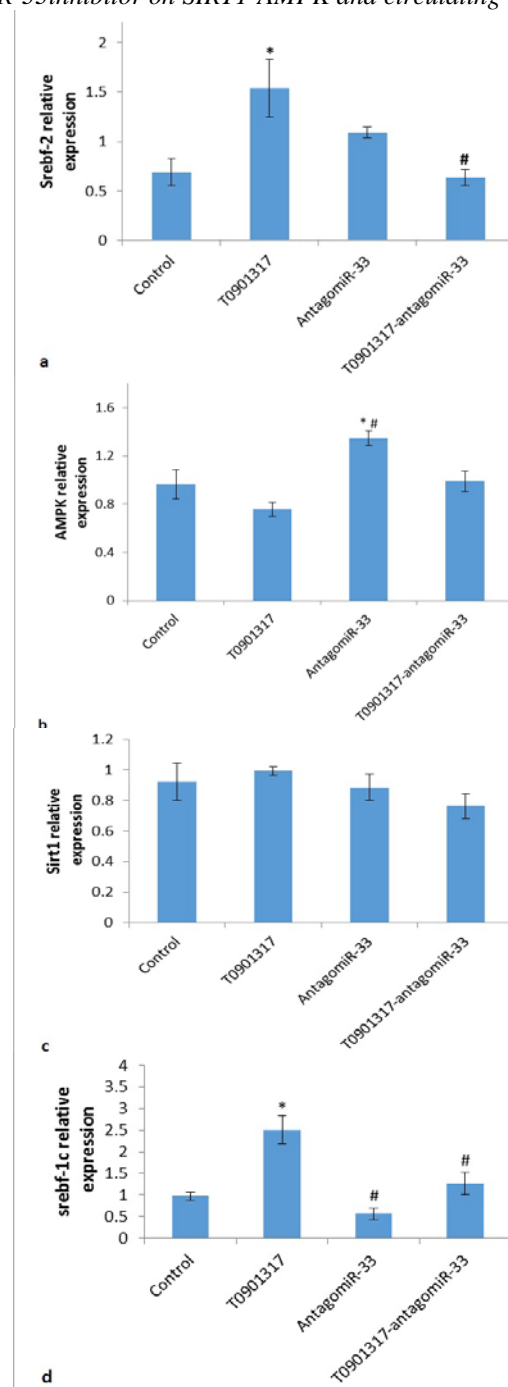

Fig 2. Evaluation of Srebf-2 (a), AMPK (b), Sirt1 (c) and Srebf1c (d) expression shown by real-time PCR in liver tissue of 4 groups of mice, I. untreated control group, II. LXR agonist (T0901317), III. AntagomiR-33 (miR-33 inhibitor), and IV. combination of T0901317 and AntagomiR-33. All data are expressed as mean ± SEM (n = 6 mice/group). *statistically significant compared to control group, # statistically significant compared to T0901317 group (p < 0.05 considered as significant).
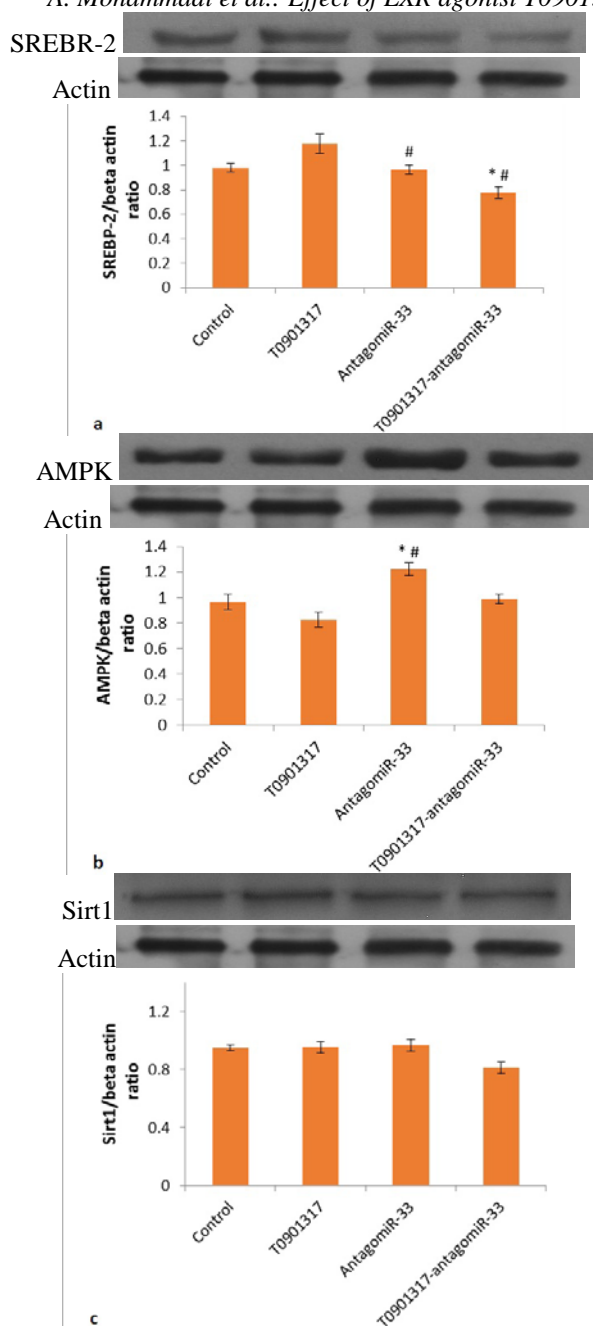
Fig 3. Western blotting of SREBP-2 (a), AMPK (b), Sirt1 (c) expressed in liver tissue of 4 groups of mice, I. untreated control group, II. LXR agonist (T0901317), III. AntagomiR-33 (miR-33 inhibitor), and IV. Combination of T0901317 and AntagomiR-33. Data are expressed as mean ± SEM (n = 6 mice/group). * statistically significant compared to control group, # statistically significant compared to T0901317 group (p < 0.05 considered as significant)

Also, there are disagreements about T0901317 effects on Srebf-2 expression. It has been reported that treatment with T0901317 for 4 days showed no effect on SREBP-2 levels [19]. Horie *et al.* proved that T0901317 has no effect on miR-33a and srebf-2 in HepG2 cell line [28]. Also, Schultz *et al.* showed that T0901317 administration increased SREBF-1c but had no effect on SREBF-2 [6]. Furthermore, Kostopoulou *et al*., found that SREBP-2 gene and miR-33a as intronic microRNA in osteoarthritic chondrocytes compared with normal chondrocytes were significantly elevated [24]. MiR-33 and Srebf-2 expression were down-regulated by high cholesterol diet in mouse peritoneal macrophages indicating that Srebf-2 and miR-33 are transcribed simultaneously [26]. It showed that T0901317 in goose hepatocytes increased SREBP-2 and HMGCR expression [23]. Other studies also have reported that T0901317 increased SREBP-2 [15, 27]. In spite of this inconsistency about LXR activation and its agonist's effect on SREBF-2 gene expression, here we showed that T0901317 increases miR-33, SREBP-2 and Srebf-2 levels in mice liver after seven days. These findings are consistent with studies which showed that T0901317 increased Srebf-2 and miR-33 expression or studies which reported that Srebf-2 and miR-33 are co-transcribed [6, 19, 28].

AMPK is a sensor of energy in the cells where it inhibits synthetic and energy consuming pathways such as lipogenesis and cholesterol biosynthesis. On the other hand, it activates catabolic pathways to increase intracellular energy levels [5, 31]. AMPK is a known target of miR-33 and there are many studies which have reported that miR-33 reduces AMPK levels and anti-miR-33 increases AMPK [2, 3, 20, 30]. In contrast to these findings, Horie *et al*. reported that in miR-33b knock-in mice, SREBP-1 and ABCA1 proteins were reduced in liver, but AMPK was unaffected by miR-33b over expression [28]. We found that administration of antagomiR-33 in mice increased hepatic AMPK levels, which is consistent with most studies [2, 3, 20, 30] and in contrast to Horie *et al.* [28], who reported no effect of miR-33 overexpression over AMPK. Also, we showed that T0901317 affected AMPK levels, but this reduction was not

Table 2. Serum lipid profile. All data are expressed as mean ± SD (n = 6 mice/group)

Groups	Triglyceride (mg/dL)	Cholesterol (mg/dL)	HDL-c (mg/dL)
Control	102.5 ±5.6	107.50±8.7	91.8±3.1
T0901317	180.8±16[a]	127.51±8.8	104±0.9[a]
AntimiR-33	106.5±6.4[b]	124.0±24.7	106.8±1.8[a]
T090+AntimiR-33	110.8±9.3[b]	114.33±7.1	111.2±1.1[a]

[a] Significant compared to control group; [b] Significant compared to T0901317 group; (p < 0.05 considered as significant)

significant. It has been reported that AMPK activation reverses hepatic fat accumulation and reduces serum TG and cholesterol [32]. Also it has been shown that Licochalcone by activation of AMPK/Sirt1 pathway is capable of suppressing the LXR-a dependent lipogenic gene expression in the liver [31]. Lee *et al.* [33] reported that AMPK activation affects LXR-Srebf1c signaling pathway, suppresses it and reduces TG levels. We found that anti-miR-33 treatment reduced TG levels, and it could be associated with increased liver AMPK contents, because AMPK activation suppresses Srebf-1c and its upstream activator, LXR-α [33, 34].

There is a crosstalk between AMPK and sirt1 and they affect each other's activity [4, 5]. Sirt1 activates LXR but inhibits SREBF-1c activity. Therefore, Sirt1 is capable of elevating Abca1 by LXR activation and reducing lipogenesis by inhibition of SREBF-1c [5, 31]. Walker *et al.*, [18] described that SIRT1 suppresses SREBP-1 and SREBP-2 target genes; however, we found no remarkable effect due to Sirt1 treatment in our study because there was no significant change in Sirt1 gene and protein levels. Escola-Gil *et al.* [14] found that Resveratrol administration (a Sirt1 agonist) and overexpression of SIRT1 showed no effect on liver LXR-target genes. This is consistent with our finding that Sirt1 did not show any significant change, thus Sirt1 has no potential downstream role after miR-33 manipulation by anti-miR-33 and LXR activation by T0901317. Unlike Sirt1, AMPK showed significant changes in our study and it seems that SREBF-1c suppression could be related to inhibitory effect of AMPK on srebf-1c and its activator, LXR. T0901317 lowers AMPK levels insignificantly, but anti-miR-33 treatment significantly increased AMPK in mice liver. Combination of T0901317 and anti-miR-33 showed that anti-miR-33 treatment attenuates the ablative effect of T0901317 on AMPK levels. Elevation of AMPK and reduction of srebf-2 gene and protein expression in this group (co-administration of T0901317 plus anti-miR-33) explains reduced serum TG levels and increased HDL in this group. Previous studies have shown that T0901317 and anti-miR-33 cause elevation of Abca1 which is directly related to HDL augmentation [3, 6, 14, 25, 35]. On the other hand, by elevation of HDL there is a flow of cholesterol from peripheral tissues to the liver, known as RCT which results in high levels of sterols in the cells [2]. High cholesterol contents cause down regulation of srebf-2 which justifys Srebf-2 reduction at gene and protein expression level.

Therefore, AMPK could be considered responsible for changes observed in lipid homeostasis in this study.

SREBP-2 activates HMGCR and increase cellular cholesterol levels, but Wong et al, also showed that SREBP-2 increase oxysterol production which is a known ligand for LXR [16, 17, 25]. So SREBP-2 can up regulate LXR activity and increase HDL levels by helping LXR dependent Abca1 expression [16]. We showed that anti-miR-33 and T0901317 co-administration significantly increased HDL levels and also reduced SREBP-2. Previous studies have shown that anti-miR-33 and T0901317 increase HDL levels through different mechanisms [6, 20, 28, 35]. We showed that co-administration of anti-miR-33 and T0901317 increased HDL levels significantly compared to control group. Hence it seems that SREBP-2 has no role in HDL elevation in this group. Co-administration of T0901317 and AntimiR-33 therapy reduced srebf-2 levels significantly. It seems that there is a synergic effect of antimiR-33 and T0901317 on cholesterol entrance to hepatocytes in mice which cause significant reduction in srebf-2 levels that is under control of sterol levels in cells.

Other study showed that anti-miR-33 therapy reduced srebf-1c expression [21]. T0901317 activates LXR and result in Srebf-1c activation which in turn activates lipogenesis and increases serum TG [6]. We showed that co-administration of anti-miR-33 and T0901317 reduce srebf-1c gene expression compared to T0901317 (activator of Srebf-1c) group (p=0.004). Then, co-administration of anti-miR-33 and LXR agonist proposes a potent therapeutic effect against atherosclerosis and other cardiometabolic diseases in which lipid imbalance exist. Horie and colleagues showed that LXR stimulation by T0901317 was not affected SREBF-2 and miR-33 levels which are absolutely in contrast with our finding that T0901317 up regulated miR-33, Srebf-2 and Srebf-1c [28]. T0901317 cause severe elevation of serum TG levels which executed from LXRa-Srebf-1c pathway as mentioned above. And this high level of serum TG was reduced by anti-miR-33 therapy in group that received both anti-miR-33 and T0901317. It is probable that AMPK can be a potent factor for this phenomenon which is because of AMPK decreasing effects on Srebf-1c gene expression [4, 5]. Rayner et al, [21] showed that anti-miR-33 therapy reduced srebf1 and FAS which confirm our observation which anti-miR-33 therapy attenuated TG levels in group that received T0901317 plus anti-miR-33.

CONCLUSIONS

It has been reported that LXR activation promotes RCT and elevate HDL-c, and Anti-miR-33 therapy increase HDL-c, AMPK and ABCA1 levels. Also it was documented that SREBP-2 increase HMGCR activity and intracellular cholesterol levels. We showed that co-administration of LXR agonist and miR-33 inhibition significantly (p<0.001) increase serum HDL-c and reduce SREBP-2 expression in mice liver. Also, co-administration of T0901317 and anti-miR-33 compared to T0901317 alone, significantly reduced serum TG levels. Thus LXR activation and miR-33 antagonism is a valuable therapeutic alternative for cardiovascular disorders. But there is a necessity of more evaluation about co-administration of LXR agonists and anti-miR-33 treatments.

***Conflict of interest:** The authors declare that there is no conflict of interest.*

REFERENCES

1. T. Horie, O. Baba, Y. Kuwabara, Y. Chujo, S. Watanabe, M. Kinoshita, M. Horiguchi, T. Nakamura, K. Chonabayashi, M. Hishizawa, K. Hasegawa, N. Kume, M. Yokode, T. Kita, T. Kimura, K. Ono, *J. Am. Heart Assoc.*, **1**, e003376 (2012).
2. V. Rottiers, A. M. Naar, *Nature Reviews Molecular Cell Biology*, **13**, 239 (2012).
3. H. Najafi-Shoushtari, F. Kristo, Y. Li, *Science*, **18**, 328 (2010).
4. N.B. Ruderman, X.J. Xu, L. Nelson, J.M. Cacicedo, A.K. Saha, F. Lan, Y. Ido, *Am. J. Physiol. Endocrinol. Metab.*, **298**, E751 (2010)
5. M. Fulco, V. Sartorelli, *Cell Cycle*, **7**, 3669 (2008)
6. J.R. Schultz, H. Tu, A. Luk, J.J. Repa, J.C. Medina, L. Li, S. Schwendner, S. Wang, M. Thoolen, D.J. Mangelsdorf, K.D. Lustig, B. Shan, *Genes & Development*, **14**, 2831 (2000).
7. O.A. Alrob, S. Khatib, S.A. Naser, *J Physiol. Biochem.*, **73**, 307 (2017).
8. K. Ono, T. Horie, T. Nishino, O. Baba, Y. Kuwabara, M. Yokode, T. Kita, T. Kimura, *Circulation Journal*, **79**, 278 (2015).
9. G.T. Bommer, O.A. MacDougald, *Cell Metab.*, **13**, 241 (2011)
10. T. Horie, T. Nishino, O. Baba, Y. Kuwabara, T. Nakao, M. Nishiga, S. Usami, M. Izuhara, N. Sowa, N. Yahagi, H. Shimano, S. Matsumura, K. Inoue, H. Marusawa, T. Nakamura, K. Hasegawa, N. Kume, M. Yokode, T. Kita, T. Kimura, K. Ono. *Nat. Commun.*, **4**, 2883 (2013).
11. H. Najafi-Shoushtari, *Curr Atheroscler. Rep.*, **13**, 202 (2011).
12. J. Laurencikiene, M. Ryden, *International Journal of Obesity*. **36**, 1494 (2012).
13. R.M. Allen, T.J. Marquart, C.J. Albert, F.J. Suchy, D.Q.-H. Wang, M. Ananthanarayanan, D.A. Ford, A. Baldan, *EMBO Mol. Med.*, **4**, 882 (2012).
14. J.C. Escola-Gil, J. Julve, G. Llaverias, *Transl. Res.*, **161**, 110 (2013).
15. J.C. Larkin, S.B. Sears, Y. Sadovsky, *Placenta*, **35**, 919 (2014).
16. S. Rong, V.A. Cortes, S. Rashid, N.N. Anderson, J.G. McDonald, G. Liang, Y.-A. Moon, R.E. Hammer, J.D. Horton, *Human Biology and Medicine,* **6**, e25015 (2017).
17. J. Wong, C.M. Quinn, A.J. Brown, *Biochem. J.*, **400**, 485 (2006).
18. A.K. Walker, F. Yang, K. Jiang, J.–Y. Ji, J.L. Watts, A. Purushotham, O. Boss, M.L. Hirsch, S. Ribich, J.J. Smith, K. Israelian, C.H. Westphal, J.T. Roders, T. Shioda, S.L. Elson, P. Mulligan, H. Najafi-Shoushtari, J.C. Black, J.K. Thakur, L.C. Kadyk, J.R. Whetsteine, R. Mostoslavsky, P. Puigserver, X. Li, N.J. Dyson, A.C. Hart, A.M. Naar. *Genes & Development.*, **24**, 1403 (2010).
19. A. Davalos, L. Goedeke, P. Smibert, C.M. Ramirez, N.P. Warrier, U. Andreo, D. Cirea-Salinas, K. Rayner, U. Suresh, J.C. Pastor-Pareja, E. Esplugues, E.A. Fisher, L.O. F. Penalva, K.J. Moore, Y. Suarez, E.C. Lai, C. Fernandez-Hernando, *PNAS*, **108**, 9232 (2011).
20. L. Goedeke, A. Salerno, C. M. Ramirez, *EMBO Molecular Medicine*, **6**, 1133 (2014).
21. K.J. Rayner, C.C. Esau, F.N. Hussain, A.L. McDaniel, S.M. Marshal, J.M. Van Gils, T.D. Ray, F.J. Sheedy, L. Goedeke, X. Liu, O.G. Khatsenko, V. Kaimal, C.J. Lees, C. Fernandez-Hernando, E.A. Fisher, R. E. Temel, K. J. Moore, *Nature*, **478**, 404 (2012).
22. I. Gerin, L.A. Clerbaux, O. Haumont, N. Lanthier, A.K. Das, C.F. Burant, I.A. Leclercq, O.A. MacDougald, G.T. Bommer, *J. Biol. Chem.*, **285**, 33652 (2010)
23. F. He, C. Han, D. Liu, H. Wan, J. Wang, H. Liu, L. Li, H. Xu, H. He, *Ital J Anim Sci.*, **13**, 2979 (2014).
24. F. Kostopoulou, K.N. Malizos, I. Papathanasiou, A. Tsezou, *Arthritis Research & Therapy*, **17**, 42 (2015).
25. T.J. Marquart, R.M. Allen, D.S. Ory, A. Baldan, *PNAS*, **107**, 12228 (2010)
26. K.J. Rayner, Y. Suárez, A. Dávalos, S. Parathath, M.L. Fitzgerald, N. Tamehiro, E.A. Fisher, K.J. Moore, C. Fernandez-Hernando. *Science.*, **328**, 1570 (2010).
27. K. Sato, T. Kamada, *Comparative Biochemistry and Physiology*, **158**, 201 (2011).
28. T. Horie, T. Nishino, O. Baba, Y. Kuwabara, T. Nakao, M. Nishiga, S. Usami, M. Izuhara, F. Nakazeki, Y. Ide, S. Koyama, N. Sowa, N. Yahagi, H. Shimano, T. Nakamura, K. Hasegawa, N. Kume,

M. Yokode, T. Kita, T. Kimura, K. Ono, *Sci. Rep.*, **4**, 5312 (2014).

29. H. Najafipour, A. Vakili, B. Shahouzehi, A. S. Hekmat, Y. Masoomi, M. Yeganeh Hajahmadi, S. Esmaeli-Mahani, *J Physiol Biochem.*, **71**, 165 (2015).

30. K.J. Rayner, C. Fernandez-Hernando, K. J. Moore, *Thrombosis and Haemostasis*, **107**, 642 (2012b).

31. J.Y. Han, S.H. Park, J.H. Yang, *Toxicol Res.*, **30**, 19 (2014).

32. M. Gao, D. Liu, *The AAPS Journal*, **15**, 744 (2013).

33. J. Lee, S.–W. Hong, S.E. Park, E.J. Rhee, C.Y. Park, K.W. Oh, S.W. Park, W.Y. Lee, *Molecular and Cellular Endocrinology*, **414**, 148 (2015).

34. Y. Li, S. Xu, M. Mihaylova, B. Zheng, X. Hou, B. Jiang, O. Park, Z. Lou, E. Lefai, J.Y.J. Shyy, B. Gao, M. Wierzbicki, T.J. Verbeuren, R.J. Shaw, R.A. Cohen, M. Zang, *Cell Metab.*, **13**, 376 (2011).

35. T. Horie, K. Ono, M. Horiguchi, H. Nishi, T. Nakamura, K. Nagao, M. Kinoshita, Y. Kuwabara, H. Marusawa, Y. Iwanaga, K. Hasegawa, M. Yokode, T. Kimura, T. Kita, *PNAS*, **107**, 17321 (2010).

ВЛИЯНИЕ НА LXR АГОНИСТ Т0901317 И miR-33ИНХИБИТОР НА SIRT1-AMPK И ЦИРКУЛИРАЩИ HDL-C НИВА

А. Мохаммади[1,2], Х. Фаллах[1], Б. Шахузехи[1]*, Х. Наджафипур[1]

[1] *Департамент по клинична биохимия, Изследователски център към Училището по медицина и физиология на Афзалипур, Кермански Университет по медицински науки, Керман, Иран*
[2] *Училище по медицински науки, Сирджан, Иран*

(Резюме)

Сърдечносъдовите заболявания са все още основната причина за заболеваемостта и смъртността в световен мащаб. Чернодробните X рецептори (LXR) и стерол-регулиращите елемент-свързващи протеини (SREBP) играят важна роля в липидната хомеостаза. LXR влияят върху SREBP и подпомагат липидния синтез и обратния холестеролов транспорт. МикроRNA-33 регулира надолу AMPK, ABCA1 и CPT1 mRNA. Sirt1 също влияе върху активността на LXR и SREBP посредством деацетилиране. Ние оценихме влиянието на LXR агонист и miR-33 инхибитор върху Srebp-2, Sirt1, AMPK експресия и липидния профил. 24 мишки бяха разделени на 4 групи (n=6) и изследването траеше 7 дни. Група I (контролна група) не получаваше лечение; група II получаваше 30 mg/kg/48 h LXR агонист (Т0901317) чрез интраперитонеална (и.п.) инжекция; група III получаваше 1 mg/kg/48 h antagomiR-33 чрез и.п. инжекция и група IV получаваше комбинация от Т0901317 и antagomiR-33. MiR-33, AMPK, Sirt1, Srebf-2 and Srebf1c генни експресии са определени количествено чрез полимеразна верижна реакция в реално време, а AMPK, Sirt1 и Srebp-2 протеинови експресии чрез western blotting тест. Прилагането на Т0901317 повишава miR-33 и srebf-2 експресии. Съвместното прилагане на Т0901317 и antagomiR-33 понижава нивата на srebf-2 и miR-33 и повишава нивата на HDL-c. AMPK намалява в групите, получаващи Т0901317. Генът Sirt1 и протеиновата експресия остават непроменени. Независимо от прогреса в откриването на нови лекарства срещу атеросклероза и метаболитни заболявания, тези болести не са напълно контолирани. Вероятно има синергичен ефект между Т0901317 и antagomiR-33, които понижават вътреклетъчните нива на стерол и повишават транспорта на холестерол към хепатоцитите, което може да се счита като терапевтична алтернатива при атеросклероза и сърдечносъдови заболявания.

Protective effect of chard extract on glycoprotein compounds and enzyme activities in streptozotocin-induced hyperglycemic rat lungs

O. Sacan[1], O. Ertik[1], Y. Ipci[2], L. Kabasakal[2], G. Sener[2], R. Yanardag[1*]

[1]Istanbul University, Faculty of Engineering, Department of Chemistry, 34320-Avcilar Istanbul, Turkey
[2]Marmara University, Faculty of Pharmacy, Department of Pharmacology, 34668-Haydarpasa, Istanbul, Turkey

In the present study, the protective effect of chard on glycoproteins, hydroxyproline, advanced oxidation protein products and enzyme activities in the lung tissue of streptozotocin (STZ) – induced hyperglycemic rats were examined. Male, Sprague Dawley rats were grouped as control, hyperglycemic, chard, insulin, chard+insulin given hyperglycemic rats. Hyperglycemia was induced by as a single dose of STZ (60 mg/kg) administered intraperitoneally. Fourteen days after the rats were made hyperglycemic, chard extract was administered to rats 2 g/kg/day by gavage and/or insulin a dose of 6U/kg/day for 45 days. Glycoprotein components, prolidase activity and levels of hydroxyproline and advanced oxidation protein products were significantly increased in the lung tissues of hyperglycemic rats; on the other hand, paraoxonase and arylesterase activities were decreased. Treatment with chard and/or insulin reversed these effects. These results suggested that chard possesses a significant beneficial effect on abnormal glycoprotein metabolism and enzyme activities in STZ- induced hyperglycemic rats.

Keywords: chard, glycoprotein, hyperglycemic, lung, rat.

INTRODUCTION

Diabetes mellitus is a disease affecting many organs such as liver, kidney, pancreas, lungs and eyes. As the lung has abundant connective tissue and diffuse microvascular circulation, it is thought to be a target organ for diabetic disease. Oxidative stress is considered to be the main factor in the development of diabetic complications and tissue injury. Many traditional herbs, through their hypoglycemic and antioxidant properties, may also protect the organs involved in diabetes mellitus.

Carbohydrates seem to play a central role in the development of chronic diabetic complications. Glycoproteins, which are carbohydrate linked protein macromolecules found on the cell surface, are some of the principal components of animal cells. Hexose, hexosamine, fucose and sialic acid are the basic sugar components found in glycoproteins and glycosaminoglycans. Glycoprotein metabolism plays a major role in the pathogenesis of diabetes mellitus. Glycoproteins have multiple and complex functions and are found as hormones, enzymes, blood group substances and as constituents of extracellular membranes [1]. They play an important role in functions such as cell differentiation and recognition, membrane transport and absorption of macromolecules [2]. In hyperglycemic state, high blood glucose levels accelerate the synthesis of basement membrane components, such as glycoproteins [3].

Chard (*Beta vulgaris* L. var. *cicla*) is a biennial leaf vegetable cultivated worldwide, in Northern India, South America, the Mediterranean countries and USA. It is an important crop due to its year round availability, high yield and low cost. Several studies have demonstrated that chard has antioxidant and antiacetylcholinesterase [4], antidiabetic [5, 6], anticancer [7], antimicrobial [8], hepatoprotective [9] and other biological activities. Phytochemical screening of *B. vulgaris* varieties have revealed the presence of some saponins, flavonoid glycosides [10], flavonoids, vitamin C, vitamin E, carotenoids and minerals [11]. In the present study, the protective effect of chard on glycoprotein levels and enzyme activities in hyperglycemic lung tissue were examined.

EXPERIMENTAL

Preparation of chard extract

Chard leaves were collected from Istanbul, Turkey. Plant material was washed with distilled water and dried at room temperature. The chard was identified by Prof. Dr. Neriman Ozhatay (Faculty of Pharmacy, Istanbul University). Dried chard leaves (100 g) were extracted with 1000 mL of distilled water and boiled for 30 min. The extract was filtered and the filtrate was evaporated under reduced pressure using a rotary evaporator. The chard extract yield was 39.48 % (w/v). Chard extract was dissolved in distilled water in order to obtain 43.33 g/55 ml extract solution.

*) To whom all correspondence should be sent:
E-mail: refiyeyanardag@yahoo.com

Experimental design

Male Sprague–Dawley rats weighing 380-420 g and aged 6-7 months were used in the study. All experimental procedures were approved by Marmara University Animal Care and Use Committee. (No: 68.2008.mar). The rats were divided into five groups. Group I (n= 8): control rats given citrate buffer; Group II (n= 8): STZ-induced hyperglycemic rats; Group III (n= 8): STZ-induced hyperglycemic rats given chard extract; Group IV (n= 8): STZ-induced hyperglycemic rats given insulin; Group V (n= 8): STZ-induced hyperglycemic rats given chard extract+insulin. Fourteen days after the rats were rendered hyperglycemic, chard extract (2g/kg/day, by gavage), insulin (6 U/kg/ day, by subcutaneous injection) and chard extracts plus insulin at the mentioned doses were administrated to rats for 45 days. On day 60, lungs of rats were removed and used for the analysis of glycoprotein components and enzyme analysis. Hyperglycemia was induced by a single intraperitoneal injection of (60 mg/kg) STZ freshly dissolved in citrate buffer (pH=4.5; 0.01 M).

Biochemical estimations

Fasting blood glucose levels after 18 h of fasting were determined using an automated glucose analyzer [6]. Rats with more than 200 mg/dl fasting plasma glucose were considered as having hyperglycemia. The lungs were homogenized in 0.9% NaCl to make up a 10% (w/v) homogenate. Hexose and hexosamine contents were estimated by the method of Winzler [12] and fucose was determined by the method of Dische and Shettles [13] in lung tissue homogenates. Sialic acid was estimated by the method of Lorentz *et al*. [14]. Furlong *et al*. [15], Gan *et al*. [16] and Chinard [17] methods were used to determine the paraoxonase (PON), arylesterase (ARE) and prolidase activities, respectively. Lung hydroxyproline and advanced oxidation protein products (AOPP) contents were assayed by the method of Reedy and Enwemeka [18] and Witko-Sarsat *et al*. [19], respectively. The protein content was estimated by the method of Lowry [20].

Statistical analysis

Biochemical results were evaluated using an unpaired *t*-test and ANOVA variance analysis using the NCSS statistical computer package. The values were expressed as mean ± SD. Comparison between control and experimental groups was performed using the Mann-Whitney test. $p < 0.05$ was considered as significant.

RESULTS

Lung tissue glycoprotein levels are presented in Table 1.The levels of glycoproteins containing hexose ($p < 0.001$), hexosamine, fucose and sialic acid were significantly increased in the hyperglycemic groups ($p < 0.0001$, respectively). Administration of chard, insulin and chard+insulin reversed these changes in the glycoprotein components in the lungs of hyperglycemic rats except hexose values ($p < 0.005$ and $p < 0.0001$, respectively).

The PON, ARE, prolidase, hydroxyproline and AOPP activities in the lung tissue are presented in Table 2. In the hyperglycemic group, the activities of PON, ARE were decreased while prolidase, hydroxyproline and AOPP activities were increased ($p < 0.005$, respectively). Administration of chard, insulin and chard+insulin significantly increased the lung paraoxonase PON and ARE activities in the hyperglycemic groups ($p < 0.005$, respectively) while lung prolidase activities, hydroxyproline and AOPP levels were significantly decreased in the hyperglycemic rats. The effect of chard was better than that of insulin and insulin+chard.

DISCUSSION

Diabetes mellitus is a chronic disease which affects various organs such as liver, brain, kidney, skin and lung. Experimental diabetes models have an important place in analyzing diabetes complications and determining treatment approaches. Lung is a target organ in diabetes mellitus. Diabetes mellitus causes a decrease in lung elasticity and neuropathy, which in turn partially affects basic lung functions [21]. Generally, abnormalites in glycoprotein metabolism are observed in both natural and experimental diabetes [22]. Altered metabolism of glycoproteins plays a major role in the pathogenesis of diabetes mellitus. Insulin deficiency and high levels of blood glucose in diabetic condition may result in an increased synthesis of glycoprotein components, which results in thickening of the basal membrane [23]. The increase in tissue glycoprotein components has been associated with the severity and duration of diabetes. In diabetes mellitus, free amino groups of proteins react slowly with the carbonyl groups of reducing sugars such as glucose, to yield a Schiff-base intermediate. Intermediate products in these reactions undergo Amadori rearrangement to form stable ketoamine derivatives [24].

Table 1. Lung tissue hexose, hexosamine, fucose and sialic acid levels of all groups.

Groups	Hexose (mg glucose/mg protein)*	Hexosamine (µg glucosamine /mg protein)*	Fucose (µg fucose /mg protein)*	Sialic acid (µmole sialic acid /g protein)*
Control	15.63 ± 1.17	5.33 ± 0.39	10.23 ± 0.06	139.78 ± 9.76
Hyperglycemic	30.65 ± 5.95[a]	16.55 ± 1.99[d]	22.41 ± 0.58[d]	442.26 ± 12.33[d]
Hyperglycemic + Chard	17.60 ± 1.44[b]	4.68 ± 0.41[c]	7.51 ± 1.28[c]	133.25 ± 18.22[c]
Hyperglycemic + Insulin	15.61 ± 1.37[c]	4.51 ± 0.94[c]	7.62 ± 0.65[c]	113.97 ± 7.66[c]
Hyperglycemic + Chard + Insulin	24.14 ± 2.08	11.98 ± 1.18[c]	10.17 ± 1.33[c]	169.73 ± 6.06[c]
P$_{ANOVA}$	0.0001	0.0001	0.0001	0.0001

*Mean ± SD ; [a] $P<0.001$ *vs* control group; [b] $P<0.005$ *vs* hyperglycemic group; [c] $P<0.0001$ *vs* hyperglycemic group; [d] $P<0.0001$ *vs* control group

Table 2. Lung tissue PON, ARE and prolidase activities, hydroxyproline and AOPP levels of all groups.

Groups	PON (U/g protein)*	ARE (U/g protein)*	Prolidase (U/g protein)*	Hydroxyproline (U/g tissue)*	AOPP (nmol/g protein)
Control	41.05 ± 2.76	7.09 ± 0.60	53.50 ± 1.27	10.00 ± 0.43	9.29 ± 0.40
Hyperglycemic	22.83 ± 2.11[a]	4.87 ± 0.38[a]	110.10 ± 5.15[a]	22.48 ± 1.55[a]	11.08 ± 0.82[a]
Hyperglycemic + Chard	49.15 ± 3.38[b]	11.88 ± 1.00[b]	38.58 ± 4.79[b]	2.03 ± 0.35[b]	8.49 ± 0.57[b]
Hyperglycemic + Insulin	29.72 ± 1.92[b]	8.90 ± 0.88[b]	56.26 ± 6.34[b]	20.87 ± 0.97[b]	8.50 ± 1.17[b]
Hyperglycemic +Chard + Insulin	31.63 ± 2.35[b]	5.40 ± 0.56	49.18 ± 2.92[b]	5.65 ± 0.30[b]	8.98 ± 0.83[b]
P$_{ANOVA}$	0.0001	0.0001	0.0001	0.0001	0.0001

*Mean ± SD; [a] $P<0.005$ *vs* control group; [b] $P<0.005$ *vs* hyperglycemic group

In this study, we observed increased levels of hexose, hexosamine, fucose and sialic acid in the lung tissue of STZ-induced hyperglycemic rats. Previous studies have shown that decrease in hyperglycemia could lead to a decrease in glycoprotein components [25, 26].

In this study, we have observed increased levels of hexose, hexosamine, fucose and sialic acid in the lung tissue of STZ-induced hyperglycemic rats. Previous studies have shown that decrease in hyperglycemia could lead to a decrease in glycoprotein components [25, 26]. In this study, chard, insulin and chard+insulin treatment to diabetic rats significantly decreased lungs glycoprotein components to near-normal levels by virtue of its antihyperglycemic effects. The most effective treatment was insulin therapy on glycoprotein levels. This could be due to the decreased hyperglycemic state with increased levels of insulin in diabetic rats [27]. In this study, it has been determined that chard decrease hexose, hexosamine, fucose and sialic acid levels in hyperglycemic rats because it increases insulin secretion from B cells of the pancreas [28].In diabetic rats with the use of chard and insulin + chard glycoprotein levels were decreased in all other parameters except hexose (Table 1). According to this results, it can be suggested that

chard decreases glycoprotein levels in lungs because its antihyperglycemic effects [28] This results show the efficiency of chard in modulating the altered glycoprotein metabolism in diabetic rats. Diabetes is characterized by high glucose concentration which leads to an increase in the production of reactive oxygen species (ROS) via several mechanisms (glucose autooxidation, stimulation of polyol pathway and formation of advanced glycation end products). The resulting oxidative stress can play a key role in diabetes pathogenesis. ROS are known to be responsible for the oxidative damage of DNA, nucleotides, proteins, lipids, carbohydrates and cell membrane structures [29].

PON is known to have an antioxidant function [30]. In humans, PON gene family has three members (PON 1, PON 2, PON 3) [31]. PON 1 has three known enzymatic molecules including paraoxonase, arylesterase and dyazoxonase. PON 1 activity is reduced in diseases associated with high oxidative stress such as coronary heart disease, dyslipidemia, cancers, inflammatory processes, hyperlipidemia, diabetes mellitus and certain neuropathies, chronic hepatitis, HDL deficiencies and Gulf War Syndrome [32-34]. Most studies have found that PON 1 activity is reduced in diabetic patients such as Type I and Type II with some

dissension [35, 36]. Chronic inflammation is closely associated with angiogenesis and PON1 activity decreases during inflammation [37]. SH groups play a role in PON 1 activities. In the present study, lung PON and ARE activities were reduced in the diabetic rats which is consistent with previous diabetic rat study [38]. Decreased PON and ARE activities in diabetes mellitus might be associated with hyperglycemia and oxidative stress. In this study, paraoxonase and ARE activities were increased after treatment with chard, chard+insulin and insulin. This fact may be due to the antioxidant effect of polyphenols, tannins and anthocyanins as well as to their direct effect on enzyme activities [11].

Prolidase activity has been reported as a marker for oxidative stress for many diseases like diabetes, diabetic neuropathy, nonulcer dyspepsia, chronic liver diseases, erectile dysfunction, osteoporosis, and so forth [39, 40]. Increased prolidase activity is an indicator of fibrosis. Fibrosis may occur in some lung diseases. This enzyme plays an important role in the recycling of proline for synhthesis and cell growth [41]. In our study, we found a significant increase in lung prolidase activity in hyperglycemic rats. We observed that chard, insulin and chard+insulin inhibited prolidase activity. These results indicate that chard extract ameliorates oxidative stress and hyperglycemia by inducing antioxidant defense in the lung of hyperglycemic rats. Based on these results, it could be argued that prevention of inflammation and oxidative stress was achieved in the lung tissue of hyperglycemic rats. Collagen is one of the proteins which contain the amino acid hydroxyproline. Some authors consider hydroxyproline as a marker of collagen content. Excessive production of collagen has been documented in disorders associated with proline derivatives such as lung fibrosis [42]. Hydroxyproline levels were increased in the lung tissues of hyperglycemic rats. This increase indicates the presence of pulmonary fibrosis in lung tissues. Surfactant protein (SP-D) is a useful and early diagnostic marker for pulmonary fibrosis. It may serve as a specific marker for lung injury. In our previous study [43], SP-D levels were determined in the lung tissue. In the present study, our data showed that STZ-induced pulmonary fibrosis led to an increase in hydroxyproline content. Treatment with chard, insulin and chard + insulin prevented these changes induced by STZ in rat and exerted a protective effect on STZ-induced pulmonary fibrosis. Administration of chard, insulin and chard+insulin restored the hydroxyproline levels to normal in the lung tissue. The reduction of hydroxyproline in rat lung *via*

122

chard treatment alone and in combination with insulin was first shown in the present study. In our manuscript, we determined that chard which was used on hyperglycemic rats was more effective than insulin on enzyme activity and hydroxyproline level (Table 2).This effect can be because of antioxidant and hypoglycemic properties of chard [4, 28]

AOPP, the dityrosine containing and cross linking protein products, are amongst the markers which indicate oxidative stress-based protein damage [44]. Accumulation of AOPP in the tissue plays an important role in the long-term complications of diabetes. Gradinaru *et al.* has mentioned the elevation of AOPP levels in diabetic patients [45]. We have also found an increased production of AOPP in the lungs of hyperglycemic rats. Treatment with chard, chard+insulin and insulin significantly reduced AOPP levels in hyperglycemic rats. This result indicated that chard, insulin and chard+insulin may be effective in preventing oxidative protein damages by reducing oxidative stress.

These results demonstrated that chard, insulin and chard+insulin consumption for 45 days may exert beneficial effects on the levels of glycoprotein, hydroxyproline, AOPP and PON, ARE and prolidase activities. Chard may have beneficial role in diabetic rats which may be due to the enhancement of insulin. Chard can be used as an effective indicator to demonstrate its effects in controlling the complications of diabetes.

REFERENCES

1. M. M. Porter-Turner, J. C. Sidmore, M. A. Khokher, B. M. Singh, C. A. Rea, *Br. J. Biomed. Sci.,* **68**, 203 (2011).
2. N. Mittal, J. Kaur, A. Mahmood, *Indian J. Exp. Biochem.,* **34**, 782 (1996).
3. R. G. Spiro, M. J. Spiro, *Diabetes,* **20**, 641 (1971).
4. O. Sacan, R. Yanardag, *Food Chem. Toxicol.,* **48**, 1275 (2010).
5. O. Ozsoy-Sacan, O. Karabulut-Bulan, S. Bolkent, R. Yanardag, Y. Ozgey, *Biosci. Biotechnol. Biochem.,* **68**, 1640 (2004).
6. S. Gezginci-Oktayoglu, O. Sacan, S. Bolkent, Y. Ipci, L. Kabasakal, G. Sener, R. Yanardag, *Acta Histochem.,* **116**, 32 (2014).
7. G. J. Kapadia, M. A. Azuıne, G. S. Rao, T. Arai, A. Iida, H. Tokuda, *Anti-Cancer Agents Med. Chem.,* **11**, 280 (2017).
8. E. Bursal, *Int. J. Food Prop.,* **16**, 1293 (2013).
9. U. V. Ustundag, S. Tunali, B. Alev, H. Ipekci, E. Emekli-Alturfan, T. Tunalı Akbay, R. Yanardag, A. Yarat, *J. Food Biochem.,* **40**, 132 (2016).
10. I. Kim, Y. W. Chin, S. W. Lim, Y. C. Kim, J. Kim, *Arch. Pharm. Res.,* **27**, 600 (2004).

11. S. Trifunović, A. Topalović, M. Knežević, V. Vajs, *Agric. Forest.*, **61**, 73 (2015).

12. R. J. Winzler, in: Methods of Biochemical Analysis. Determination of serum glycoproteins, D. P. Glick, (ed.), vol. 2, Interscience Publisher Inc., New York, 1955, p. 279.

13. Z. Dische, L. B. Shettles, *J. Biol. Chem.*, **175**, 595 (1948).

14. K. Lorentz, T. Weiss, E. Kraas. *J. Clin. Chem. Clin. Biochem.*, **24**, 189 (1986).

15. C. E. Furlong, R. J. Richter, S. L. Seidel, A. G. Motulsky, *Am. J. Hum. Genet.*, **43**, 230 (1988).

16. K. N. Gan, A. Smolen, H.W. Eckerson, B. N. La Du, *Drug Metab. Dispos.*, **19**, 100 (1991).

17. F. P. Chinard, *J. Biol. Chem.*, **199**, 91 (1952).

18. G. K. Reedy, C.S. Enwemeka, *Clin. Biochem.*, **29**, 225 (1996).

19. V. Witko-Sarsat, M. Friedlander, C. Capeillére-Blandin, T. Nguyen-Khoa, A. T. Nguyen, J. Zingraff, P. Jungers, *Kidney Int.*, **49**, 1304 (1996).

20. O. H. Lowry, N. J. Rosebrough, A. L. Farr, R. J. Randall, *J. Biol. Chem.*, **193**, 265 (1951).

21. M. Aktürk, I. Olcay, S. Karaahmetoğlu, F. Berk, *Toraks Dergisi*, **3**, 217 (2002).

22. L. Pari, N. Ashokkumar, *Therapie*, **61**, 125 (2006).

23. M. E. Patti, A. Virkamäki, E. J. Landaker, C. R. Kahn, H. Yki-Järvinen, *Diabetes*, **48**, 1562 (1999).

24. R. Bucala, in: Oxidative stress and vascular disease. Advanced glycosylation end products and diabetic vascular diseases. J. F. Keaney (ed.), Kluwer Academic Publishers, Dordrecht, 2000, p. 287.

25. G. Saravanan, P. Ponmurugan, G. P. Senthil Kumar, T. Rajarajan, *Phytomedicine*, **17**, 1086 (2010).

26. L. Pari, P. Murugan, *Plant Foods Hum. Nutr.*, **62**,25 (2007).

27. G. Saravanan, P. Ponmurugan, G.P. Senthil kumar, T. Rajarajan, *J. Appl. Biomed.*, **7**, 151 (2009).

28. S. Bolkent, R. Yanardağ, A. Tabakoğlu-Oğuz, Ö. Özsoy-Saçan, *J. Ethnopharmacol.*, **73**, 251 (2000).

29. J. P. Kuyvenhoven, A. E. Meinders, Eur. *J. Int. Med.*, **10**, 9 (1999).

30. E. Bodolay, I. Seres, P. Szodoray, I. Csípo, Z. Jakab, J. Vegh, A. Szilagyi, G. Szegedi, G. Paragh, *J. Rheumatol.*, **35**, 237 (2008).

31. P. Davidsson, J. Hulthe, B. Fagerberg, B. M. Olsson, C. Hallberg, B. Dahllöf, G. Camejo, *J. Lipid Res.*, **46**, 1999 (2005).

32. B. Mackness, P. N. Durrington, M. I. Mackness, *Biochem. Biophys. Res. Commun.*, **276**, 729 (2000).

33. H. Balci, H. Genc, C. Papila, G. Can, B. Papila, H. Yanardag, H. Uzun, *J. Clin. Lab. Anal.*, **26**, 155 (2012).

34. S. Siewert, I. I. Gonzalez, R. O. Lucero, M. S. Ojeda, *J. Diabetes Investig.*, **6**, 67 (2015).

35. A. Jamuna Rani, S. V. Mythili, S. Nagarajan, *J. Physiol. Pharmacol.*, **58**, 13 (2014).

36. S. P. Nair, N. C. Shah, A. Taggarsi, U. Nayak, *Diabetes Metab. Syndr.*, **5**, 126 (2011).

37. A. Chait, C. Y. Han, J. F. Oram, J. W. Heinecke, *J. Lipid Res.*, **46**, 389 (2005).

38. S. Tas, S. Celikler, S. Ziyanok-Ayvalik, E. Sarandol, M. Dirican, *Cell Biochem. Funct.*, **29**, 108 (2011).

39. A. B. Erbağci, M. Araz, A. Erbağci, M. Tarakcioğlu, E. S. Namiduru, *Clin. Biochem.*, **35**, 263 (2002).

40. E. Uzar, Y. Tamam, O. Evliyaoglu, A. Tuzcu, C. Beyaz, A. Acar, B. Aydin, N. Tasdemir, *Neurol. Sci.*, **33**, 875 (2012).

41. A. G. Lenz, H. Hinze-Heyn, A. Schneider, J. Behr, K. HÄussınger, S. Heindi, F. Stanzel, K. L. Maier, *Respir. Med.*, **98**, 737 (2004).

42. A. Wangoo, I. N. Brown, B. G. Marshall, H. T. Cook, D. B. Young, R. J. Shaw, *Clin. Exp. Immunol.*, **119**, 92 (2000).

43. F. Oztay, O. Sacan, O. Kayalar, S. Bolkent, Y. Ipci, L. Kabasakal, G. Sener, R. Yanardag, *Pharm. Biol.*, **53**, 1639 (2015).

44. V. Rajani Kanth, P. Uma Maheswara Reddy, T. N. Raju, *Acta Diabetol.*, **45**, 243 (2008).

45. D. Gradinaru, C. Borsa, C. Ionescu, D. Margina, *J. Proteomics*, **92**, 313 (2013).

ЗАЩИТЕН ЕФЕКТ НА ЕКСТРАКТ ОТ ЦВЕКЛО ВЪРХУ ГЛЮКОПРОКТЕИНОВИТЕ СЪЕДИНЕНИЯ И ЕНЗИМНАТА АКТИВНОСТ В БЕЛИТЕ ДРОБОВЕ НА СТРЕПТОЗОДОЦИН-ИНДУЦИРАНИ ХИПЕРГЛИКЕМИЧНИ ПЛЪХОВЕ

О. Сакан[1], О. Ертик[1], У. Ипчи[2], Л. Кабасакал[2], Г. Сенер[2], Р. Янардаг[1*]

[1] *Истанбулски университет, Факултет по инженерство, Отдел по химия, 34320-Авчилар, Истанбул, Турция*
[2] *Университет Мармара, Факултет по фармация, Департамент по фармакология, Истанбул, Турция*

(Резюме)

В настоящата статия е изследван защитният ефект на цвеклото върху глюкопротеините, хидроксипролина, продуктите от окислението на протеина и ензимната активност в белодробната тъкан на стрептозоцин (СТЦ)-индуцирани хипергликемични плъхове. Мъжки плъхове от вида Sprague Dawley са групирани както следва: контролна група, хипергликемична група, третирани с цвекло, третирани с инсулин и третирани с инсулин и цвекло. Хипергликемия е индуцирана чрез единично интраперитониално вкарване на СТЦ (60 mg/kg). След 14 дни на плъховете се дава със стомашна сонда екстракт от цвекло 2 g/kg/ден и/или инсулин 6U/kg/ден в продължение на 45 дни. Глюкопротеиновите компоненти, пролидазната активност, нивата на хидроксипролин и продуктите от окислението на протеина значително нарастват в белодробната тъкан, докато параоксоназната и арилестеразната активност намаляват. Третирането с цвекло и/или инсулин обръща тези ефекти. Резултатите показват, че цвеклото притежава значително благоприятно действие върху абнормалния глюкопротеинов метаболизъм и ензимната активност в СНЦ-индуцирани хипергликемични плъхове.

Evaluating the process efficiency of industrial wastewater treatment plants using data envelopment analysis approach case study: Khuzestan steel company treatment plant

K. Rahbari[1], A. H. Hassani[*2], M. R. Mehrgan[3], A. H. Javid[4]

[1] *Department of Environmental Science, Faculty of Enviroment and Energy, Tehran Science and Research Branch, Islamic Azad University, Tehran, Iran*
[2] *Department of Environmental Engineering, Faculty of Environment and Energy, Tehran Science and Research Branch, Islamic Azad University, Tehran, Iran*
[3] *Department of Management, University of Tehran, Iran*
[4] *Department of Environmental Science, Faculty of Marine Science and Technology, Tehran Science and Research Branch, Islamic Azad University, Tehran, Iran*

Designing a mathematical model with the possibility of changing the experimental parameters and variables not only helps to evaluate the performance of the treatment plant but also predicts its behavior. In this paper, to assess the efficiency of Khuzestan steel company treatment plant, data envelopment analysis (DEA) model was used. Input and output parameters of the treatment plant (Oil, COD, TSS, pH) were determined (2009-2014). Malmquist Productivity Index was used to express the changes in total productivity and Window Analysis was employed for calculation of efficiency and performance trends over time. The results showed that the treatment plant efficiency in the removal of COD, Oil, TSS and pH from the input wastewater was 68%, 62%, 81% and 4%, respectively. Treatment plant efficiency in removing pollutants (COD, TSS, Oil) was approximately 70%, so the performance of the system is efficient and the produced wastewater matches environmental standards. On the other hand, the results showed the high power of DEA models in the calculation and classification of years in terms of efficiency.

Keywords: Treatment plant, Khuzestan steel company, Evaluating efficiency, Data envelopment analysis

INTRODUCTION

One of the most important issues before the design and implementation of any wastewater treatment plant is the selection of the best treatment process. Although the wide variety of types of wastewater treatment plants, especially in terms of capacity and specific local conditions, makes it difficult to introduce a general rule that applies to all cases of selection of treatment process, in terms of priority of the treatment process, certain criteria may be applied that will be usable in most treatment plants. It is important to choose the best process for wastewater treatment, and in this regard, few studies have been conducted using a variety of mathematical techniques. If industrial treatment plants are efficient and sewage is collected and re-used in the best way, the possible efficiency and productivity will gain a special place in all sectors and can play an important role in sustainable development of Iran.

Some research has been conducted in the world which has used mathematical models to measure the efficiency and evaluate the performance of the systems. One of these mathematical models is the Data Envelopment Analysis (DEA). Few studies in the world have used this model to assess the performance of wastewater treatment plants. This technical model is adopted to measure the relative efficiency of decision making units by calculating the ratio of weighted total output variables to weighted total input variables. This efficiency is a good indicator to identify optimum units [2]. In 2009, Venkata Mohan *et al.* used DEA and Taguchi's methodology of experimental design to assess and optimize hydrogen production and wastewater treatment processes [3]. In 2009, Hernández and Sala-Garrido used DEA approach to analyze the technical efficiency and cost of wastewater treatment processes. In 2011, in order to compare the efficiency of wastewater treatment technologies, Sala-Garrido *et al.* used the DEA model. In 2012, they also evaluated the efficiency of wastewater treatment plants under the conditions of uncertainty by using DEA approach with tolerance [4].

Also in Iran, some research has been conducted in the field of evaluating the performance of treatment plants, some of which will be mentioned. It should be noted that so far in Iran DEA models have not been employed to measure the performance of treatment plants.

In 2003, Miranzadeh and Babamir evaluated the efficiency of Ekbatan wastewater treatment plant by reviewing COD, BOD and TSS parameters over the

---

period of one year. The results showed that, with the removal of 92, 94 and 96% of pollutants, respectively, the aforementioned treatment plant has a good efficiency in wastewater treatment [5].

In another study in Bukan conducted by Hosseini and Rahimzadeh (2006), the efficiency of the aeration lagoon of a treatment plant with values of 82, 38 and 4.3 mg/L for COD, Oil and TSS, respectively, in the output wastewater was confirmed. Efficiency of removal at this treatment plant during the four seasons was an average of 9.82, 45.88 and 75.80% respectively, for the abovementioned parameters [6].

The steel industry is one of the most important consumers of water and Khuzestan Steel Complex, due to climatic conditions of its location, consumes large amounts of water for various purposes.

This research designs and presents a new approach based on models of data envelopment analysis (DEA) to assess the performance of wastewater treatment plant of Khuzestan Steel Company that can be adopted to evaluate the current performance of the treatment plant in removal of pollutants and also forecast the quality of the output wastewater in the future. Therefore, to measure the performance of the treatment plant during the studied years (2009-2014), first the treatment processes were examined and input and output parameters of the treatment plant (Oil, COD, TSS, pH) were determined. Then, a CCR multiplier model was used for ranking efficient units and for measuring the performance of the treatment plant compared to the previous year; Malmquist Productivity Index (MPI) was used for calculating the efficiency and performance trends over time; Window Analysis was used in the form of data envelopment analysis models (DEA). The results of the analysis of the efficiency of the treatment plant over the studied years using these models demonstrated the power of DEA models to calculate and distinguish the years in terms of efficiency.

RESEARCH METHOD

Studied area: Khuzestan Steel Company Treatment Plant

With an area of 8.3 square kilometers, Khuzestan Steel Company is located on the 10th kilometer of Ahwaz-Imam Khomeini Port road. Khuzestan Steel Company wastewater treatment plant was established in 2006 and began operation in 2008. Wastewater treatment plant was constructed next to the south wing of the factory. The current capacity of the wastewater treatment plant is 3000 m³/h and in the future, it can be increased to 5715 m³/h. The wastewater produced by various units of Khuzestan Steel Complex enters the main canal through two (eastern- southern) canals.

This treatment plant uses physical/chemical treatment methods in several stages during the operation (such as increasing polyelectrolyte and alum and directing the wastewater to settling basins in order to reduce suspended materials, etc.). The effluent is discharged directly to Maleh River by considering environmental standards and eventually enters Shadegan international wetland and some of it is employed to irrigate the company's green area. (Khuzestan Steel Company Public Relations Department, 2012). The treatment process of this plant is shown in Figure 1.

Sampling and analysis methods

In this research, the data from raw sewage and output wastewater of Khuzestan Steel Company industrial wastewater treatment plant were studied. Since for modeling data that have a high degree of accuracy and richness in the studied period are required, parameters and quality indicators were used that create an output for an input (2009-2014). Thus, Oil, COD, TSS and pH factors were selected. Raw sewage and output wastewater were sampled to measure and monitor the above-mentioned parameters and based on the book *Standard Methods for the Examination of Water and Wastewater*, input sewage samples were kept in polyethylene and glass containers on which the date, time and place of sampling, as well as the water temperature at the time of sampling had been written and these containers were immediately transferred to the laboratory of Khuzestan Steel Company where tests were performed on the parameters.

Algorithm of evaluating the performance and efficiency of the process using DEA

First step: Collecting the data related to Decision Making Units (DMUs) input/output. In the study of real systems, to calculate the efficiency, the first step is to determine the inputs and outputs of each DMU or decision making unit so that they reflect the efficiency. In analyzing the efficiency of treatment plants, determining inputs and outputs is particularly important because each DMU or time period has numerous inputs and outputs, considering a lot of them or ignoring them will cause some problems. After determining
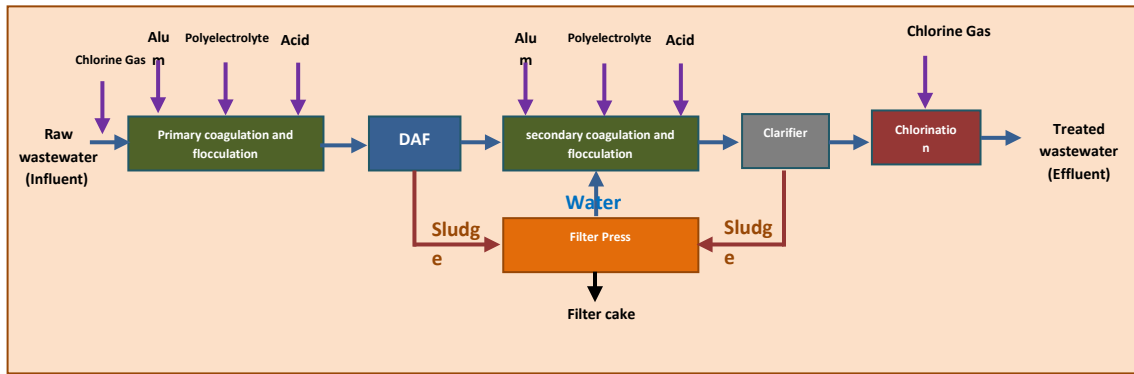
Figure 1. Schematic of the process of Khuzestan Steel Company industrial wastewater treatment plant

the inputs and outputs of each DMU, to compare and measure the efficiency of DMUs, the data related to each DMU were collected.Each year, 24 samples (2 samples per month) were taken for the 4 input and output parameters (Oil, COD, TSS, pH) and it could be stated that each year we had 24 DMUs and over a six-year research period, a total of 144 DMUs were calculated.

Second step: After collecting the data, efficiency of all DMUs was calculated using a CCR model. In this research, the data related to all DMUs from 2009 to 2014 (each year includes 24 DMUs, where DMU-1 represents August and DMU-24 represents July) were used for the input (Oil, COD, TSS, pH) and output (Oil, COD, TSS, pH) parameters. (Similar input and output parameters).

Third step: Using Malmquist criterion, the performance of units was compared to the previous year.

Fourth step: Using Windows Analysis, the performance trend of a single unit over time was calculated.

Analysis of the data and modeling

It is noteworthy that for analyzing the data, modeling the evaluation of the performance of the treatment house and determining its efficiency, GAMS software was used.

Treatment process inputs and outputs

As mentioned above, input and output parameters have been assumed to be similar, that is, for any number of inputs, there will be the same number of outputs. Table 1 shows the input and output parameters. In Table 1, I stands for the number of input parameters and O stands for the number of output parameters. It should be noted that the number of DMUs for each input and output parameter is 144 (144 inputs and 144 outputs for each parameter).

Table 1. Inputs and outputs of the model

Parameter	Output	Parameter	Input
Oil	O_1	Oil	I_1
COD	O_2	COD	I_2
TSS	O_3	TSS	I_3
pH	O_4	pH	I_4

Data Envelopment Analysis (DEA)

DEA is a method adopted to measure the relative efficiency of decision making units (DMUs). In DEA, the criteria are not weighted by the decision maker and this is done by the model in a way that each decision making unit (DMU) achieves its highest level of efficiency.

Efficiency is defined as the ratio of output to input. When there are multiple inputs and outputs, efficiency is defined as the ratio of weighted total outputs to weighted total inputs. If the values of the inputs and outputs are known, efficiency is simply calculated as follows:

$$TE_i = \frac{u_1 y_{1i} + \ldots + u_s y_{si}}{v_1 x_{1i} + \ldots + v_m x_{mi}}$$

where v is the input value and u is the output value of the i-th unit.

DEA-CCR model: In this method, with the help of some simple assumptions and using the data obtained from the units, the efficiency frontier is determined and by calculating the distance of each unit from the determined frontier (in one direction) the efficiency of units is calculated. CCR can be considered as the most rudimentary model of this family which was developed by Charnes, Cooper and Rhodes in 1987 inspired by the work of Farrell (1957) [10].

The linear programming model which is employed to calculate the efficiency of CCR is as follows:

$$\text{Max } \theta = \frac{1}{Eff_{DEA-CCR}^O}, \qquad \sum_{j=1}^{n} \lambda_j Y_j \leq X_o, \sum_{j=1}^{n} \lambda_j Y_j \geq \theta Y_o$$

Malmquist Productivity Index (MPI): To set a quantitative goal related to the value of efficiency, the past trends of the evaluated units should be examined and MPI is a powerful tool to study the past. MPI considers two factors: the unit's changes compared to its previous condition and the changes in production frontier which is determined by the best members of the target population.

$$MPI = \frac{\theta^{t+1}(x_p^{t+1}, y_p^{t+1})}{\theta^t(x_p^t, y_p^t)} \sqrt{\frac{\theta^t(x_p^t, y_p^t) \times \theta^t(x_p^{t+1}, y_p^{t+1})}{\theta^{t+1}(x_p^t, y_p^t) \times \theta^{t+1}(x_p^{t+1}, y_p^{t+1})}}$$

The first fraction measures the efficiency change between the periods t+1 and t and the second fraction shows the technical change or, in other words, the change in production frontier. The amount of technical change, efficiency change and MPI change for each unit was presented. As mentioned previously, productivity index is divided into the two factors of efficiency change and technical change. The slightest change in either one affects MPI and the following cases are possible:

MPI>1 indicates an increase in efficiency and progress is observed.

MPI<1 indicates a decrease in efficiency and progress is not observed.

MPI=1 indicates that no efficiency change has occurred between t and t+1. [10]

Windows Analysis model: One criticism of DEA models is that the efficiency calculated using this method is past efficiency. In other words, the efficiency calculated using this method is forgotten efficiency.

Window analysis is a time-dependent version of data envelopment analysis models. The main idea of this approach is that each unit in each period is considered as a separate unit from other periods. But each unit is not compared with all units in all the periods. A subset of the total time data is selected and each unit is measured separately from other periods of that subset. Window analysis generalizes the concept of moving means to detect the efficiency of the units over time. According to this model, each unit in each time window is treated as an independent unit at other times. This approach enables us to compare the efficiency of each unit at different periods. By increasing the number of units, window analysis also increases the separability of the DEA models. Remember that selecting the width of the window (a subset of the overall data) is the most important part. This choice should be small enough to minimize unfair comparisons over time and also large enough to provide a suitable data sample [9].

RESULTS

The present research was conducted based on the data gathered over a period of six years from 2009 to 2014. The results of the analyses conducted on Oil, COD, TSS and pH parameters of the raw sewage entering the treatment plant and the output wastewater are presented in Table 2 in the form of decision making units (DMUs).

Table 2. Inputs and outputs of decision making units (DMUs). The measurement unit of Oil, COD and TSS parameters in the input and output of the treatment plant is mg/L.

Year		Input (Oil)	Input (COD)	Input (TSS)	Input (pH)	Output (Oil)	Output (COD)	Output (TSS)	Output (pH)
2009	Mean	9.733	85.817	58.092	7.938	4.242	43.929	14.000	7.700
	Std. Dev.	8.470	59.619	53.557	0.186	4.311	23.760	7.945	0.232
	Min	1.3	26	9	7.5	0.3	11	3	7.2
	Max	37	254	271	8.3	20	115	35	8.1
2010	Mean	4.317	69.333	45.775	8.075	1.883	25.458	12.896	7.850
	Std. Dev.	4.473	53.921	35.277	0.217	2.676	10.371	4.191	0.159
	Min	0.6	25	14	7.8	0.2	3	6	7.6
	Max	22	261	150	8.6	11	40	22	8.2
2011	Mean	4.279	55.133	55.825	7.942	2.333	38.500	21.750	7.725
	Std. Dev.	2.960	9.644	26.411	0.289	1.001	6.711	8.774	0.285
	Min	1.2	40	26	7.1	0.6	25	6	6.9
	Max	15	81	129	8.5	4.5	53	48	8.2
2012	Mean	7.435	62.058	71.446	7.982	2.863	33.083	13.917	7.663
	Std. Dev.	8.430	20.317	38.274	0.261	0.283	13.897	5.770	0.300
	Min	2.9	22	17	7.5	2.4	6	4	7
	Max	40	103	162	8.6	3.5	62	32	8.5
2013	Mean	4.571	65.221	74.168	8.079	3.596	20.747	15.333	7.854
	Std. Dev.	1.926	23.135	39.179	0.257	1.434	10.448	11.126	0.195
	Min	2.9	33.8	20	7.6	2.6	13	9	7.5
	Max	11.3	111	210	8.6	10.1	64	66	8.2
2014	Mean	3.617	46.625	61.583	8.004	2.775	23.417	20.833	7.800
	Std. Dev.	0.725	14.832	33.628	0.146	0.182	6.928	17.264	0.147
	Min	2.8	29	23	7.7	2.2	12	11	7.4
	Max	5.1	98	143	8.3	3.1	40	99	8

As you can see, the range of annual mean of Oil in the raw input sewage varies from 62.3 mg/L in 2014 to 73.9 in 2009 and in the output wastewater from 88.1 mg/L in 2010 to 24.4 in 2009. The total mean in the raw input sewage and the output wastewater has been estimated to be 66.5 and 95.2 mg/L, respectively. Also, regarding TSS, BOD and pH parameters, according to Table 2, the range of annual mean of COD in the raw input sewage varies from 63.46 mg/L in 2014 to 82.85 in 2009 and in the output wastewater from 75.20 mg/L in 2013 to 93.43 mg/L in 2009. The total mean in the raw input sewage and output wastewater were estimated to be 84.63 and 86.30 mg/L, respectively. The range of annual mean of TSS in the raw input sewage varies from 78.45 mg/L in 2010 to 17.74 in 2013 and in the output wastewater from 92.12 mg/L in 2010 to 75.21 in 2011. The total mean in the raw input sewage and the output wastewater was estimated to be 15.61 and 45.16 mg/L, respectively. Finally, the annual mean of pH in the range of the raw input sewage varies from 93.7 in 2009 to 98.8 in 2013 and the output wastewater varies from 66.7 mg/L in 2012 to 86.7 in 2013. The total mean in the raw input sewage and the output wastewater was estimated to be 8 and 77.7, respectively.

Results of process performance evaluation using DEA: As explained above, in order to measure efficiency and compare the units, the data from 2009 till 2014 were used. Decision making units (DMUs), which are the years studied in this research, are presented in Table 3. Efficiency of the treatment

system during these years was calculated based on inputs and outputs using DEA-RCC, the results of which are shown in Table 3. According to the results, the number of efficient units in 2014, 2013, 2012, 2011, 2010 and 2009 was 7, 7, 9, 8, 12 and 10, respectively, and the number of inefficient units in 2014, 2013, 2012, 2011, 2010 and 2009 was 17, 17, 15, 16, 12 and 14, respectively (Table 3).

In order to compare the performance of the units with the previous year, Malmquist Productivity Index was used, the results of which are presented in Table 4. Furthermore, to compare the efficiency of each unit in different periods and, in other words, determine the efficiency of each unit over time, Window Analysis was used, the results of which are presented in Table 5.

Results of Malmquist productivity index (MPI) model based on CCR: A summary of the results obtained from the MPI model based on DEA distance function over the studied years (2009-2014) is presented in Table 4. It should be noted that TC represents Technical Change, EC represents Efficiency Change and MPI represents Malmquist Productivity Index.

Results of Window Analysis: In the present study, the length of the window was 3 years. The first window (W1) includes Oil, TSS, COD and pH parameters in 2009, 2010 and 2011; the second window (W2) includes Oil, TSS, COD and pH parameters in 2010, 2011 and 2012; the third window (W3) includes COD, TSS, Oil and pH parameters in 2011, 2012 and 2013 and the fourth window (W4) includes Oil, TSS, COD and pH parameters in 2012, 2013 and 2014.

Table 3. Results obtained from the DEA-RCC model

	2009	2010	2011	2012	2013	2014
DMU01	0.7725	1	1	1	0.9133	1
DMU02	0.7844	0.9083	1	1	1	0.9727
DMU03	0.7958	0.8589	1	0.9398	0.8331	1
DMU04	0.8638	0.88	0.8658	0.9674	0.9204	0.9443
DMU05	0.785	0.8967	0.9551	0.9917	1	0.9429
DMU06	0.7956	1	0.8404	1	1	0.8661
DMU07	0.8907	0.8626	0.7691	0.9257	0.8966	1
DMU08	0.7252	1	1	1	0.9217	1
DMU09	0.8779	0.9269	0.9039	0.8701	0.7732	0.9047
DMU10	0.6869	0.9609	1	0.9368	1	0.9326
DMU11	1	1	0.9813	0.9499	0.8907	0.9573
DMU12	0.9331	0.9707	1	1	0.9405	0.9769
DMU13	1	0.9487	0.9815	0.8352	1	1
DMU14	0.8512	0.8611	1	0.9688	1	1
DMU15	1	1	0.955	0.967	0.8197	1
DMU16	0.8149	0.9298	0.89	0.9318	0.9185	0.9612
DMU17	0.9565	0.9084	1	1	1	1
DMU18	0.9006	0.9076	0.8591	0.9336	0.8992	0.9194
DMU19	1	0.8569	0.9433	0.9255	1	0.8817
DMU20	1	0.7996	0.9183	0.9683	1	1
DMU21	1	0.9231	0.7956	0.8819	0.8172	0.839
DMU22	0.8895	1	0.9532	0.8811	1	0.9161
DMU23	0.8362	1	0.8483	1	1	0.9657
DMU24	1	0.8827	1	1	1	1
# of efficient units	7	7	9	8	12	10
# of inefficient units	17	17	15	16	12	14

Table 4. Summary of the results obtained from Malmquist Productivity Index

Year	Mean(geometric)	Mean(arithmetic)	MPI Std. Dev.	Min	Max
2009/2010					
MPI	1.194	1.261	0.511	0.790	3.258
EC	1.047	1.049	0.067	0.948	1.197
TC	1.141	1.191	0.425	0.776	2.836
2010/2011					
MPI	0.572	0.603	0.189	0.219	1.006
EC	0.966	0.968	0.062	0.842	1.061
TC	0.593	0.624	0.193	0.252	1.060
2011/2012					
MPI	0.921	1.000	0.429	0.363	2.397
EC	1.034	1.036	0.065	0.924	1.165
TC	0.891	0.961	0.404	0.363	2.397
2012/2013					
MPI	0.870	0.885	0.153	0.431	1.150
EC	0.979	0.982	0.063	0.835	1.091
TC	0.888	0.900	0.136	0.464	*1.055
2013/2014					
MPI	1.062	1.071	0.143	*0.848	1.379
EC	1.021	1.023	0.071	0.911	1.183
TC	1.040	*1.045	0.097	0.848	1.281

In these windows, units of each period are independent of other periods.Thus, there are 72 units. (As stated in section 3 on methodology, each year includes 24 DMUs, DMU1 stands for August and DMU24 stands for July) In other words, these 72 units comprise the efficiency frontier. For each unit, there are 3 types of data that their efficiency should be calculated by using the frontier created by these 72 units. Table 5 shows the efficiency of the decision making units (DMUs) in multiple windows. For example, in the first row, it shows the data related to the mean of windows 1 to 4 for DMU01.

by calculating the mean of efficiencies calculated from these 4 windows, the mean efficiency of the first unit in the period 2009 to 2014 was calculated, which is equal to 92.0. The results of the Window Analysis model are summarized in Table 5.Then, in order to determine the most important factors affecting efficiency, sensitivity analysis was performed, in which the input and output parameters (TSS, Oil, COD and pH) were removed to determine which changes occur in the efficiency of the units. The results obtained from the sensitivity analysis are presented in Table 6.

Table 5. Summary of the results obtained from Window Analysis model

	W1	W2	W3	W4	Mean
DMU01	0.9049	0.9254	0.9089	0.9622	0.925
DMU02	0.8658	0.8972	0.9143	0.9498	0.907
DMU03	0.8548	0.8647	0.8622	0.9257	0.877
DMU04	0.8484	0.8673	0.8676	0.9242	0.877
DMU05	0.8625	0.8983	0.9446	0.9703	0.919
DMU06	0.8641	0.913	0.8954	0.9105	0.896
DMU07	0.8529	0.8344	0.8206	0.9293	0.859
DMU08	0.9139	0.9779	0.9505	0.9607	0.951
DMU09	0.8673	0.8854	0.8123	0.8813	0.862
DMU10	0.9053	0.9107	0.9192	0.9623	0.924
DMU11	0.9659	0.9244	0.8774	0.9463	0.929
DMU12	0.9496	0.9797	0.929	0.9522	0.953
DMU13	0.9404	0.8882	0.9129	0.9696	0.928
DMU14	0.9376	0.9813	0.9371	0.9559	0.953
DMU15	0.9656	0.9646	0.9067	0.9534	0.948
DMU16	0.9101	0.9018	0.8862	0.9418	0.910
DMU17	0.9332	0.9853	0.9911	1	0.977
DMU18	0.8829	0.8807	0.8836	0.9425	0.897
DMU19	0.8872	0.8865	0.942	0.9441	0.915
DMU20	0.923	0.9083	0.895	0.9888	0.929
DMU21	0.8927	0.8458	0.7985	0.8773	0.854
DMU22	0.886	0.9035	0.8871	0.9365	0.903
DMU23	0.8742	0.9125	0.8848	0.9877	0.915
DMU24	0.9137	0.889	0.889	0.9498	0.910

Each of these windows has a mean value of efficiency that is associated with that unit. Finally,

Table 6. Mean efficiency change of the units in the Window-Sensitivity analysis

	Oil	COD	TSS	pH
DMU01	0.0313	0.0281	0.0248	0.3526
DMU02	0.0535	0.0041	0.0418	0.3679
DMU03	0.0186	0.0154	0.0357	0.4038
DMU04	0.0254	0.0067	0.0095	0.5029
DMU05	0.0227	0.0062	0.0441	0.3640
DMU06	0.0094	0.0240	0.0832	0.3214
DMU07	0.0478	0.0239	0.0138	0.4301
DMU08	0.0141	0.0067	0.0313	0.2733
DMU09	0.0155	0.0065	0.0150	0.5228
DMU10	0.0366	0.0197	0.0352	0.4202
DMU11	0.0045	0.0261	0.0140	0.3842
DMU12	0.0111	0.0047	0.0365	0.4148
DMU13	0.0082	0.0111	0.0652	0.3983
DMU14	0.0377	0.0035	0.0269	0.4628
DMU15	0.0019	0.0200	0.0652	0.4370
DMU16	0.0203	0.0048	0.0450	0.4558
DMU17	0.0175	0.0133	0.0611	0.2950
DMU18	0.0272	0.0132	0.0141	0.4021
DMU19	0.0035	0.0283	0.0387	0.5134
DMU20	0.0300	0.0116	0.0188	0.4615
DMU21	0.0198	0.0173	0.0102	0.4589
DMU22	0.0260	0.0167	0.0389	0.4132
DMU23	0.0323	0.0100	0.0391	0.3095
DMU24	0.0144	0.0200	0.0532	0.3466
Mean	0.0220	0.0142	0.0359	0.4047
Std. Dev	0.0134	0.0081	0.0196	0.0674

DISCUSSION AND CONCLUSION

In this paper, the performance of Khuzestan Steel Company treatment plant was studied using Data Envelopment Analysis based on the model inputs and outputs. Based on the results related to 144 decision making units, evaluation of the performance of the treatment plant during 2009-2014 indicates that in removal of pollutants, the highest removal efficiency was that of COD in the wastewater entering the treatment plant with an efficiency of 68% in 2013, the highest removal efficiency of Oil was 62% in 2012, the highest removal efficiency of TSS was 81% in 2012 and the highest efficiency in reduction of pH was 4% in 2012. In general, it can be concluded that Khuzestan Steel Company industrial wastewater treatment plant with removal of 81% of TSS from wastewater accounts for the highest efficiency in the removal of the pollutants (Figure 1). Then, Malmquist Productivity Index (MPI) was adopted to explain the changes in total productivity. Based on the results obtained from this index presented in Table 4 and Figure 2, the performance of Khuzestan Steel Company wastewater treatment plant from 2009 to 2010 has made progress both in terms of efficiency and technique (values larger than one) and therefore, it has been efficient from 2009 to 2010 (Malmquist

productivity index is larger than 1). However, during the 2010-2011 period, there has been a great technical drawback (value of 59.0 for TC) but in terms of efficiency, the performance has been the same as in the previous year and there has been no progress (the value of EC is close to 1).

By multiplying these two factors into each other, the productivity index for this unit during 2010-2011 will be 57.0 which indicates that during this period the unit has not been efficient and had negative progress. During the 2011-2012 period, it had progress in terms of technical and efficiency change (TC value is 89.0 and EC value is 03.1) and finally, the value of productivity index during the 2011-2012 period will be 1, which indicates that during this period, the unit has been efficient and has made progress. Figure 2 confirms the fact that during these periods (2009-2010 and 2011-2012), there has been no considerable progress in the performance of the treatment plant in terms of efficiency and the differences in the productivity index have been due to technical progress made in some units. However, in 2013 and 2014, the efficiency of the treatment plant had a considerable progress. Also, Window Analysis and Sensitivity Analysis were employed to measure efficiency and performance trend over time in the form of Data Envelopment Analysis (DEA) models. Based on the results obtained from Window
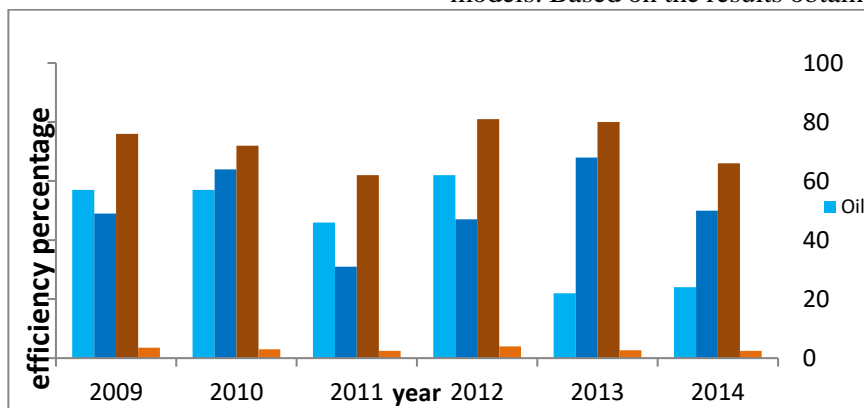
Fig. 1. Percentage of efficiency of removal of COD, TSS, Oil and pH from the output wastewater of Khuzestan Steel Company treatment plant during 2009-2014

	2009-2010	2010-2011	2011-2012	2012-2013	2013-2014
(TC)Technical Change	1.14	0.59	0.89	0.88	1.04
(EC)Efficiency Change	1.04	0.96	1.03	0.97	1.02
(MPI)Malmquist Productivity Index	1.19	0.57	0.92	0.87	1.06
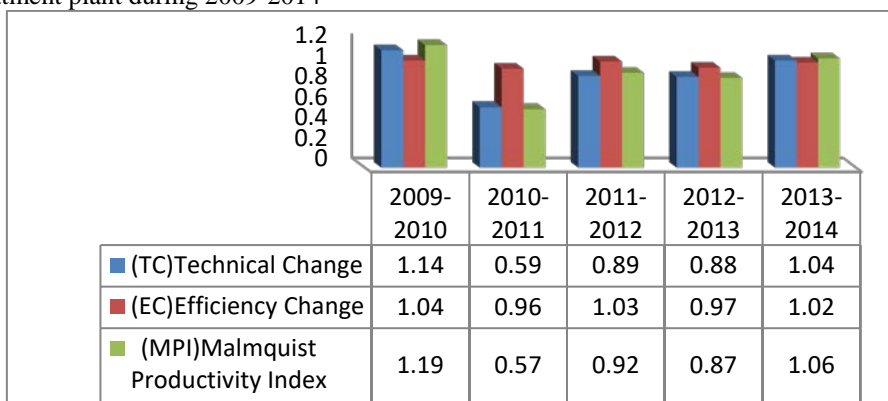
Fig. 2. Results of mean changes of Malmquist productivity index during the studied period (2009-2014)

Analysis presented in Table 5, there is no considerable difference between the amounts of efficiency obtained in Window Analysis of the units over the studied years. Table 6 and Figure 3 confirm that removing COD, Oil, TSS and pH indices change the mean efficiency of each unit 01.0, 02.0, 03.0 and 40.0, respectively. In case of pH, this change is considerable. Generally, it could be stated that, considering the used models and conducted analyses in each part, it is clear that based on the results obtained from the models used in this article, except for few of the units, no conspicuous difference between the performances of the units was observed. Regardless of the individual performance of the units, it could be stated that there is a conspicuous balance in the system.

Finally, in order to reuse the wastewater or discharge it to surface water resources, the amount of each of Oil, COD, TSS and pH parameters should be within the standard limits. In this regard, the Iranian Environmental Protection Agency has provided guidelines based on the type of use of the wastewater. According to these standards, in order to discharge the wastewater into the surface water resources, density of Oil, COD and TSS must be 10, 40 and 60 mg/L, respectively and pH must be 5.6-5,8 [10].

The average density of the abovementioned parameters during the studied years in the output wastewater of Khuzestan Steel Company treatment plant is as follows: Oil=95.2, COD=86.30 and TSS=45.16 mg/L and pH is 5.6-5.8, which indicates compliance with the standards of the Iranian Environmental Protection Agency for discharging wastewater into surface water resources.

Comparisons were made between the present research and previous studies in this area, some of which are mentioned in the following. In a study, the efficiency of the aeration lagoon of Bukan treatment plant conducted by Hoseini and Rahimzadeh (2006), with values of 82, 38 and 4.3 mg/L for COD, Oil and TSS, respectively, in the output wastewater was confirmed. The efficiency of the system with values of 82, 38 and 4.3 mg/L for COD, Oil and TSS, respectively, in the output wastewater was confirmed. Efficiency of removal at this treatment plant during the studied seasons was an average of 9.82, 45.88 and 75.80%, respectively, for the abovementioned parameters [3] which is consistent with the present research.

In a study conducted by Kimiyai *et al.,* Oil, TSS and COD qualitative parameters in the input and output sewage of the wastewater treatment plant of Buali Industrial City, Hamedan were evaluated and pollutants removal efficiency for the studied parameters was calculated as 68, 88.89 and 25.79%, respectively [11], which is consistent with the data of the present research. In a study conducted by Ardabilian *et al.,* the efficiency of removal of BOD, TSS and COD from the input sewage of Zanjan City treatment plant was found to be 25.87, 91.77 and 29.87%, respectively [12], which is consistent with the data of the present research. Also, given the limitation of water resources in Iran and Ahvaz City, as well as the current critical condition of the local area and considering the high efficiency of Khuzestan Steel Company industrial wastewater treatment plant system in removing pollutants and the level of the studied key parameters (Oil, COD, TSS) which is lower than the permissible environmental level in the output wastewater, it is recommended that advanced treatment methods be used for treatment of output wastewater and the treated wastewater be used for industrial plants which do not need high-quality water.
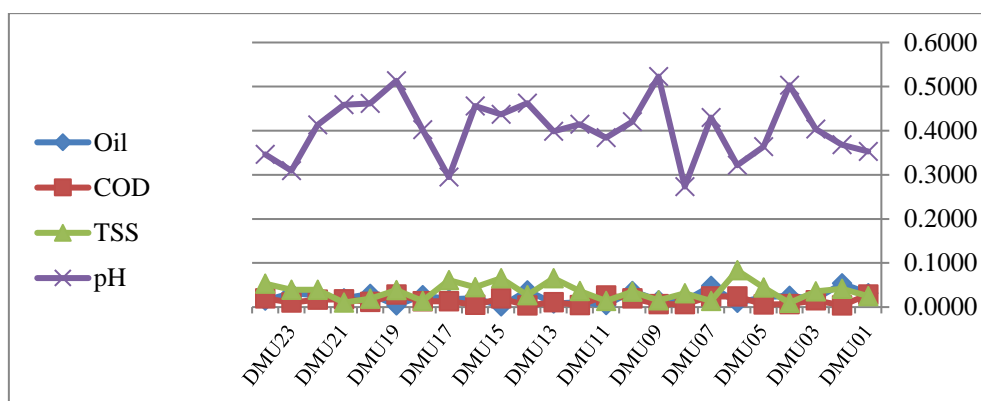
Fig. 3. Mean efficiency changes of the units in the Window-Sensitivity analysis

REFERENCES

1. J.-L. Hu, Sh.-Ch. Wang, F.-Y. Yeh, Total-factor water efficiency of regions in China. *Resources Policy*. 31, 217, 2006.
2. R. Khorram, Mehdi. Modern Steps in Fundamental Studies of Comprehensive Urban Sewage Plans, Daneshjoo Publication, 2002.
3. S. Venkata Mohan, S. Veer Raghavulu, G. Mohanakrishna, S. Srikanth, P.N. Sarma, Optimization and evaluation of fermentative hydrogen production and wastewater treatment processes using data enveloping analysis (DEA) and Taguchi design of experimental (DOE) methodology, *International Journal of Hydrogen Energy*. 34 (1), 216 (2009).
4. R. Sala-Garrido, F. Hernández-Sancho, M. Molinos-Senante, Assessing the efficiency of wastewater treatment plants in an uncertain context: a DEA with tolerances approach, *Environmental Science & Policy*. 18, 34 (2012).
5. M. M. Bagher, B. Sh. O'Sadat, A Study of the Efficiency of Ekbatan City Wastewater Treatment Plant during 2000-2001. *Feyz Scientific-Research Quarterly, Kashan University of Medical Sciences and Healthcare, Iran*, 25, 40 (2003).
6. H. M. Mokhtar, R. Esmail, A Study of the Efficiency of the Lagoon Using Mechanical Aerator in Reducing the Level of TSS and COD in Bukan Wastewater Treatment Plant in 2006. *The Tenth National Conference on Environmental Health, Hamedan, Iran*. 2007.
7. M. Pourtarghabeh, Alireza, M. Shokouhiyan, Evaluation of the Performance of Industrial Wastewater Treatment Plants Using Artificial Neural Network. *The Sixth National Conference on Environmental Engineering, Faculty of Environmental Sciences*, University of Tehran, Tehran, Iran. 2012.
8. L. Castelli, R. Pesenti, W.Ukovich, DEA- like models for the efficiency evaluation of hierarchically structured units, *European Journal of Operational Research*, **154**, 465 (2004).
9. L. Liang, F. Yang, W.D. Cook, J. Zhu, DEA models for supply chain efficiency evaluation, *Annals of Operations Research*, **145**, 35 (2006).
10. The Environmental Protection Agency. Environmental Regulations and Standards. Published by The Environmental Protection Agency. 1999.
11. K. Alireza, A. Ghasem, J. M. Javad, M. T. Abulfazl, A Study of the Performance of Aeration Lagoons in the wastewater treatment of Buali Industrial City, Hamedan, *The Tenth National Conference on Environmental Health*, Hamedan, Iran. 2007.
12. P. Ardabilian, H. Sadeghi, A. Nabai, M. Ardabilian, Evaluation of the Performance of Zanjan Sewage Treatment Plant, *Health and Hygiene Quarterly*. 1(3), 67 (2010).

ОЦЕНКА НА ЕФЕКТИВНОСТТА НА ПРЕЧИСТВАТЕЛНИ СТАНЦИИ ЗА ИНДУСТРИАЛНА ОТПАДНА ВОДА С ИЗПОЛЗВАНЕ НА АНАЛИЗ НА ОБХВАТА НА ДАННИТЕ С ПРИМЕРЕН СЛУЧАЙ ПРЕЧИСТВАТЕЛНАТА СТАНЦИЯ НА ХУЗЕСТАНСКИЯ ЗАВОД ЗА ПРОИЗВОДСТВО НА СТОМАНА

К. Рахбари[1], А. Х. Хасани[*2], М. Р. Мерган[3], А. Х. Джавид[4]

[1] *Департамент по наука за околната среда, Факултет по околна среда и енергия, Техерански клон за наука и изследвания, Ислямски Азад университет, Техеран, Иран*

[2] *Департамент по инженерство на околната среда, Факултет по околна среда и енергия, Техерански клон за наука и изследвания, Ислямски Азад университет, Техеран, Иран*

[3] *Отдел по мениджмънт, Техерански университет, Иран*

[4] *Департамент по наука за околната среда, Факултет по наука и технология на морето, Техерански клон за наука и изследвания, Ислямски Азад университет, Техеран, Иран*

(Резюме)

Разработването на математически модел, позволяващ промяна на експерименталните параметри и променливи дава възможност не само за оценка, но и за прогнозиране на работата на пречиствателни станции. В настоящата статия, за оценка на ефективността на пречиствателната станция на Хузестанския завод за стомана е използван моделът на анализ на обхвата на данните (АОД). Входните и изходните параметри (химически необходим кислород, масло, общоо количество на твърди вещества и pH) са определени през периода (2009-2014 г.). Коефициентът на продуктивност на Malmquist е използван за изразяване на промените в тоталната продуктивност, а Window анализът – за изчисляване на ефективността и тенденциите за работа с времето. Резултатите показват, че ефективността на пречиствателната станция по отношение на химически необходимия кислород, маслото, общото количество на твърди вещества и pH е съответно 68%, 62%, 81% и 4%. Ефективността на станцията за отстраняване на замърсители е около 70%, така че системата работи ефективно и изходящата вода съответства на стандартите за околна среда. Резултатите показват също така широките възможности на АОД моделите за изчисляване и класифициране на ефективността по години.

Study on intrinsic sulfidation of iron oxides and oxidation behavior of sulfidation products

L. Shang[1,2]*, J. Li[1], Sh. Zhao[2], Y. Tian[1], Zh. Zhang[2], L. Zhang[3]

[1] *School of Metallurgy, Northeastern University, Shenyang 110004, China;*
[2] *College of Chemistry, Chemical Engineering and Environmental Engineering, Liaoning Shihua University, Fushun 113001, China;*
[3] *College of Petroleum Engineering, Liaoning Shihua University, Fushun 113001, China*

The study simulated the sulfur corrosion process in an oil tank to evaluate intrinsic sulfidation of iron oxides and oxidation behavior of sulfidation products at room temperature. The methods of SEM and EDS were used to characterize the microstructure and surface state of the sulfidation products of Fe_2O_3, Fe_3O_4 and $Fe(OH)_3$, which are the dominant components of rust. The surface chemical state of sulfidation and oxidation products was characterized by XPS measurement to analyze the oxidation degree and oxidation mechanism of the sulfidation products. The results showed that three kinds of iron oxides can produce the same kind of iron-sulfur compounds after sulfidation, but the microstructure and elemental distributions of these iron-sulfur compounds are different. The main components of the sulfur corrosion products of the three iron oxides are identical. The sulfur corrosion process of iron oxides converts iron oxides into FeS_2 and $FeSO_4$, which is accompanied by the formation and transformation of FeS and S_8. At room temperature the sulfidation products of iron-sulfur compounds are finally oxidized to Fe_2O_3 and $FeSO_4$.

Keywords: iron oxides; sulfidation; oxidation; iron-sulfur compounds; XPS.

INTRODUCTION

In the process of oil refining, storage and transportation, the active sulfur in the oil will react with the rust (the dominant components are iron oxides such as Fe_2O_3, Fe_3O_4 and $Fe(OH)_3$) on the inner wall of the device, which can generate iron-sulfur compounds with a certain pyrophoricity. Fire and explosion accidents caused by self-ignition of corrosion products of sulfur occasionally happen [1-3]. Many scholars have extensively investigated the mechanisms of spontaneous combustion of iron-sulfur compounds [4-8].

Corrosion of iron in H_2S containing solutions is a general problem in crude oil and natural gas production, and is generally referred to as sour corrosion. Aqueous H_2S solutions promote corrosion of steels [9-15], but the exact nature and mechanisms of corrosion strongly depend on the reaction conditions [16-18]. While the process has been widely investigated for pure iron and carbon steels, there is still a lack of understanding of the reaction path of the corrosion products. The chemistry of the corrosion products formed during H_2S-triggered corrosion is rather complex, as there are many different solids consisting only of iron and sulfur. X-ray photoemission spectroscopy (XPS) has been used to confirm the presence of the reaction products [19-22]. On the other hand, the corrosion product can be rapidly oxidized in the air and release heat. Different types of materials for the

formation of sulfur compounds and changed sulfidation environment will make the sulfidation products have different oxidation pyrophoricity.

Although there were many investigations about the sour corrosion and oxidation process of sulfidation products, it is not totally clear what happens in the course of the sulfidation process and oxidation process. The objective of this work was to investigate intrinsic sulfidation behaviors of iron oxides in H_2S, N_2 and O_2 gas atmosphere and the oxidation behaviors of sulfidation products at room temperature. In this paper, dry Fe_2O_3, Fe_3O_4 and $Fe(OH)_3$ were used by reacting with a mixture of sulfidation gas at a certain temperature, to simulate the sulfur corrosion process in an oil tank containing sulfur. Following the oxidation process of the sulfidation products, the chemical morphology of the reaction products was identified by XPS. It would be highly desirable to understand the sulfidation mechanism of iron oxides and the oxidation mechanism of sulfidation products in order to better understand the sulfidation process and oxidation process. The experimental results provided a theoretical basis for the prevention of spontaneous combustion of sulfur compounds.

EXPERIMENTAL

Experimental method

The scheme of the experimental apparatus of the sulfidation and oxidation tests is shown in Fig. 1. In the experiments, three groups of three-necked

*) To whom all correspondence should be sent:
E-mail: lyshang2011@126.com

flasks were installed in parallel to a gas bag and filled with Fe_2O_3, Fe_3O_4 and $Fe(OH)_3$, separately. This is to make sure that the sulfidation processes of the three iron oxides take place under the same conditions.
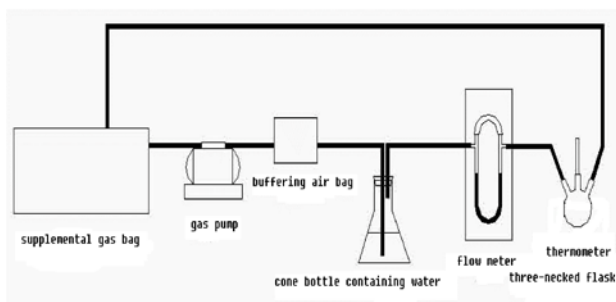
Fig. 1. Apparatus for the sulfidation and oxidation processes

Desired concentration of sulfidation gas (volume ratio of $H_2S:O_2:N_2 = 5:1:4$) was pre-configured and the gas was stored in the gas bag. Quantities of Fe_2O_3, Fe_3O_4 and $Fe(OH)_3$ samples were placed in the three-necked flasks separately. The mixture of sulfidation gas in the gas bag was pumped by a gas pump and passed through the buffering air bag, water containing cone bottle and flow meter which can detect and control flow, and then entered the three-necked flasks. The sulfidation reaction of iron oxides was carried out in the three-necked flasks. The sulfidation products were divided in two, one part was directly exposed to the air; the other part was sealed with ethanol. EDS and XPS analysis were carried out using the ethanol sealed sulfidation products. The sulfidation products directly exposed to the air were used for the oxidation process. Open both sides of the stopper, let air get into the reaction flask and react with corrosion products. The temperature was measured by a thermocouple thermometer inside the reactor. The final products were analysed by XPS.

Characterization method

The sulfided and oxidized samples were analysed by scanning electron microscopy with energy-dispersive X-ray spectroscopy (DEM-EDS) at the acceleration voltage of 30 KV and X-ray photoelectron spectroscopy (XPS) technique with an ESCALAB 250 spectrometer using monochromatic Al Kα X-ray (1486.6 eV).

RESULTS AND DISCUSSION

DEM-EDS characterization of sulfidation products

The spontaneous oxidation reaction of the sulfidation products has a strong relationship with their microstructure, and the specific surface area is different, which leads to different contact areas with oxygen. The results of sulfidation products of Fe_2O_3, Fe_3O_4 and $Fe(OH)_3$ characterized by SEM technique are shown in Fig. 2. As can be seen, there are some differences in the microstructure of the three sulfidation products. The sulfidation product of $Fe(OH)_3$ mostly consists of sheets or blocks which are more regular, and the particle size is relatively large, the specific surface area is relatively small, and is disadvantageous for the adsorption and diffusion of O_2 molecules. The particles of the sulfidation products of Fe_3O_4 and Fe_2O_3 are fine, porous, loose and the surface area is big. The small particles of the Fe_3O_4 sulfidation products are polygons, and the pore structure is more obvious, but the Fe_2O_3 sulfidation products are approximate pellets and slightly denser.
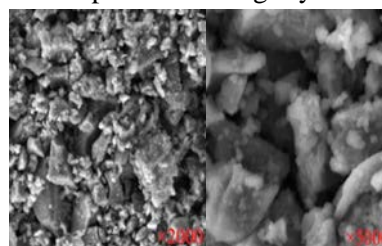
(a)　sulfidation products of $Fe(OH)_3$
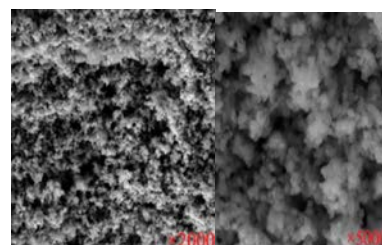
(b)　sulfidation product of Fe_3O_4
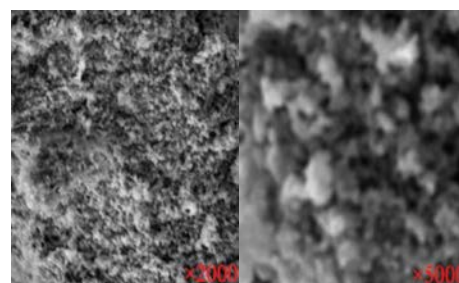
(c)　sulfidation product of Fe_2O_3

Fig. 2. SEM photographs of sulfidation products, Left: 500×, Right: 2000×

Table 1. Contents of Fe, S, O in samples (%, mass fraction)

Sample	Fe	S	O
Sulfided Fe(OH)$_3$	24.76%	38.54%	36.70%
Sulfided Fe$_3$O$_4$	22.24%	16.82%	60.94%
Sulfided Fe$_2$O$_3$	25.29%	39.08%	35.63%

(a)

(b)

(c)
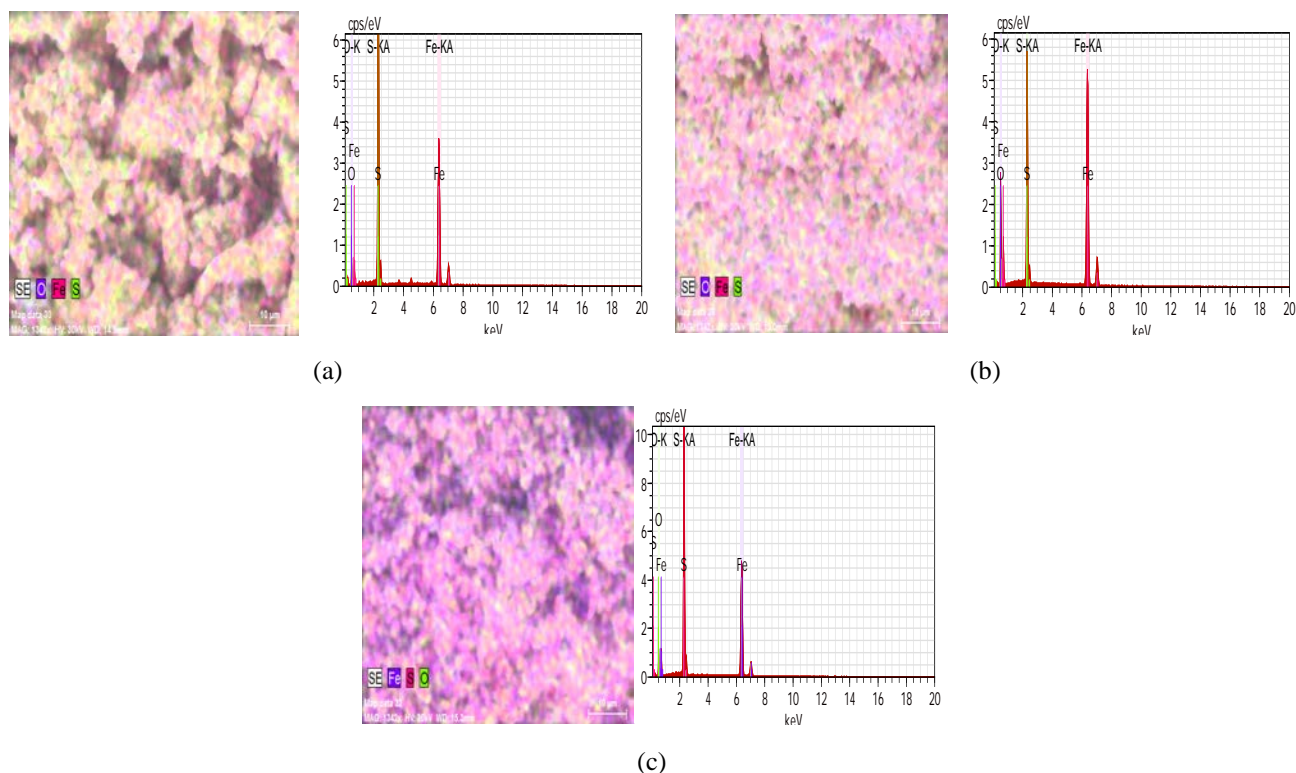
Fig. 3. EDS of sulfidation products (a) Fe(OH)$_3$ (b) Fe$_3$O$_4$ and (c) Fe$_2$O$_3$

The scanning results of Fe, S, O in the sulfide products are shown in Fig. 3. The distribution of Fe and S on the surface of the Fe(OH)$_3$ sulfidation products is more uniform, but that of O is less so. For the Fe$_3$O$_4$ sulfidation products, the distribution of various elements on the surface was more average, except for S which was more dispersed. However, the distribution of S on the surface of Fe$_2$O$_3$ sulfidation products was more concentrated, and Fe was mainly distributed in pores. The results showed that the element type of the three kinds of sulfidation products was the same, but the distribution was different. The contents of Fe, S and O in the sample are listed in Table 1.

XPS characterization of S

The binding energies of S 2p in the sulfidation products before and after oxidation are shown in Fig. 4. The binding energy at 161~161.7 eV most likely belonged to FeS. The binding energy at 161.7~163.4 eV most likely belonged to FeS$_2$. The peaks at 163.3~164.5 eV were considered to be S$_8$. The peaks at 168.3~169.4 eV were considered to be SO$_4^{2-}$. The results of curve fitting are presented in Table 2. It can be seen from Table 2 that before oxidation the S atoms in the three kinds of sulfidation products were mainly FeS$_2$, which accounted for 42.66%, 53.98% and 31.45%, respectively. Small amounts of reduced FeS, S$_8$ and partially SO$_4^{2-}$ were also contained. The SO$_4^{2-}$ in the sulfidation product after oxidation was the main form of S in the sample, and the atomic contents were by 29.71%, 17.28% and 37.39% higher than those before oxidation. After the oxidation process, the contents of FeS$_2$ and FeS decreased significantly, or even disappeared.

From the content of S, the SO$_4^{2-}$ component in the sulfide product after oxidation sharply increased, while the FeS$_2$ and FeS contents in the reduced state were obviously reduced and the S content increased in some varieties and decreased in others. It was illustrated that the low-valence S was oxidized to the high-valence SO$_4^{2-}$ in the oxidation process. However, some of the S was only oxidized to S$_8$, indicating that S of different sulfide products was oxidized to a different degree.

(a) Fe_2O_3 (in ethanol)

(b) Fe_3O_4 (in ethanol)

(c) $Fe(OH)_3$ (in ethanol)

(d) Fe_2O_3 (in air)

(e) Fe_3O_4 (in air)

(f) $Fe(OH)_3$ (in air)
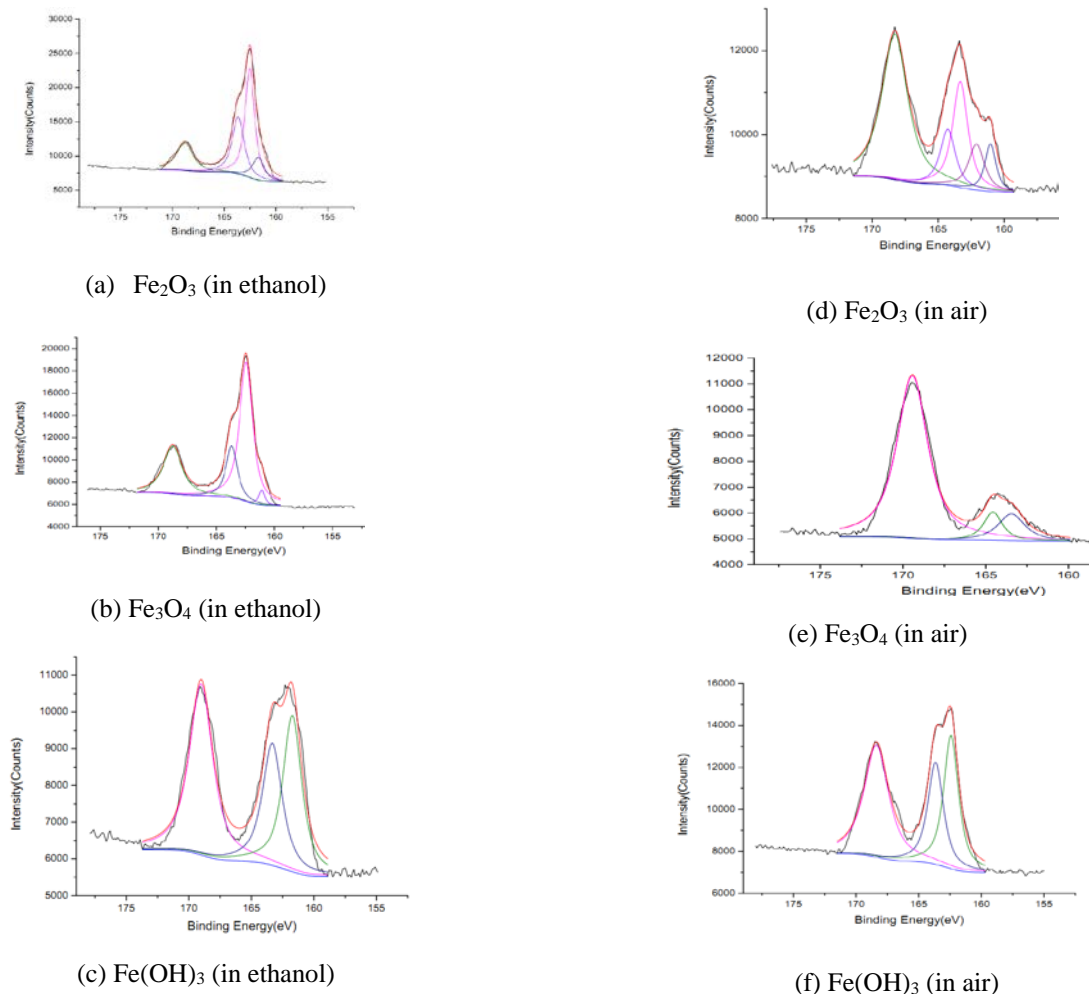
Fig. 4. XPS spectra of S 2p of sulfidation products.

XPS characterization of Fe

The binding energy of Fe 2p before and after oxidation of the three ferrosulfide compounds is shown in Fig. 5. As can be seen, the binding energy of Fe 2p existing in the form of FeS_x (mainly FeS_2) was 706.7 ~ 708.3 eV, the binding energy of Fe 2p existing in the form of Fe_2O_3 was 711.1 ~ 711.9 eV, and the binding energy of Fe atom bonded to SO_4^{2-} was 711.1 ~ 711.9 eV. The results of curve fitting are shown in Table 3. It can be seen that before oxidation, the species of Fe in the three sulfidation products were FeS_2, FeO, Fe_2O_3, and $FeSO_4$ in addition to their own non- sulfured iron oxides.

After being fully oxidized in the air, the form of Fe changed little, but the content of each component changed greatly. Comparing the three sulfidation products (Fe_2O_3, Fe_3O_4 and $Fe(OH)_3$) before and after oxidation, the contents of Fe in the form of Fe_2O_3 increased from 49.50%, 26.81% and 26.28% to 82.68%, 46.91% and 33.69%, respectively. The contents of Fe in the form of $FeSO_4$ increased from 5.82%, 12.48% and 17.78% to 11.27%, 14.31% and 26.60%, respectively. With the progress of oxidation, more and more Fe_2O_3 and

$FeSO_4$ were produced. However, the content of FeS_x and FeS_2 was greatly reduced during the oxidation process. Only 6.05% of Fe was found to be FeS_x in the oxidation product of Fe_2O_3 sulfidation product, and the existence of FeS_x was not detected in the other two oxidation products.

Analysis of the sulfidation behavior of iron oxides

In the process of iron oxide sulfidation, the reaction process of iron oxide (FO) and pure H_2S is very straightforward [23]: FO $\xrightarrow{H_2S}$ FeS+S+H_2O. The FeS produced by the reaction further reacts with S to form FeS_2: FeS $\xrightarrow{S}$ FeS_2. The change in the content of each component from the sample can be used to estimate the trend of mutual conversion between the various components.

Through the analysis above, in the actual reaction process, the remaining FeS is very little and even almost undetectable, but the content of FeS_2 is much higher. This is presumably due to the progress of the sulfidation process; H_2S is continuously oxidized to elemental S, the composition of the system, the temperature and other conditions changes will lead to the reaction of elemental S and FeS to form FeS_2 as the main

136

Table 2. Results of curve fitting of S 2p of sulfidation products

Sample	Before oxidation (in ethanol)			After oxidation (in air)		
	BE	S atom percentage (%)	Chemical state	BE	S atom percentage (%)	Chemical state
Sulfided Fe$_2$O$_3$	161.7	10.93	FeS	161	6.13	FeS
	162.5	42.66	FeS$_2$	162.0, 163.3	36.49	FeS$_2$
	163.6	27.97	S$_8$	164.3	9.23	S$_8$
	168.8	18.44	SO$_4^{2-}$	168.3	48.15	SO$_4^{2-}$
Sulfided Fe$_3$O$_4$	161	2.59	FeS			
	162.4	53.98	FeS$_2$	162.4	31.37	FeS$_2$
	163.7	17.19	S$_8$	163.6	25.11	S$_8$
	168.7	26.24	SO$_4^{2-}$	168.3	43.52	SO$_4^{2-}$
Sulfided Fe(OH)$_3$	161.7	31.45	FeS$_2$	163.4	11.41	FeS$_2$
	163.3	25.75	S$_8$	164.5	8.40	S$_8$
	169.0	42.80	SO$_4^{2-}$	169.4	80.19	SO$_4^{2-}$
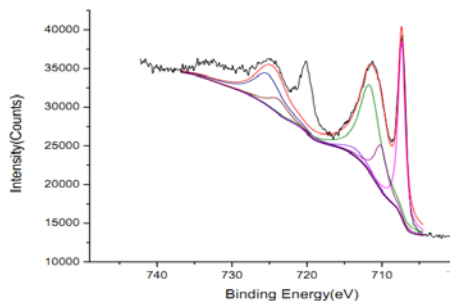
(a) Fe$_2$O$_3$ (in ethanol)
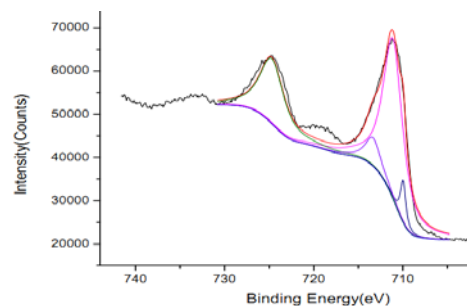
(d) Fe$_2$O$_3$ (in air)
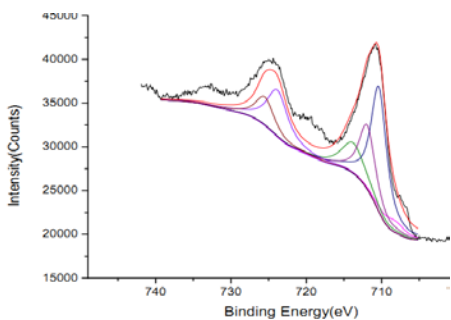
(b) Fe$_3$O$_4$ (in ethanol)
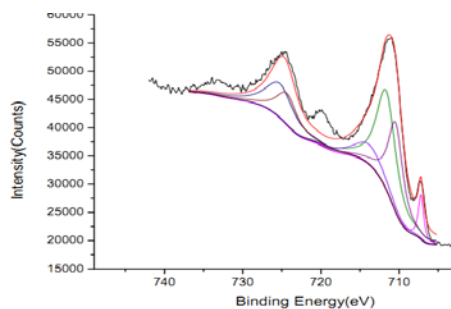
(e) Fe$_3$O$_4$ (in air)
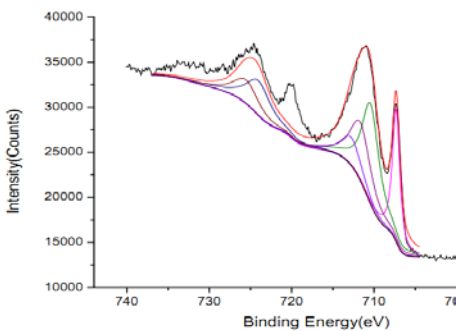
(c) Fe(OH)$_3$ (in ethanol)
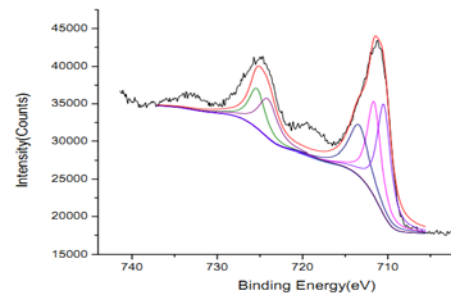
(f) Fe(OH)$_3$ (in air)

Fig. 5. XPS spectra of Fe 2p of sulfidation products.

Table 3 Results of curve fitting of Fe 2p of sulfidation products

Sample	In ethanol			In air		
	BE	Fe atom percentage (%)	Chemical state	BE	Fe atom percentage (%)	Chemical state
Fe$_2$O$_3$	707.3	34.40	FeS$_2$	710.0	6.05	FeS$_x$
	710.1	10.28	FeO			
	711.5	49.50	Fe$_2$O$_3$	711.1	82.68	Fe$_2$O$_3$
	713.4	5.82	FeSO$_4$	713.0	11.27	FeSO$_4$
Fe$_3$O$_4$	707.3	22.22	FeS$_2$	707.0	5.98	FeS$_2$
	710.4	38.49	Fe$_3$O$_4$	710.4	32.80	Fe$_3$O$_4$
	711.6	26.81	Fe$_2$O$_3$	711.6	46.91	Fe$_2$O$_3$
	712.8	12.48	FeSO$_4$	713.8	14.31	FeSO$_4$
Fe(OH)$_3$	706.7, 708.3	6.63	FeS$_x$			
	710.3	49.31	FeO(OH)	710.4	39.71	FeO(OH)
	711.9	26.28	Fe$_2$O$_3$	711.6	33.69	Fe$_2$O$_3$
	713.7	17.78	FeSO$_4$	713.4	26.60	FeSO$_4$

reaction, which makes the content of FeS$_2$ in the sulfidation product greatly increase. The main component in the iron oxide-sulfide products is FeS$_2$, and contains some intermediate products, such as FeS, and elemental S. The XPS result shows that some FeSO$_4$ is formed in the sulfide products, and a small amount of FeO is detected in the Fe$_2$O$_3$ sulfidation product. It is presumed that because of the presence of a small amount of O$_2$ in the sulfidation system, resulting FeS oxidizing reaction occurs: FeS$\xrightarrow{O_2}$FeSO$_4$, FeO. Due to the relatively small amount of oxygen in the oxidation system, the contents of FeSO$_4$ and FeO in the sulfide products are not high.

Analysis of the oxidation behavior of sulfidation products

The previous studies have shown that iron sulfide compounds such as FeS are pulverized and ground and can be slowly oxidized at room temperature [24]. But the tendency of spontaneous oxidation of FeS will be weakened after the temperature rises to 50℃. In addition, the FeS has the tendency to be converted into FeS$_2$, so the FeS$_2$ has stronger spontaneous oxidation ability during exothermic oxidation.

Buckley and Woods studied the surface of pyrite (FeS$_2$, FeS, etc.) exposed to oxygen by XPS [25]. It was concluded that FeSO$_4$ was generated quickly and stably, and S$_8$ was formed during the oxidation process. After the prolonged oxidation, with the disappearance of elemental S, the iron oxides appeared.

At room temperature, O$_2$ in the environment can oxidize the S atom of the sulfur compounds into elemental S and release heat. The concentration of the heat makes the oxidation reaction further strengthened, and the S atom of the iron-sulfur compound is oxidized to SO$_2$, while releasing heat.

This is also the reason for the irritating odor generated in the experiment.

$$FeS_2 \xrightarrow{O_2} Fe_2O_3+S; \quad FeS \xrightarrow{O_2} Fe_2O_3+S;$$
$$FeS_2 \xrightarrow{O_2} Fe_2O_3+SO_2\uparrow; \quad FeS \xrightarrow{O_2} Fe_2O_3+SO_2\uparrow.$$
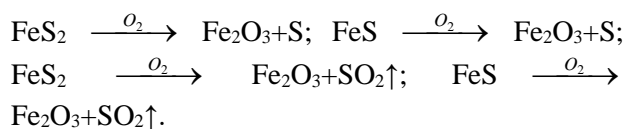
Due to a substantial increase in the content of Fe$_2$O$_3$ after oxidation, whereas, the content of other iron oxide is almost unchanged, it is considered that the oxide of iron produced after oxidation is mainly Fe$_2$O$_3$, which mainly involves the reaction:

$$FeS_2 \xrightarrow{O_2} Fe_2O_3+S; \quad FeS \xrightarrow{O_2} Fe_2O_3+S;$$
$$FeS_2 \xrightarrow{O_2} Fe_2O_3+SO_2\uparrow; \quad FeS \xrightarrow{O_2} Fe_2O_3+SO_2\uparrow.$$
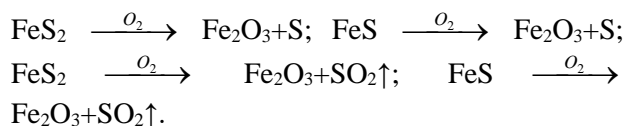
After the oxidation reaction, the content of FeSO$_4$ in the product was significantly increased, indicating that the S atom was further oxidized to the higher valence SO$_4^{2-}$ except for the above occurring oxidation reaction. During the experiments, a small amount of droplets were generated on the inner wall of the reacted three-necked flasks, which was due to the condensation of the water vapor carried in the reaction gas.

$$FeS_2 \xrightarrow{O_2,\ H_2O} FeSO_4+H_2SO_4;$$
$$FeS \xrightarrow{O_2,\ H_2O} FeSO_4 \cdot 7H_2O.$$
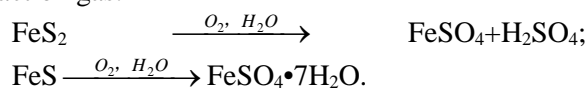
It was found that the presence of H$_2$O greatly increased the spontaneous combustion of sulfur compounds [26]. The oxidation process is:

$$FeS_2 \xrightarrow{O_2,\ H_2O} FeSO_4+H_2SO_4;$$
$$FeS \xrightarrow{O_2,\ H_2O} FeSO_4 \cdot 7H_2O.$$
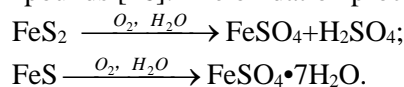
From the results of XPS it follows that when the sulfidation product is oxidized at room temperature, the content of elemental sulfur in the oxidation product is dramatically reduced, but the amounts of Fe$_2$O$_3$ and FeSO$_4$ obviously increase. It is shown

that the generation of sulfur is only in the initiation process of oxidation reaction. With the progress of oxidation reaction, the reducing substances such as FeS_2, FeS and S in the sulfidation product are gradually oxidized to Fe_2O_3 and $FeSO_4$.

CONCLUSIONS

In order to simulate the sulfur corrosion process in the oil tank, a method for vulcanizing the wet H_2S gas containing a small amount of oxygen with three kinds of iron oxides, Fe_2O_3, Fe_3O_4 and $Fe(OH)_3$, was proposed. The results of SEM and EDS showed that various iron oxides can produce the same kind of iron-sulfur compounds after sulfidation, only their microstructure and elemental distribution are different. The analysis by XPS indicated that the different iron oxides have the same sulfur corrosion products, mainly FeS_2, FeS, elemental S and a small amount of $FeSO_4$. The oxidation process of iron oxides is the process of converting iron oxides into FeS_2 and $FeSO_4$, which are accompanied by the formation and transformation of FeS and S_8. The presence of a small amount of oxygen in the sulfide gas is the main reason for the formation of $FeSO_4$. In addition, the oxidation reaction involved oxygen which promoted the conversion of FeS to FeS_2 which has a stronger ability of spontaneous oxidation.

At room temperature, the oxidation process of the sulfidation products is a process of gradually oxidizing the reducing substances, such as FeS_2, FeS, S, etc. Through temperature monitoring it is found that the oxidation exothermic process belongs to the low-temperature oxidation process, which required a temperature below 300 ℃. However, the presence of H_2O promotes the oxidation reaction, and the reducing substances in the vulcanized product are finally oxidized to Fe_2O_3 and $FeSO_4$.

REFERENCES

1. Zh. Miao, W. Song, Zh. Chen, J. Wang, *Process Safety Progress*, **35**(3), 260-269 (2016).
2. Lei Shi, Jian Shuai, Kui Xu, *J. Hazard. Materials*, **278**, 529 (2014).
3. B. Wang, Y. Chen, A. Cui, Chemical mechanism and control technology for sulfide spontaneous combustion in oil tanks, *China Safety Sci. J.*, **13**, 23 (2003).
4. Y. Sh. Li, L. Zh. Shan, W. T. Yan , H. Zh. Zhen, W. X. Shu, L. Ping, *Adv. Mater. Research*, **881-883**, 234 (2014).
5. M. Martínez, G. Márquez, F. J. Alejandre, J. J. Del Río, A. Hurtado, *J. South Amer. Earth Sci.*, **27**), 211 (2009).
6. Y. A. Beilin, L. A. Nisellson, I. R. Begishev, *Protection of Metals*, **43**, 269 (2007).
7. M. Riley, R. S. Daniel, *Surface Sci. Reports*, **64**, 1 (2009).
8. Z. H. Zhang, S. L. Zhao, P. Li, *Acta Petrolei Sinica (Petroleum Processing)*, **28**, 113 (2012).
9. Y.G. Zheng, B. Brown, S. Nesic,. *Corrosion*, **70**, 351 (2014).
10. D. Jingen, Y. Wei, L. Xiaorong, D. Xiaoqin, *Petroleum Sci. Technol.*, **29**, 1387 (2011).
11. P. Chatterjee, D. D. N. Singh, *Anti-Corrosion Methods and Materials*, **38**, 4 (1991).
12. D.L. Gao, Z.X. Zhao, *CMC-Computers Materials and Continua*, **26**, 157 (2011).
13. S. Arzola, J. Genescá, *J. Solid State Electrochem.*, **9**, 197 (2005).
14. G. Deli, Z. Zhao, *Int. Conference on Computational and Experimental Engineering and Sciences,* **16**, 29 (2011).
15. P. H. Tewari, A. B. Campbell, *Canad.J. Chem.,* **57**, 188 (1979).
16. J. Tang, Y. Shao, T. Zhang, G. Meng, F. Wang, *Corrosion Sci.*, **53**, 146 (2011).
17. M. Liu, J. Wang, W. Ke, *Corrosion Eng. Sci. Technol.*, **48**, 380 (2013).
18. Y. K. Fan, J. H. Guo, L. Xu, *Adv. Mater. Research*, **314-316**, 1087 (2011).
19. D. Mandrino, B. Podgornik, *Appl. Surface Sci.,* **396**, 554 (2017).
20. P. A. Gokturk, U. Salzner, L. Nyulászi, B. Ulgut, C. Kocabas, S. Suzer, *Electrochim. Acta*, **234**, 37 (2017).
21. M. Taheri, M. Konuma, F. S. Razavi, *Surface Interface Analysis*, **49**, 122 (2017).
22. S. A. Chambers, *Hard X-ray Photoelectron Spectroscopy (HAXPES),* **59**, 341 (2016).
23. X. Wan, Sh. Zhao, *Sci. Technol. Eng.*, **9**, 2554 (2009).
24. G. F. Pavelko, *Russian J. Inorg. Chem.,* **53**, 981 (2008).
25. A. N. Buckle, R. Woods, *Appl. Surf. Sci.,* **27**, 156 (1987).
26. X. Wan, Sh. Zhao. *Journal of Qingdao University of Science and Technology (Natural Science Edition)*, **30**, 304 (2009).

Изследване на сулфидирането на железни оксиди и поведението на сулфидираните продукти при окисление

Л. Шанг[1,2*], Дж. Ли[1], Ш. Жао[2], И. Тиан[1], Ж. Жанг[2], Л. Жанг[3]

[1] *Училище по металургия, Североизточен университет, Шенянг, 110004, Китай;*

[2] *Колеж по химия, инженерна химия и инженерство на околната среда, Ляонинг Шихуа Университет, Фушин, 113001, Китай;*

[3] *Колеж по петролно инженерство, Ляонинг Шихуа Университет, Фушин, 113001, Китай;*

(Резюме)

С цел да се оцени сулфидирането на железните оксиди и окислителното поведение на продуктите на сулфидирането при стайна температура, в настоящата статия е симулиран серният корозионен процес в маслен контейнер. Микроструктурата и състоянието на повърхността на продуктите на сулфидирането на Fe_2O_3, Fe_3O_4 и $Fe(OH)_3$, които са основните компоненти на ръждата, са характеризирани чрез SEM и EDS. Химичният състав на повърхността на сулфидираните и окислените продукти е характеризиран чрез XPS с оглед да се изясни степента на окисление и механизмът на окисление на продуктите на сулфидирането. Установено е, че трите вида оксиди на желязото дават един и същ вид съединения на желязото и сярата след сулфидиране, но с различна микроструктура и разпределение на елементите. Основните компоненти на серните корозионни продукти на трите железни оксида са идентични. Серният корозионен процес на железните оксиди ги превръща съответно в FeS_2 and $FeSO_4$, което се съпровожда с образуване и трансформация на FeS и S_8. При стайна температура окислителният процес на продуктите на сулфидирането завършва с превръщане на съединенията между желязото и сярата в Fe_2O_3 и $FeSO_4$.

A prediction model for equilibrium adsorption capacity of the saline soil in the estuary region of Yangtze River

A.J. Shao, S.W. Wang[*], D.Y. Sun

Hebei GEO University, Hebei,China

In order to study the changes of water and salt in the estuary region of Yangtze River, the composition and the proportion of the salt in Yinyang and Daxing were determined by long-term monitoring. To understand the relationship between the salt in the soil and in external solutions in these areas, adsorption experiments of the soil samples in Yinyang and Daxing at different concentrations (0~10g/L) were carried out. The adsorption capacity of the soil in these areas is negative, which means that the soils in these areas are mainly desorbed in solutions with concentrations in the range of 0~10g/L. It is found that these soils are well described by using the Freundlich linear isothermal formula. The fitting formula provides a kind of guidance for future production practice.

Keywords: estuary region of Yangtze River, adsorption; desorption, saline soil, Freundlich model

INTRODUCTION

Adsorption is a process in which the solute is transferred from a liquid phase to a solid surface by ion exchange, while desorption is the opposite process in which the ions of a substance in the solid phase enter the liquid phase [1]. Adsorption reduces the concentration of the substance in the solution and desorption increases its concentration in the solution. Adsorption and desorption are two opposite processes of the same chemical function, so they can share the same predictive model.

The adsorption process is extremely complex and has important theoretical significance and application value [2-5]. Since the 1970s, scholars at home and abroad have done a lot of researches on solute adsorption characteristics of saturated soil and unsaturated soil, and established the corresponding adsorption model. The most commonly used adsorption models are Langmuir adsorption model and Freundlich adsorption model [6-12]. The adsorption and desorption of solute are mainly related to the concentration of solute in the solid phase and in the liquid phase. The mathematical expression of the reaction concentration relation is the adsorption mode. However, because of the complexity of the adsorption process, many problems are still unclear. So it is impossible to accurately construct the expression of the whole adsorption process. Researchers usually use empirical expressions to describe the adsorption progress.

The Freundlich adsorption model belongs to the linear isothermal adsorption formula, which has the advantages of a smaller number of parameters and a better effect [13-15]. So the Freundlich adsorption model was chosen to determine the parameters of the saline soil in the Changjiang estuary, which can reduce the workload of adsorption experiments and provide some guidance for production practice.

STUDY AREA

The estuary region of Yangtze River covers up to Anhui Datong and down to the Subaqueous Delta front. The full length is around 700 km. There is northern subtropical monsoon climate in this area, which has long sunshine time and abundant rainfall. Rainfalls are mainly concentrated from May to September, which accounts for more than 60% of the annual rainfall. From February to June and in September, the rainfall is larger than the evaporation, which decreases the salt content in the soil. In the other months, evaporation is higher than the rainfall, which increases the salinity of the soil. The solute concentrations in the soil are in a dynamic change process.

In order to study the change of water and salt in the estuary region of Yangtze River, the Yinyang town and Daxing town in Jiangsu province were monitored. The distance between Yinyang and the estuary region of Yangtze River is 4 km. The distance between Daxing and the estuary region of Yangtze River is 22 km. The monitoring surface directions are nearly north-south and perpendicular to the river dike or parallel to the adjacent river. There are 3 monitoring points from south to north at a distance from the river embankment of 200 m, 500 m and 1000 m, respectively (Fig. 1). The salt content of soil was determined by a salt sensor every five days and the water salinity of the Yangtze river was determined by a conductivity meter every five days. The chemical composition (eight ions) of soil salt content was determined twice a year in May and October, respectively.

---

*) To whom all correspondence should be sent:

E-mail: wsw84946108@163.com

Fig. 1. Layout of monitoring section

EXPERIMENTAL

Based on the measured results of the water and salt in the estuary region of Yangtze River, the groundwater is composed of HCO_3^-, Cl^-, SO_4^{2-}, K^+, Na^+, Ca^{2+}, Mg^{2+}. Therefore, according to the proportion of these 8 ions the solution was configured to simulate the impact of groundwater on soil adsorption. The chemical composition of the solution is shown in Table 1.

After drying and filtering the soil of Yinyang and Daxing, 100 g samples of soil were added into wide-mouth bottles. According to the soil:water ratio of 1:0.5 (close to saturated water content), then 50 mL of solutions of concentration of 0 g/L, 0.5 g/L, 1 g/L, 2 g/L, g/L, 6 g/L, 10 g/L were added to the soils under stirring with glass rods. The wide-mouth bottles should be placed in a room with a small temperature change after capping the lid. The solution concentration was measured after the adsorption reached the equilibrium.

According to the previous data [13], the solution adsorption can achieve equilibrium in 20 days. Therefore, the samples were allowed to stay for 20

days, and then the soil solution was centrifuged out. The concentration of the solutions was determined by conductivity method (Table 2). The conductivity and solution concentration were fitted (Fig. 2).
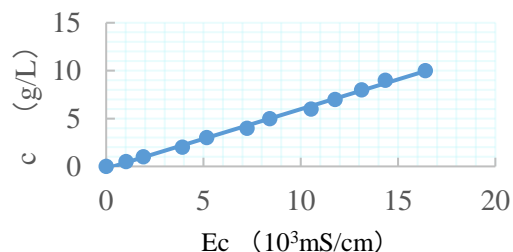
Fig. 2. Relationship between conductivity and solution concentration..

The empirical formula of conductivity and solution concentration is as follows:

$$c = 0.6209Ec - 0.2282 \quad R = 0.998 \qquad (1)$$

In this formula, c is solution concentration (g/L), Ec is electrical conductivity (mS/cm). The adsorption capacity of salt in soil can be calculated by formula (2).

$$S = \frac{\omega(c_0 + c_1 - c)}{m} \qquad (2)$$

In this formula, S is the amount of salt adsorbed by the soil, that is, the quantity of salt adsorbed by the dry soil of the unit mass (g/kg); ω is the volume of the solution (in this study is 50 ml); m is the soil sample mass (in this study is 100 g); c is the concentration of the soil solution when it is balanced (g/L); c0 is the concentration of soil solution when adding distilled water (solution concentration is 0 g/L and c1 is the concentration of the added solution (0.5g/L, 1 g/L, 2 g/L, 4 g/L, 6 g/L, 10 g/L). When S is positive, it indicates that the soil sample has adsorbed salt from the solution. When S is negative, it indicates that the salt in the soil sample desorbs into solution.

Table 1. Chemical composition of solution

Chemical composition	Molecular weight	Proportional/m mol	100 mmol/L mass g	10g/L mass g	10L mass concentration 10g/L
CaCl$_2$	110.99/2	10	0.555	0.9609	9.609
Na$_2$SO$_4$	142.04/2	10	0.7102	1.2295	12.295
MgCl$_2$ (6H$_2$O)	203.31/2	15	0.712 (1.5248)	1.2335 (2.6398)	26.398
NaCl	58.4/2	65	3.4986	6.5761	65.761
Total		100	5.776 (6.5886)	10 (11.4063)	114.063

Note: The data in brackets are the quality plus 6H$_2$O.

Table 2, Conductivity of solution at different concentrations

c (g/L)	0	0.5	1	2	3	4	5	6	7	8	9	10
Ec (10^{3}mS /cm)	0.005	1.010	1.910	3.920	5.165	7.230	8.400	10.530	11.765	13.125	14.340	16.400

Table 3. Results of adsorption experiments

Preparation of solution concentration c_1	g/L	0	0.5	1	2	4	6	10
Yinyang	c (g/L)	3.252	3.786	4.398	5.524	7.710	9.849	13.835
	S (g/kg)	0.000	-0.017	-0.073	-0.136	-0.229	-0.299	-0.292
Daxing	c (g/L)	0.311	0.845	1.482	2.510	4.832	6.953	11.293
	S (g/kg)	0.000	-0.017	-0.086	-0.099	-0.260	-0.321	-0.491

The dry soils of Yinyang and Daxing were respectively added to seven different concentrations of solutions. Every specimen has a parallel sample, and the experimental results were obtained by the arithmetic average value. The results of the adsorption experiment are shown in Table 3.

The saline soil adsorption amounts s of Yinyang and Daxing are negative, indicating that the saline soils in these areas mainly desorbed in the solutions of 0~10 g/L concentration. The amount of desorption increases as the solution concentration increases. The increasing rate of desorption of the saline soil in Daxing is greater than in Yinyang.

MODEL

The concentration of soil solution was tested compared with the concentration of soil solution when distilled water was added. So the desorption amount of the soil sample should be subtracted from the value in the distilled water when the data are collated. The adsorption amount of salt in the solution was fitted with the solution concentration (Fig.3).
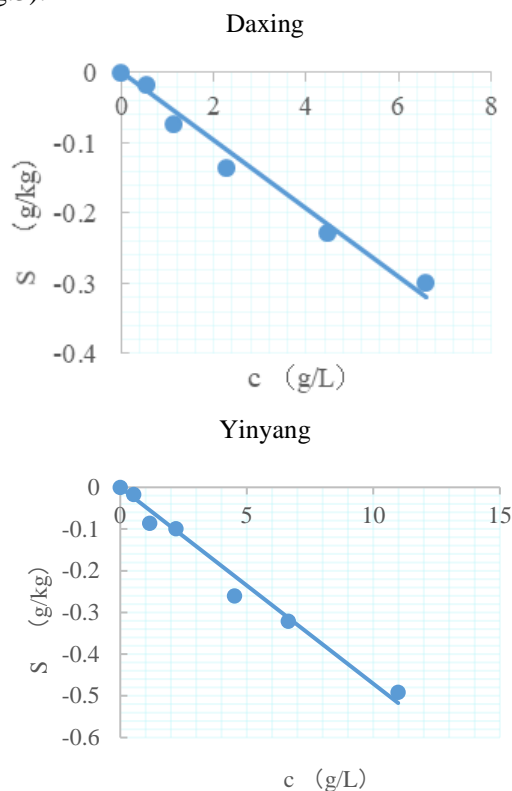
Fig. 3. Relationship between desorbed quantity and solution concentration

The desorption amount of Yinyang and Daxing soil sample is linearly related to solution concentration, which conforms to Freundlich linear isothermal adsorption formula. The linear model of soil in Yinyang area is S=-0.0484c, R=0.99. The linear model of soil in Daxing is S=-0.0471c, R=0.99. Both of them fit well with Freundlich linear isothermal adsorption formula.

CONCLUSION

(1) In this paper, the salinity changes of two observation points (Yinyang and Daxing) in the estuary region of Yangtze River were observed for *a long time, and the main composition and proportion of salt in the area were obtained.

(2) The adsorption experiment of the soil in Yinyang and Daxing area was carried out, and the adsorption of the soil was calculated by conductivity method. The adsorption amount of the soil in the 0~10g/L solutions of Yinyang and Daxing area are negative, which indicates that the soil in 0~10g/L solution is the desorption process in this area.

(3) The adsorption models of saline soil in Yinyang area and Daxing area fit Freundlich linear isothermal adsorption formula well

REFERENCES

1. A.J. Shao, J.P. Peng, Numerical simulation of soil water and salt transport, *Beijing: Geology Press*, 2007.
2. M. Karatas, *J. Hazard. Materials*, **199-200**, 382 (2012).
3. Y.Q. Qiu, A study on the characteristics of phosphate adsorption-desorption and the control of phosphorus loss under typical soils in Hunan, *Changsha:* Central South University of Forestry&Technology, 2012.
4. Y.Q. Wang, Q.H. Fan, P. Li, X.B. Zheng, J.Z. Xu, Y.R. Jin, W.S. Wu, *J. Radioanalyt. Nuclear Chem.*, **287**, 231 (2011).
5. K.P. Vignesh, M. Sekar, A. Basker, P.V. Subha, *Int. J. Eng. Technol. Research*, **1**, 77 (2013).
6. Y.R. Wang, J.F. Hou, J.H. Guo, B. Huang , Z.X. Luo, L. Chen, *J. Agro-Environ. Sci.*, **36**, 566 (2017).
7. X.G. Li, R. Liu, M.R. Huang, *Chem. Materials*, **17**, 5411 (2005).
8. L.X. Zhao, Sorbent concentration effect on adsorption phenomenon at solid-liquid interface, Jinan: Shandong University, 2013.
9. M. Carmo, L. S. Hundal, M. L. Thompson, *Environ. Sci. Technol.*, **34**, 4363 (2012).
10. X.P. Tan, X. Zhou, J.Y. Zhang, C. Zhang, D.Y. Wang, Environ. Sci., **38**, 608 (2017).
11. X.D. Zhou, C.Y. Li, P.C. Gao, et al, *Microbiology China*, **44**, 1182 (2017).

12. Z.J. Zhang, J.T. Liu, L. Feng, et al, *Journal of Northeastern University (Natural Science)*, **32**,749 (2011).
13. H.B. Shi, Y.X. Chen, *Acta Pedologica Sinica*, **33**, 258 (1996).
14. J.B. Shi, G.J. Liu, *University Chemistry*, **30**, 76 (2015).
15. J.M. Wei, L.Z. Lu, G.B. Jiao, J.Y. Liu, J.H. Lu, *Biotechnol. Bull.*, **33**, 1 (2017).

МОДЕЛ ЗА ПРЕДСКАЗВАНЕ НА РАВНОВЕСНОТО АДСОРБИРАНО КОЛИЧЕСТВО ОТ СОЛЕНА ПОЧВА В ЕСТУАРНАТА ОБЛАСТ НА РЕКА ЯНЦЗЕ

А. Шао, Ш. Уанг[*], Д. Сун

ГЕО университет на Хебей, Хебей, Китай

(Резюме)

За изучаване на промените във водата и солеността в естуарната област на река Янцзе са проследени дългосрочно съставът и съотношението на солите в районите на градовете Инянг и Даксинг. За установяване на връзката между съдържанието на сол в почвата и във водите в тези райони са проведени адсорбционни опити с почвени проби от Инянг и Даксинг при различни концентрации (0~10g/L). Адсорбционният капацитет на почвите в тези райони е негативен, което означава, че тези почви основно се десорбират в разтворите с концентрация в областта от 0~10g/L. Установено е, че тези почви се описват добре с линейната изотермна формула на Freundlich. Тази формула дава основа за бъдеща производствена практика.

Effect of boron and boron-nickel on low-temperature impact toughness of hot-rolled

Nb-added HSLA H-beams

G.T. Cui[1]*, Z.C. Wang[2], X.B. Wang[2], X. Wang[2], J.Q. Gao[3]

[1] School of Electromechanical Engineering, Heze University, Heze, 274015, Shandong, China

[2] Key Laboratory for Liquid-Solid Structural Evolution & Processing of Materials Ministry of Education, Shandong University, Jinan, 250061, Shandong, China

[3] Laiwu Iron and Steel Company Ltd., Laiwu, 271104, Shandong, China

Nb-treated HSLA steels alloyed with 11ppm of B and 11ppm of B + 0.5mass% of Ni were studied to find an effective method to improve the low-temperature impact properties of HSLA H-beams. The mechanical properties and microstructure of the experimental steels were investigated by uniaxial tensile test, Charpy impact test (V-notch), transmission electron microscopy (TEM) and X-ray diffraction (XRD), respectively. The results indicated that the absorbed energy at -50℃ can reach up to 44.4 J from 13 J with the addition of 11ppm of B, and to 121 J with the addition of 11 ppm of B + 0.5 mass% of Ni. The precipitate of Nb carbonitride and the grains can be significantly refined by B addition, and precipitates with diameter up to 30 nm were detected. The $Fe_{23}(C,B)_6$ precipitates were suppressed by the simultaneous addition of B and Nb. No Fe-Ni intermetallic was detected by using XRD method. It was assumed that the B in solid solution state and the homogeneously distributed Ni have beneficial effects on the low-temperature impact properties of Nb-treated HSLA steels.

Key words: boron, nickel, niobium, low-temperature impact toughness, H-beam

INTRODUCTION

H-beams are widely used in various fields of modern society because of their economical features. Currently, there is increasing interest in the study of high-grade hot-rolled H-beams, especially, with advanced low-temperature impact properties, due to the intensive exploration of scientific and energy resources in high-latitude and cold regions.

Presently, the properties of high-strength low-alloy (HSLA) steels are mainly improved by grain refinement [1], as the decrease in grain size is accompanied by an improvement in mechanical properties, as can be represented by the Hall-Petch relation [2]. Thermo-mechanical control processing (TMCP) consisting of controlled rolling [3] provides a powerful method to refine the grains of HSLA steels. Generally, intensive plastic deformation and rapid cooling are required in TMCP to obtain a refined microstructure. However, TMCP is improper to produce H-beams, because the rolling parameters of H-beams are predetermined and not easy to change [4], thus, intensive deformation which is required in control rolling is hard to realize. Moreover, it is very complicated to prevent cracks and distortion in a rapid cooling process, because of its complex cross-section.

The behavior of small amount of B in steels has been elucidated by many researchers. Boron addition can slow down the coarsening of austenite grains during reheating [5], and the segregated B on moving new austenite boundaries can suppress the grain growth and retard the recrystallization of austenite after high- temperature deformation to a significant degree [5-8]. Thus, a fine-grained austenite structure can be obtained. The segregated B in austenite boundaries can suppress the ferrite transformation [9], because the segregated B can occupy the preferential sites of ferrite and reduce the grain boundaries energy [5,10]. However, when B is added alone, coarse precipitates like $Fe_{23}(C,B)_6$ will appear and the positive effects of B addition will be reduced [11,12]. For this reason, the synergistic effects of B and Nb have drawn attention. It is reported that when B is added to Nb-treated steel, the Nb carbonitrides can be refined and the total density of the precipitates increased as compared with steels with only Nb added [13]. Also the formation and coarsening of $Fe_{23}(C,B)_6$ are suppressed by the simultaneous addition of B and Nb [11]. Thus, the segregated B along the γ grain boundaries increases and an enhanced pinning effect and solute drag effect on grain boundaries can be obtained by fine precipitates and solute atoms. Lee *et al*. [14] have researched the L1$_2$-type Cu-added zirconium

---

trialuminide intermetallics and found that the segregated B in grain boundaries can result in an increase of the grain boundary cohesion by forming strong interatomic bonds, which can sharply increase the ductility and effectively suppress intergranular fracture.

Ni can stabilize in the steel and form substitutional solid solution with ferrite. The comprehensive mechanical properties of the steel can benefit a lot from the addition of Ni. The steel containing 0.5 mass % of Ni is widely used to produce low-temperature pressure vessel steel, which can be used in the range from -40℃ to -60℃. However, subsequent heat treatment is generally required, which is impracticable for the production of hot-rolled H-beams.

Based on our previous research [4,15-18], the objective of this article was to characterize the effects of B and Ni on the low-temperature impact toughness of hot-rolled Nb-treated HSLA H-beams. Particular attention was paid to link the B addition to the refinement of precipitates and microstructure. Also, the Ni species in the steels was investigated by using XRD method.

MATERIALS AND EXPERIMENTAL PROCEDURE

The investigation involved three different steels, a carbon-manganese structural steel conforming to GB/T 1591-2008, grade Q345E was selected as the reference material. In order to find out the effects of B and of the combined addition of B and Ni, the other two steels were designed to be of the same composition as the reference steel alloyed with 11 ppm of B and 11 ppm of B + 0.5 mass% of Ni, respectively. The chemical composition of the steels is listed in Table 1. All steels were prepared by convert steelmaking process. The H-beam blanks were firstly reheated at 1250°C for 1 h and rolled in universal H-beam rolling mill with a final rolling temperature of 910°C, then air-cooled to room temperature.

Tensile tests were performed using a universal testing machine at room temperature. The standard Charpy V-notch impact test was carried out over the temperature range from -10°C to -70°C. Standard Charpy V-notch specimens of 10mm×10mm cross-section were machined with the longitudinal direction parallel to the rolling direction of the H-beams, and the V-notch was machined through the thickness direction perpendicular to the rolling plane.

All samples for metallographic observation were mechanically polished and etched with a 4% nital solution. The microstructure was characterized using a Su-70 thermal field emission scanning electron microscope (FE-SEM).

The transmission electron microscopy (TEM) investigations were carried out on an H-800 microscope with X-ray energy dispersive spectroscope (XEDS) operating at an accelerating voltage of 150kV. High resolution TEM was also used to observe the very fine particles in the steels. The X-ray diffraction analyses of the mechanically polished samples were performed on a DMAX-2500 X-ray diffractometer using Cu Kα radiation, operating at V=50 kV, I=40 mA. A scanning rate of 0.02°/s was applied to record the patterns in the 2θ range from 10° to 100°.

RESULTS AND DISCUSSION

Mechanical Properties

Table 2 shows the mechanical properties of the experimental steels. It can be seen from Table 2 that all steels exhibit good comprehensive mechanical properties. It can also be seen that the yield strength of the experimental steels increases from 385 MPa to 420 MPa with the addition of 11ppm of B, and to 440 MPa with the addition of 11ppm of B + 0.5% mass of Ni. This may due to the grain refinement effects of the B addition and the solid solution strengthening effects of Ni addition. No changes of tensile strength and elongation the experimental steels were registered.

Figure 1 shows the variations of absorbed energy as a function of test temperature for different experimental steels.

Table 1. Chemical composition of the experimental materials (mass %)

Steels	C	Si	Mn	P	S	Ni	Nb	B
1#	0.18	0.24	1.26	0.012	0.005	0.01	0.024	—
2#	0.18	0.23	1.31	0.013	0.004	0.01	0.023	0.0011
3#	0.18	0.21	1.32	0.012	0.005	0.51	0.020	0.0011

Table 2. Mechanical properties of experimental steels

Steels	Yield strength/MPa	Tensile strength/MPa	Elongation/%
1#	385	530	30.0
2#	420	530	29.0
3#	440	570	29.5
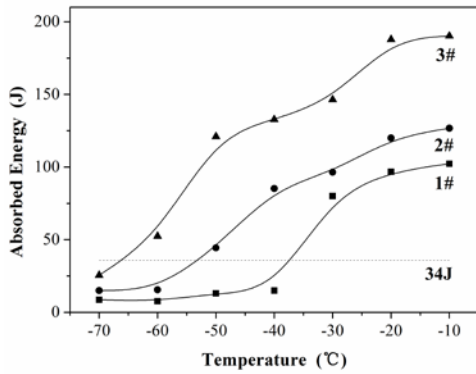
Fig. 1. Charpy V-notch absorbed energy *versus* temperature

As can be seen, the absorbed energy of 1# steel at -10 ℃ reaches 102.3 J, but a sharp ductile-to-brittle transition was observed as the temperature decreased, and absorbed energy is 15J when the temperature drops to -40℃. In fact, the average absorbed energy of H-beams for preventing brittle fracture at -40 ℃ specified in GB/T 1591-2008 is 34 J. Compared to 1# steel, 2# steel shows better impact toughness with decreasing temperature down to -50℃, and when the absorbed energy is at 34 J the temperature decreases by 20℃. It is suggested that the addition of trace B strongly enhances the impact toughness of the steels, especially the low temperature impact toughness. 3# steel displays the highest toughness among the experimental steels, more precisely, the absorbed energy of 3# steel at -10℃ is 190.2 J, and at -50℃ it still maintains most of its impact toughness with the absorbed energy of 121 J, even at -60℃ the absorbed energy of 3# steel remains at 52.4 J. Compared to 1# and 2# steels, the temperature at absorbed energy of 34J decreases by 30℃ and 10℃, respectively. The fracture surfaces of the experimental steels at -40℃ were also analyzed by scanning electron microscopy, utilizing a Hitachi Su-70 FE-SEM. The area of the fracture surface towards the middle of the width of the specimen and a few millimeters below the notch was the main area of investigation. The fracture surfaces are shown in Figure 2. We can see that the fracture mode of 1# steel at -40℃ was entirely brittle fracture, and the fracture surface mainly contained trans-granular cleavage-like fracture zones. The fracture surface of 2# steel consisted mainly of shallow microvoids with some regions of larger dimples. The fracture surface appearance of the 3# steel tested at -40℃ was ductile and consisted of large dimples.

Microstructure observation and XRD results

To reveal the effects of B and Ni, the microstructure and precipitation characteristics were investigated. Figure 3 shows the SEM graphs of the experimental steels. It can be seen that the microstructures of all three alloys consist of ferrite and perlite. While the average grain diameter of 1# steel was the largest one (9.66 μm), followed by 2# steel (8.17 μm), it decreased to 6.05 μm in 3# steel. As all three experimental steels were produced with the same process, it indicates that the B addition to Nb-added HSLA steels has a beneficial effect on grain refinement, and this effect seems to be enhanced by the combined addition of B and Ni.
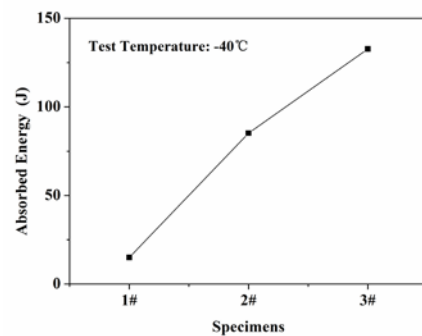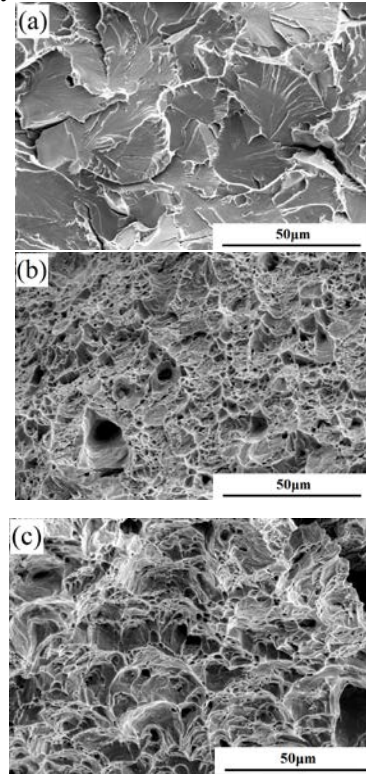
Fig. 2. Fracture surfaces of experimental steels tested at -40℃. The CVN impact energy is shown for reference. (a) 1# steel; (b) 2# steel; (c) 3# steel.

The TEM graphs (Figure 4) of extraction replica for the experimental steels reveal that the precipitates can be significantly refined by the simultaneous addition of B and Nb. The total density of the precipitates of 2# and 3# steels increased as compared with that in 1# steel (only Nb-added).
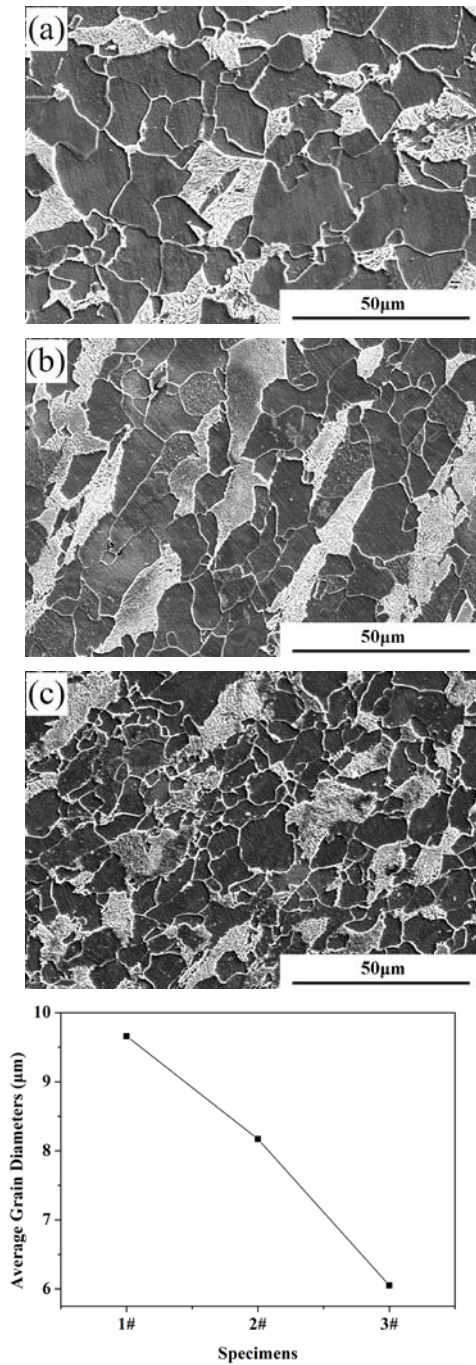
Fig. 3. SEM graphs of the experimental steels. The average grain diameters are shown for reference. (a) 1# steel; (b) 2# steel; (c) 3# steel.

Thus, the grain boundaries pinning effects in recrystallization and the phase transition process can be enhanced by the fine precipitates, and finally a finer grain structure can be obtained.

The precipitates were identified by EDS and TEM methods (Figure 5). Considering the Nb-containing precipitates, only Nb(C,N) and Nb(C,N) were detected. No Nb(C,B) particles, which were reported in many studies [7,12,13], were detected. This may due to the very fine particles of Nb(C,B) and the incapability of the equipment used in this study. And no coarse

$Fe_{23}(C,B)_6$ particles which were reported in B-containing steels [7,11,19] were detected. It indicates that the simultaneous addition of B and Nb can suppress the precipitation of $Fe_{23}(C,B)_6$, which consumes a large amount of B and has adverse effects on fulfilling the potential of B. Based on the characterization results of the particles in the steels, we can conclude that the existence form of B in the steels is mainly solid solution status. It can segregate in the moving new boundaries during recrystallization and phase transition process, and produce solution dragging effects to decrease the motion of the boundaries. Thus, a fine microstructure can be obtained. Moreover, the boundary cohesion is supposed to be enhanced by the segregated boron as reported in other studies [14].
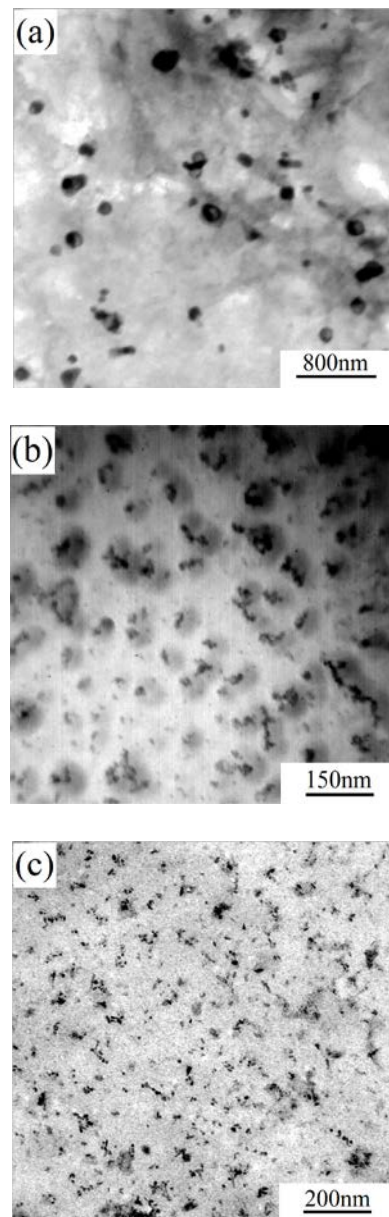
Fig. 4. TEM images of extraction replica of experimental steels. (a) 1# steel; (b) 2# steel; (c) 3# steel
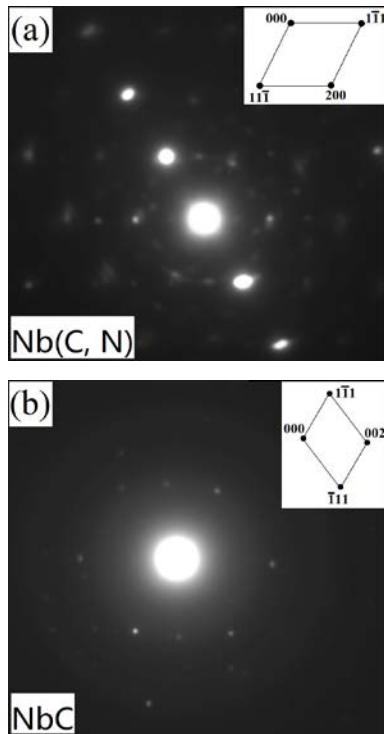
Fig. 5. Selected area diffraction pattern and the key diagram of Nb(C,N) and Nb(C,N). a-SDP of Nb(C, N); b-SDP of NbC\
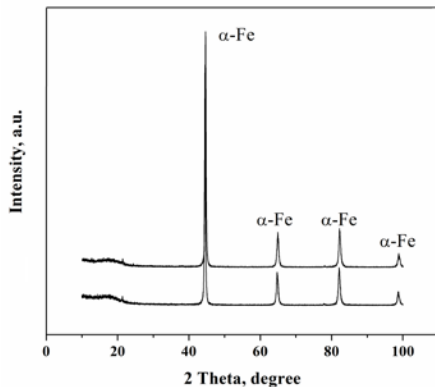
Fig. 6. XRD patterns of 2# and 3# steel
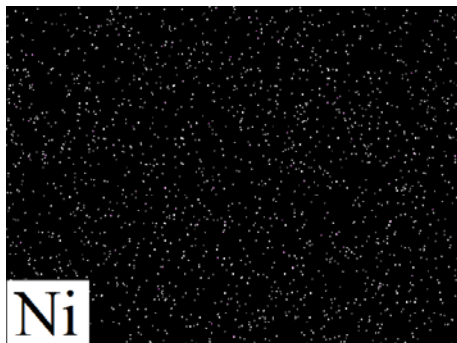
Fig. 7. The distribution of Ni in 3# steel

To reveal the effects of Ni in this study, the existence form of Ni was observed using XRD and the distribution of Ni was investigated using EDS, the results are shown in Figure 6 and Figure 7. The

XRD results of 2# steel and 3# steel, showed that only α-Fe diffraction peaks were detected. It indicates that the effects of 0.5 mass% of Ni on improving low-temperature impact toughness are not due to the formation of Fe-Ni solid solutions which are considered as a main reason for Ni to enhance the toughness of steels. Figure 8 shows that Ni is distributed homogeneously in 3# steel. However, the interaction of B and Ni needs further investigation in the following studies.

CONCLUSIONS

The effects of B and of the simultaneous addition of B with Ni on the low-temperature impact toughness of industrial Nb-added HSLA H-beams were investigated, and the following conclusions can be derived:

(1) Compared to the single addition of Nb, finer grain structure can be obtained by the simultaneous addition of B and Nb under the same production conditions. The microstructure can be further refined when 0.5 mass% of Ni was added to the Nb, B-added steels. This can be attributed to the grain boundaries pinning effects by the fine precipitates which are obtained by the simultaneous addition of B and Nb and the solute dragging effects of boundary segregated B and homogeneous distributed Ni atoms.

(2) Besides the pinning effects and the solute dragging effects of boundary segregated boron, the boundary cohesion is supposed to be increased by the segregated boron.

(3) No Fe-Ni solid solution was detected in this study. The effects of Ni are supposed to be pinning effects of the homogeneous distributed Ni atoms.

(4) Practical manufacture shows that it is an economical method to improve the low-temperature impact toughness by adding 11 ppm of B and 0.5 mass% of Ni to the investigated H-beams. The production process does not need to be adjusted compared to the steels with only Nb-added.

REFERENCES

1. Y.M. Wang, M.Y. Li, G. Wei, The control rolling and control cooling of steels. Metallurgy Industrial Press, Beijing, 2007.
2. E.O. Hall, *Proc. Phys. Soc. Lond.*, **64**, 747 (1951).
3. Y.C. Liu, F.X. Zhu, Y.M. Li, G.D. Wang, *ISIJ Int.*, **45**, 851 (2006).
4. G.T. Cui, Z.C. Wang, T. Sun, W.M. Guo, X.L. Zhao, J.Q. Gao, C.X. Dong, Effect of boron on low temperature impact toughness of hot-rolled Nb-added HSLA H-section steel and its mechanism. ICAMP-5, 2008.
5. X.M. Wang, X.L. He, *ISIJ Int.,* **42** (Suppl. 2002), S38 (2002).

6. L.T. Mavropoulos, J.J. Jonas, *Can. Metall Quart.* **28**, 159 (1989).

7. L.T. Mavropoulos, J.J. Jonas, *Can. Metall Quart.*, **27**, 235 (1988).

8. S. Watanabe, H. Ohtani, T. Kunitake, *Trans. ISIJ*, **23**, 31 (1983).

9. T. Hara, H. Asahi, R. Uemori, H. Tamehiro, *ISIJ Int.,* **44**, 1431 (2004).

10. J.E. Morral, T.B. Cameron, The hardenability mechanism of boron. In: Banerji SK, Morral JE (eds.) Boron in steel. Metallurgy Industrial Press, Beijing, 1985.

11. H. Tamehiro, M. Murata, R. Habu, M. Nagumo, *Tetsu-to-Hagane*, **72**, 458 (1986).

12. X.L. He, M. Djahazi, J.J. Jonas, J. Jackman, *Acta Metall. Mater.,* **39**, 2295 (1991).

13. E. El-Kashif, K. Asakura, T. Koseki, K. Shibata, *ISIJ Int.*, **44**, 1568 (2004).

14. S.H. Lee, S.U. Lee, K.I. Moon, K.S. Lee, *Mater. Sci. Eng.* A, **382**, 209 (2004).

15. Z.C. Wang, G.T. Cui, T. Sun, W.M. Guo, X.L. Zhao, J.Q. Gao, C.X. Dong, *Int. J. Mod. Phys.* B, **23**, 1885 (2009).

16. G.T. Cui, Z.C. Wang, W.M. Guo, T. Sun, J.Q. Gao (in Chinese), *J. Build. Mater.*, **15**, 103 (2012).

17. G.T. Cui, Z.C. Wang, T. Sun, W.M. Guo, J.Q. Gao, *Appl. Mech. Mater.* **174-177**, 1030 (2012).

18. X. Wang, Z.C. Wang, X.B. Wang, Y.R. Wang, J.Q. Gao, X.L. Zhao, *J. Iron Steel Res. Int.,* **19**, 62 (2012).

19. E. El-Kashif, K. Asakura, K. Shibata, *ISIJ Int.* **42**, 1468 (2002).

ВЛИЯНИЕ НА БОР И БОР-НИКЕЛ ВЪРХУ ЯКОСТТА НА УДАР НА ГОРЕЩО ВАЛЦУВАНИ НИСКО ЛЕГИРАНИ ГРЕДИ С ВИСОКА ЯКОСТ, СЪДЪРЖАЩИ ДОБАВЕН НИОБИЙ

Г.Т. Куи[1]*, З.К. Уанг[2], Кс.Б. Уанг[2], Кс. Уанг [2], Дж.С. Гао[3]

[1] *Училище по електрохимично инженерство, Университет на Хезе, Хезе, 274015, Шандонг, Китай*

[2.] *Лаборатория по течно-твърдо структурно развитие и обработка на материали, Министерство на образованието, Университет на Шандонг, Джинан, 250061, Шандонг, Китай*

[3] *Лайу компания за желязо и стомана, Лайу, 271104, Шандонг, Китай*

(Резюме)

Nb-съдържащи ниско легирани стомани са сплавени с 11 ppm B и 11 ppm B + 0.5 мас.% Ni и са изследвани с оглед намиране на ефективен метод за подобряване на нискотемпературните якостни свойства на ниско легирани греди с висока якост. Механичните свойства и микроструктурата на стоманите са изследвани съответно чрез едноосов тест на опън, Charpy ударен тест с V-бразда, ТЕМ и XRD. Установено е, че абсорбираната енергия при -50℃ от 13 J може да достигне 44.4 J с добавка от 11 ppm B и 121 J с добавка от 11 ppm B + 0.5 мас. % Ni. Утайката от ниобиев карбонитрид става значително по-фина с добавка на бор – измерени са зърна с диаметър до 30 nm. Утаяването на $Fe_{23}(C,B)_6$ се подтиска от едновременното добавяне на бор и ниобий. Не е установено наличие на твърди разтвори от Fe-Ni чрез XRD. Направено е предположение, че борът в твърдия разтвор и хомогенно разпределеният никел имат благоприятно влияние върху нискотемпературната якост на удар на Nb –съдържащи ниско легирани стомани.

Arsenate and arsenite removal by Fe-modified activated carbon supported nano-TiO2: influence factors and adsorption effect

F. X. Qin[1,2], C. F. Wei[1*], Z. K. Wang[3], G. Li[2], X. L. Li[2], Y. J. Li[2]

[1] *College of Resources and Environment, Southwest University, Chongqing 400716, China;*
[2] *Key Laboratory for Information System of Mountainous Areas and Protection of Ecological Environment of Guizhou Province, Guizhou Normal University, Guiyang 550001, China;*
[3] *College of Eco-Environmental Engineering, Guizhou Minzu University, Guiyang, 550025, China*

In this paper, the preparation of Fe-modified activated carbon supported nano-TiO2 (Fe-TiO2/AC) particles and the test results of the properties of the synthesized material, including crystallinity structure, surface morphology, functional groups, and surface texture, obtained using X-ray diffraction, transmission electron microscopy, scanning electron microscopy, and Fourier transform infrared spectroscopy, are presented. The removal rates of arsenic were evaluated using batch tests under several simulated conditions, including pH, ionic strength, material dosage, and initial arsenic concentration. The results indicated that arsenic removal was effective in weak alkaline conditions, and the maximum adsorption for arsenic was observed at pH = 8. The arsenic removal rate was improved by increasing the ionic strength and the adsorbent dosage. The adsorption of As(III) and As(V) reached equilibrium within 3 h and 1.14 h, respectively. The pseudo-second-order model satisfactorily described the adsorption processes. Isotherm data were fitted using the Freundlich equation. The isotherm results showed that the maximum adsorption capacities of Fe-TiO2/AC were 28.66 mg$\cdot$g^{-1} for As(III) and 35.22 mg$\cdot$g^{-1} for As(V). In the adsorption process, nano-TiO2 and Fe2O3 played key roles in increasing the adsorption efficiency and converting As(III) to As(V). Moreover, the presence of Fe(III) accelerated the oxidation of arsenic.

Keywords: Fe-TiO2/AC, Arsenic removal, Adsorption, Redox, Chemical characterization.

INTRODUCTION

Arsenic (As) is a metalloid, which exists in the form of As(III) and As(V) [1,2] and can be widely detected in both natural and anthropogenic sources [3]. Serious health threats for humans and other living organisms have attracted considerable attention because of their high toxicity [4,5]. From the perspective of natural pollution, both As(III) and As(V) are found in soil, organisms, and water, and are mobilized through a combination of natural processes such as rock weathering, biological activities, and volcanic emissions [6]. In the case of anthropogenic activities, arsenic contaminations were mainly caused by combustion of fossil fuels, petroleum refineries, mining, and nonferrous smelting activities [7-9]. In China, the living surroundings are exposed to different degrees of arsenic pollution; moreover, arsenic pollution exceeds its threshold level (10 μg$\cdot$L^{-1}) in drinking water [10]. Therefore, effective removal of arsenic or conversion from As(III) to As(V) at the highest oxidation rate for the purpose of reducing its toxicity and other detrimental effects is a key issue in arsenic pollution control and treatment.

A large number of methods, including physical-chemical treatment processes such as precipitation, ion-exchange, adsorption, and membrane filtration, have been used for removing toxic elements from water and, subsequently, for alleviating water pollution [10-16]. Among them, adsorption is one of the most preeminent removal methods because of its low cost, ease of operation, and high efficiency [17]. A higher efficiency of arsenic removal can be achieved by indirectly adsorbing arsenic or converting As(III) to As(V) through a pre-oxidation process, as As(III) is difficult to be removed directly by using most of the existing techniques.

Titanium dioxide [18] and its modified counterparts [19] exhibit excellent removal arsenic efficiency by adsorbing it from the polluted water. In brief, the adsorption can be attributed to their special physical and chemical properties, such as high theoretical adsorption capacity, large specific surface area, oxidation behavior, photo-catalytic efficiency, and high affinity of the surface hydroxyl groups [20]. In addition, the particle size of the adsorbent affects the adsorption capacity for arsenic [18]. Bang *et al.* [21] found that the arsenic species had a high affinity for the surface sites of TiO2. Although TiO2-doped materials exhibit excellent adsorption performance, the effective load amount may hinder an extensive use of traditionally prepared nano-TiO2-doped materials. Long and Tu

---

*) To whom all correspondence should be sent:
E-mail: weicf@swu.edu.cn

[22] studied arsenic removal by using activated-carbon-supported granular nano-TiO₂, but they found that the nano-TiO₂ loaded amount was too low to decrease the arsenic level. To improve the loaded amount of nano-TiO₂, tetrabutyl titanate doped with activated carbon powder was produced using the sol-gel method in our experiment. In addition, arsenic was adsorbed widely by iron compounds (granular ferric hydroxide and ferric oxide) and several common minerals such as goethite and ferrihydrite [23].

In this article, we have attempted to modify TiO₂-doped activated carbon powder using iron. Here, we have focused on whether the modification of supported TiO₂ can enhance its adsorption ability to arsenic by iron compounds. Thus, in this study, a new adsorbent was prepared and used to remove As(III) and As(V) from an aqueous solution. The effects of pH, adsorbent dosage, and ionic strength were elucidated to explore the optimum removal conditions. The adsorption kinetics and isotherms were investigated to probe the adsorption efficiency and the maximum adsorption capacity for arsenic. The main objectives of this research were as follows: (a) to produce a sufficient amount of a uniform adsorption material with preloaded TiO₂ and iron content, (b) to evaluate the arsenic adsorption by the material and determine its maximum adsorption capacity for As(III) and As(V), and (c) to explain the adsorption mechanism of the material.

EXPERIMENTAL
Materials

Nitric acid (HNO₃), anhydrous ethanol (C₂H₅OH), tetrabutyl titanate (C₁₆H₃₆O₄Ti), and glacial acetic acid (CH₃COOH) were purchased from Sinopharm Chemical Reagent Co., Ltd (China). Ammonium sulfate [(NH₄)₂SO₄, analytical reagent] was supplied by Tianjin Kermel Chemical Reagent Co., Ltd. (China). Activated carbon powder was obtained from Hunan Deban Activated Carbon Co., Ltd. (China). NaAsO₂ was the source for preparing 1000 mg·L⁻¹ of As(III). 1000 mg·L⁻¹ of As(V) was prepared by the oxidation of a stock solution of As(III) using excess potassium peroxydisulfate (K₂S₂O₈). The NaCl, NaOH (0.1 mol·L⁻¹), and HCl (0.1 mol·L⁻¹) solutions were prepared using deionized water (18.2 MΩ·cm). Stock solutions were stored in dark before the experiments. Unless otherwise stated, all chemicals were of analytical grade and above.

Fe-TiO₂/AC powder preparation

The preparation of the adsorbent powder is described in detail in [24]. In brief, the procedure was as follows: 16.4 g of the activated carbon powder was pre-soaked in HNO₃ and then, added to a mixture of 70 mL anhydrous C₂H₅OH and 20 mL tetrabutyl titanate at a pH of 2–3 (adjusted using glacial acetic acid) to obtain solution A. Next, 20 mL of anhydrous ethanol (C₂H₅OH), 60 mL of water, 2.4 g of ammonium sulfate [(NH₄)₂SO₄], and ferric nitrate were mixed in a clean breaker; the mixture was stirred continuously by using a magnetic stirrer. Then, acetic acid (CH₃COOH) was used to regulate the pH in the range of 2–3, resulting in the mixed solution B. Solution B was dropped slowly to mix with solution A using a speed stirring process (200 rpm), and the resulting mixture was continuously stirred by using a magnetic mixer at 400 rpm at room temperature (25–28°C) for 2 h. Further, the Fe-TiO₂/AC soliquid was produced as follows: The Fe-TiO₂/AC sol was rested for 24 h and then, smoothly ground after drying at 100°C. The resulting powder was roasted in a covered crucible in a muffle furnace at 500°C for 2 h and then, naturally cooled down to room temperature. The result was Fe-TiO₂/AC powder.

Material characterization

The new material was characterized using X-ray diffraction (XRD), transmission electron microscopy/scanning electron microscopy (TEM/SEM), and Fourier transform infrared spectroscopy (FTIR) methods. The XRD (DY2862, Holland) method was used to explore the crystal structure of the material. TEM (JEM-2100F, Japan) and SEM (JSM-6490LV, Japan) were used for determining the shapes of the adsorbent. The functional groups of the adsorbent were observed using FTIR (TENSOR27, Bruker, Germany). The titanium content and the iron content were determined using ICP-OES (Optima 5300V, Perkin Elmer, America), and the TiO₂ loaded amount was calculated.

Batch adsorption experiments

All glassware and polyethylene bottles were soaked in 10% HNO₃ for at least 24 h before each experiment and then, washed thrice with distilled water and dried in an oven. NaCl was used to adjust the ionic strength of the solution, and HCl and NaOH (both 0.1 mol·L⁻¹) were used for the required pH adjustment. The pH values were measured using a pH meter (3E, Shanghai Leici Inc., China). 1000 mg·L⁻¹ of As(III) and As(V) solution was diluted to obtain the required concentrations. The reaction volume was selected to be 25 mL, and the adsorbent was added in the appropriate dosage and at the appropriate time at room temperature

(25−28°C) and settled for 20 min. The sample was then centrifuged for 30 min (4000 rpm), and equilibrium arsenic solution was moved into sample vials and analyzed using atomic fluorescence spectrometry (AFS 933, Beijing Titan Instruments Co., Ltd., China) and inductively coupled plasma optical emission spectroscopy (ICP-OES, Optima $\frac{t}{Q_t}$ 5300V, PerkinElmer, America). The effects of pH, ionic strength, adsorbent dosage, and time were evaluated. All of the adsorption samples were shaken continuously and uniformly in the oscillator (HY-5,Changzhou Huanyu Scientific Instrument Factory, China). The resulting solution samples were analyzed within 24 h.

Adsorption results calculations

The arsenic removal rate and the amount of arsenic adsorbed on the manufactured materials were calculated using equations (1) and (2):

$$\text{Arsenic removal rate(\%)} = \frac{c_1 - c_2}{c_1} \times 10 \quad (1)$$

Adsorption capacity by a unit mass of adsorbent

$$\text{As/adsorbent(mg g}^{-1}) = \frac{(c_1 - c_2) \times}{M} \quad (2)$$

where C_1 is the initial arsenic concentration (mg·L^{-1}), C_2 is the arsenic concentration after adsorption (mg·L^{-1}), V is the solution volume (L), and M is the adsorbent dosage (g).

Adsorption kinetic test

Two kinetic models, namely the pseudo-first-order kinetic model and the pseudo-second-order kinetic model, were used to fit the experimental data in order to estimate the adsorption rate.

The form of the pseudo-first-order kinetic model is as follows [25]:

$$\frac{dQ_t}{dt} = K_1(Q_e - Q_t) \quad (3)$$

The following is its linear equation:

$$\ln(Q_e - Q_t) = \ln Q_e - \ln K_1 \quad (4)$$

The pseudo-second-order kinetic model can be expressed as follows [25]:

$$\frac{dQ_t}{dt} = K_2(Q_e - Q_t)^2 \quad (5)$$

Its linear equation is as follows:

$$\frac{t}{Q_t} = \frac{1}{K_2 Q_e^2} + \frac{t}{Q_e} \quad (6)$$

where Q_e is the amount of adsorbed arsenic at the adsorption equilibrium (mg·g^{-1}); Q_t is the amount of adsorbed arsenic at a certain point of time t (mg·g^{-1}); K_1 and K_2 are the adsorption rate constants of the pseudo-first-order kinetic model (h^{-1}) and the pseudo-second-order kinetic model, respectively; and t is the adsorption time (h). K_1 is calculated by fitting a straight line equation of ln($Q_e - Q_t$) – t, and the reaction rate increases with an increase in K_1. K_2 is calculated by fitting the straight line equation of $\frac{t}{Q_t}$ and t.

Adsorption isothermal test

The Langmuir and Freundlich isotherm equations can be expressed as follows [26]:

Langmuir equation:

$$\frac{C_e}{Q_e} = \frac{C_e}{Q_m} + \frac{t}{K_L Q_m} \quad (7)$$

Freundlich equation:

$$\lg(Q_e) = \lg(K_F) + \frac{1}{n}\lg(C_e) \quad (8)$$

where Q_e is the amount of adsorbed arsenic at the adsorption equilibrium (mg·g^{-1}), C_e is the arsenic concentration at the adsorption equilibrium (mg·L^{-1}), Q_m is the calculated constant related to the adsorption capacity (mg·g^{-1}), K_L is the Langmuir adsorption equilibrium constant related to the affinity of the binding sites and the adsorption heat, K_F is the Freundlich constant, and n is a parameter related to the adsorption strength. Large values of K_F and n indicated better adsorption performance of the adsorbent.

RESULTS AND DISCUSSION

Characterization of Fe-TiO₂/AC

For the characterization of the Fe-TiO₂/AC powder, we initially examined the prepared Fe-TiO₂/AC sample using TEM and SEM, as shown in Fig. 1. Fig. 1(a) shows the presence of a dense microstructure. The powdered activated carbon and nano-TiO₂ or Fe₂O₃ particles were interlaced. We observed that the powder was an irregular ellipsoid with many filamentous network chains around it. Further, we inferred that the irregular ellipsoid was nano-TiO₂ and the black particles in the external network chain were Fe₂O₃. Fig. 1(a) also shows that particles of different sizes were wrapped around each other. We observed amorphous particles, microcrystalline particles, and nanocrystalline particles. Thus, we concluded that the adsorption channels of the material had stacking-capillary

pores formed by the accumulation of nanoparticles [27]. Fig. 1(b) shows that some of the nano-TiO_2 and Fe_2O_3 particles attached to the surface of the activated carbon and a small number of particles entered into the channels of the activated carbon. The supported particles exhibited a variety of particle sizes.
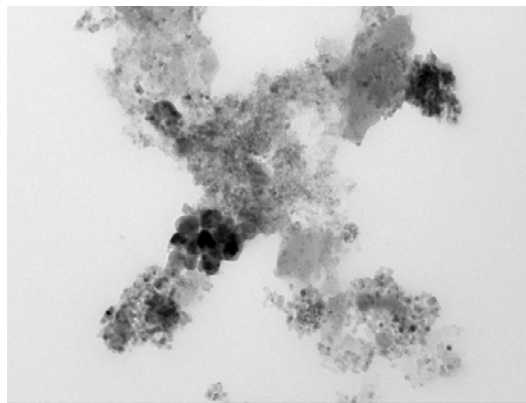
a
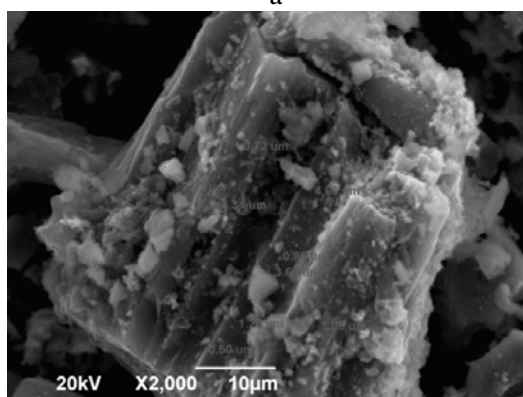
b

Fig. 1. TEM and SEM images of the TiO_2/AC sample: TEM and (b) SEM;

On the basis of these observations and the TEM results for the material, we concluded that supported nano-TiO_2 with relatively large particles was produced by agglomeration of small nano-TiO_2 particles. The average particle size of the adsorbent was around 10 – 52 nm.

The FTIR spectrum of the material is shown in Fig. 2. This figure shows that the broad characteristic band at 3418.22 cm^{-1} is assigned to the O-H stretching vibration [19]. At around 1640 cm^{-1}, a free water molecule H-O-H bending vibration was discovered [28]. The bending vibration at 1100 cm^{-1} belonged to the hydroxyl groups on the surface of the metal oxides [29]. The broad wavenumber range of around 550 – 800 cm^{-1} was attributed to the characteristic bands of the Ti-

O-Ti bond [30]. The band of 570 cm^{-1} belonged to the Fe-O bond.
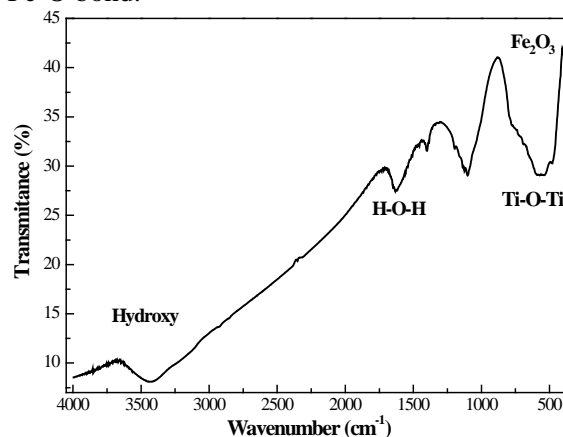
Fig. 2. FTIR spectrum of TiO_2/AC

The prepared material particles were exposed to an XRD test. As shown in Fig. 3, the diffraction peaks of the material were at 25.51°, 37.82°, 48.13°, 53.92°, and 75.13°, which showed a good consistency with the diffraction structure of TiO_2. Further, according to the JCPDS standard card (No.71-1167), the crystal form of TiO_2 was anatase [31]. The peak at $2\theta = 26.6°$ matched with the characteristic diffraction peak of SiO_2. The Fe-TiO_2/AC particles included a considerable proportion of hematite-Fe_2O_3, because the diffraction peaks of Fe-TiO_2/AC were observed at 33.52°, 35.92°, 49.81°, and 54.01°, which were assigned to the diffraction of Fe_2O_3 and the peak structure was more obvious as the Fe(III) doping improved the crystallinity of the adsorbent.

Using this technique, we determined the concentration of TiO_2 and Fe_2O_3 to be 250 and 114 mg·g^{-1}, respectively. Furthermore, we demonstrated that the supported TiO_2 species were particularly stable under acidic conditions, as no leached TiO_2 was detected following a treatment with aqua regia (5 vol%).
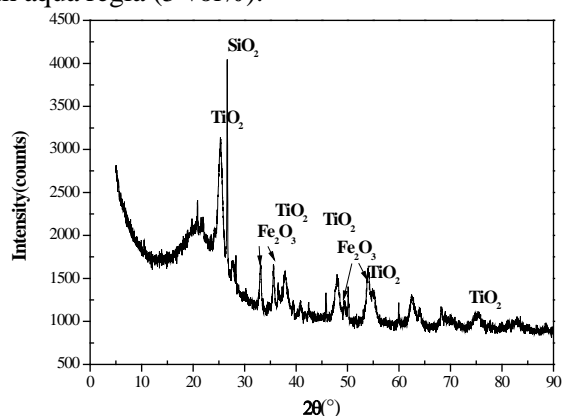
Fig. 3. XRD pattern of the TiO_2/AC

Effect of pH on arsenic removal

pH is an important influencing factor for the arsenic removal process [32]. The surface charges of the adsorbent and the arsenic compound forms are influenced by pH variation, thus affecting the arsenic adsorption [33].

The effect of pH on As(III) and As(V) removal was determined at pH values ranging from 3 to 11. Fig. 4 shows that arsenic adsorption was strongly influenced by pH. The arsenic removal rate and the amount of adsorbed arsenic increased with an increase in pH and then decreased until pH = 11. The removal rate of As(V) gradually increased from 90.88% to 99.00% when the solution pH increased from 3 to 8, and then, rapidly decreased from 99.00% to 82.39% with an increase in pH from 8 to 11. The amounts of adsorbed As(V) increased from 0.038 to 0.409 mg·g^{-1} and then, decreased to 0.035 mg·g^{-1} on the Fe-TiO₂/AC particles. A similar As(V) adsorption behavior by P25 [34] and ferric hydroxides [35] was reported earlier. The amount of As(III) adsorbed onto the Fe-TiO₂/AC particles increased steadily from 0.028 to 0.034 mg·g^{-1} at pH values of 3–8 and then, declined gradually to 0.029 mg·g^{-1}.

The increasing removal rate and amount of As(V) adsorbed resulted from a progressive competition between the arsenate and hydroxyl anions for titanium bonding and iron bonding when pH increased from 3 to 8. The arsenic removal rate and the amount of arsenic adsorbed onto Fe-TiO₂/AC reached a maximum at pH = 8, which was attributed to the fact that arsenic combines more easily with titanium and iron in a weakly alkaline medium where arsenic is mainly present in anion forms such as AsO_3^{3-}, $HAsO_3^{2-}$, H_2AsO^{3-}, and $HAsO_4^{2-}$, and the nano-TiO₂ surface has a positive charge; here, the uptake of arsenic is rapid because of the repulsion from its surface at pH values higher than 8 [36].
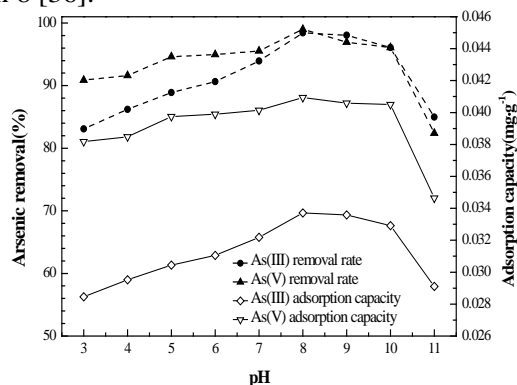
Fig.4. Effect of pH on arsenic removal at room temperature under the following conditions: initial concentration of As(III) 70 μg·L^{-1} and As(V) 84 μg·L^{-1}, solution volume 25 mL, adsorbent dosage 0.05 g, and ionic strength 0.01 mol·L^{-1}

Note that more As(V) than As(III) was removed because $H_2AsO_4^-$ and $HAsO_4^{2-}$ are the primary As(V) forms observed at pH 3–11. Therefore, the As(V) removal results were possibly caused by the interaction between the neutralization of the anionic and the positive charges. As(III) is mainly present as H₃AsO₃, which remains as a neutral molecule in a non-alkaline environment. However, in a weakly alkaline environment, H₃AsO₃ is gradually transformed into anionic $H_2AsO_3^-$ because of the protonation effect and the surface of nano-TiO₂ produced more adsorption sites with positive charges by removing hydroxyl ions; thus, more As(III) was adsorbed [37].

When pH > 8, the removal rate and the amount of adsorbed arsenic decreased because of the decrease in the proportion of the positive charges on the adsorbent surface [36] and the competitive adsorption of OH$^-$ and arsenic compounds; we expected to achieve arsenic desorption in strongly acidic or alkaline solutions. Note that the As(III) removal by FeCl₃ decreased with an increase in the pH value from 9 to 10 and depended primarily on the incomplete precipitation of Fe(III) and then on the repulsion between $H_2AsO_3^-$ and negatively charged iron hydroxide flocs [38]. The trend of the As(III) removal rate and the amount of As(III) adsorbed onto Fe-TiO₂/AC showed a sharp decrease at pH values of 10–11 and was consistent with the adsorption of anions of the weak acid on the oxide-water interface [23]. We also proved that the adsorbent was a combination of iron oxides and titanium because this phenomenon was observed in the case of iron (hydr)oxides [35] and titanium dioxide-adsorbed As(III) [39]. The finding that the removal rate and the adsorbed amount of As(III) onto Fe-TiO₂/AC were more favorable than those of As(V) at pH values of 8–11 [36,40] was attributed to the following two reasons: (a) changes in the form of the As(III) compound (from H₃AsO₃ to $H_2AsO_3^-$) and (b) the initial concentration difference. Qiao *et al.* [38] observed the same difference: the As(V) removal was more favorable than the As(III) removal at a lower pH, but the opposite trend was observed at higher pH values. From pH 4 to 11, the adsorption efficiency of As(V) and As(III) was similar because of the photocatalytic oxidation of TiO₂ in the presence of dissolved oxygen and light [41]. In addition, the surface potential of metal oxides became more negative and considerable adsorption of As(V) and As(III) was observed when pH > point of zero charge (PZC), which indicated that the arsenic species were adsorbed on TiO₂ through surface complexation and not through electrostatic interactions [21,41]. The results of the present study revealed that pH 8 was the optimal adsorption condition for removing arsenic.

Effect of initial arsenic concentration on arsenic removal

The removal rate and the amount of arsenic adsorbed onto Fe-TiO$_2$/AC as functions of the initial arsenic concentration are illustrated in Fig. 5 at the optimal pH. The arsenic removal rate decreased with an increase in the initial concentration. The amount of adsorbed arsenic increased because of the incomplete combination of the adsorption sites with arsenic and the inability of the adsorbed arsenic to reach saturation at a low initial arsenic concentration. In addition, a higher amount of As(V) than As(III) was adsorbed under the simulated operating conditions. The As(III) removal rate decreased continuously from 98.62% to 54.99% when the initial concentration increased to 10 mg·L^{-1} and significantly declined at the initial concentration of 0.05–2 mg·L^{-1}; thereafter, the downward trend appeared to be gentle at the initial concentration of 2–10 mg·L^{-1} and the amount of As(III) adsorbed onto Fe-TiO$_2$/AC increased from 0.023 to 2.674 mg·g^{-1} with an obvious increase at the initial concentration of 1–10 mg·L^{-1}. As(V) displayed similar variation trends. The removal rate decreased from 99.12% to 65.9% when the initial concentration increased to 10 mg·L^{-1}, and the amount of As(V) adsorbed onto the Fe-TiO$_2$/AC particles increased from 0.026 to 3.259 mg·g^{-1}. The As(V) removal rate decreased sharply at the initial concentration of 0.05−5 mg·L^{-1} and then, remained almost constant, and the adsorption amount of As(V) onto Fe-TiO$_2$/AC exhibited an obvious increase at the initial concentration of 1–10 mg·L^{-1}.
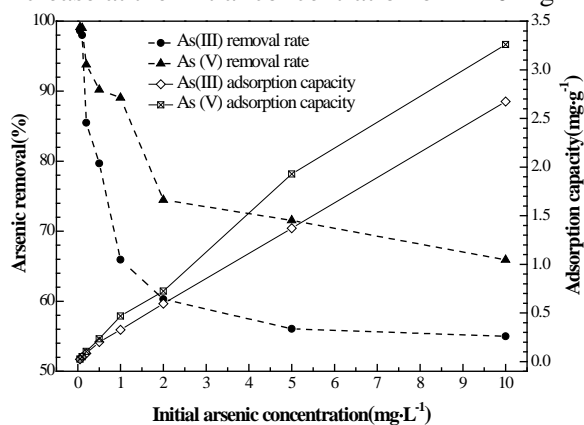
Fig.5. Effect of initial concentration on arsenic removal at room temperature under the following reaction conditions: pH = 8, solution volume 25 mL, adsorbent dosage 0.05 g, and ionic strength 0.01 mol·L^{-1}

Effect of the adsorbent dosage

The effect of the adsorbent dosage on the removal result is shown in Fig. 6. This figure shows that the As(III) and As(V) removal efficiencies are strongly influenced by the absorbent dosage: 0.5 g

dosage was sufficient to reach the adsorption equilibrium when the initial arsenic concentration was 1.3 mg·L^{-1}, and Fe-TiO$_2$/AC was significantly efficient with respect to As(V) adsorption as compared to As(III) adsorption at an equivalent adsorbent level. The removal rate of arsenic increased with an increase in the adsorbent dosage, but the amount of adsorbed arsenic decreased. Further, a steep change occurred when the adsorbent dosage increased from 0.01 to 0.5 g, and a constant removal result was maintained with a further increase in the adsorbent dosage in the adsorption process. When 0.5 g of Fe-TiO$_2$/AC was added to 25 mL of an arsenic solution, more than 93% of As(V) and 95% of As(III) were adsorbed, but the amounts of As(V) and As(II) adsorbed were 0.055 mg·g^{-1} and 0.065 mg·g^{-1}, respectively. The amount of arsenic adsorption decreased with an increase in the adsorbent dosage. When the dosage was less than 0.5 g, the amount of adsorbed arsenic sharply decreased and then reached equilibrium. Thus, we concluded that a higher adsorbent dosage resulted in a higher removal rate and a lower adsorption amount before the adsorption equilibrium was reached because the number of adsorption sites for the removal of arsenic increased with an increase in the adsorbent dosage and led to a higher removal rate, but the arsenic concentration remained unchanged in the adsorption process. The adsorption equilibrium was reached when the adsorbent dosage was 0.5 g. More adsorption sites were produced when the adsorbent dosage increased from 0.5 to 3.0 g, but these adsorption sites could not be fully utilized, which continued to keep arsenic adsorption capacity onto the adsorbent. Genç-fuhrman *et al*. [42] observed a similar phenomenon during arsenate removal from water by using neutralized red mud.
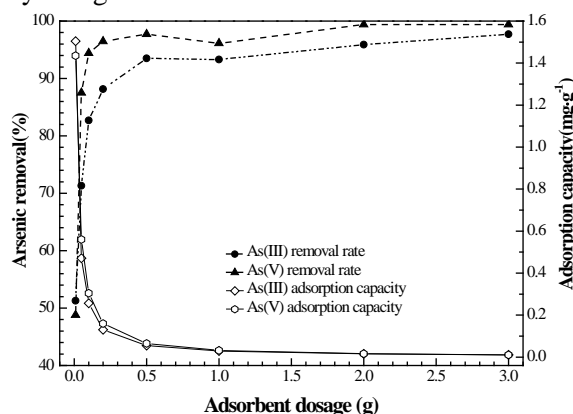
Fig.6. Effect of adsorbent dosage on arsenic removal at room temperature under the following reaction conditions: pH = 8, initial As concentration 1.3 mg·L^{-1}, solution volume 25 mL, and ionic strength 0.01 mol·L^{-1}

Effect of ionic strength

In this section, the removal rate of arsenic onto Fe-TiO$_2$/AC is discussed, and the results are shown in Fig. 7. As(III) adsorption was clearly more dependent on ionic strength than As(V) adsorption. In the adsorption process, the arsenic removal efficiency increased when the ionic strength increased to 0.5 mol·L^{-1}. The removal rate of As(III) increased from 89.71% to 94.70%. The amount of As(III) adsorbed onto Fe-TiO$_2$/AC increased from 0.058 to 0.061 mg·g^{-1}. Further, the removal rate of As(V) increased from 93.83% to 97.47%. The amount of As(V) adsorbed onto Fe-TiO$_2$/AC increased from 0.061 to 0.063 mg·g^{-1} with an increase in the ionic strength. This was attributed to the linking of the surface hydroxyls of the adsorbent and arsenic by a ligand exchange reaction and the formation of inner surface complexes [43].

Adsorption kinetics

Adsorption kinetics experiments were conducted to determine the rate of arsenic removal. In this process, As(III) and As(V) removal by the material was conducted under the same conditions. The experimental results are presented in Fig. 8. It shows that arsenic removal rate was enhanced with increasing adsorption time before adsorption equilibrium was reached. The arsenic removal rate increased at a quick pace. The As(V) removal rate remains relatively constant within 70 min (1.17 h) to 1440 min (24 h) by the material under the current experimental conditions. In other words, the adsorption of As(V) reached equilibrium in 70 min (1.17 h). For As(III), adsorption equilibrium was attained in 90 min (1.5 h).
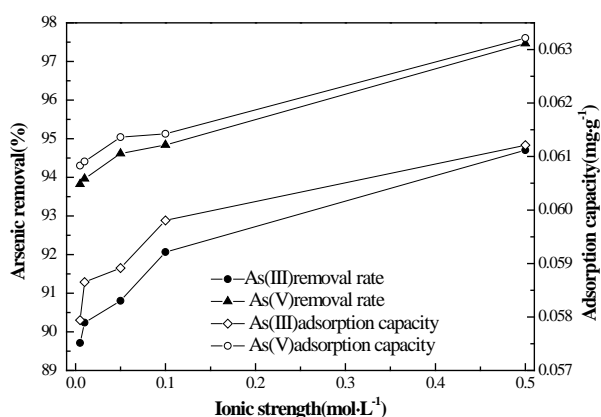
Fig.7. Effect of ionic strength on arsenic removal at room temperature under the following reaction conditions: pH = 8, initial As concentration 1.3 mg·L^{-1}, solution volume 25 mL, and adsorbent dosage 0.5 g

The kinetic parameters of the adsorption obtained using equation (4) are shown in Table 1. The correlation coefficients of the As(V) and As(III) adsorption were 0.7854 and 0.7835, respectively. The pseudo-first-order

kinetic model was used to describe the experimental data of As(V) and As(III) in the current conditions, but it failed to explain the arsenic adsorption onto Fe-TiO$_2$/AC. Therefore, we concluded that physical adsorption could not be ignored in the arsenic removal process, which implied that the adsorption rate of As(V) onto the adsorbent was faster than that of As(III). The experimental data were consistent with the information reflected by the K_1 value.

The pseudo-second-order kinetic parameters are presented in Table 2. The data regarding the As(III) and As(V) adsorption onto the adsorbent were well described by the pseudo-second-order model. The obtained correlation coefficients were higher than 0.9999 and were in the following order: As(V) > As(III). K_2 followed the order As(V) > As(III).

As compared to the pseudo-first-order model, the pseudo-second-order model fitted the experimental data very well, which implied that the arsenic adsorption onto the adsorbent was a complex process involving surface adsorption, inter-components, and intra-particle diffusion [44]. An excellent effect of arsenic adsorption onto the adsorbent was obtained using physical adsorption and chemical adsorption, and chemical bonds were the main factors influencing the chemical adsorption process [45].

Adsorption isotherms

The adsorption isotherm experiments were performed at different initial concentrations ranging from 0.2 to 562.1 mg·L^{-1}. The adsorption equilibrium time was maintained at 3 h for the As(III) removal and 70 min for the As(V) removal.
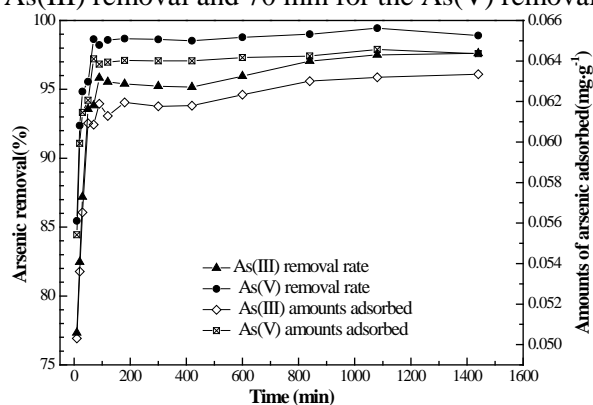
Fig.8. Kinetic curve of arsenic removal by the adsorbent at room temperature under the following reaction conditions: pH = 8, initial As concentration 1.3 mg·L^{-1}, solution volume 25 mL, and adsorbent dosage 0.5 g

Table 1. Pseudo-first-order parameters and equation for As(III) and As(V) removal

Parameters	As(III)	As(V)
K_1	1.6405	2.1026
R^2	0.7835	0.7854
Fitting equation	$\ln(Q_e - Q_t) = -1.641t - 4.551$	$\ln(Q_e - Q_t) = -2.103t - 4.648$

Table 2. Pseudo-second-order parameters and equation for As(III) and As(V) removal

Parameters	As(III)	As(V)
K_2	212.8190	581.9038
R^2	0.99996	0.99999
Fitting equation	$t/Q_t = 15.776t + 1.170$	$t/Q_t = 15.511t + 0.413$

The Freundlich and Langmuir parameters are presented in Table 3 and Table 4, respectively. These results indicated that the arsenic adsorption data fitted the Freundlich isotherm better than the Langmuir isotherm, and the corresponding good correlation coefficient values were between 0.9528 and 0.9780, which indicated that the arsenic adsorption by the material was heterogeneous adsorption on a non-uniform surface. The n value of the Freundlich equation was greater than 1; this indicated that the adsorption of arsenic was easy. The KF value of As(V) was relatively large, which implied that the removal of As(V) was more favorable than that of As(III). According to the isotherm results, the maximum adsorption capacities of Fe-TiO₂/AC were 28.66 mg·g⁻¹ and 35.22 mg·g⁻¹ for As(III) and As(V), respectively. As compared to many other adsorbents, the new material exhibited excellent adsorption capacity. For instance, Pena *et al.* [41] found that 8.30 mg·g⁻¹ of As(III) and 11.20 mg·g⁻¹ of As(V) were removed by nanocrystalline TiO2. Altundoğan *et al.* [46] estimated the maximum adsorption capacities of red mud for As(III) and As(V) to be 0.33 mg·g⁻¹ and 0.35 mg·g⁻¹, respectively.

Table 3. Freundlich isotherm constants

Parameters	As(III)	As(V)
K_F	0.3538	1.5172
R_2	0.9780	0.9528
n	1.4215	1.7184
Fitting equation	$\lg Q_e = -0.45119 + 0.70348\lg Ce$	$\lg Q_e = 0.18103 + 0.58195\lg Ce$

Table 4. Langmuir isotherm constants

Parameters	As(III)	As(V)
K_F	0.025	0.228
R_2	0.8824	0.8967
Q_m	14.63	16.71
Fitting equation	$C_e/Q_e = 0.0684 C_e + 2.735$	$C_e/Q_e = 0.0598 C_e + 0.263$

Adsorption mechanism

Arsenic removal from an aqueous solution by Fe-TiO₂/AC requires simultaneous physical and chemical adsorption. Further, a sufficient number of adsorption sites are required for arsenic removal. The positive charge on the TiO₂ surface facilitates arsenate adsorption by electrostatic interactions at pH = 8, where the arsenate is present mainly as anion. The deprotonation of arsenite may remove the hydroxyl ions from the coordinating layer of the TiO₂ support, and thus, some adsorption sites with a positive charge are created on the adsorbent surface

to adsorb the As(III) anions in the process [37]. A nano-TiO₂ loading can complete the partial conversion of As(III) to As(V) because the catalytic oxidation activity of TiO₂ and arsenic can form monodentate or bidentate complexes at the surface of TiO₂ [23,47]. In the adsorption process, As-O-AsO₄³⁻ and As-O-H₂AsO₄⁴⁻ groups were formed during the As(V) removal by nano-TiO₂ with anatase crystals, and As-O-AsO₃³⁻ and As-O-HAsO₄²⁻ were found under mild conditions during the As(III) removal and the adsorption of As(V) and As(III) on TiO₂ by the As-O-Ti and As-O bonds [18]. The Fe(III) supports of the Fe-TiO₂/AC particles accelerated the oxidation of As(III) to As(V) [48]. Then, the arsenic anions and Fe-OH of Fe-TiO₂/AC formed bidentate or binuclear complexes [49,50]. Further, iron-modified activated carbon was effective in arsenic adsorption because the oxyanionic arsenic species were adsorbed at the iron oxyhydroxide surface by forming complexes with the surface sites [51]. Therefore, the adsorption mechanism of arsenic on Fe-TiO₂/AC was mainly influenced by the complex formation.

CONCLUSIONS

Fe-TiO₂/AC powder was synthesized using the sol-gel method; it was mesoporous and had a particle size ranging in nanometers. Further, it had a high adsorption capacity for arsenic in a weakly alkaline solution, and the maximum adsorption capacity of the material was observed at pH = 8. An increased amount of arsenic was adsorbed by increasing the ionic strength, material dosage, and initial arsenic concentration. The adsorbent was better at removing As(V) than at removing As(III). The adsorption kinetics and the adsorption isotherms were described well by the pseudo-second-order kinetic equation and the Freundlich isotherm model, respectively. Further, the arsenic adsorption equilibrium by the adsorbent was reached within 3 h.

REFERENCES

1. J.F. Ferguson, J. Gavis, *Water Res.*, **6**(11), 1259 (1972).
2. Y. Wu, X.Y. Zhou, M. Lei, J. Yang, J. Ma, P.W. Qiao, T.P. Chen., *Appl. Geochem.,* **77**, 44 (2017).
3. M. Yu, *Aus. J. Chem.,* **67**(5), 813 (2014).
4. M. Tuzen, K.O. Saygi, I. Karaman, M. Soylak, *Food Chem. Toxicol.,* **48**(1), 41 (2010).

5. T. Luo, J. Yu, *J. Resid. Sci.Technol.,* **12**, S17 (2015).

6. P.L. Smedley, D.G. Kinniburgh, *Applied Geochem.,* **17**(5), 517 (2002).

7. B.A. Manning, S. Goldberg, *Environ. Sci. Technol.,* **31**(7), 2005 (1997).

8. M. Berg, H.C. Tran, T.C. Nguyen, H.V. Pham, R. Schertenleib, A.W. Giger, *Environ. Sci. Technol.,* **35**(13), 2621 (2001).

9. M.L. Pierce, C.B. Moore, *Environ. Sci. Technol.,* **14**(2), 214 (1980).

10. G. Yu, D. Sun, Y. Zheng, *Environ. Health Persp.,* **115**(4), 636 (2007).

11. F. Fu, Q. Wang, *J. Environ. Manage.,* **92**(3), 407 (2011).

12. A. Dabrowski, Z. Hubicki, P. Podkościelny, E. Robens, *Chemosphere,* **56**(2), 91 (2004).

13. G. Yan, T. Viraraghavan, *Water Res.,* **37**(18), 4486 (2003).

14. G. Chen, Sep. *Purif. Technol.,* **38**(1), 11 (2004).

15. T.A. Kurniawan, G.Y.S. Chan, W.H. Lo, S. Babel, *Chem. Eng. J.,* **118**(1–2), 83 (2006).

16. D. Mohan, P.C. Jr, *J Hazard. Mater.,* **142**(1–2), 1 (2007).

17. A. Demirbas, *J. Hazard. Mater.,* **157**(2–3), 220 (2008).

18. L. Ma, S. Tu, *Environ. Chem. Lett.,* **9**(4), 465 (2011).

19. T.S. Anirudhan, L. Divya, J. Parvathy, *J. Chem. Technol. Biot.,* **88**(5), 878 (2013).

20. H. Cao, B. Li, J. Zhang, F. Lian, X. Kong, M. Qu, *J. Mater. Chem.,* **22**(19), 9759 (2012).

21. S. Bang, M. Patel, L. Lippincott, X. Meng, *Chemosphere,* 60(3), 389 (2005).

22. X. Long, S. Tu, *Indust. Water Treat.,* **32**(4), 29 (2012).

23. M. Pena, X. Meng, G.P. Korfiatis, C. Jing, *Environ. Sci. Technol.,* 40(4), 1257 (2006).

24. L.I. Rong, X. Xiao, C. Wang, *Mater. Rev.,* **25,** 68 (2011).

25. P. Pillewan, S. Mukherjee, T. Roychowdhury, S. Das, A. Bansiwal, S. Rayalu, *J. Hazard. Mater.,* **186**(1), 367 (2011).

26. X. Fan, D.J. Parker, M.D. Smith, *Water Res.,* **37**(20), 4929 (2003).

27. A. Manceau, *Geochim. Cosmochim. Acta,* **59**(17), 3647 (1995).

28. Y. Guo, Z. Zhu, Y. Qiu, J. Zhao, *Environ. Sci.,* **25**(5), 944 (2013).

29. Z.J. Li, S.B. Deng, G. Yu, J. Huang, C. Lim, *Chem. Eng. J.,* **161**(1), 106 (2010).

30. S. Abbasizadeh, A.R. Keshtkar, M.A. Mousavian, *J. Ind. Eng. Chem.,* **20**(4), 1656 (2014).

31. I.R. Bellobono, A. Carrara, B. Barni, A. Gazzotti, *J. Photoch Photobiol. A.,* **84**(1), 83 (1994).

32. S. Bekkouche, S. Baup, M. Bouhelassa, S. MolinaBoisseau, C. Petrier, *Desalin. Water Treat.,* 37(1–3), 364 (2012).

33. L. Zhang, Y. Zhu, H. Li, N. Liu, X. Liu, X. Guo, *Rare Metals,* **29**(1), 16 (2010).

34. H. Lee, W. Choi, *Environ. Sci.Technol.,* **36**(17), 3872 (2002).

35. X. Meng, S. Bang, G.P. Korfiatis, *Water Res.,* **34**(4), 1255 (2000).

36. T.F. Lin, J.K. Wu, *Water Res.,* **35**(8), 2049 (2001).

37. P.K. Dutta, A.K. Ray, V.K. Sharma, F.J. Millero, *J. Colloid. Interf. Sci.,* **278**(2), 270 (2004).

38. J. Qiao, Z. Jiang, B. Sun, Y. Sun, Q. Wang, X. Guan, *Sep. Purif. Technol.,* **92**(1), 106 (2012).

39. D. Xie, L. Cao, J. Cui, *Chin. J. Environ. Eng.,* **7**(4), 1279 (2013). (In Chinese).

40. X. P. Yan, R. Kerrich, M. J. Hendry, *Geochim. Cosmochim. Acta,* **64**(15), 2637 (2000).

41. M. E. Pena, G.P. Korfiatis, M. Patel, L. Lippincott, X. Meng, *Water Res.,* **39**(11), 2327 (2005).

42. H. Genç-Fuhrman, J.C. Tjell, D. Mcconchie, *J. Colloid Interf. Sci.,* **264**(2), 327 (2003).

43. Z. J. Wu, H.N. Liu, H.F. Zhang, *Environ. Chem.,* **29**(6), 997 (2010).

44. U. Farooq, J.A. Kozinski, M.A. Khan, M. Athar, *Bioresource Technol.,* **101**(14), 5043 (2010).

45. Y.S. Ho, *Water Res.,* 40(1), 119 (2006).

46. H.S. Altundoğan, S. Altundoğan, F. Tümen, M. Bildik, *Waste Manage.,* **20**(8), 761 (2000).

47. G. He, M. Zhang, G. Pan, *J. Phys. Chem. C.,* **113**(52), 21679 (2009).

48. P. Mondal, C. Balomajumder, B. Mohanty, *J Hazard. Mater.,* **144**(1),420 (2007).

49. B.A. Manning, S.E. Fendorf, S. Goldberg, *Environ. Sci. Technol.,***32**(16), 2383 (1998).

50. S.D. And, J.G. Hering, *Environ. Sci. Technol.,* **37**(18), 4182 (2003).

51. W. Chen, R. Parette, J. Zou, F.S. Cannon, B.A. Dempsey, *Water Res.,* **41**(9), 1851 (2007).

ИЗВЛИЧАНЕ НА АРСЕНАТ И АРСЕНИТ С ПОМОЩТА НА НАНО-TiO₂, НАНЕСЕН ВЪРХУ МОДИФИЦИРАН С ЖЕЛЯЗО АКТИВЕН ВЪГЛЕН: ВЛИЯЕЩИ ФАКТОРИ И АДСОРБЦИОНЕН ЕФЕКТ

Ф. Кин[1,2], Ч. Уей[1,*], Ж. Уанг[3], Г. Ли[2], Кс. Ли[2], И. Ли[2]

[1] *Колеж по ресурси и околна среда, Югозападен университет, Чонгкинг 400716, Китай*
[2] *Лаборатория по информационни системи за планински области и опазване на околната среда на провинция Гуижоу, Университет на Гуижоу, Гуянг 550001, Китай*

[3] *Колеж по екоинженерство, Университет на ГуижоуМинцу, Гуянг, 550025, Китай*

(Резюме)

В статията е представено получаването на нано-TiO₂, нанесен върху активен въглен, модифициран с желязо (Fe-TiO₂/AC), както и резултатите от изпитването на свойствата на материала, включително кристална структура, повърхностна морфология, функционални групи и повърхностна текстура. Резултатите са получени с помощта на рентгенова дифракция, трансмисионна електронна микроскопия, сканираща електронна микроскопия и Fourier трансформираща инфрачервена спектроскопия. Степента на извличане на арсена е оценена чрез статични експерименти при симулирани условия на pH, йонна сила, количество адсорбент и изходна концентрация на арсена. Установено е, че извличането на арсена протича ефективно в слабоалкална среда и максимална адсорбция се наблюдава при pH 8. Извличането на арсена се подобрява при повишаване на йонната сила и количеството адсорбент. Адсорбцията на As(III) и As(V) достига равновесие съответно за 3 ч и 1.14 ч. Моделът от псевдовтори порядък описва задоволително адсорбционните процеси. Експерименталните данни съответстват на уравнението на Freundlich. Изотермичните резултати показват, че максималният адсорбционен капацитет на Fe-TiO₂/AC е 28.66 mg·g⁻¹за As(III) и 35.22 mg·g⁻¹ за As(V). Нано-TiO₂ и Fe₂O₃ играят ключови роли за повишаване на адсорбционната способност и превръщането на As(III) в As(V). Наличието на Fe(III) ускорява окислението на арсена.

Isotope signatures and hydrochemistry as tools in assessing nitrate source in shallow aquifer of Hebei, China

H.C. Pang[1], J.J. Fang[2], Y.F. Liu[1], H.S. Cai[3], F.L. Liu[4], T.Z. Gao[1*]

[1]School of Environmental Science and Engineering & Key Laboratory of Biological Technology for Containment Prevention in Hebei Province, Hebei University of Science and Technology, Shijiazhuang 050018, China
[2]Department of Geological Engineering, Hubei Land Resources Vocational College, Wuhan 430090, China
[3]School of Environmental Studies & State Key Laboratory of Biogeology and Environmental Geology, University of Geosciences, Wuhan 430074,China
[4]Institute of Hydrogeology and Environmental Geology, CAGS, Shijiazhuang 050061, China

Hebei Plain plays an important role in China, where municipal, agricultural and industrial water supplies are highly dependent on groundwater resources. It is crucial to investigate hydrochemical characteristics in shallow aquifer for sustainable utilization of groundwater resources. Major components of groundwater samples showed obvious zonation patterns from the piedmont area, the central area to the coastal area, the hydrochemical types changed from HCO_3-SO_4-Ca-Mg and HCO_3-Cl-Ca-Mg types to HCO_3-SO_4-Na-Ca, SO_4-Cl-Na-Ca and SO_4-Cl-Na types. A study using stable deuterium and oxygen isotopes was performed to elucidate groundwater flow and occurrence. Groundwater is of meteoric origin, and a large proportion is subject to evaporation. In the area, the aquifer system is recharged from irrigation return flow and seawater intrusion, which significantly affects groundwater chemistry. But data show that excessive nitrate nitrogen seriously polluted the groundwater environment in Hebei plain. This paper determined and monitored the composition characteristics of stable nitrogen and oxygen isotopes to trace the source of nitrogen pollutionfrom 2009 to 2015. The results indicated that the average concentrations of nitrate nitrogen were 0.00 to 121.50 mg·L^{-1}, the total average over the seven-year monitoring period was 17.64±1.55 mg·L^{-1}. Each area displayed various concentrations of nitrate nitrogen. The largest value of nitrate nitrogen, 29.49 mg·L^{-1}, was found in the coastal area, which exceeded the Standard for Drinking Water Quality of China(SDWQC) by a factor of 2.95; followed by the value in the piedmont area, 15.78 mg·L^{-1}, exceeding the Standard by a factor of 1.58 and the lowest value was found in the central area, 3.88 mg·L^{-1}, below the Standard. According to isotope signatures, the source of groundwater nitrate is dominated by manure and waste in the coastal area and the central area, whereas in the piedmont area it is dominated by agricultural fertilizers.

Keywords: Hydrogeochemistry, $\delta^{15}N_{NO3}$, $\delta^{18}O_{NO3}$, Nitrate nitrogen, Contamination

INTRODUCTION

Groundwater is the main source of drinking water for many arid and semi-arid regions of the world and is endangered by many kinds of contaminations[1-3]. Although groundwater is considered to be available close to the point of use and always clean and safe, its quality is uncertain due to the natural processes and significant land use changes that do not take into account impacts on the underlying aquifers [4]. This calls for determination of groundwater quality and identification of the contamination sources so as to understand the actual cause of water quality deterioration and coming up with water quality remediation and control mechanisms [4]. The nitrate pollution in groundwater is one of the most prevalent water environmental problems worldwide [5-9] increasing the risk of many cancers including colon cancer, esophageal cancer, etc. [10]. In response to these problems, environmental policies have been implemented in many countries [11]. In the European Union for instance, legislation including the Nitrates Directive 91/676/EEC and the Groundwater Directive 2006/118/EC prohibits nitrate concentrations in aquifers to exceed the mandatory limit of 50 mg L^{-1} NO_3^- and requires that actions be taken in order to reverse or prevent any infringement[12]. NO_3^- has several sources including atmospheric deposition, nitrogenous fertilizers, soil organicnitrogen (SON), animal manure and discharge of domestic sewage [13]. In addition, nitrogen loss in vulnerable environments with thin soil is a serious problem for vegetation because nitrate is an important nutrient for plant growth [14, 15].The effective management of NO_3^- to preserve water quality requires identification of actual N sources and an understanding of the processes affecting local NO_3^- concentrations [16]. However, the determination of N concentrations cannot be solely used in order to detect the specific N sources and biogeochemical processes [16].

Accurate source identification is critical for reasonable protection and prevention of water from nitrate contamination [17]. However, the interlacing of various sources and biogeochemical processes

---

along the nitrogen cycle determining sources of NO_3^- is difficult. The presence of fecal coliform jointly with NO_3^- in groundwater may indicate recent NO_3^- contamination by human sewage or animal droppings provided this is confirmed by another reliable technique [1]. Stable nitrogen isotope techniques enable the identification of sources based on the characteristic or distinctive nitrogen isotope compositions and are valuable tools for the detection of the origin. Different sources of stable isotope characteristic values are not affected by changes in concentrations within water; therefore, the isotope forms of NO_3^- in water are relatively stable [18].

Dual isotope analysis of nitrate ($\delta^{15}N$-NO_3^- and $\delta^{18}O$-NO_3^-) has been frequently used to differentiate NO_3^- sources because of the distinct isotopic characteristics of the main NO_3^- sources, such as rain, chemical fertilizers, and NO_3^- derived from nitrification [19, 20]. Sacchi *et al.*[21] used the isotopes to trace the nitrate-N in the groundwater of the central Po plains in Italy and they discovered that in the higher plains, groundwater pollution mainly originated from four sources: (1) a high osmotic pressure aquifer in the vadose zone of the region; (2) a higher underground water level; (3) an intensive cattle industry that produces a large amount of fecal matter; and (4) a large amount of irrigation water. Kelley*et al.* [20] used nitrogen and oxygen isotope ratios to identify nitrate sources and dominant nitrogen cycle processes in a tile-drained dryland agricultural field. Liu *et al.* [22] tracked sources of groundwater nitrate contamination using nitrogen-oxygen dual isotopes around Beijing, China. Nitrogen-oxygen dual isotope analysis has been established as a tool in providing important information regarding the origin of nitrate contamination in groundwater, the contribution of different sources to a multi-source plume, and the rate and mechanisms of the contamination, as well as in evaluating the success of contaminated site remediation. Zhang *et al.* [23] used the ^{15}N isotope to analyze groundwater nitrate pollution and sources in Beijing's Fangshan district, and the results suggested that NO_3^--N in groundwater mainly originated from animal waste, wastewater, and organic soil nitrogen. Westover *et al.*[24]investigated water quality and sources and processes influencing NO_3^- in the Kettle River basin using a combination of chemical and isotopic techniques. Based on $\delta^{15}N$ values and concentration data, NO_3^- in surface waters originates primarily

from natural soil nitrification processes, with additional influences from anthropogenic activities, such as waste water effluents at sampling locations downstream from population centres.

This study aims to define the NO_3^--N sources and understand the contamination of groundwater in Hebei plain (HP) and provide a scientific basis for controlling NO_3^--N pollution in the groundwater of HP and utilization of groundwater. We first investigated data from 21 wells in the shallow groundwater of HP, evaluated the NO_3^--N pollution concentrations in the groundwater, compared the NO_3^--N pollution concentrations of groundwater in different areas, and traced the sources of NO_3^--N.

STUDY SITE

Hebei Plain is south of Beijing and Tianjin, and spans to Bohai in the east and abuts the Taihang Mountains in the west. The study region is situated between a latitude $36°03'$ to $40°02'$ and a longitude $114°15'$ to $119°50'$, and is one of the alluvial fan plain zones(Figure 1). The area has a continental, semi-arid climate with a mean annual temperature of 12-13ºC, and summer maximum and winter minimum of 45.8 and -28.2 ºC, respectively and with annual precipitation of 400-800 mm. The precipitation is dominated by the Asia summer monsoon during July and August, which accounts for about 70% of the annual precipitation. There is usually only 40-60 mm of rainfall, or even no rainfall, for more than 100 days in spring. The variation of seasonal precipitation is so large that it is the common case to have dry spring and flooding summer. Mean potential evaporation ranges from 1,100 to 1,800 mm. Based on landforms, HP can be divided into three areas: the piedmont area, the central area, and the coastal area [25, 26].

The HP accessible groundwater mainly occurred in the Quarternary sediment aquifers. The regional Quaternary aquifers consist of fluvial fans, alluvial fans and lacustrine deposits [27]. Vertical distribution of the aquifer has been described in detail. A thick sedimentary sequence has been deposited in the HP, with a depth of 500-600 m in depressions, 350-450 m in uplift areas, and 150-300 m around the alluvial fan. From the top to the bottom, sediments can be divided into four aquifer groups according to the lithologic properties, geological age, the distribution of aquifers and aquicludes, and hydrodynamic conditions (Figure 1) [28].
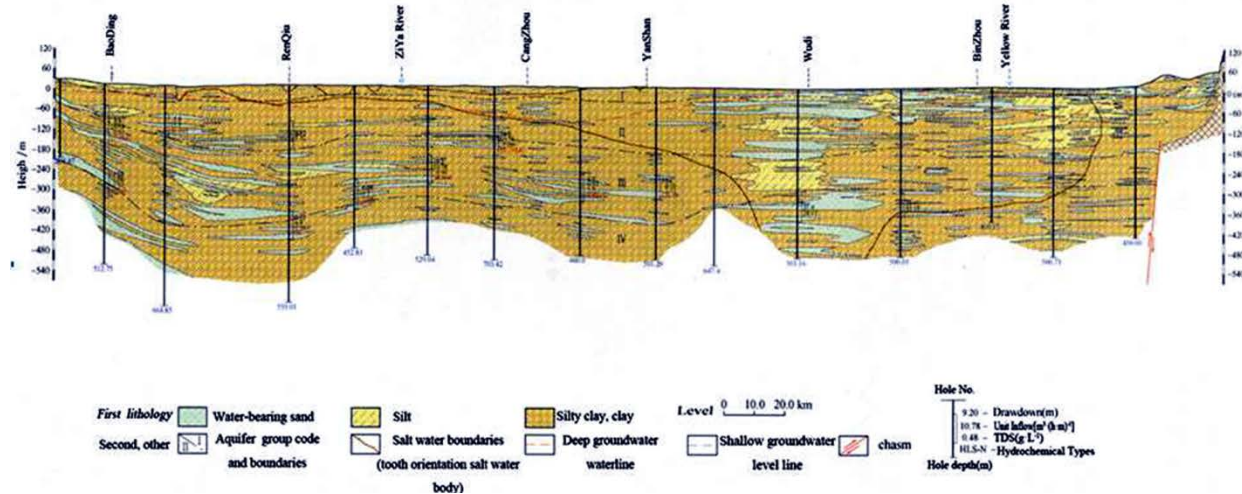
Fig.1. Baoding-Cangzhou hydrogeologic profile in Hebei Plain

The depth of the first aquifer group (shallow unconfined aquifer) ranged between 10 and 50 m, with coarse-grained sand in the piedmont area to fine-grained sand in the littoral plain. The second aquifer group was a series of shallow semi-confined aquifers with buried depths of 120-210 m, with sandy gravel, medium to fine sand. The second group was the major aquifer for groundwater exploitation for agricultural irrigation. The third aquifer group, underlying the second aquifer group, had lower boundary between 170 and 3 350 m. This formation consists of sandy gravel in the piedmont area and medium to fine sand in the central and littoral plain.

The fourth aquifer group lays below 350 m with a thickness of 50-60 m, which consists of cemented sandy gravel and thin layers of weathered sand [29].According to groundwater exploitation and aquifer distribution, groundwater can be divided into shallow groundwater mainly occurring in the first aquifer group (shallow aquifers), while deep groundwater occurs in the latter three groups (deep aquifers).

EXPERIMENTAL

Groudwater sampling and analytical methods

Groundwater samples, including 21 wells of the National hydrological monitoring network, were collected from three areas of Hebei plain in May and September from 2009 to 2015, representing 10.09 % of the Monitoring network in HP. The well depths of the quaternary groundwater ranged from 4.5 to 50 m. Eight samples (numbers 1-8) were taken from the piedmont area of Shijiazhuang, six samples (numbers 9-14) were taken from the central area ofHengshui and seven samples (numbers 15-21) were taken from the coastal area of Cangzhou(Figure2). Water samples were collected from active pumping wells used either for domestic or agricultural purposes, and were initially preserved in a cold box and later transferred to a refrigerator in the laboratory. Samples were filtered with 0.45μm

membrane filters for measurement of ion concentrations and isotopic compositions. The concentrations of major cations and anions were measured by inductively coupled plasma-optical emission spectrometry (ICP-OES) and ion chromatography(IC), respectively. Ion charge imbalances were within ±5%.
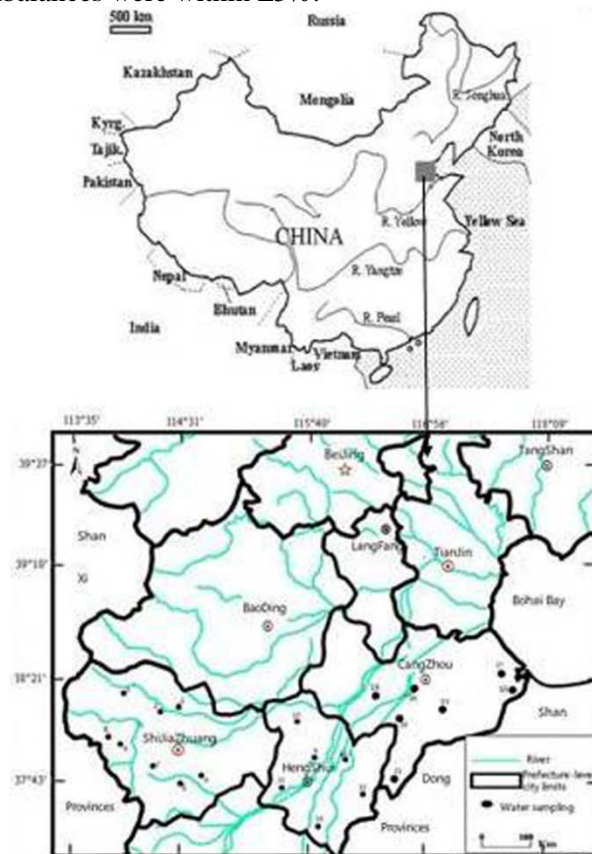
Fig. 2. Location of the shallow groundwater sampling sites in the study area.

Eight samples (numbers 1-8) were collected from Shijiazhuang to represent the Piedmont Plain. Six samples (numbers 9-14) were collected from Hengshui to represent the Central Plain. Seven samples (numbers 15-21) were collected from Cangzhou to represent the Eastern Coastal Plain.

163

Stable isotope ratios were reported in parts per thousand (‰) using the conventional delta notation: $\delta_{sample}=[(R_{sample}-R_{standard})/R_{standard}]\times1000‰$, where R represents the $^{18}O/^{16}O$, or $^{2}H/^{1}H$ ratios of the samples and standards, respectively. $\delta^{18}O_{H2O}$ and δD were determined at the Key Laboratory of Groundwater Sciences and Engineering, Ministry of Land and Resources, Chinese Academy of Geological Sciences (CAGS), using online thermal conversion elemental analysis isotope ratio mass spectrometry (TC/EA-IRMS). The precision of measurements was ±0.1‰ and ±1‰, respectively, and results were reported relative to V-SMOW. In the field, 3-5 L samples were collected to ensure 60—80 mg of nitrate on the cation exchange resin. After removing SO_4^{2-} by addition of $BaCl_2$ to 300 mL of water, the water was passed through the cation exchange resin and became acidity, with a flow rate of 2-5 mL·min^{-1} by adjusting the stopcock on the separatory funnel. The KNO_3 and KCl solutions were produced by adding 1 mol·L^{-1} KOH solution eluent to neutral, and were dried at 90ºC. $\delta^{15}N_{NO3}$ and $\delta^{18}O_{NO3}$ were determined at the same time in one sample input using online high-temperature pyrolysis of 500 µg KNO_3. N_2 and CO generated by KNO_3 and C reaction were separated through a chromatographic column at 60ºC coupled with ConFloIV and IRMS, and the precision of $\delta^{15}N$ and $\delta^{18}O$ was 0.25‰ and 0.6‰, respectively, compared with that of 0.1‰ and 0.5‰ abroad. All experiments were performed in duplicate and thedata were populated in Excel and plotted with Origin 9.0.

RESULTS

Chemical concentrations of groundwater

The chemical and isotopic compositions of the groundwater are listed in Table1 and Figure3, respectively. Chemical elements of shallow groundwater were analyzed to derive the statistical analysis of anion and cation concentrations in the study areas. The average cation concentrations in Shijiazhuang ranked as follows: $Ca^{2+}>Na^{+}>Mg^{2+}>K^{+}$; anion concentrations ranked as follows: $HCO_3^->SO_4^{2-}>Cl^->NO_3^->CO_3^{2-}$. The average cation concentrations in Hengshui ranked as follows: $Na^{+}>Mg^{2+}>Ca^{2+}>K^{+}$; anion concentrations ranked as follows: $SO_4^{2-}>HCO_3^->Cl^->NO_3^->CO_3^{2-}$. The average cation concentrations in Cangzhou ranked as follows: $Na^{+}>Ca^{2+}>Mg^{2+}>K^{+}$; anion concentrations ranked as follows: $Cl^->HCO_3^->SO_4^{2-}>NO_3^->CO_3^{2-}$. Both Table 1 and Fig. 3 show that the sum of SO_4^{2-} and Cl^- averagely accounted for between 40% and 60% of total anions in the piedmont area, around 70% in the central area, and 90% in the coastal area. Besides, the sum of Ca^{2+} and Mg^{2+} averagely accounted for 80% of total cations in the piedmont area, 50% in the central area, and 40% in the coastal area.

The order of the average of the anion concentrations was $HCO_3^->SO_4^{2-}>Cl^->NO_3^->CO_3^{2-}$; greater than 25 Meq% were HCO_3^- and SO_4^{2-}, and that of the cation concentrations was $Ca^{2+}>Na^{+}>Mg^{2+}>K^{+}$ in the piedmont area. The order of the average of the anion concentrations was $SO_4^{2-}>HCO_3^->Cl^->NO_3^->CO_3^{2-}$; greater than 25 Meq% were Cl^-, SO_4^{2-}, and that of the cation concentrations was $Na^{+}>Mg^{2+}>Ca^{2+}>K^{+}$ in the central area. The order of the average of the anion concentrations was $Cl^->HCO_3^->SO_4^{2-}>NO_3^->CO_3^{2-}$; greater than 25 Meq% were Cl^-, and that of the cation concentrations was $Na^{+}>Ca^{2+}>Mg^{2+}>K^{+}$ in the coastal area. According to Shoka Lev's classification method, the main hydrochemical types from the piedmont area, the central area to the coastal area changed from HCO_3-Ca·Mg, through HCO_3·SO_4-Na·Ca and SO_4·Cl^--Na·Ca, to SO_4·Cl^--Na.

Table1. Results for hydrochemistry and isotopes in shallow groundwater, a-rural, town; b-farmland.

Sampling Point	Depth (m)	NO_3^- (mg·L^{-1})	Cl^- (mg·L^{-1})	SO_4^{2-} (mg·L^{-1})	$\delta^{15}N$ (‰)	$\delta^{18}O$ (‰)	δ^2H (‰)	$\delta^{18}O$ (‰)
1. Sanhepu[a]	15.0	17.95	23.60	105.21	2.62	-3.36	-54	-8.7
2. Hantai[a]	30.0	14.49	41.23	112.92	5.08	-5.47	-62	-8.4
3. Licun[b]	30.0	15.14	54.46	144.76	8.43	-4.86	-57	-7.6
4. Ciyu[a]	17.0	15.21	44.97	118.20	—	—	-61	-8.2
5. Shanyincun[b]	12.0	17.73	56.75	165.95	13.31	-1.31	-60	-8.4
6.Luquanchengguan[a]	16.2	16.99	54.52	178.95	8.78	-4.14	-62	-8.4
7. Yongbi[a]	34.0	10.76	109.21	123.75	10.7	-3.95	-63	-8.6
8. Luquanshiqu[a]	30.0	17.95	205.03	145.37	8.24	-5.24	-63	-8.7
9. Balizhuang[a]	10.0	2.34	547.58	596.75	—	—	-61	-7.6
10. Nanjili[b]	13.0	1.56	167.81	210.24	—	—	-64	-8.7
11. Zhangquan[b]	20.0	5.47	1448.25	562.73	18	6.64	-56	-7.3
12. Wanglou[b]	38.0	6.28	377.02	359.47	11.96	-1.53	-62	-8.5
13.Donganzhuang[b]	36.0	4.73	565.67	902.91	13.04	-1.78	-59	-7.8
14. Xiaoying[b]	29.0	2.89	1857.80	1457.49	—	—	-58	-7.9
15. Mengcun[b]	30.0	9.72	1088.23	531.72	14.06	4.34	-62	-8.4
16. Xiasanbao[a]	4.5	61.14	514.16	390.79	18.06	-4.86	-57	-7.9
17.Yangerzhuang[a]	5.8	78.64	773.71	346.83	20.46	-2.13	-65	-8.9
18. Hechengjie[b]	50.0	16.05	323.10	412.01	—	—	-63	-8.7
19. Jiaohe[b]	12.0	7.61	521.68	507.95	17.09	0.77	-69	-9.2
20. West of Cangzhou[a]	12.0	9.78	578.64	494.47	30.99	9.94	-50	-6.4
21. Xinji[a]	6.2	23.48	1728.98	487.00	—	—	-51	-6.4
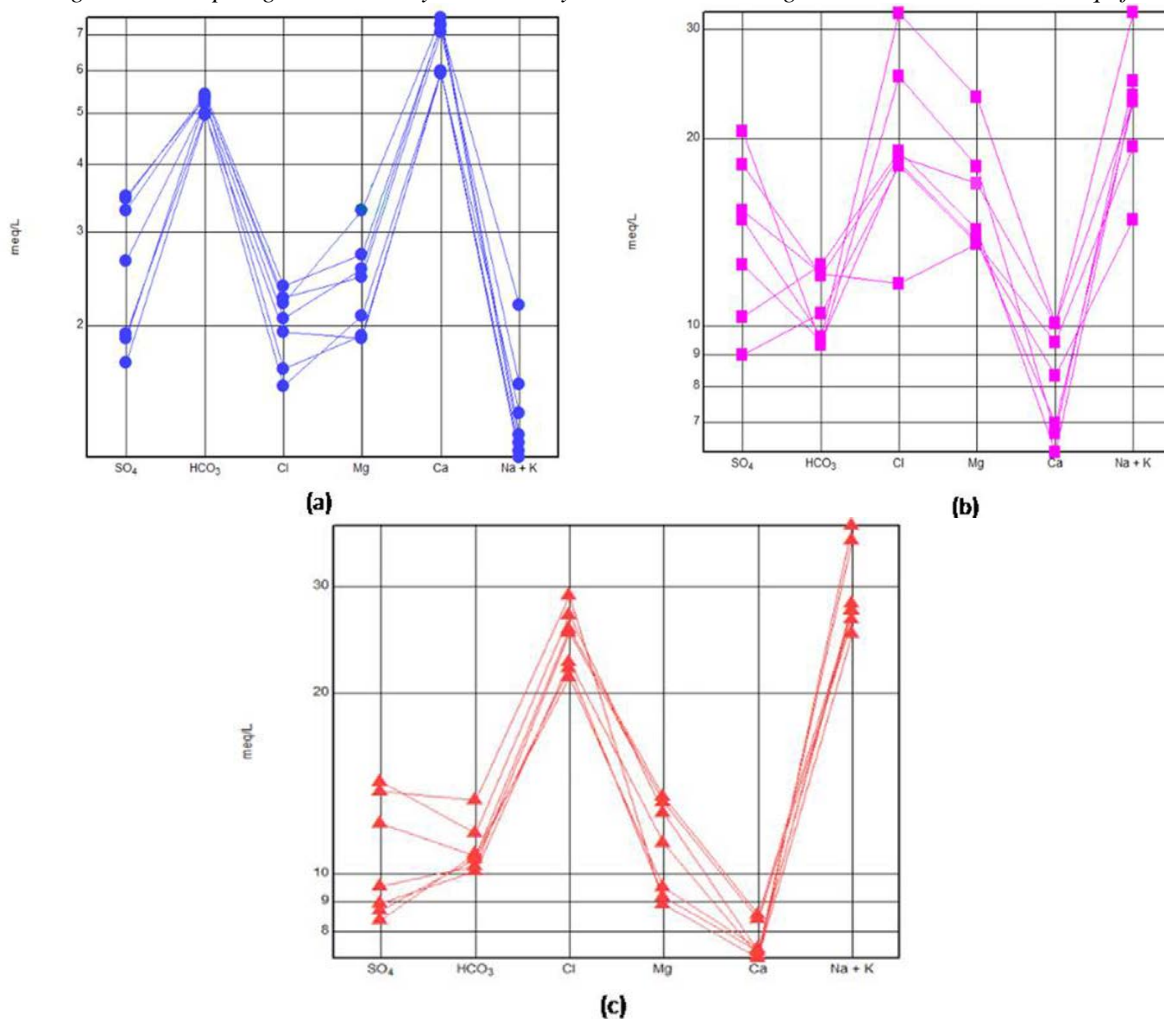
Fig.3. Hydrochemical composition of Shijiazhuang(a) , Hengshui(b) and Cangzhou(c).
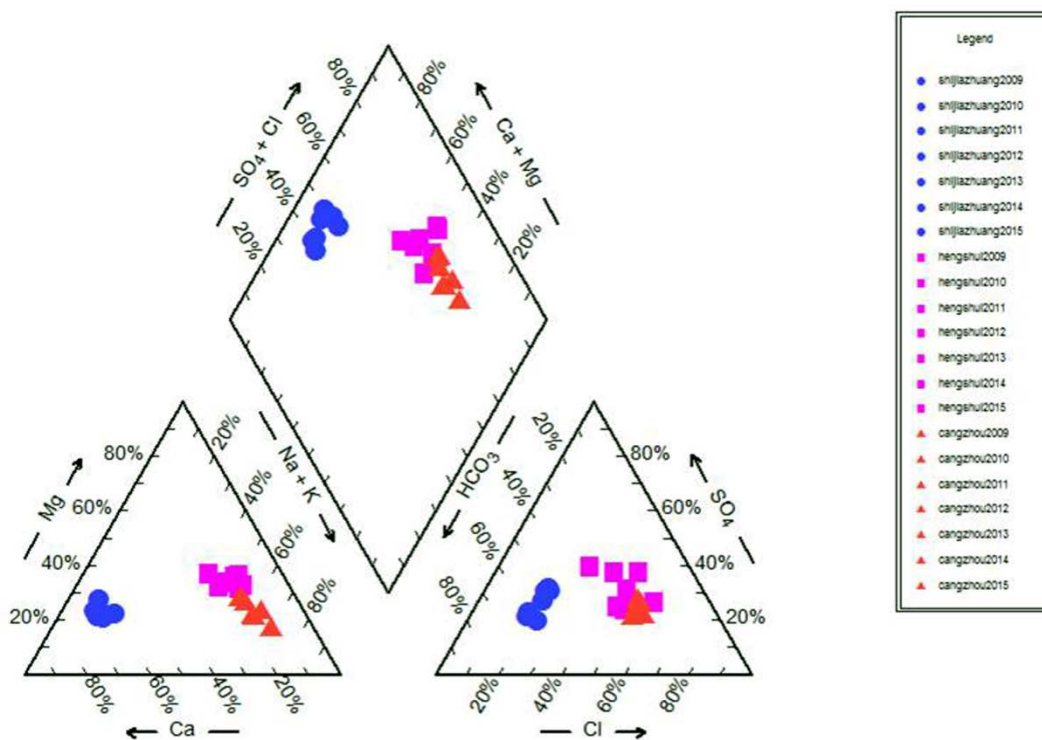
Fig.4. Piper figure of water chemistry of Shijiazhuang, Hengshui and Cangzhou.

165

As seen from Piper diagram of water chemistry(Figure 4), anion and cation distribution was again more scattered from the piedmont area to the coastal area, and the hydrochemical type changed from bicarbonate-type to sulfate-chloride type and chloride-type, and salinity gradually increased.It confirmed that in the piedmont area and the central area, the chloride-type area decreased, while the bicarbonate-type and sulfate-chloride type areas increased, as shallow groundwater constantly gained riverside-leakage and recharged from water sources and precipitation. The coastal area experienced larger salinity due to seawater intrusion, in addition to evaporation.

In the Piedmont Plain and the Central Plain, the chloride-type area was small, while the bicarbonate-type and sulfate-chloride type areas were larger, as shallow groundwater constantly gained riverside-leakage and recharged from water sources and precipitation. The Eastern Coastal Plain experienced larger salinity due to seawater intrusion, in addition to evaporation.

Isotope compositions ofwater

Table1 and Figure 5 illustrate the 21 stable deuterium and oxygen isotopes determining results of the shallow groundwater samples. In the piedmont area, $\delta 2H$ and $\delta 18O$ values ranged from -63‰ to -54‰, and -8.7‰ to -7.6‰, respectively, and mean values were -60.25‰ and -8.38‰, respectively. In the central area, $\delta 2H$ and $\delta 18O$ values ranged from -64‰ to -56‰, and -8.7‰ to -7.3‰, respectively, and mean values were -60‰ and -7.97‰, respectively. In the coastal area, $\delta 2H$ and $\delta 18O$ values ranged from -69‰ to -50‰, and -9.2‰ to -6.4‰, respectively, mean values were -59.57‰ and -7.99‰, respectively. Based on the comparison, the $\delta 2H$ and $\delta 18O$ values of groundwater in the piedmont area are relatively small while the values in the central area are relatively large.

Because most of the world's precipitation is derived from evaporation of seawater, the $\delta 2H$ and $\delta 18O$ compositions of precipitation throughout the world are linearly correlated. In Figure 5, all data were close to the LMWL($\delta 2H=7.02341$ $\delta 18O+1.72339$, R2=0.95) [23], and shifted to the right of the global meteoric water line(GMWL) [30]. It suggests that groundwater was mainly derived from local meteoric water. Most of samples were enriched in $\delta 18O$ isotope and were located to the right of the LMWL, which indicates that the meteoric water experienced different extents of evaporation before the precipitation recharged. From the relationship shown in Figure 5, the linear relationship is approximately parallel to the RMWL, showing that aquifer of the study area has been recharged by precipitation.
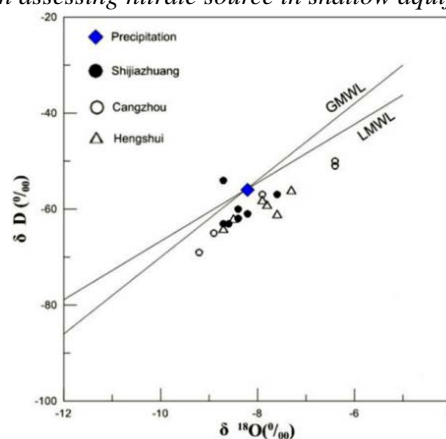
Fig.5. Plots of δ^2H and $\delta^{18}O$ in groundwater of Hebei Plain.Legend of lines: GMWL line indicates global meteoric water line; LMWL line indicates North China Plain's meteoric water line.

DISCUSSION

Distribution of nitrate-N

The range of NO_3^--N concentrations was 1.56-78.64 mg·L^{-1} in shallow groundwater of HP. The lowest level was collected in Balizhuang in the central area, and the highest level was in Yang'erzhuang in the coastal area. The mean concentration of NO_3^--N was 15.78 mg·L^{-1} in the piedmont area, 3.88 mg·L^{-1} in the central area, and 29.49 mg·L^{-1}, the largest concentration, in the coastal area.

Figure 6 illustrates the trends of NO_3^--N and chloride in HP. Chloride ranged from 27.98 to 2086.75 mg·L^{-1}, with a mean value of 518.16 mg·L^{-1}; NO_3^--N ranged from 3.08 to 92.59 mg·L^{-1}, with a mean value of 17.96 mg·L^{-1}; and sulfate ranged from 57.04 to 1324.21 mg·L^{-1}, with a mean value of 416.78 mg·L^{-1}. The lowest concentrations of NO_3^--N were in the central area, the largest changes in NO_3^--N concentrations were in the coastal area, and the lowest concentrations of chloride were in the piedmont area.
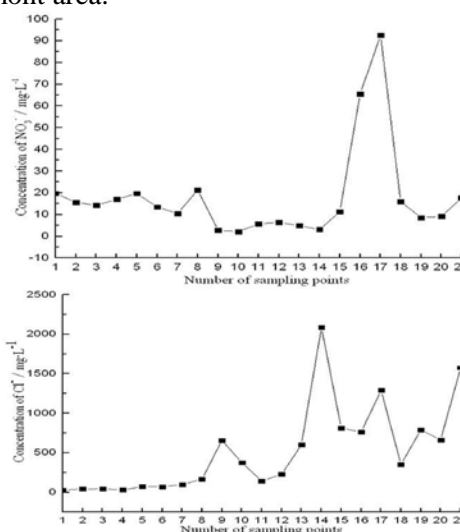
Fig.6. Contents of chloride and nitrate ions atthe sample points of the study area.

Table2.NO_3^--N content from 2009 to 2015

Year	Nitrate – N ranges	Average of May ±standard error (mg·L^{-1})	Average of September ±standard error (mg·L^{-1})	Annual averages	10mg·L^{-1} Exceeding factor (%)
2009	0.00~108.45	16.09±6.22	16.33±6.10	16.21	33.33
2010	0.00~87.30	18.74±4.57	15.66±4.43	17.20	54.76
2011	0.00~102.74	17.51±5.31	17.24±5.23	17.37	52.38
2012	0.00~121.50	21.97±5.92	21.29±5.78	21.63	59.52
2013	0.30~103.00	20.74±4.91	21.63±5.04	21.18	71.43
2014	0.44~58.53	18.09±3.63	13.32±3.27	15.70	46.34
2015	0.00~56.20	16.22±3.62	12.08±2.46	14.15	50.00

Average concentrations of chloride and nitrate at the Piedmont Plain, the Central Plain, and the Eastern Coastal Plainsampling points are along the abscissa and the content of the sampling points along the vertical axis.

The mean concentrations of chloride in the piedmont area, the central area, and the coastal area were 73.72, 827.36, and 789.79 mg·L^{-1}, respectively. SO_4^{2-}/Cl^- ratios were 1.86, 0.82, and 0.57, respectively, and SO_4^{2-}/Cl^- ratios of the three areas were quite different. This significant variation indicates that the chloride and sulfate in the groundwater have different sources. Unlike SO_4^{2-}/Cl^-, NO_3^-/Cl^- ratios differed slightly between the three areas. The NO_3^-/Cl^- ratio of the piedmont area ranged from 0.09 to 0.76, with a mean value of 0.32; the central area ratio ranged from 0.00 to 0.12, with a mean value of 0.01; and the coastal area ratio ranged from 0.01 to 0.12, with a mean value of 0.05. The narrow range of the NO_3^-/Cl^- ratios suggests that the input of NO_3^--N and chloride reached a steady state [31].

General chardcteristics of nitrate

Table2 shows the overall state of NO_3^--N in groundwater of HP from 2009 to 2015. An obvious upward trend in NO_3^--N levels appeared. The NO_3^--N concentrations escalated from 16.21 mg·L^{-1} in 2009 to 21.18 mg·L^{-1} in 2013. However, NO_3^--N concentrations differed between sampling sites; areas of low concentration were mainly located in Nanjili and Xiaoying in the central area, and areas of high concentration were mainly in Yang'erzhuang and Xiasanbao in the coastal area.According to the SDWQC (10 mg·L^{-1}), the concentrations of NO_3^--N in groundwater of HP from 2009 to 2015 exceeded the standard. Analyzing the NO_3^--N in samples determined a large range of NO_3^--N concentrations in groundwater of HP was found, 0.00-121.50 mg·L^{-1}, and the mean value was 17.64 mg·L^{-1} during the seven-year monitoring period, exceeding the SDWQC (10 mg· L^{-1})by a factor of 1.76.

According to Muller's established groundwater geochemistry background value of 2.0 mg·L^{-1} of NO_3^--N [32], the influence of human activity on NO_3^--N concentrations in groundwater had increased.

The maximum concentration occurred between 2009 and 2010, rising from 33.33% to 54.76%, an increase of 21.43%. There were 25 valuesexceeding 10 mg·L^{-1}, accounting for 59.52% of all samples in 2012; 30 values exceeding 10 mg·L^{-1}, accounting for 71.43% of all values in 2013; and the values exceeding the SDWQC reached 46.34% in 2014, and 50.00% in 2015. Nitrate concentration was higher in May than in September except in 2009 and 2013 due to heavier rainfall in July and August, it may have resulted from relatively abundant rainfall, and enhanced the link between a saturated zone and an unsaturated zone [33].The soil of unsaturated zone exhibits strong adsorption of ammonia-nitrogen. Ammonia-nitrogen was prone to nitrification by oxidation in alkaline groundwater, resulting in nitrate, nitrite, and nitrate-nitrogen produced by nitrite due to its instability, thus increasing NO_3^--N concentrations in groundwater [34].

Regional changes of nitrate-N

Figure 7 shows the trend of NO_3^--N concentrations in the three main sub-plains of HP from 2009 to 2015. Changing concentrations of NO_3^--N are evident in three areas, while the coastal area had the highest concentrations of NO_3^--N, followed by the piedmont area, and then the central area, which was the lowest one, although it, too, showed an increasing trend.
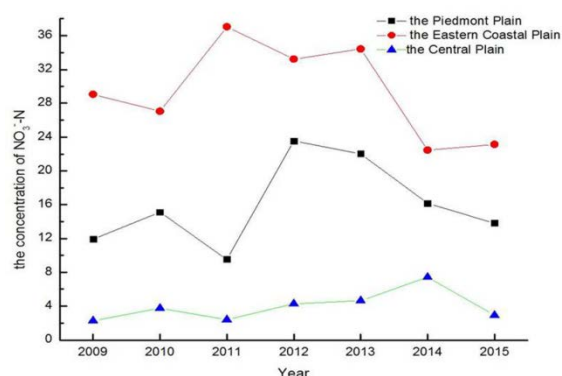
Fig.7. Variation of shallow groundwater nitrate-N concentration in sub-plain of Hebei plain.

Trend of NO_3^--N concentrations in the three main sub-plains of Hebei Plain from 2009 to 2015.

There were evident changes in NO_3^--N concentrations in each sub-plain, with the highest concentrations of NO_3^--N recorded in the Eastern Coastal Plain, followed by the Piedmont Plain and the Central Plain, which, while lowest, still exhibited an increasing trend.

The coastal area, with the highest NO_3^--N concentrations, had an annual mean value of 29.49 mg·L^{-1}, exceeding the SDWQC (10 mg·L^{-1}) by a factor of 2.95. The value of NO_3^--N in this area remained greater than 25 mg·L^{-1} during the study period, with peak value reached in May 2012 about 37.42 mg·L^{-1}, exceeding the SDWQC by a factor of 3.74. The lowest value was 19.41 mg·L^{-1} in September 2014, exceeding the standard by a factor of 1.95. The high NO_3^--N concentrations in the coastal area from 2009 to 2015 may be related to manure and waste emissions, as well as the structure and composition of the unsaturated zone, which greatly influences the infiltration of pollutants, resulting in contamination of shallow groundwater.

The mean concentration of NO_3^--N in the piedmont area was 15.78 mg·L^{-1}, exceeding SDWQC by a factor of 1.58. The minimum level, 9.71 mg·L^{-1}, was recorded in May 2011, and the next lowest level, 9.34 mg·L^{-1}, was recorded in September 2011; hence, the measurements taken in 2011 were the only two during the study period in this area that did not exceed the SDWQC. The maximum concentration, 23.71 mg·L^{-1}, was recorded in May 2012, which could have resulted from the larger solids of that vadose zone. The wider the granules in a vadose zone, the stronger permeability it offered, and thus easier nitrification. Due to this characteristic, coupled with an accumulation of NO_3^--N from excessive fertilization carried through rainfall or irrigation, NO_3^--N leached through the vadose zone to shallow groundwater, resulting in a generally higher nitrate concentration in the area.

The mean concentration of NO_3^--N in the central area was 3.88 mg·L^{-1}. It was, therefore, the least polluted of the three areas. Low concentration mainly result because the central area had fine rock particles in the unsaturated zone, and more clay interlayer [35], which are conducive to denitrification. Still, NO_3^--N concentrations in this area demonstrated a rising trend overall. The minimum value occurred in May 2009, 1.67 mg·L^{-1}, and the highest concentration was recorded in May 2014, 11.34 mg·L^{-1}. From 2009 to 2013, the NO_3^--N concentration levels did not exceed the SDWQC. However, the 2014 levels exceeded the standard by a factor of 1.13, which may have resulted from the topography of the central area. Within this area, sources of pooling along the groundwater flow coming water after entering the contaminated area, which increases its NO_3^--N concentration.

Sources of NO_3^--N

The $\delta^{15}N$ and $\delta^{18}O$ results of the shallow groundwater are shown in Table 1. In the three areas, nitrogen and oxygen isotopes demonstrated significant changes. In the piedmont area, $\delta^{15}N$ and $\delta^{18}O$ values ranged from 2.62‰ to 13.31‰, from -5.47‰ to -1.31‰, respectively, with mean values of 8.17‰ and -4.05‰, respectively. Changes of nitrogen and oxygen isotope values of the central area were small compared to the piedmont area. $\delta^{15}N$ and $\delta^{18}O$ values ranged from 11.96‰ to 18.00‰, from -1.78‰ to 6.64‰, respectively, with mean values of 14.33‰ and 1.11‰, respectively. Oxygen and nitrogen isotopes of the coastal area showed the greatest changes in the three areas. $\delta^{15}N$ and $\delta^{18}O$ values ranged from 14.06‰ to 30.99‰, from -4.86‰ to 9.94‰, respectively, with mean values of 20.13‰ and 1.61‰, respectively.

Different values of $\delta^{15}N$ can be used to determine different sources of NO_3^--N in water. Generally, we can use $\delta^{15}N$ as a tracer of NO_3^- sources; however, there is an overlapping phenomenon in some sources of $\delta^{15}N$, such as sewage and manure. Therefore, in this study, $\delta^{18}O$ was combined with $\delta^{15}N$ to determine nitrate contamination.

Research byFenech *et al*. [30]indicated that $\delta^{15}N$ compositions of most terrestrial material fall between -10‰ to +25‰, and, as a result, isotope values of N and O can be useful in identifying the origin of groundwater NO_3^-. The $\delta^{15}N$ from atmospheric nitrogen deposition is about 0‰ to +13‰ and from manure about +5‰ to +25‰. Fertilizers generally have $\delta^{15}N$ values between 0‰ ± 4‰, and organic soil N is characterized by $\delta^{15}N$ values between 4‰ and 9‰. The $\delta^{18}O$ from atmospheric deposition isfrom +25‰ to +70‰. The $\delta^{18}O$ values of atmospheric precipitation range between +20‰ to +70‰. Generally, synthetic fertilizers have $\delta^{18}O$ values between 22‰ ± 3% [36]

Figure 8 shows the sources of NO_3^--N in HP. The main sources of NO_3^--N in shallow groundwater were from manure and waste. NO_3^--N contamination in the piedmont area came from fertilizers, whereas NH_4^+ came from rainfall and soil nitrogen. The main forms of agriculture crop consisted of wheat and corn in which no manure was applied. Additionally, atmospheric-N deposition and soil nitrogen cannot significantly elevate the NO_3^--N concentrations. Therefore, it was demonstrated that fertilizers were a major source of NO_3^--N. Contamination of NO_3^--N in the central area and the coastal area was mainly derived from manureand waste.Sources of NO_3^--N of the Piedmont Plain originated mostly from fertilizers, while NO_3^--N of the Central Plain and the Eastern Coastal Plain was mainly derived from septic tank waste.
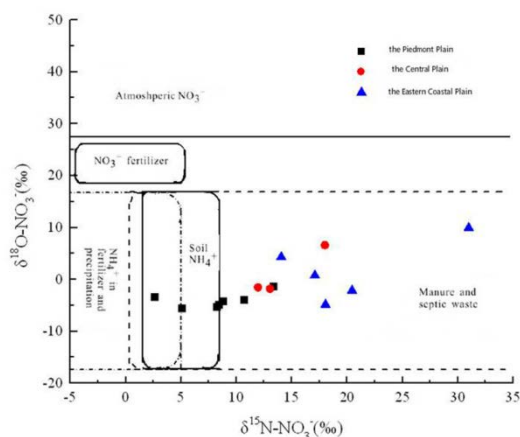
Fig.8. Sources of NO_3^--N in shallow groundwater of the study area.

CONCLUSIONS

(1) In the study area, the average chloride concentration was 527.73 mg·L^{-1}; the NO_3^--N mean concentrations were 16.95 mg·L^{-1}; and the sulfate mean concentrations were 397.88 mg·L^{-1}.The SO_4^{2-}/Cl$^-$ ratios of the three areas differed significantly and NO_3^-/Cl$^-$ ratios were only slightly different, indicating that chloride, NO_3^--N, and sulfate in groundwater had different sources.

(2) From 2009 to 2015, the NO_3^--N concentrations in groundwater ranged from 0.00-121.5 mg·L^{-1}, and the mean values was 17.64 mg·L^{-1}, exceeding the SDWQC by a factor of 1.76. Different areas had different concentrations of NO_3^--N.

The coastal area displayed the highest concentration, 29.49 mg·L^{-1}, which exceeds the SDWQC by a factor of 2.95. The piedmont area maximum concentration was 15.78 mg·L^{-1}, exceeding by a factor of 1.58. The concentration of NO_3^--N in the central area was the lowest one, averaging 3.88 mg·L^{-1}, and did not exceed SDWQC.

(3) Hydrochemical types in the study area displayed obvious differences. The hydrochemical type changes from bicarbonate-type to sulfate-chloride type and then to chloride-type, as shallow groundwater in the areas follows a migration pattern from the piedmont area to the coastal area and salinity gradually increased. The coastal area, with the largest salt content, experiences seawater intrusion. Groundwater was of meteoric origin, and a large proportion was subject to evaporation. In the area, the aquifer system was recharged from irrigation return flow and seawater intrusion.

(4) The isotope analysis of $\delta^{15}N$ and $\delta^{18}O$ in shallow groundwater of the three areas indicated that the NO_3^--N was mainly due to manure and waste, NH_4^+- to fertilizers. NO_3^--N of the coastal area and the central area was mainly due to manure and waste; and NH_4^+- mainly to fertilizers in the piedmont area.

REFERENCES

1. 1. H.Amiri, M. Zare, D. Widory,*Isot. Environ. Healt. S.*, **51** (3), 392 (2015).
2. 2.I.Matiatos,*Sci. Total Environ.*, **541**, 802(2016).
3. 3.K.M.Rogers, E. Nicolini, V. Gauthier,*J. Contam. Hydrol.,* **138-139**, 93(2012).
4. 4.E.Elisante,A.N.N. Muzuka,*Environ. Earth Sci.,* **75**(3), 277(2016).
5. 5.Z.X.Chen,L. Yu, W.G. Liu, MHW Lam,G.J. Liu, N Ornelas-Soto,*Environ. Earth Sci.,***71**(1), 217(2014).
6. 6.A.E.Lawniczak, J. Zbierska, B. Nowak, K. Achtenberg, A. Grzeskowiak, K.Kanas, *Environ.Monit. Assess.,***188**(3),172(2016).
7. 7.C.Tamez-Meléndez, A. Hernández-Antonio, P.C. Gaona-Zanella,N. Ornelas-Soto,J. Mahlknecht, *Environ.Earth Sci.,***75**(9),1(2016).
8. 8.L.Xing, H. Guo, and Y. Zhan, *J. Asian Earth Sci.*, **70–71**(1),250(2013).
9. 9.J.Zhi, A. Ding, S. Zhang, *Desalin. Water Treat.,* **57**(18),8243(2016).
10. 10.J.-j.Fang,A.-g. Zhou, C.-m. Ma, C.-f. Liu, H.-s Cai,Y.-q. Gan, Y.-d. Liu,*J. Cent.South Univ.*, **22** (2), 610 (2015).
11. 11.E.Minet, C.E. Coxon, R. Goodhue,K.G. Richards,R.M. Kalin, W. Meier-Augenstein,*Water Res.*, 46 (12),3723 (2012).
12. 12.P.Saccon, A. Leis, A. Marca, J. Kaiser, L. Campisi, M.E. Böttcher, J.Savarino, P. Escher, A.Eisenhauere, J.Erbland, *Appl. Geochem.*, **34** (4),75 (2013).
13. 13.A.R.Albertin, J.O. Sickman, A. Pinowska, R.J. Stevenson, *Biogeochemistry*, **108** (1),219 (2012).
14. 14.S.L.Li, C.Q. Liu, J. Li, Z. Xue, J. Guan, Y. Lang, H.Ding, L.Li, *Environ. Earth Sci.,***68** (1)219 (2013).
15. 15.G.Michalski, M. Kolanowski, K.M. Riha, *Isot. Environ.HealtS.,***51**(3),382(2015).
16. 16.F.J.Yue,C.Q. Liu, S.L. Li, Z.Q. Zhao, X.L.Liu, H. Ding, B.J. Liu, J.Zhong, *J. Hydrol.,***519**,329 (2014).
17. 17.W.Wang, X. Song, Y. Ma, *Environ.Earth Sci.,***75**(11),1(2016).
18. 18.S.K.Wexler, K.M. Hiscock, P.F. Dennis, *J. Hydrol.,***468–469**, 85(2012).
19. 19.A.Nestler,M. Berglund, F. Accoe, S. Duta, D. Xue, P. Boeckx, P. Taylar, *Environ. Sci. and Pollut. R.*, **18** (4), 519 (2011).
20. 20.C.J.Kelley, C.K. Keller, R.D. Evans, C.H.Orr, J. L.Smith, B. A.Harlow, *Soil Biol. Biochem.,***57** (3),731 (2013).
21. 21.E.Sacchi, M. Acutis, M. Bartoli, S. Brenna, C.A. Delconte, A. Laini, M. Pennisi,*Appl. Geochem.,* **34**(4), 164 (2013).

22. 22.M.Liu, A.S.M. Seyf-Laye, T. Ibrahim, D.B. Gbandi, H. Chen,*Environ. Earth Sci.*, **72** (3),707 (2014).

23. 23.X.Y.Zhang, B.D. Xin, W.C. Liu, Y.Q. Ji, X.H. Wang, W. Zhao,*Safety & Environ. Engin.,***12** (3),15 (2011).

24. 24.M.D.Westover, L.K. Hall, C.C. Day, R.N. Knight, R.T. Larsen, Brock R. McMillan, *Annual Meeting of the American Society of Mammalogistsat Portland, Oregon,*2011.

25. 25.X.D. Li, *Water Sciences & Engineering Technology*, **236**(7),21(2013).

26. 26.F.Zhang, F. Shi, X. Li, X.Jia. *Int. Conference on Bioinformatics and Biomedical Engin.*, 2010.

27. 27.X.Lu, M. Jin, M.T.V. Genuchten, B.Wang, *Groundwater,***49** (2), 286 (2011).

28. 28.Q.Sun, R. Kröbel, T. Müller, V. Römheld, Z.Cui, F.Zhang, X.Chen, *Agr. Water Manage.,* **98** (5),808 (2011).

29. 29.Z.W.Xu, X.Y. Zhang, G.R. Yu, X.M. Sun, X.F. Wen, *Environ. Sci.,***35** (8),3230 (2014).

30. 30.C.Fenech,L. Rock, K. Nolan, J. Tobin, A. Morrissey, *Water Res.*, **46** (7), 2023(2012).

31. 31.Y.Uchida, T. Ishii, Y. Taguchi, *Bull.Geological Survey Japan,***60**(1/2),87(2009).

32. 32.O.Rahmati, A.M. Melesse, *Sci.Total Environ.*, **568**,1110(2016).

33. 33.X.N.Zhou, S.Y. Liu, Z. Wang, Z.C. Zhou, *Water Sci. Engin. Technol.*, **2**,15(2008).

34. 34.J.Pei, H. Yao, H. Wang, J. Ren, X. Yu, *Water Res.,* **99**, 122 (2016).

35. 35.J.M.Thomas, A.H. Welch, M.D. Dettinger, *Psychopathology*, **37**(6),285(1996).

36. 36.Q.Yi, Y. Gao, H. Zhang, H. Zhang, Y.Zhang, M. Yang,*Chem. Engin. J.*, **300**, 139 (2016).

ИЗОТОПНА ИДЕНТИФИКАЦИЯ И ХИДРОХИМИЯ КАТО ИНСТРУМЕНТИ ЗА ОЦЕНКА НА ИЗТОЧНИЦИТЕ НА НИТРАТИ В ПЛИТКИЯ ВОДОНОСЕН ХОРИЗОНТ НА РАВНИНАТА ХЕБЕЙ, КИТАЙ

Х. Панг[1],Дж. Фанг[2], И. Лиу[1],Х.Цаи[3],Ф. Лиу[4], Т. Гао[1*]

[1]*Училище по наука за околната среда и инженерство и лаборатория по биологична технология за предотвратяване на аварии в провинция Хебей, Хебейски университет по наука и технология, Шиджиажуанг, 050018, Китай*

[2]*Департамент по инженерна геология, Професионален колеж по земни ресурси на Хебей, Ухан 430090, Китай*

[3]*Училище по околната среда и лаборатория по биогеология и геология на околната среда, Университет по геонауки,Ухан 430074, Китай*

[4]*Институт по хидрогеология и геология на околната среда, CAGS, Шиджиажуанг, 050061,Китай*

(Резюме)

Равнината Хебей играе важна роля в Китай, където градските, земеделските и промишлените води силно зависят от подпочвените водни ресурси. За устойчиво използване на подпочвените водни ресурси е необходимо да се изследват хидрохимичните характеристики на плитката водоносна зона. Основните компоненти на подпочвените води свидетелстват за ясно зониране от предпланинската област през централната област до крайбрежната област, като хидрохимичният тип се променя от HCO$_3$-SO$_4$-Ca-Mgи HCO$_3$-Cl-Ca-Mgtypesдо HCO$_3$-SO$_4$-Na-Ca, SO$_4$-Cl-Na-Caи SO$_4$-Cl-Na. Проведено е изследване с помощта на деутерий и стабилни изотопи на кислорода за изясняване на потоците от подпочвени води. Подпочвените води имат валежен произход и голяма част от тях е подложена на изпаряване. В изследваната област, водоносната система се възстановява от напояване и навлизане на морска вода, което влияе върху химичния състав на водата. Изследванията показват, че подпочвената вода в равнината Хебей е значително замърсена с нитратен азот. Чрез измерване на характеристиките на стабилните изотопи на азота и кислорода са определени източниците на замърсяване с азот за периода от 2009 до 2015 г. Средните концентрации на нитратния азот са между 0.00 и 121.50 mg·L^{-1}, средната стойност за 7-годишния период е 17.64±1.55 mg·L^{-1}. Концентрациите на нитратен азот в различните райони са различни. Най-висока стойност на нитратен азот, 29.49 mg·L^{-1}, е установена в крайбрежния район, която надвишава 2.95 пъти стандарта за качество на питейната вода в Китай, следвана от стойността в предпланинския район, 15.78 mg·L^{-1}, надвишаваща стандарта 1.58 пъти. Най-ниска стойност е измерена в централния район, 3.88 mg·L^{-1}, която е под стандарта. Съгласно идентифицираните изотопи, в крайбрежния и централния район източниците на нитрати в подпочвените води са основно оборски тор и отпадъци, а в предпланинския район – земеделски торове.

Experimental study on the feasibility of reducing coal dust by alkaline solution

H. Y. Guo[1, 2, 3], Zh. X. Gao[1], Ch. Y. Fu[1], Y. Luo[1], D. P. Xia[1, 3] *

[1] *State and Local Joint Engineering Laboratory for Gas Drainage & Ground Control of Deep Mines (Henan Polytechnic University), Jiaozuo 454000, China*
[2] *State Key Laboratory Cultivation Base for Gas Geology and Gas Control (Henan Polytechnic University), Jiaozuo 454000, China*
[3] *Collaborative Innovation Center of Coalbed Methane and Shale Gas for Central Plains Economic Region, Jiaozuo 454000, China*

In order to investigate the feasibility of reducing coal dust by alkaline solution, three representative samples of bituminous D, bituminous C and bituminous B coal with different metamorphic degrees were collected and soaked in0.2 mol/L, 0.5 mol/L, 1.0 mol/L NaOH, respectively, for 5 days. The variation characteristics of coal wettability index were analyzed by the ways of contact angle, pulverized coal subsidence, reverse permeation and scanning electron microscopy (SEM). The results showed that the contact angle of coal samples after soaking in the alkaline solution decreased, the reverse permeation effect obviously increased, and the sedimentation effect of pulverized coal also increased. At the same time, the coal wettability index tended to increase with the decrease of metamorphic degree of the coal and the increase of NaOH concentration. After the samples were soaked in alkaline solution, the pores and fissures, and the roughness of the coal surface significantly increased, and the change trend was consistent with wettability, which indicated that the contact of alkaline solution with the coal structure was the main reason for the enhancement of coal wettability. The study provided experimental support for application of alkaline solution in coal mine dust removal, and had potential application foreground.

Keywords: Alkaline solution; Coal dust; Wettability; Contact angle; Reverse permeation; Microstructure

INTRODUCTION

Coal dust is one of the main disaster sources in coal mines; it not only causes pneumoconiosis of miners, reduces the service life of equipment, but also causes serious casualties such as coal dust explosions. The traditional methods of dedusting mainly rely on coal seam water infusion and water mist spraying, but the coal dust is not easy to be quickly wetted and agglomerated by water because of its hydrophobicity and the large surface tension of water [1]. The coal mines have achieved a certain effect in dust removal by adding sodium salts, surfactants and other agents to reduce the surface tension of water [2-6]. However, the over-standard concentration of dust is still a serious security problem in coal production because the coal seam water infusion is difficult and coal water content rate does not reach the standard.

There is a significant amount of organic matter in low-rank coals, which can react with alkaline solution to significantly change the physicochemical structure [7, 8]. In addition, low-rank coals are rich in various organic components and minerals, and some scholars have found that sulfurous functional groups and minerals in coal are easy to react with alkaline solution, which is mainly used in coal chemical industry for deashing, desulfurization and catalysis [9-12].

Recently, researchers have found that alkaline solution can significantly reduce the mechanical strength of coal, which is beneficial to the prevention of rock burst [13, 14] and H_2S disasters in mines [15]. Besides, alkaline solution can improve the pore structure of the coal reservoir and is beneficial to the seepage and extraction of gas [16-17]. However, the research of alkaline solution for the control of coal dust has not received enough attention. In order to explore the feasibility of coal dust treatment with alkaline solution, various indices of coal wettability such as contact angle, pulverized coal sedimentation, reverse permeation and microstructures were analyzed in this paper to provide a reference for the extended application of alkaline solution in coal mine dust removal.

SAMPLE COLLECTION AND ANALYSIS

Fresh coal samples were collected from the coal face of the Qianqiu mine in Yima, Henan, the Yongdingzhuang mine in Datong, Shanxi, and the Shaqu mine in Liulin, Shanxi respectively. The industrial components and the vitrinite reflectance were analyzed (Table 1).

---

* To whom all correspondence should be sent:
E-mail: 569689819@qq.com

Table 1 Coal sample information

Sample source	Horizon	Times	V_{daf}%	M_{ad}%	A_{ad}%	Coal rank	$R_{o,max}$%
Qianqiu mine	2-3	J_2y	40.01	0.98	10.31	Bituminous D	0.56
Yongdingzhuang mine	14#	J_2d	32.15	2.33	3.33	Bituminous C	0.74
Shaqu mine	4#	P_1sh	22.31	2.09	8.32	Bituminous B	1.51

EXPERIMENTAL RESULTS AND DISCUSSION

Contact angle experiment

The bituminous D, bituminous C and bituminous B coal samples were dried and pulverized into 200 mesh, and each coal sample was divided into four parts. One of the four parts was the raw coal sample and was numbered D0, C0, B0, respectively; the others were soaked in 0.2 mol/L, 0.5 mol/L and 1 mol/L NaOH for 5 days, numbered D1, C1, B1, D2, C2, B2, D3, C3, B3, respectively. Then the coal samples were cleaned, centrifuged, and dried, respectively, together with the raw coal sample. Then the pulverized coal was made into a round calendaring plane test piece with a mean thickness of 1 mm. The contact angle between each test piece and water was measured by JC2000B2 three times in different positions (Figure 1). The averages are shown in Table 2. The contact angles between the raw coal samples and water were more than 90°, as seen in Table 2, showing strong hydrophobicity and poor wettability. However, the contact angles sharply decreased after soaking the samples in alkaline solution, which indicated that the hydrophilicity and the wettability of the coal samples increased. With the increase in alkaline solution concentration, the contact angle decreased in a different degree. Especially the change of contact angle of bituminous D belonging to low-rank coal is most obvious, the contact angle decreased from 106.5° to 41°, and the decrease amplitude was more than 60%; the contact angle of bituminous C decreased from 109.5° to 63°, and the decrease amplitude was more than 40%; the contact angle of bituminous B decreased from 97.5° to 63.5°, and the decrease amplitude was more than 30%. The results showed that the contact angle gradually decreased with the increase in coal metamorphism.

Sedimentation experiment of pulverized coal

After soaking the pulverized coal in different concentrations of alkaline solution for 5 days , the samples were dried, the sedimentation experiment was carried out together with the raw coal (Figure 2). The sedimentation effect becomes worse with the increase in coal metamorphism: the sedimentation effect of bituminous D is the best, followed by bituminous C and bituminous B. The sedimentation effect of coal samples soaked in different concentrations of alkaline solution follows the rule 0.2 mol/L < 0.5mol/L < 1 mol/L and the raw coal has basically no sedimentation.
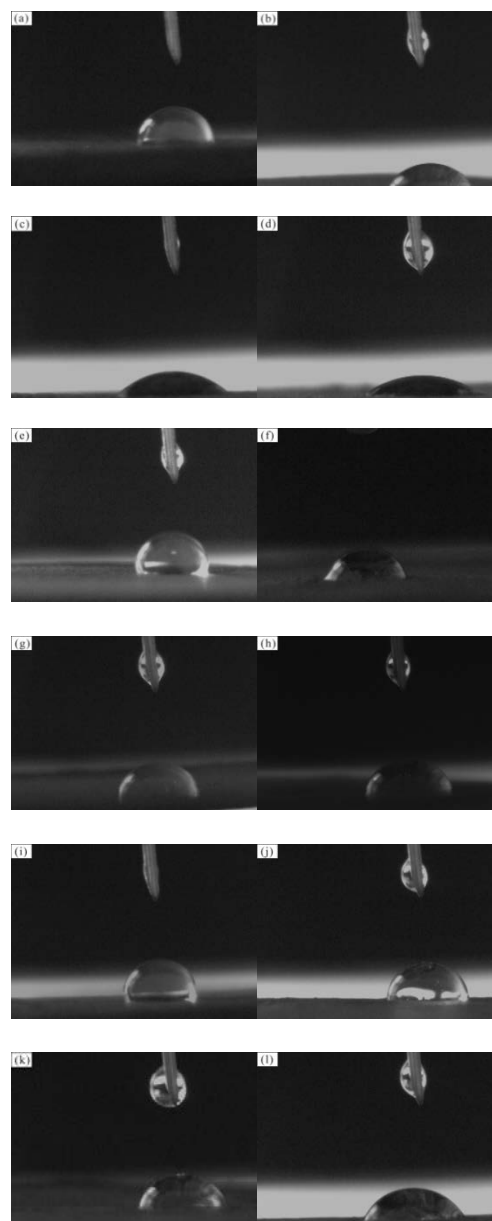
Fig.1. Changes of contact angle of coal soaked in NaOH solutions of different concentrations ((a, e, i) represent D0, C0, B0; (b, f, j) represent D1, C1, B1; (c, g, k) represent D2, C2, B2; (d, h, l) represent D3, C3, B3; respectively).

At the sedimentation time of 15~30 min, all bituminous B samples displayed no changes in sedimentation, while bituminous D and bituminous C after alkaline solution treatment have sedimented and the raw coal (bituminous D, bituminous C) little changed.
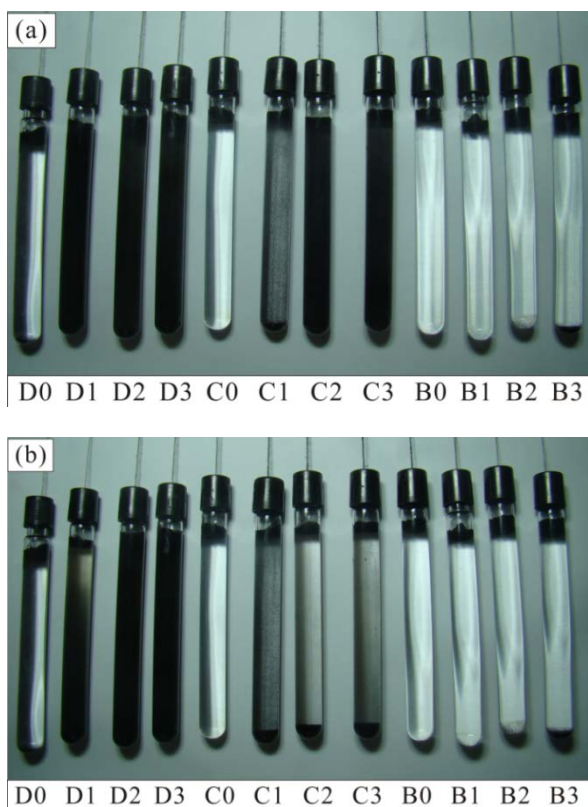
Fig. 2. Sedimentation changes of coal samples soaked in alkaline solution over time (a) 15 min; (b) 45 min.

Reverse permeation experiment of pulverized coal

The experimental device of the reverse permeation is shown in Figure 3. The pulverized coal of 1 g was put into a glass tube with an inner diameter

of 5.5 mm, height of 10 cm and tap of which the bottom end was sealed with permeable rubberized fabric and put it into water. When the liquid height in the glass tube no longer raised, the glass tube was taken out to calculate the weight of the pulverized coal. Each sample was measured 3 times. The averages are shown in Table 3 and Figure 4. As seen in Figure 4, the water absorption of the raw coal is relatively poor. However, the water absorption significantly increased after NaOH treatment. As the concentration of alkaline solution increased, the water absorption gradually increased, but the change range was relatively small when the concentration of alkaline solution was between 0.5 mol/L and 1 mol/L.
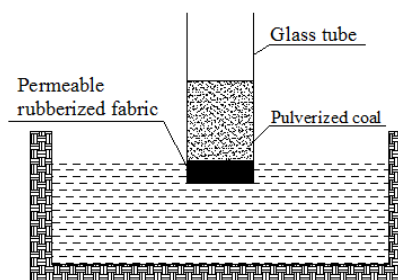
Fig. 3. Experimental device of the reverse permeation.

Compared with bituminous C and bituminous B samples, the metamorphic degree of bituminous D is lower, and the water absorption effect is the most obvious after NaOH treatment, while the change range of the medium-rank coal (bituminous C, bituminous B) is far less than of bituminous D.

Table 2. Test results of contact angle (/°)

Bituminous D		Bituminous C		Bituminous B	
Sample number	Contact angle	Sample number	Contact angle	Sample number	Contact angle
D0	106.5	C0	109.5	B0	97.5
D1	62.5	C1	105	B1	93.5
D2	47	C2	81	B2	74.5
D3	41	C3	63	B3	63.5

Table 3. Water absorption of the raw coal and the coal samples soaked in alkaline solution/g.

Sample number	Water absorption	Sample number	Water absorption	Sample number	Water absorption
D0	0.0128	C0	0.0045	B0	0.0022
D1	0.5041	C1	0.1421	B1	0.1855
D2	0.6786	C2	0.2174	B2	0.2844
D3	0.6796	C3	0.2584	B3	0.3527
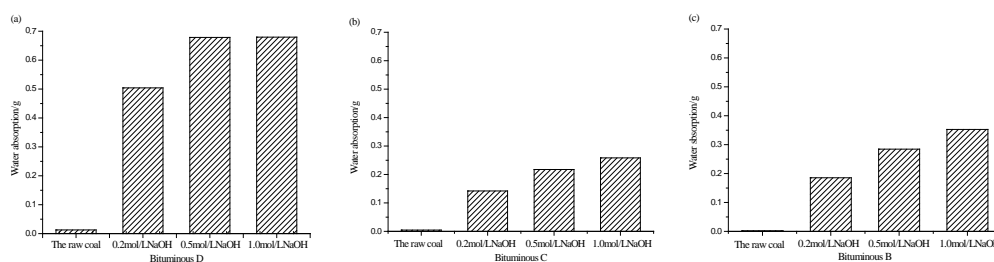
Fig.4. Comparison of water absorption of the raw coal and the coal samples soaked in alkaline solution (a) Bituminous D; (b) Bituminous C; (c) Bituminous C.

Experiment of alkaline solution on the surface structure of coal

Small pieces of bituminous D, bituminous C and bituminous B coal were prepared and soaked in 0.2 mol/L, 0.5 mol/L, 1.0 mol/L NaOH solution for 5 days, respectively. Then the treated coal and raw coal samples were dried in oven and were placed into the 108 Auto Cressington Sputter Coater to pump vacuum, plat with gold, and then were observed by Quanta 250 environmental scanning elecrron microscope (Figure 5).
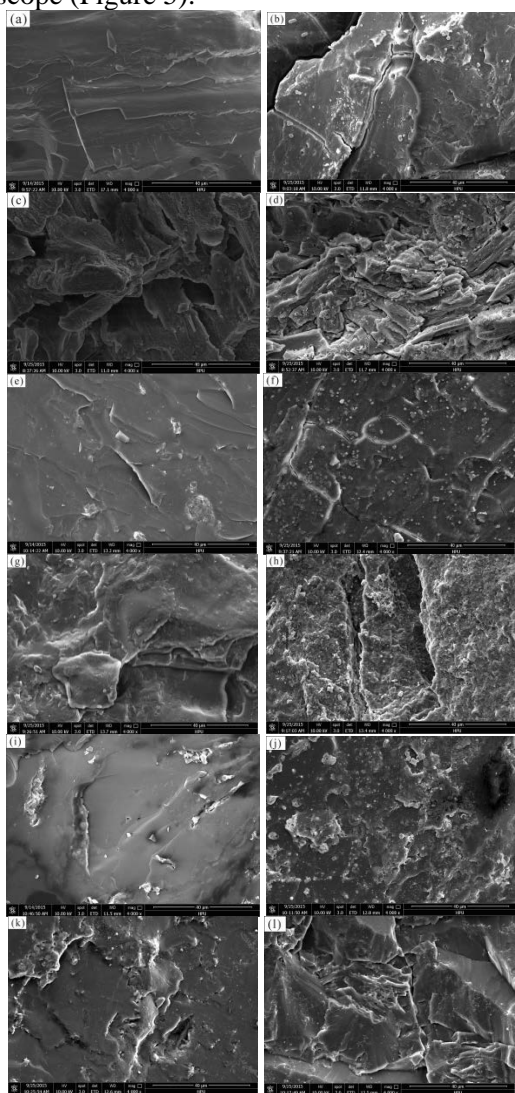
Fig.5. Variation characteristics of the surface structure of the coal samples before and after treatment with the alkaline solution ((a, e, i) represent D0, C0, B0; (b, f, j) represent D1, C1, B1; (c, g, k) represent D2, C2, B2; (d, h, l) represent D3, C3, B3; respectively).

By comparing the micro-morphology of the coal samples before and after treatment with the alkaline solution (Figure 5), we found that the surface of the raw coal was flat and smooth. However, the surface of the coal sample appeared more microporous and the roughness increased markedly after soaking in the alkaline solution. The effect of alkaline solution

on coal samples gradually weakened when the metamorphic degree of coal increased. The surface of bituminous D was seriously etched after soaking in 1 mol/l NaOH, while the change degree of bituminous B was relatively small. When the concentration of alkaline solution decreased, the etching on coal surface gradually decreased.

CONCLUSIONS

The results of contact angle, pulverized coal sedimentation, and reverse permeation experiments showed that the wettability of raw coal is poor, but significantly increased after NaOH treatment. The wetting effect gradually weakened when the metamorphic degree of coal increased, but the wettability correspondingly increased when the concentration of alkaline solution increased, and the change range was stable.

The microstructure observation proved that the surface porosity and roughness significantly increased after NaOH treatment, and the change trend was basically identical with that of the results of wettability experiments, which means that the change of coal structure caused by alkaline solution was the internal factor of wettability improvement. Besides the effect on bump proneness of coal, permeability and H_2S disaster, the alkaline solution can effectively improve wettability of pulverized coal and has a significant engineering value on the reduction of coal dust.

REFERENCES

1. Zh.B. Zhao, C. Yang, Ch.Y. Sun, X.Q. Shu, *J. China Coal Soc.*, **36**, 442 (2011).
2. Q.G. Yao, C.C. Xu, Y.S. Zhang, D. Wang, *Process Safety&Environ. Protection*, **111**, 726 (2017).
3. J.L. Li, F.B. Zhou, H. Liu, *Int. J. Coal Prepar. Utiliz.,* **36**, 192 (2015).
4. J. Yang, Y.Zh. Tan, Zh.H. Wang, Y.D. Shang, W.B. Zhao, *J. China Coal Soc,*, **32**, 737 (2007).
5. K.S. Zeng, N.L Hu, W.M. Cheng, G. Zhou, P. Yang, *J. China Coal Soc.*, **34**, 1675 (2009).
6. Z. Xi, M. Jiang, J. Yang, X. Tu, *Process Safety&Environ. Protection*, **92**, 637 (2014).
7. S. Erdogan, M. Zahir Duz, M. Merdivan, C. Hamamci, *Energy Sources*, **27**, 423 (2005).

8. C. Xu, S.S. Yu, X.S. Cong, J.S. Ma, N. Nie, J.X. Chen, *J. Shenyang Univ. Chem. Technol.*, **25**, 35 (2011).

9. J. Xiao, F.Ch. Li, S.Y. Deng, Q.F. Zhong, Y.Q. Lai, J. Li, *J. Central South Univ. (Science and Technology)*, **47**, 14 (2016).

10. N. Mketo, P. N. Nomngongo, J. C. Ngila, *Environ. Sci. Pollution Res. Int.*, **24**, 19852 (2017).

11. B. Baatar, T. Ganerdene, M. Myekhlai, U. Otgonbayar, C. Majaa, Y. Turmunkh, N, Javkhlantugs, *Energy Sources, Part A, Recovery, Utilization & Environmental Effects*, **39**, 1 (2017).

12. P. S. Dash, S. S. Kumar, P. K. Banerjee, S. Ganguly, *Mineral Process. Extract. Metallurgy Review*, **34**, 223 (2013).

13. H.Y Guo, X.B. Su, D.P. Xia, J.Q. Ma, Sh. B. Zhang, X. Liu, J.X. Song, H.X. Lin, ZL 201310010316.4.

14. D.P Xia, H.Y. Guo, Y. Luo, J.Q. Ma, Sh.L. Chen, Zh. Wang, *J. China Coal Soc.*, **40**, 1768 (2015).

15. K.X. Wang, X.H. Fu, *Coal Sci. Technol.*, **35**, 94 (2007).

16. L.L. Song, L. Feng, J.T. Liu, Y. Zhang, X.H. Wang, Zh.Y. Miao, *J. China University of Mining & Technology*, **41**, 629 (2012).

17. C.X. Hou, Sh. Zhang, Y.H. Liang, J.W. Du, L.H. Fan, *Coal Conversion*, **39**, 19 (2016).

ЕКСПЕРИМЕНТАЛНО ИЗСЛЕДВАНЕ НА ВЪЗМОЖНОСТИТЕ ЗА НАМАЛЯВАНЕ НА ВЪГЛИЩНИЯ ПРАХ С ПОМОЩТА НА АЛКАЛЕН РАЗТВОР

Х. Гуо[1, 2, 3], Ж. Гао[1], Ч. Фу[1], И. Луо[1], Д. Ксиа[1, 3] *

[1] *Държавна и местна инженерна лаборатория за дрениране на газ и контрол на терена на дълбоки мини (Политехнически университет на Хенан), Джаозуо 454000, Китай*

[2] *Държавна лаборатория и и култивационна база за газова геология и газов контрол (Политехнически университет на Хенан), Джаозуо 454000, Китай*

[3] *Съвместен иновационен център по въглищен метан и шистов газ за икономическата област на Централните равнини, Джаозуо 454000, Китай*

(Резюме)

За изследване на възможностите за намаляване на въглищния прах в мини с помощта на алкален разтвор са взети три представителни проби от битуминозни D, битуминозни C, и битуминозни B въглища с различна степен на метаморфоза и са държани съответно в 0.2 mol/L, 0.5 mol/L и 1.0 mol/L NaOH в продължение на 5 дни. Промяната на умокряемостта на въглищата е проследена чрез измерване на контактния ъгъл, седиментацията на прахообразните въглища, обратната пропускливост и SEM. Установено е, че контактният ъгъл на въглищните проби намалява след престоя в алкален разтвор, ь обратната пропускливост и утаяването на прахообразните въглища нарастват. Същевременно, индексът на умокряне на въглищата клони към намаляване при понижаване на степента на метаморфоза и повишаване на концентрацията на NaOH. След престой в алкален разтвор порите и цепнатините, както и грапавостта на въглищната повърхност значително се увеличават и тази тенденция е в съгласие с умокряемостта. Това показва, че контактът на алкалния разтвор с въглищната структура е основната причина за повишаване на умокряемостта. Изследването дава експериментално потвърждение за приложението на алкален разтвор за отстраняване на въглищен прах.

Instructions about Preparation of Manuscripts

General remarks: Manuscripts are submitted in English by e-mail The text must be typed on A4 format paper using Times New Roman font size 11, normal character spacing. The manuscript should not exceed 15 pages (about 3500 words), including photographs, tables, drawings, formulae, etc. Authors are requested to use margins of 2 cm on all sides

Manuscripts should be subdivided into labelled sections, e.g. **Introduction, Experimental, Results and Discussion**, *etc*. **The title page** comprises headline, author's names and affiliations, abstract and key words. Attention is drawn to the following:

a) **The title** of the manuscript should reflect concisely the purpose and findings of the work. Abbreviations, symbols, chemical formulas, references and footnotes should be avoided. If indispensable, abbreviations and formulas should be givenin parentheses immediately after the respective full form.

b) **The author**'s first and middle name initials and family name in full should be given, followedby the address (or addresses) of the contributing laboratory (laboratories). **The affiliation** of the author(s) should be listed in detail by numers (no abbreviations!). The author to whom correspondence and/or inquiries should be sent should be indicated by asterisk (*) with e-mail address.

The abstract should be self-explanatory and intelligible without any references to the text andcontaining not more than 250 words. It should be followed by key words (not more than six).

References should be numbered sequentially in the order, in which they are cited in the text. The numbers in the text should be enclosed in brackets [2], [5, 6], [9–12], etc., set on the text line. References are to be listed in numerical order on a separate sheet. All references are to be given in Latin letters. The names of the authors are given without inversion. Titles of journals must be abbreviated according to Chemical Abstracts and given in italics, the volume is typed in bold, the initial page is given and the year in parentheses. Attention is drawn to the following conventions:a) The names of all authors of a certainpublications should be given. The use of "*et al*." inthe list of references is not acceptable.b) Only the initials of the first and middle names should be given. In the manuscripts, the reference to author(s) of cited works should be made without giving initials, e.g. "Bush and Smith [7] pioneered...". If the reference carries the names of three or more authors it should be quoted as "Bush *et al*. [7]", if Bush is the first author, or as "Bush and co-workers [7]", if Bush is the senior author.

Footnotes should be reduced to a minimum. Each footnote should be typed double-spaced at thebottom of the page, on which its subject is first mentioned.**Tables** are numbered with Arabic numerals on the left-hand top. Each table should be referred to inthe text. Column headings should be as short as possible but they must define units unambiguously.The units are to be separated from the preceding symbols by a comma or brackets. Note: The following format should be used when figures, equations, *etc*. are referred to the text (followed by the respective numbers): Fig., Eqns., Table, Scheme.

Schemes and figures. Each manuscript should contain or be accompanied by the respective illustrative material as well as by the respective figure captions in a separate file (sheet).As far as presentation of units is concerned, SI units are to be used. However, some non-SI units are also acceptable, such as °C, ml, l, etc.The author(s) name(s), the title of the manuscript, the number of drawings, photographs, diagrams, etc., should be written in black pencil on the back of the illustrative material (hard copies) inaccordance with the list enclosed. Avoid using more than 6 (12 for reviews, respectively) figures in the manuscript. Since most of the illustrative materials are to be presented as 8-cm wide pictures, attention should be paid that all axis titles, numerals, legend(s) and texts are legible.

The authors are required to submit the text with a list of three individuals and their e-mail addresses that can be considered by the Editors as potential reviewers. Please, note that the reviewers should be outside the authors' own institution or organization. The Editorial Board of the journal is not obliged to accept these proposals.

The authors are asked to submit **the final text** (after the manuscript has been accepted for publication) in electronic form by e-mail. The main text, list of references, tables and figure captions should be saved in separate files (as *.rtf or *.doc) with clearly identifiable file names. It is essential that the name and version of the word-processing program and the format of the text files is clearly indicated. It is recommended that the pictures are presented in *.tif, *.jpg, *.cdr or *.bmp format.

The equations are written using "Equation Editor" and chemical reaction schemes are written using ISIS Draw or ChemDraw programme.

EXAMPLES FOR PRESENTATION OF REFERENCES

REFERENCES
1. D. S. Newsome, *Catal. Rev.–Sci. Eng.*, **21**, 275 (1980).
2. C.-H. Lin, C.-Y. Hsu, *J. Chem. Soc. Chem. Commun.*, 1479 (1992).
3. R. G. Parr, W. Yang, Density Functional Theory of Atoms and Molecules, Oxford Univ. Press, New York, 1989.
4. V. Ponec, G. C. Bond, Catalysis by Metals and Alloys (Stud. Surf. Sci. Catal., vol. 95), Elsevier, Amsterdam, 1995.
5. G. Kadinov, S. Todorova, A. Palazov, in: New Frontiers in Catalysis (Proc. 10th Int. Congr. Catal., Budapest,(1992), L. Guczi, F. Solymosi, P. Tetenyi (eds.), Akademiai Kiado, Budapest, 1993, Part C, p. 2817.
6. G. L. C. Maire, F. Garin, in: Catalysis. Science and Technology, J. R. Anderson, M. Boudart (eds), vol. 6, SpringerVerlag, Berlin, 1984, p. 161.
7. D. Pocknell, *GB Patent* 2 207 355 (1949).
8. G. Angelov, PhD Thesis, UCTM, Sofia, 2001, pp. 121-126.
9 JCPDS International Center for Diffraction Data, Power Diffraction File, Swarthmore, PA, 1991.
10. CA **127**, 184 762q (1998).
11. P. Hou, H. Wise, *J. Catal.*, in press.
12. M. Sinev, private communication.
13. http://www.chemweb.com/alchem/articles/1051611477211.html.

Texts with references which do not match these requirements will not be considered for publication!!!

CONTENTS

СЪДЪРЖАНИЕ